Institut National de la Recherche Scientifique (INRS)
Énergie Matériaux Télécommunications (EMT)

Strong Light-Matter Interaction in Terahertz Plasmonic Nano-Resonators

Par

Xin Jin

Thèse présentée pour l'obtention du grade de Philosophiæ Doctor (Ph.D.)
en Sciences de l'Énergie et des Matériaux

Jury d'évaluation

Président du Jury et Examinateur Interne	François Vidal INRS-EMT, Université du Québec
Examinateur Externe	Pablo Bianucci Université Concordia
Examinateur Externe	François Blanchard École de Technologie Supérieure
Directeur de Recherche	Luca Razzari INRS-EMT, Université du Québec

ACKNOWLEDGEMENTS

I would like to thank my supervisor Prof. Luca Razzari for his constant support, brilliant guidance, and great encouragement that he has provided throughout my doctoral study. I am deeply grateful to him for recruiting me as his Ph.D. student, which offered me an excellent opportunity to learn a large amount of knowledge, to have chance to embrace the cutting-edge technologies, to prove myself the capability of starting a scientific career in future. I have been so fortunate to have a supervisor who cared so much about my study, my work, and my life as well. His remarkable insight and enthusiasm in my research inspired me a lot and gave me a new level of confidence. His careful editing contributed enormously to the production of our scientific publications and of course also this thesis. Being able to study under his supervision is one of the most important achievements in my life.

I am eternally grateful to my mother Qingzhu Zheng and my father Yongri Jin. If without their love and encouragement, I would have never fulfilled my dreams one by one. They gave me life and taught me being a person with essential virtues such as integrity, loyalty, and responsibility. All of these help me establishing confidence and winning respect. All through my childhood till now, I cherish and enjoy all the beautiful moments with my parents, and I will never forget. I love them forever.

I sincerely want to thank Prof. Andrea Toma from the Italian Institute of Technology, who gave me invaluable support during my whole Ph.D. period. I also profoundly thank Andrea Cerea and Vincenzo Aglieri, who fabricated and characterized a myriad of samples for me. Without their help, my designs would never embrace reality.

I also sincerely thank Prof. Jérôme Claverie and Prof. Jianming Zhang. They are my collaborators and best friends. I thank Jérôme for his hospitality; I enjoyed many lunches and dinners with him, his friends and family, including every year's Christmas. I thank Jianming very much for the brotherhood we shared; he encouraged me a lot, and always helped me to move forward.

I want to thank my former supervisor during my Master's period, Prof. Zhengbiao Ouyang. If without his encouragement, I would never go abroad to pursue my Ph.D. degree. He cultivated the essential qualities of my scientific research, which I benefited a lot during my doctoral study.

I thank all the members of my thesis evaluation committee. They are Prof. François Vidal, Prof. Pablo Bianucci, Prof. François Blanchard, and Prof. Luca Razzari. I appreciate their time

and efforts to evaluate my thesis. The quality of my thesis has been significantly improved after their valuable comments and suggestions.

I also sincerely thank all the members of my research group. They are Riccardo Piccoli, Younggyun Jeong, Andrea Rovere, Vincenzo Aglieri, Diego Caraffini, Luca Zanotto, Atiye Pezeshki, and Yuechen Jia. I appreciate their tremendous help. In particular, I would like to convey my sincere gratitude to Riccardo and Younggyun for their altruistic support. I have been working with these two guys almost five years, they supported me in many aspects of research and life, including improving the quality of this thesis.

I thank all the internship students I have supervised till now. They are Pablo Israel Morales-Guzmán, Artem Nazartchouk, Ulises Félix Rendon, Dilyn Fullerton, Siwei Luo, and Jean-Baptiste Billeau. They helped me to speed up my research in many different aspects. Meanwhile, I also learned a vast scope of knowledge from them.

I thank all the friends at INRS, including Holger Breitenborn, Alessandro Tomasino, Shuhui Sun, Gaixia Zhang, Miao Wang, Qiliang Wei, Daling Cui, Fan Yang, Xin Chai, Qingzhe Zhang, Élissa Haddad, Maxime Pinsard, etc. In particular, I thank Élissa for the French text translation. Special thanks to my officemates Fabiola Navarro Pardo, Juan Carlos Abrego Martínez, Domenico Bongiovanni, Jiabin Liu, and Patrick Kilcullen. I thank them very much for their great kindness and friendship. I really enjoyed the office past-time with them.

I thank all the collaborators during my doctoral period. Besides the names mentioned above, they are Prof. Roberto Morandotti, Prof. Mirko Prato, Prof. Andrea Perucchi, Gabriele C. Messina, Prof. Stefano Lupi, Francesco De Donato, Francisco Palazon, Paola Di Pietro, Francesco De Angelis, Prof. Remo Proietti Zaccaria, Prof. Hong Liu, Prof. Hua Zhang, Prof. Fiorenzo Vetrone, Prof. Dongling Ma, Prof. Emanuele Orgiu.

I thank the departmental and technical staff at INRS-EMT. They are kind, helpful, and have beautiful hearts. For example, I just name a few, Ms. Hélène Sabourin, Prof. Tsuneyuki Ozaki, Ms. Hélène Tanguay, Ms. Louis Hudon, and Ms. Michelle Marcotte.

Finally, I wish to acknowledge the following organizations for their financial support: the Natural Sciences and Engineering Research Council of Canada (NSERC) and the Fonds de recherche du Québec – Nature et technologies (FRQNT).

RÉSUMÉ

Les phonons sont des vibrations de réseau quantifiées qui représentent un canal important de dissipation d'énergie dans les systèmes à l'état solide, en particulier actuellement en nanophotonique et en nanoélectronique. Étant donné que la réponse phononique est généralement considérée comme une caractéristique essentielle d'un matériau spécifique, elle peut créer un goulot d'étranglement ultime par exemple en limitant le fonctionnement des nanodispositifs fonctionnels par rapport au transport de charge et à l'émission de lumière. Pour surmonter ce goulot d'étranglement, la modification du niveau d'énergie des phonons des nanomatériaux peut ouvrir une nouvelle plateforme de réacheminement de l'énergie dissipée. Ainsi, le sujet principal de ma thèse consiste à examiner la possibilité de modifier la réponse phononique optique des nanomatériaux en exploitant le couplage fort dans les nanocavités térahertz. À cet égard, comme preuve de principe, j'ai étudié le mode de phonon optique de Fröhlich dans les nanocristaux semi-conducteurs polaires, car il est reconnu pour son couplage efficace avec le rayonnement térahertz. D'autre part, les nanocavités plasmoniques térahertz sont généralement les nanogaps situés entre les extrémités des nanoantennes plasmoniques, qui peuvent efficacement capter la lumière térahertz et la réduire à l'échelle nanométrique. Par conséquent, mon système de banc d'essai est obtenu en combinant la résonance de phonon optique de Fröhlich de nanocristaux de sulfure de cadmium et des nanocavités plasmoniques térahertz. En couplant ces phonons de Fröhlich à des plasmons térahertz, j'espère ouvrir une série de pistes de recherche prometteuses pour la manipulation de l'interaction lumière-matière dans les térahertz à l'échelle nanométrique.

Grâce à une conception et à une modélisation minutieuses du système, nous avons obtenu un fort couplage plasmon-phonon qui a conduit à l'hybridation de la résonance phononique, bien visible dans les mesures térahertz directes. De plus, il a été constaté que la réponse phononique de Fröhlich aux dipôles actifs des nanocristaux de sulfure de cadmium était modifiée, même en l'absence d'illumination térahertz directe, via le champ électrique du vide élevé des nanocavités plasmoniques, comme le montrent les mesures Raman. Les propriétés vibrationnelles intrinsèques des nanoparticules étudiées se sont révélées très différentes à l'intérieur et à l'extérieur des nanocavités. En outre, dans les nanocavités, le signal Raman de la résonance hybride semble être augmenté d'environ deux ordres de grandeur. Pour améliorer encore plus la force du couplage, j'ai également conçu une structure de nanoantenne en forme de lune, qui améliore le champ et réduit le volume modal, tout en garantissant un couplage plus efficace.

Les résultats de cette thèse donnent accès à une myriade de perspectives excitantes tant au niveau fondamental, comme pour l'émission de lumière vibro-polaritonique et les non-linéarités accrues par fort couplage plasmon-phonon, qu'à un niveau plus appliqué tel que pour la résolution des problèmes qui nuisent au fonctionnement optimal des dispositifs électroniques à l'échelle nanométrique.

Mots clés: Couplage fort vibrationnel, Technologie térahertz, Plasmonique, Nanocristaux.

ABSTRACT

Phonons are quantized lattice vibrations that represent a significant channel of energy dissipation in solid-state systems, especially in nowadays nanophotonics and nanoelectronics. Since the phonon response is usually considered as an essential feature of a specific material, it may set an ultimate bottleneck that restricts the operation of functional nanodevices, such as limited charge transport and light emission. To overcome this bottleneck, modifying the phonon energy level of nanomaterials may open a new platform for rerouting the dissipated energy. Thus, the main focus of my thesis is to investigate the possibility of modifying the optical phonon response of nanomaterials by exploiting strong coupling in terahertz nanocavities. In this regard, as a proof of principle, I have studied the Fröhlich optical phonon mode of polar semiconducting nanocrystals, since it is known to effectively couple to terahertz radiation. On the other hand, terahertz plasmonic nanocavities are usually the nanogaps between plasmonic nanoantenna tips which can efficiently harvest the terahertz light and squeeze it into the nanoscale. Therefore, my testbed system is obtained combining the Fröhlich optical phonon resonance of cadmium sulfide nanocrystals and terahertz plasmonic nanocavities. By coupling these Fröhlich phonons with terahertz plasmons, I expect to open up a series of promising research directions for the manipulation of terahertz light-matter interaction at the nanoscale.

Through careful design and modeling of the system, we have achieved a strong plasmon-phonon coupling that resulted in the hybridization of the phonon resonance, well visible in direct terahertz measurements. Moreover, the dipole-active Fröhlich phonon response of the cadmium sulfide nanocrystals was found to be modified even in the absence of a direct terahertz illumination, via the high vacuum electric field of plasmonic nanocavities, as shown by Raman measurements. The intrinsic vibrational properties of the investigated nanoparticles were found to be very different inside and outside of the nanocavities. In addition, in the nanocavities, the Raman signal of the hybridized resonance appears to be enhanced by about two orders of magnitude. To improve the coupling strength further, I also designed a moon-shaped nanoantenna structure, which features an increased field enhancement and a reduced mode volume and guarantees a more efficient coupling.

The findings of this thesis can open a myriad of exciting perspectives both at the fundamental level such as vibro-polaritonic light emission, enhanced nonlinearities by plasmon-phonon strong coupling, as well as at the more applied one such as overcoming the issues that hamper the optimal operation of nanoscale electronic devices.

Keywords: Vibrational strong coupling, Terahertz technology, Plasmonics, Nanocrystals.

TABLE OF CONTENTS

COVER ..... **I**
ACKNOWLEDGEMENTS ..... **I**
RÉSUMÉ ..... **III**
ABSTRACT ..... **IV**
TABLE OF CONTENTS ..... **V**
LIST OF FIGURES ..... **VIII**
LIST OF TABLES ..... **XVI**
LIST OF ABBREVIATIONS ..... **XVII**
LIST OF PUBLICATIONS (DURING THE DOCTORAL PERIOD) ..... **XVIII**
1. PUBLICATIONS RELATED TO THIS THESIS WORK XVIII
2. OTHER PUBLICATIONS XX
LIST OF SCHOLARSHIPS AND AWARDS (DURING THE DOCTORAL PERIOD) ..... **XXII**
1 INTRODUCTION **1**
1.1 MOTIVATION AND OBJECTIVE 1
1.2 LIGHT-MATTER INTERACTION IN ELECTROMAGNETIC WAVE CAVITIES 2
1.3 STRONG COUPLING EXPERIMENTS: FROM FABRY-PEROT CAVITIES TO PLASMONIC NANORESONATORS AND FROM ELECTRONIC TRANSITIONS TO PHONONS 9
1.4 THESIS ORGANIZATION AND ACHIEVEMENTS 19
2 THEORETICAL DESCRIPTION OF A LIGHT-MATTER COUPLING SYSTEM **20**
2.1 CLASSICAL COUPLED-OSCILLATOR MODELS 20
2.1.1 An Analogy - Mechanical Model *20*
2.1.2 Two-Coupled-Oscillator Model *24*
2.1.3 Power Dissipation in the Damped Model *25*
2.1.4 Splitting Spectrum of Unevenly-Damped Oscillators *26*
2.1.5 Power Dissipation in the Damped Three-Coupled-Oscillator Model *28*
2.2 PHENOMENOLOGICAL QUANTUM MODELS 29
2.2.1 Two-Level Coupling System *29*
2.2.2 Damped Model for Two-Level coupling System *30*
2.2.3 Three-Level Coupling System *31*
3 DESIGNING A PLASMON-PHONON COUPLING SYSTEM: BASIC CONCEPTS **33**
3.1 DRUDE MODEL FOR GOLD THIN FILMS IN THE THZ REGION 33
3.2 LORENTZ MODEL FOR SEMICONDUCTORS 35
3.3 SURFACE PHONONS OF SEMICONDUCTING NANOCRYSTALS 37
3.3.1 Bulk Permittivity of Polar Semiconductors in the Reststrahlen Region *37*

3.3.2 Surface-Phonon Resonance of a Polar Semiconducting Nanocrystal 39
3.3.3 An Effective Medium Theory – The Maxwell-Garnett Mixing Rule 41
3.4 Locating the Lattice Modes: Wood-Rayleigh Anomalies 42
3.5 Numerical Simulation Environment 45
3.6 Setting the Illumination Condition 46
3.7 Calculation of Absorption, Scattering, and Extinction Cross-Sections 48
3.8 Calculation of the Mode Volume 49

4 PHONON RESONANCE MODIFICATION OF NANOCRYSTALS INSIDE A THZ PLASMONIC NANOCAVITY 50
4.1 Design of End-to-End Nanoantenna Arrays in Numerical Simulations 51
4.1.1 Simulation Platform and General Settings 51
4.1.2 Setting the Background Field 53
4.1.3 Extracting the Permittivity of CdS Nanocrystals from the Experimental Results 55
4.1.4 Verifying the Appropriateness of the Effective Medium Theory to Describe Compact Layers of Nanocrystals 56
4.1.5 Simulated Array Response with and without CdS Nanocrystals 58
4.1.6 Estimation of the Mode Volume and the THz Vacuum Electric Field 60
4.1.7 Lattice Mode Calculation for the Nanoantenna Arrays 61
4.2 Nanoantenna Fabrication and Nanocrystal Synthesis 63
4.2.1 Fabrication of Gold Nanoantenna Arrays 63
4.2.2 Synthesis of CdS Nanocrystals 63
4.2.3 CdS@CdS Giant Nanocrystal Layer Preparation on THz Gold Nanoantenna Arrays 64
4.2.4 Estimation of the Number of Nanocrystal Layers 65
4.3 THz Characterization – Synchrotron Measurements 66
4.4 Raman Measurements 68
4.4.1 Evaluation of the Rabi Splitting from the Raman Spectra 69
4.4.2 Polarization Properties of Raman Spectra 70
4.4.3 Estimation of the Raman signal enhancement for the hybridized resonance 72
4.5 Discussion 73
4.5.1 Phonon Resonance Hybridization in a THz Plasmonic Nanocavity 73
4.5.2 Scaling of the Rabi Splitting with the Number of Nanocrystal Layers: THz Spectroscopy and Raman Measurements 75
4.5.3 Fitting the Vibro-polariton Traces by Means of the Three-Coupled-Oscillator Model 78
4.5.4 The Extinction Spectrum Evaluated using the Dissipated Power Model 82
4.5.5 Chapter Summary and Impact 82

5 NOVEL NANOCAVITY DESIGN: MOON-SHAPED NANOANTENNAS 84
5.1 Design of the Moon-Shaped Nanoantenna Array 84

5.1.1 Inspiration 84
5.1.2 Geometrical Tuning of the Moon-Shaped Nanoantennas 85
5.1.3 Extracting the THz Response of a Monolayer of CdS Nanocrystals 88
5.1.4 Moon-shaped Nanoantenna Array Response with and without CdS Nanocrystals 88
5.1.5 THz Absorption of CdS Nanocrystals in the Gap of a Moon-Shaped Nanoantenna 90
5.1.6 Estimation of the Mode Volume and THz Vacuum Electric Field for Nanocavities of Moon-Shaped Nanoantennas 92
5.1.7 Lattice Modes for the Moon-Shaped Nanoantenna Arrays 93
5.1.8 Comparison between Simulation and Dissipated Power Calculation 93
5.2 Fabrication and THz Characterization 94
5.3 Discussion 97
6 CONCLUSION AND FUTURE WORKS 99
BIBLIOGRAPHY 102
SOMMAIRE RÉCAPITULATIF (SUMMARY IN FRENCH) 111
1 Motivation et objectif 111
2 Interaction lumière-matière dans les cavités électromagnétiques 113
3 Modification de la résonance de phonon de nanocristaux dans une nanocavité plasmonique THz 117
4 Une force de couplage améliorée dans les réseaux de nanoantennes en forme de lunes 127
5 Conclusion et travaux futurs 131
APPENDIX 135
1 Dissipated Power Calculation (Classical Two Coupled Oscillators) 135
2 Roots of the Three-level Coupling System (Phenomenological Quantum Model) 137
3 Decomposition of the Illumination Condition 138

LIST OF FIGURES

FIGURE 1.1 AN ATOM IN A RESONANT CAVITY: V_{MOD} IS THE MODE VOLUME, G_0 THE COUPLING STRENGTH, γ_1 THE CAVITY DECAY, AND γ_2 THE NON-RESONANT ATOMIC DECAY. 4

FIGURE 1.2 ILLUSTRATION OF THE JAYNES-CUMMING MODEL. WHEN THE PHOTON NUMBER IS "0", THERE IS STILL A RESONANCE SPLITTING DUE TO THE VACUUM FIELD. 6

FIGURE 1.3 (A) SKETCH OF A CAVITY QED SYSTEM WITH A SINGLE TWO-LEVEL ATOM. (B) SKETCH OF AN OPTICAL CAVITY COUPLED TO MANY QUANTUM EMITTERS. (C) AN EXAMPLE OF WEAK COUPLING: THE SPONTANEOUS- EMISSION DYNAMICS OF SINGLE QUANTUM DOTS CAN BE CONTROLLED BY A PHOTONIC- CRYSTAL NANOCAVITY [44]. (D) AN EXAMPLE OF STRONG COUPLING: RYDBERG ATOMS STRONGLY COUPLED TO A SUPERCONDUCTING MICROWAVE FABRY–PEROT RESONATOR, DISPLAYING CLEAR VACUUM RABI OSCILLATIONS IN TIME [27]. (E) AN EXAMPLE OF ULTRASTRONG COUPLING: MICROWAVE SPECTROSCOPY OF A SYSTEM WITH A SUPERCONDUCTING FLUX QUBIT COUPLED TO A COPLANAR- WAVEGUIDE RESONATOR [45]. (F) AN EXAMPLE OF DEEP COUPLING: MAGNETO- THZ TRANSMISSION MEASUREMENTS ON A THZ METAMATERIAL COUPLED TO THE CYCLOTRON RESONANCE OF A 2D ELECTRON GAS [46]. ALL PANELS IN THIS FIGURE ARE REPRODUCED WITH PERMISSION FROM REF [4], NATURE PUBLISHING GROUP. 8

FIGURE 1.4 (A)-(C) OBSERVATION OF THE VACUUM RABI SPLITTINGS WHEN CESIUM ATOMS ARE IN A FABRY-PEROT CAVITY (AS CAN BE SEEN, THE INTRA-CAVITY PHOTON NUMBER $\bar{N}$ IS WELL BELOW 1, CONFIRMING WEAK EXCITATION CONDITIONS). (D)-(E) OBSERVATION OF THE EXCITON-PHOTON STRONG COUPLING IN A SEMICONDUCTOR MICROCAVITY. (D) REFLECTION SPECTRA IN A MICROCAVITY STRUCTURE (MEASURED AT THE TEMPERATURE OF 5K) FOR VARIOUS DETUNING CONDITIONS. (E) SPLITTING PEAK POSITIONS AS A FUNCTION OF CAVITY MODE DETUNING. PANELS (A)-(C) AND (D)-(E) ARE REPRODUCED WITH PERMISSION FROM REF [48] AND REF [51], AMERICAN PHYSICAL SOCIETY..... 10

FIGURE 1.5 (A) SKETCH OF THE INVOLVED STRUCTURE. THE BLUE ARROW IN THE GAP BETWEEN THE NANOPARTICLE AND THE MIRROR LOCATES THE TRANSITION DIPOLE MOMENT OF THE EMITTER. THE INSET ABOVE SHOWS THE SIMULATED LOCAL FIELD OF THE PLASMONIC RESPONSE IN THE CAVITY, WITH MAXIMUM ELECTRIC FIELD ENHANCEMENT OF ABOUT 400, AND FIELD ORIENTED VERTICALLY (IN THE Z-DIRECTION). (B) SCATTERING SPECTRA RESULTING FROM ISOLATED SAMPLES ACCORDING TO THE ORIENTATION OF THE EMITTER. (C) COMPARISON OF SCATTERING SPECTRA FROM DIFFERENT SAMPLES. (D) RESONANT POSITIONS OF METHYLENE-BLUE (Ω_0), PLASMON (Ω_P) AND HYBRID MODES (Ω_+ AND Ω_-) AS A FUNCTION OF EXTRACTED DETUNING. FOR THE MEASUREMENTS CONDUCTED IN PANELS (B), (C) AND (D), THE NUMBER OF MOLECULES IN EACH CAVITY WAS ESTIMATED AS 100. (E) ENERGY OF RABI OSCILLATIONS VERSUS MEAN NUMBER OF DYE

molecules. All panels in this figure are reproduced with permission from Ref [59], Nature Publishing Group. 13

Figure 1.6 (a) Energy-level diagram representing Raman scattering under vibrational strong coupling. (b) Schematic description of the Fabry-Perot cavity used in the experiment, which is composed of two thin Ag mirrors spaced by a Polyvinyl acetate (PVAc) layer. (c) Transmission spectra of a thin PVAc film (red and dashed black curves, measured and calculated, respectively), a bare cavity detuned from the vibrational transition (dashed green), and the same cavity filled with molecules (blue). The inset shows the C=O band and uncoupled cavity mode dispersion. (d) Off-resonance Raman scattering measurement on the cavity (red) compared to a reference molecule film. (e) On-resonance transmission measurements of a bare cavity (dashed green) and of the same cavity filled with molecules (solid blue). (f) On-resonance Raman measurement. Upper (VP+) and lower (VP-) polaritons were observed with significant Raman enhancement. All panels in this figure are reproduced with permission from Ref [61], Wiley-VCH. 15

Figure 1.7 (a) Energy level sketch of the vibrational strong coupling system for IR emission. A thermal heater is placed beneath the Fabry-Perot microcavity (left). (b) Emissivity spectrum of a 4 mm thick film of PMMA at 100 °C (red curve) and transmission spectrum of PMMA (blue curve). (c) Emissivity (red curve) and simulated cavity reflection (black dashed curve) spectra of the strongly coupled cavity at 100 °C. All panels in this figure are reproduced with permission from Ref [30], ACS. 16

Figure 1.8 (a) Schematic cross-section showing the interface between a metallic split-ring structure and a silica layer on top of a silicon substrate. (b) Schematic detail of the split-ring resonator array. (c) Measured (blue) and simulated (red) resonant frequencies of the coupled system, compared to the analytical model for two coupled oscillators (black line). (d) Simulated normal mode splitting when the metasurface is directly in contact with the silica substrate. (e) Optical (left) and scanning electron microscope (right) images of the graphene nanoribbon array device. (f) Calculated loss plot with extracted peak frequencies overlaid. The red dashed line shows the calculated dispersion of the uncoupled graphene plasmon. The white, light grey and grey dashed lines show the calculated frequency of the three surface optical phonons. Panels from (a) to (d) in this figure are reproduced with permission from Ref [33], ACS. Panels (e) and (f) in this figure are reproduced with permission from Ref [35], ACS. 17

Figure 2.1 Mechanical analog of a coupled system 20

Figure 2.2 Motion and frequency analysis of two uncoupled (a) and coupled (b) oscillators. .. 23

FIGURE 2.3 (A) DISSIPATED POWER SPECTRUM AS A FUNCTION OF THE COUPLING STRENGTH *V*. (B) RABI SPLITTING AS A FUNCTION OF COUPLING STRENGTH. $\Omega_R^{(dis)}$ (BLUE) IS THE RABI SPLITTING EXTRACTED FROM THE CURVE OF DISSIPATED POWER DESCRIBED BY EQUATION (2.30), AND Ω_R (RED) IS THE RABI SPLITTING CALCULATED FROM EQUATION (2.32). 28

FIGURE 2.4 TWO-COUPLED-OSCILLATOR MODEL. 30

FIGURE 2.5 THREE-COUPLED-OSCILLATOR MODEL. 31

FIGURE 3.1 EXAMPLE OF PERMITTIVITY (A) AND REFRACTIVE INDEX (B) OF A DEMONSTRATING MATERIAL IN THE RESTSTRAHLEN BAND. 38

FIGURE 3.2 (A) THE FR PHONON MODE OF A 10-NM NANOPARTICLE MADE OF THE DEMONSTRATING MATERIAL INTRODUCED IN THE PREVIOUS PARAGRAPH AND SURROUNDED BY AIR. (B) NEAR FIELD DISTRIBUTION AT THE PEAK FREQUENCY OF 9.7 THZ. THE MIE CALCULATIONS IN (A) AND (B) WERE FULFILLED USING THE MATLAB CODE. 40

FIGURE 3.3 THE PRIMARY LATTICE MODES IN THE RECIPROCAL SPACE WHEN THE ORDER NUMBERS l AND m HOLD THE VALUE ±1 AND 0. k_{xy} IS THE PROJECTION OF WAVEVECTOR $\mathbf{k}$ IN THE X-Y PLANE. 45

FIGURE 3.4 THE SCHEMATIC OF INCIDENT LIGHT WITH BOTH S (A) AND P (B) POLARIZATIONS. 46

FIGURE 4.1 ENERGY DIAGRAM EXEMPLIFYING THE PLASMON–PHONON RESONANCE HYBRIDIZATION 51

FIGURE 4.2 (A) THE SCHEMATIC OF AN END-TO-END NANOANTENNA ARRAY. (B) THE GRAPHICAL REPRESENTATION OF A PLASMONIC NANOANTENNA ARRAY COVERED WITH A MONOLAYER OF CDS NANOCRYSTALS. 51

FIGURE 4.3 THE SKETCH OF A CASSEGRAIN OBJECTIVE. 53

FIGURE 4.4 (A) THE WAVE VECTOR (IN ORANGE) AND POLARIZATION PROJECTIONS (RED) ON THE X-Y PLANE. (B) THE SCHEMATIC DESCRIBING THE RELATION BETWEEN α AND φ. THE GREEN ARROW INDICATES THE K-VECTOR. 54

FIGURE 4.5 (A) RELATIVE TRANSMITTANCE SPECTRUM (BLUE CIRCLES: EXPERIMENTAL MEASUREMENT, RED LINE: FIT WITH EQUATION (3.23)) OF A 2.5-µM-THICK CDS NANOCRYSTAL LAYER. THE RELATIVE TRANSMITTANCE IS OBTAINED NORMALIZING THE SAMPLE TRANSMISSION TO THE ONE OF A BARE SILICON SUBSTRATE. (B) THE ABSORPTION SPECTRUM OF A MONOLAYER OF CDS NANOCRYSTALS, AS OBTAINED USING EQUATION (3.23) AND THE PARAMETERS EXTRACTED FROM THE FIT IN (A). . 55

FIGURE 4.6 FR RESONANCE ABSORPTION PEAK RETRIEVED BY MEANS OF NUMERICAL SIMULATIONS FOR DIFFERENT NANOCRYSTAL SHAPES AND LATTICE ARRANGEMENTS (FILLING FACTOR F = 0.75). THE CDS NANOPARTICLES ARE ON A SILICON SUBSTRATE. 56

FIGURE 4.7 FR RESONANCE FOR DIFFERENT NUMBER OF NANOCRYSTAL LAYERS (A) AND INPUT POLARIZATION ORIENTATION (B)..... 57

FIGURE 4.8 FR RESONANCE FOR DIFFERENT NANOCRYSTAL SIZES (A) AND DIFFERENT FILLING FACTORS (B).57

FIGURE 4.9 (A) EXTINCTION EFFICIENCY FOR SIX DIFFERENT NANOANTENNA LENGTHS. (B) CORRESPONDING FIELD ENHANCEMENT VALUES, ESTIMATED IN THE CENTER OF THE NANOCAVITY. 58

FIGURE 4.10 (A) 2D MAP SHOWING THE EXTINCTION SPECTRUM FOR DIFFERENT NANOANTENNA LENGTHS, IN THE CASE OF THE BARE ARRAYS. (B) SAME AS IN (A), WHEN THE ARRAYS ARE COVERED WITH A 10-NM-THICK "EFFECTIVE" LAYER OF CDS NANOCRYSTALS. (C) LATERAL VIEW OF THE GEOMETRICAL ARRANGEMENT ADOPTED IN THE SIMULATIONS FOR THE CDS NANOCRYSTAL LAYER. (D) CORRESPONDING ELECTRIC FIELD DISTRIBUTION (FREQUENCY: 8 THZ, NANOANTENNA LENGTH: 5.75 μM). 59

FIGURE 4.11 SIMULATED TRANSMISSION SPECTRA FOR BARE ARRAYS (A), AND ARRAYS COVERED WITH 1 (B), 2 (C), AND 3 (D) CDS NANOCRYSTAL LAYERS. THE ANTENNA LENGTHS ARE FROM 4.75 TO 6.75 μM. 59

FIGURE 4.12 THE LOCAL ELECTRIC FIELD DISTRIBUTION IN THE AREA OF A NANOCAVITY. ALL THE 2D PROJECTIONS ARE TAKEN ON A PLANE PASSING THROUGH THE NANOCAVITY GEOMETRICAL CENTER. PICKED FREQUENCY: 8 THZ; NANOANTENNA LENGTH: 5.75 μM 60

FIGURE 4.13 SIZE COMPARISON BETWEEN THE GEOMETRICAL NANOCAVITY VOLUME AND THE MODE VOLUME. 61

FIGURE 4.14 LATTICE MODE DEPENDENCE ON THE ARRAY SPACING, ESTIMATED FOR A FIXED ANTENNA LENGTH OF 5.75 μM. THE COLORED CURVES ARE THE SIMULATED TRANSMISSION SPECTRA, WHILE THE CORRESPONDING VERTICAL LINES INDICATE THE LATTICE RESONANCE POSITIONS CALCULATED USING EQUATION (4.5)..... 62

FIGURE 4.15 (A) SCHEMATIC VIEW OF THZ ANTENNAS ON THE SI SUBSTRATE. (B) SEM IMAGE OF A NANOANTENNA CHAIN IN FALSE COLORS. (C) SKETCH SHOWING THE DETAILS OF THE GAP BETWEEN TWO NANOANTENNAS (UPPER PANEL) AND CORRESPONDING SEM PICTURE (LOWER PANEL). 63

FIGURE 4.16 TEM IMAGES OF CDS CORES (A) AND CDS@CDS GIANT NANOCRYSTALS (B)..... 64

FIGURE 4.17 PSEUDO-COLORED SEM PICTURE: A MONOLAYER OF CDS NANOCRYSTALS (10 NM IN SIZE) COVERS A THZ NANOANTENNA CAVITY AREA. 64

FIGURE 4.18 EXAMPLE OF THE VISUAL ESTIMATE OF THE NUMBER OF NANOCRYSTALS IN A PLASMONIC NANOCAVITY; (A) SEM TOP VIEW. (B) TILTED VIEW, ALLOWING TO APPRECIATE FURTHER DETAILS OF THE NANOCRYSTALS POSITIONING WITHIN THE CAVITY. (C) ACTUAL COUNTING OVER THE TOP VIEW (RED CROSSES: NANOCRYSTALS AT THE BOTTOM OF THE CAVITY; GREEN CROSSES: NANOCRYSTALS ON THE CAVITY SIDEWALLS). 65

FIGURE 4.19 SCHEMATIC LAYOUT OF THE EXPERIMENTAL LABORATORY AT THE SISSI BEAMLINE: A BRUKER 70V FTIR SPECTROMETER IS DIRECTLY COUPLED TO THE SYNCHROTRON SOURCE, AND THEN A HYPERION IR MICROSCOPE IS USED TO PERFORM THZ TRANSMISSION MEASUREMENTS. 67

FIGURE 4.20 MEASURED TRANSMISSION SPECTRA FOR BARE ARRAYS (A), AND ARRAYS COVERED WITH 1 (B), 1.5 (C), AND 2 (D) CDS NANOCRYSTAL LAYERS. THE ANTENNA LENGTHS ARE FROM 4.75 TO 6.75 μM. THE DASH LINES IN (A) AND (B) ARE THE LATTICE MODE AND FR PHONON MODE, RESPECTIVELY. 67

FIGURE 4.21 RAMAN SPECTRA TAKEN AT DIFFERENT LASER POWER LEVELS ON A NANOCAVITY FEATURING A NUMBER OF NANOCRYSTAL LAYERS $N \approx 1.5$. $N-$ AND $N+$ ARE THE FREQUENCY OF LOWER AND UPPER VIBRO-POLARITONS, RESPECTIVELY. THE SPECTRA ARE VERTICALLY SHIFTED FOR CLARITY. 69

FIGURE 4.22 EXAMPLES OF THE FITTING PROCEDURE OF THE RAMAN SPECTRA DESCRIBED ABOVE. 70

FIGURE 4.23 RAMAN SPECTRA COLLECTED IN THE SAME NANOCAVITY WITH THE POLARIZATION OF THE EXCITING LASER SOURCE SET PARALLEL (RED LINE) AND PERPENDICULAR (BLUE LINE) TO THE LONG AXIS OF THE ANTENNAS. A SPECTRUM COLLECTED JUST OUTSIDE THE GAP REGION (BLACK LINE) IS ALSO SHOWN AS A REFERENCE. 71

FIGURE 4.24 POLARIZED RAMAN SPECTRA TAKEN WITH THE INPUT POLARIZATION SET EITHER ALONG THE LONG (A) OR SHORT (B) AXIS OF THE NANOANTENNAS AND THE ANALYZER SET AT THE ANGLE REPORTED IN THE FIGURE LEGEND. THE MEASUREMENTS IN (A) AND (B) WERE PERFORMED ON TWO NANOCAVITIES WITH A SIMILAR NUMBER OF NANOCRYSTAL LAYERS $N \approx 2.3$. 72

FIGURE 4.25 (A) SKETCH OF THE EMPLOYED PLATFORM. (B) RAMAN SPECTRA COLLECTED IN A NANOCAVITY REGION (SOLID RED LINE) AND JUST OUTSIDE THE NANOCAVITY ON THE SILICON SUBSTRATE (GREEN DASHED LINE) FOR A SAMPLE COVERED WITH A NANOCRYSTAL MONOLAYER; LENGTH OF NANOANTENNAS $L = 5.75$ MM. (C) EXPERIMENTAL THZ EXTINCTION SPECTRA OF THE ARRAY FEATURING NANOANTENNAS OF LENGTH $L = 5.75$ MM WITH (SOLID RED LINE) AND WITHOUT (GREEN DASHED LINE) A NANOCRYSTAL MONOLAYER ON ITS SURFACE; BLUE DASHED LINE: ABSORPTION SPECTRUM OF A SINGLE LAYER OF NANOCRYSTALS. THE EXTINCTION IS EXTRACTED FROM ONE MINUS THE TRANSMITTANCE. 74

FIGURE 4.26 RABI SPLITTING VS. NUMBER OF NANOCRYSTAL LAYERS. EXPERIMENTAL (A–C) AND NUMERICAL (D–H) 2D MAPS OF THE POLARITON BRANCHES DISPERSION FOR DIFFERENT VALUES OF NANOCRYSTAL LAYER NUMBER N. AS A REFERENCE FOR THE EXPERIMENTAL DATA, $N_{EST} = 1$ CORRESPONDS TO AN AVERAGE NUMBER OF NANOCRYSTALS INSIDE A NANOCAVITY OF AROUND 86 (SEE SECTION 4.2.4). THE RED (LOW-ENERGY POLARITON) AND BLUE (HIGH-ENERGY POLARITON) LINES ARE THE BEST FIT WITH A THREE-COUPLED-OSCILLATOR MODEL (SEE DISCUSSION IN SECTION 4.5.3). THE PURPLE DASHED LINE IS THE LOCATION OF THE FIRST LATTICE MODE OF THE ARRAYS. 75

FIGURE 4.27 (A) RAMAN SPECTRA OF THE NANOCRYSTALS TAKEN IN A NANOCAVITY REGION FOR DIFFERENT VALUES OF L. (B) RAMAN SPECTRA OF THE NANOCRYSTALS TAKEN ON AN ARRAY WITH L = 5.75 μM: IN DIFFERENT POSITIONS ALONG THE NANOANTENNAS COMPOSING A NANOCAVITY (BLACK LINES), IN THE NANOCAVITY REGION (RED LINE), AT THE END OF ONE NANOANTENNA CHAIN (GREEN LINE), AND JUST OUTSIDE THE CAVITY ON THE SILICON SUBSTRATE (BLUE LINE). THE SPECTRA ARE VERTICALLY SHIFTED FOR CLARITY. 76

FIGURE 4.28 (A) RAMAN SPECTRA FOR L = 5.75 MM AND THREE DIFFERENT VALUES OF NANOCRYSTAL LAYER NUMBER N. SOLID LINES INDICATE SPECTRA TAKEN IN A NANOCAVITY REGION AND DASHED LINES INDICATE SPECTRA TAKEN JUST OUTSIDE THE RESPECTIVE CAVITY (USING THE SAME EXPERIMENTAL PARAMETERS) ON THE SILICON SUBSTRATE. (B) RABI SPLITTING Ω_R AS A FUNCTION OF $\sqrt{N}$, EXTRACTED FROM: THE THREE-COUPLED-OSCILLATOR MODEL (BLACK LINE), NUMERICAL SIMULATIONS (RED BORDERED SQUARES), THZ EXTINCTION (GREEN CROSSES), AND RAMAN MEASUREMENTS (PURPLE CIRCLES). FOR EACH RAMAN DATA POINT, N IS EVALUATED CONSIDERING THE NUMBER OF NANOCRYSTALS CONTAINED INSIDE THE SPECIFIC NANOCAVITY UNDER MEASUREMENT (SEE SECTION 4.2.4). 77

FIGURE 4.29 RESONANCE WAVELENGTH AS A FUNCTION OF THE ANTENNA LENGTH FOR BARE ARRAYS. 79

FIGURE 4.30 POLARITON TRACE FIT OF THE SIMULATION RESULTS FOR THE CASE OF 1 NANOCRYSTAL LAYER (COMPARED TO FIGURE 4.26D, HERE THE AXES ARE EXTENDED TO FREQUENCY VALUES ABOVE 10 THZ). THE RED DASHED LINE MARKS THE UNCOUPLED PLASMON RESONANCE POSITION. 80

FIGURE 4.31 (A) RELATIVE COEFFICIENTS FOR THE LOW-ENERGY POLARITON BRANCH, IN THE CASE OF 1 NANOCRYSTAL LAYER. (B) SAME AS IN (A), FOR THE HIGH-ENERGY POLARITON BRANCH..... 80

FIGURE 4.32 EXTINCTION SPECTRA COMPARISON AMONG THE DISSIPATED POWER MODEL, NUMERICAL SIMULATIONS, AND THZ MEASUREMENTS. IN THIS SYSTEM, THE DAMPING FACTOR (Γ_1) ASSOCIATED WITH THE NANOANTENNA RESONANCE IS ABOUT 5 TIMES LARGER THAN THE ONE (Γ_2) OF THE CDS FR OPTICAL PHONONS MODE. ALL THE FITTING PARAMETERS REPORTED IN THE TABLE ABOVE ARE IN UNITS OF THZ, EXCEPT "F" THAT HAS NO UNITS (SEE SECTION 2.2 FOR DETAILS REGARDING THE MODEL). 82

FIGURE 5.1 INSPIRATION: TAPERING STRAIGHT NANOANTENNAS FOR AN IMPROVED FIELD LOCALIZATION [113]. 84

FIGURE 5.2 SELECTION OF THE APPROPRIATE GEOMETRY. 85

FIGURE 5.3 SCHEMATIC OF A MOON-SHAPED NANOANTENNA ARRAY. THE PERIODICITY OF OUR DESIGN IS G_X = G_Y = 9 μM, WHILE THE THICKNESS OF GOLD NANOANTENNAS IS 100 NM. 86

FIGURE 5.4 SCHEMATIC OF AN INDIVIDUAL MOON. 87

FIGURE 5.5 (A) FIELD ENHANCEMENT AT THE CENTER OF THE NANOGAP OF THE MOON-SHAPED NANOANTENNAS, FOR MOON FACTOR VALUES F_M VARYING FROM 1 TO 12 AND FOR A FIXED NANOANTENNA LENGTH L = 8 μM. (B) THE CORRESPONDING RELATIVE TRANSMITTANCE. 87

FIGURE 5.6 MEASURED (OPEN CIRCLES) AND SIMULATED (RED LINE, FOR A FILLING FACTOR OF 0.81) TRANSMITTANCE OF A MONOLAYER OF THE NEW BATCH OF CDS NANOCRYSTALS OVER A SILICON SUBSTRATE. 88

FIGURE 5.7 SIMULATED TRANSMISSION SPECTRA FOR BARE MOON-SHAPED NANOANTENNA ARRAYS (A), AND ARRAYS COVERED WITH 1 (B), 2 (C), AND 3 (D) CDS NANOCRYSTAL LAYERS. THE ANTENNA LENGTHS ARE FROM 7 TO 9 μM. 89

FIGURE 5.8 (A) FIELD ENHANCEMENT FOR THE NANOANTENNA LENGTHS CONSIDERED IN THE PREVIOUS FIGURE. THE VALUES ARE ESTIMATED IN THE CENTER OF THE NANOCAVITY (B) CORRESPONDING EXTINCTION CROSS-SECTION. 90

FIGURE 5.9 SIMULATED ABSORPTION RATE AT THE LAYER CENTER POINT. A BARE CDS NANOCRYSTAL MONOLAYER ON TOP OF A SILICON SUBSTRATE (A); 1 (B), 2 (C), AND 3 (D) CDS NANOCRYSTAL LAYERS COVERING MOON-SHAPED NANOANTENNA ARRAY. FOR (B), (C), AND (D), THE POINT PROBES ARE PLACED AT THE NANOCAVITY CENTERS. THE ANTENNA LENGTHS VARY FROM 7 TO 9 μM. ALL THE ABSORPTION SPECTRA ARE NORMALIZED BY THE MAXIMUM VALUE OF THE BARE MONOLAYER CASE. 91

FIGURE 5.10 ABSORPTION SPLITTING AT THE CENTER POINT OF THE NANOCAVITY WITHIN THE CDS NANOCRYSTAL LAYERS. (A) THE SKETCH INDICATING THE LOCATION OF THE POINT PROBE. (B) THE POINT ABSORPTION 2D MAP AS A FUNCTION OF ANTENNA LENGTH AND FREQUENCY. THE VALUES WERE EXTRACTED FROM THE SIMULATION MODEL OF NANOANTENNA ARRAYS COVERED WITH 2 LAYERS OF CDS NANOCRYSTALS. 91

FIGURE 5.11 ELECTRIC FIELD ENHANCEMENT DISTRIBUTION OF A BARE NANOANTENNA ARRAY WITH L = 8 μM, F_M = 6. (A) THE FIELD ENHANCEMENT AT RESONANCE (~7.8 THZ) SHOWN IN DB ($10*\log_{10}(E/E_0)$, E: FULL FIELD; E_0: BACKGROUND FIELD). (B) SAME AS IN (A) BUT IN LINEAR SCALE (MAGNIFIED MAP OF THE NANOCAVITY REGION) 92

FIGURE 5.12 VOLUME RATIO OF THE MOON-SHAPED NANOANTENNA ARRAYS FOR (A) FIXED ANTENNA LENGTH L = 8 μM AND MOON FACTORS FROM 1 TO 12, AND FOR (B) FIXED MOON FACTOR F_M = 6, AND ANTENNA LENGTHS FROM 7 TO 9 μM. 93

FIGURE 5.13 EXTINCTION SPECTRUM COMPARISON BETWEEN SIMULATION AND DISSIPATED POWER MODEL. ALL THE FITTING PARAMETERS ARE IN UNITS OF THZ, EXCEPT "*F*" THAT HAS NO UNITS. THE SIMULATED EXTINCTION IS EXTRACTED FROM A NANOANTENNA ARRAY (L = 8 μM) COVERED WITH A MONOLAYER OF CDS NANOCRYSTALS. 94

FIGURE 5.14 (A) AN SEM PICTURE OF A FABRICATED MOON-SHAPED NANOANTENNA ARRAY. (B) A ZOOMED-IN SEM IMAGE OF A NANOGAP..... 95

FIGURE 5.15 (A) AN SEM PICTURE OF A CDS-NANOCRYSTAL-COVERED (1.5 LAYER) MOON-SHAPED NANOANTENNA. (B) THE ZOOMED-IN SEM IMAGE OF (A)..... 95

FIGURE 5.16 MEASURED TRANSMISSION SPECTRA FOR BARE ARRAYS (A), AND ARRAYS COVERED WITH 1 (B), 1.5 (C), AND 2 (D) CDS NANOCRYSTAL LAYERS. THE ANTENNA LENGTHS ARE FROM 6.25 TO 9.5 μM. TO AVOID COMPLETE RE-DISSOLUTION OF THE ALREADY DEPOSITED NANOCRYSTALS, IN THE 2 LAYERS CASE (D), 1-NM ALUMINA SEPARATOR WAS DISPOSED ON TOP OF THE FIRST LAYER. 96

FIGURE 5.17 MEASURED EXTINCTION 2D MAPS OF BARE MOON-SHAPED NANOANTENNA ARRAYS (A), AND THE SAME ARRAYS COVERED WITH 1 (B), 1.5 (C), AND 2 LAYERS OF CDS NANOCRYSTALS..... 97

FIGURE 5.18 RAMAN SPECTRUM FOR A MOON-SHAPED NANOANTENNA WITH L = 8 MM AND COVERED BY 2 LAYERS OF CDS NANOCRYSTALS. THE SOLID LINE INDICATES THE SPECTRUM TAKEN IN A NANOCAVITY REGION, AND THE DASHED LINE CORRESPONDS TO THE SPECTRUM TAKEN JUST OUTSIDE THE SAME NANOCAVITY..... 98

LIST OF TABLES

TABLE 4.1 ESTIMATION OF THE NANOCRYSTAL LAYER NUMBER 66

TABLE 4.2 ENHANCEMENT VALUES FOR THE HYBRIDIZED RAMAN PEAKS IN FIGURE 4.28A 73

TABLE 4.3 FITTING COEFFICIENTS FOR THE SIMULATED POLARITON TRACES 81

TABLE 4.4 FITTING COEFFICIENTS FOR THE EXPERIMENTAL POLARITON TRACES 81

LIST OF ABBREVIATIONS

THz	Terahertz
IR	Infrared
CdS	Cadmium Sulfide
FWHM	Full-Width at Half-Maximum
QED	Quantum ElectroDynamics
TO	Transverse Optical
FR	Fröhlich
LO	Longitudinal Optical
SEM	Scanning Electron Microscope
TEM	Transmission Electron Microscope
XRD	X-Ray Diffraction
EDX	Electron Dispersive X-Ray
SERS	Surface Enhanced Raman Scattering
TMD	Transition Metal Dichalcogenide

LIST OF PUBLICATIONS
(DURING THE DOCTORAL PERIOD)

1. Publications related to this thesis work

1.1. Articles in refereed journals

[1] **X. Jin**†, A. Cerea†, G. C. Messina, A. Rovere, R. Piccoli, F. De Donato, F. Palazon, A. Perucchi, P. Di Pietro, R. Morandotti, S. Lupi, F. De Angelis, M. Prato, A. Toma, and L. Razzari, "Reshaping the Phonon Energy Landscape of Nanocrystals inside a Terahertz Plasmonic Nanocavity," ***Nature Communications***, **9**, 763 (2018) † **Equal contribution**

[2] H. Wang, H-Y. Wang, H-B. Sun, A. Cerea, A. Toma, F. De Angelis, **X. Jin** (**wrote chapter 7**), L. Razzari, D. Cojoc, D. Catone, F. Huang, and R. P. Zaccaria, "Dynamics of Strongly Coupled Hybrid States by Transient Absorption Spectroscopy," ***Advanced Functional Materials***, **28**, 1801761 (2018) (**Invited Review**)

[3] A. Tomasino, A. Mazhorova, M. Clerici, M. Peccianti, S.P. Ho, Y. Jestin, A. Pasquazi, A. Markov, **X. Jin**, R. Piccoli, S. Delprat, M. Chaker, A Busacca, J. Ali, L. Razzari, and R. Morandotti, "Solid-state-biased Coherent Detection of Ultra-broadband Terahertz Pulses," ***Optica***, **4**, 1358-1362. (2017)

[4] **X. Jin**†, V. Aglieri†, Y. Jeong, A. Rovere, R. Piccoli, R. Macaluso, R. Morandotti, A. Toma, and L. Razzari, "Vibrational Strong Coupling between Semiconducting Nanocrystals and Moon-Shaped Nanoantennas," in preparation. † **Equal contribution**

[5] **X. Jin**, V. Aglieri, A. Pezeshki, Y. Jeong, Y. Jia, R. Macaluso, E. Orgiu, A. Toma, and L. Razzari, " Extracting the Dipole-Active Phonon Resonance of a Tungsten Diselenide Monolayer from Enhanced Spectroscopy using X-Shaped Terahertz Nanoslots" in preparation

[6] V. Aglieri, **X. Jin**, A. Rovere, R. Piccoli, D. Caraffini, S. Tuccio, F. De Angelis, R. Morandotti, R. Macaluso, A. Toma, and L. Razzari, "Terahertz Antenna Optimization for Improved Near-Field Enhancement in Nanocavities," in preparation

1.2. Refereed international conferences (the presenter is underlined)

[1] **X. Jin**, A. Cerea, G. C. Messina, A. Rovere, R. Piccoli, F. De Donato, F. Palazon, A. Perucchi, P. Di Pietro, R. Morandotti, S. Lupi, F. De Angelis, M. Prato, A. Toma, L. Razzari, "Modifying

the Optical Phonon Response of Nanocrystals inside Terahertz Plasmonic Nanocavities," *CLEO/EUROPE-EQEC 2019*, Munich, Germany (2019) **Oral presentation**

[2] V. Aglieri, **X. Jin**, A. Rovere, R. Piccoli, D. Caraffini, S. Tuccio, F. De Angelis, R. Morandotti, R. Macaluso, A. Toma, and L. Razzari, "Antenna Tapering Strategy for Near-field Enhancement Optimization in Terahertz Gold Nanocavities", CLEO/EUROPE-EQEC 2019, Munich, Germany (2019) **Oral presentation**

[3] **X. Jin**, A. Cerea, G. C. Messina, A. Rovere, R. Piccoli, F. De Donato, F. Palazon, A. Perucchi, P. Di Pietro, R. Morandotti, S. Lupi, F. De Angelis, M. Prato, A. Toma, L. Razzari, "Altering the Phonon Response of Nanomaterials inside a Terahertz Nanocavity," *The 8th International Conference on Optical Terahertz Science and Technology (OTST) 2019*, Santa Fe, New Mexico, United States (2019) **Oral presentation**

[4] **X. Jin**, L. Razzari, "Modeling Strong Coupling of Unevenly-Damped Oscillators," *Photonics North (PN) 2019 IEEE*. Quebec City, Quebec, Canada (2019) **Poster**

[5] **X. Jin**, A. Cerea, G. C. Messina, A. Rovere, R. Piccoli, F. De Donato, F. Palazon, A. Perucchi, P. Di Pietro, R. Morandotti, S. Lupi, F. De Angelis, M. Prato, A. Toma, L. Razzari, "Enhanced Terahertz Light-Matter Coupling in Plasmonic Nanocavities," *META 2018*, Marseille, France (2018) **Invited Talk**

[6] **X. Jin**, A. Cerea, G. C. Messina, A. Rovere, R. Piccoli, F. De Donato, F. Palazon, A. Perucchi, P. Di Pietro, R. Morandotti, S. Lupi, F. De Angelis, M. Prato, A. Toma, and L. Razzari, "Plasmonic Nanocavities for Enhanced Terahertz Light-Matter Coupling," *Photonics North (PN) 2018 IEEE*. Montreal, Quebec, Canada (2018) **Invited Talk**

[7] **X. Jin**, A. Cerea, G. C. Messina, A. Rovere, R. Piccoli, R. Morandotti, F. De Angelis, A. Toma, L. Razzari, "Modeling Light-matter Interaction in Terahertz Plasmonic Nanocavities," *Photonics North (PN) 2018 IEEE*. Montreal, Quebec, Canada (2018) **Poster**

[8] V. Aglieri, **X. Jin**, A. Rovere, R. Piccoli, D. Caraffini, A. Cerea, F. De Angelis, R. Morandotti, R. Macaluso, A. Toma, and L. Razzari, "Near-Field Enhancement Optimization by Tapering Terahertz Gold Nanoantennas," *Photonics North (PN) 2018 IEEE*. Montreal, Quebec, Canada (2018) **Oral presentation**

[9] A. Tomasino, A. Mazhorova, M. Clerici, M. Peccianti, S.P. Ho, Y. Jestin, A. Pasquazi, A. Markov, **X. Jin**, R. Piccoli, S. Delprat, M. Chaker, A Busacca, J. Ali, L. Razzari, and R. Morandotti, "Scaling Mechanisms in CMOS-Compatible Sensors for Ultra-Broadband THz

Coherent Detection," *Photonics North (PN) 2017 IEEE*. Ottawa, Ontario, Canada (2017) **Oral presentation**

[10] A. Tomasino, A. Mazhorova, M. Clerici, M. Peccianti, S.P. Ho, Y. Jestin, A. Pasquazi, A. Markov, **X. Jin**, R. Piccoli, S. Delprat, M. Chaker, A Busacca, J. Ali, L. Razzari, and R. Morandotti, "Affordable, Ultra-broadband Coherent Detection of Terahertz Pulses via CMOS-Compatible Solid-state Devices," *CLEO: QELS_Fundamental Science* (pp. FW1H-7) Optical Society of America. (2017) **Oral presentation**

[11] D. Caraffini, R. Piccoli, **X. Jin**, S. Tuccio, R. Morandotti, and L. Razzari, "On the Optimization of Tapered Nanoantennas Resonating in the Terahertz Range," *Photonics North (PN) 2016 IEEE*. Quebec City, Quebec, Canada (2016) **Oral presentation**

2. Other publications

To broaden my knowledge in photonics, during my Ph.D. period, I also participated in other investigations within the framework of nanoantenna enhanced light-matter interaction. Among these collaborations, I designed and optimized the plasmonic structures for specific performance optimization. In particular, I contributed to the proposition of a novel design for plasmonic photocatalysts, exploiting whispering gallery mode resonances in the semiconducting moiety of the catalysts themselves, which was found to improve the photocatalytic activity greatly. By introducing this physical concept to the chemical community, we opened up a new venue to optimize photocatalysts.

2.1. Articles in refereed journals

[1] J. Zhang†, **X. Jin**†, P.I. Morales-Guzman, X. Yu, H. Liu, H. Zhang, L. Razzari, and J.P. Claverie, "Engineering the Absorption and Field Enhancement Properties of Au–TiO2 Nanohybrids via Whispering Gallery Mode Resonances for Photocatalytic Water Splitting," ***ACS Nano***, **10**, 4496-4503 (2016) † **Equal contribution**

[2] J. Zhang†, Y. Huang†, **X Jin**†, A. Nazartchouk, M. Liu, X. Tong, Y. Jiang, L. Ni, S. Sun, Y. Sang, H. Liu, L. Razzari, F. Vetrone, J. Claverie, "Plasmon Enhanced Upconverting Core@Triple-Shell Nanoparticles as Recyclable Panchromatic Initiator (Blue to Infrared) for Radical Polymerization," ***Nanoscale Horizons***, **4**, 907-917 (2019) † **Equal contribution**

[3] J. Zhang, **X. Jin**, X. Yu, Y. Sang, L. Razzari, H. Liu, J. P. Claverie, "An In Situ Polymerization-Encapsulation Approach to Prepare TiO2–Graphite Carbon–Au Photocatalysts for Efficient Photocatalysis," ***Particle & Particle Systems Characterization***, **35**, 1700297 (2018)

[4] Q. Zhang, **X. Jin**, Z. Xu, J. Zhang, U. Rendon, L. Razzari, M. Chaker, D. Ma, "Plasmonic Au Loaded Hierarchical Hollow Porous TiO_2 Spheres: Synergistic Catalysts for Nitroaromatic Reduction," ***Journal of Physical Chemistry Letters***, 9,5317-5326 (2018)

[5] M.-A. Stoeckel, Y. Olivier, M. Gobbi, D. Dudenko, V. Lemaur, M. Zbiri, A. Y. Guilbert, G. D'Avino, F. Liscio, N. Demitri, **X. Jin**, Y.-G. Jeong, M.-V. Nardi, L. Pasquali, L. Razzari, D. Beljonne, P. Samorì, E. Orgiu, "Freeing Electrons from Extrinsic and Intrinsic Disorder Yields Band-like Transport in n-type Organic Semiconductors," ***arXiv preprint arXiv:1909.05344*** (2019) under review

2.2. Refereed international conferences (the presenter is underlined)

[1] H. E. Limodehi, R. Mohajeri, **X. Jin**, L. Razzari, F. Légaré, "A Tunable Thermo-mechanical Fiber Optic Temperature Sensor," *Photonics North (PN) 2018 IEEE*. Montreal, Quebec, Canada (2018)

[2] J. Zhang, J.P. Claverie, **X. Jin**, L. Razzari, "Enhancement of the Activity of Plasmonic Photocatalysts," *Conference on Hybrid Optically Active Nanomaterials, META 2017*, Incheon, Korea (2017)

[3] **X. Jin**, J. Zhang, J. Claverie, L. Razzari, "Novel Photocatalysts Acting as Optical Resonators," *Plasma-Quebec 2017,* University of Montreal, Montreal, Quebec, Canada (2017) **Poster**

[4] **X. Jin**, J. Zhang, P.I. Morales-Guzman, J. Claverie, and L. Razzari, "Photocatalysts Acting as Optical Resonators – A Novel Route for Boosting Solar Water Splitting," *Photonics North (PN) 2016 IEEE*. Quebec City, Quebec, Canada (2016) **Oral presentation**

[5] **X. Jin**, J. Zhang, P. I. Morales-Guzman, J. Claverie, and L. Razzari, "Boosting Solar Water Splitting in Hybrid Plasmonic Photocatalysts," *Conference on Optical Engineering, Laser science and ultrafast optics, IONS 2016*, Quebec City, Quebec, Canada (2016) **Oral presentation**

[6] L. Razzari, J. Zhang, **X. Jin**, P. I. Morales-Guzman, X. Yu, H. Liu, H. Zhang, and J. Claverie, "Engineering the Electromagnetic Properties of Plasmonic Nanohybrids for Solar Water Splitting," *Conference on Metamaterials, Photonic Crystals and Plasmonics, META 2016*, Malaga, Spain (2016)

LIST OF SCHOLARSHIPS AND AWARDS
(DURING THE DOCTORAL PERIOD)

[1] **Bourse d'Excellence pour Étudiants Étrangers – Bourses de Doctorat en Recherche** (PBEEE, **Merit Scholarship Program for Foreign Students – Doctoral Research Scholarship – V1**), May 2015 to Aug. 2018, $ 70 334 CAD, funded by Fonds de Recherche du Québec – Nature et Technologies (FRQNT).

[2] **NSERC CREATE – Guided Light** – An International Training Program. Sep. 2017 to Jan. 2019, $ 21 250 CAD, funded by Natural Sciences and Engineering Research Council of Canada (NSERC).

[3] **Chinese Government Award for Outstanding Self-financed Students Abroad**, Jan. 2019, $ 6 000 USD, awarded by China Scholarship Council (CSC).

[4] **EPS-QEOD Travel Grant Student Awards**, Jun. 2019, €1 000 EURO, awarded by "CLEO/Europe-EQEC 2019", European Physical Society (EPS), in Munich, Germany.

1 Introduction

1.1 Motivation and Objective

Light-matter interaction within resonant cavities has been extensively studied in the last four decades [1-4]. In particular, electronic transitions in condensed matter systems, such as the ones featured by quantum dots and nanocrystals, have been investigated [1, 5-8]. It is already well known that such emitters can modify their spontaneous emission rate by tailoring the electromagnetic properties of the surrounding environment (e.g., by placing the emitter in an optical cavity) [9, 10]. However, the emission frequency remains in this case unaltered. This usually happens when the interaction between the emitter and the cavity is weak and the energy exchange rate between the two resonances (matter and cavity) does not overcome the energy loss of the systems (i.e., the weak-coupling regime). In contrast, when the interaction becomes strong enough (i.e., when the energy exchange rate between the emitter and the cavity becomes – at least - comparable with the loss of the system), the energy level associated to the target transition is modified, and splits explicitly into two new distinct states [1, 11]. This condition is known as strong coupling. The signature of this condition is the anti-crossing behavior of the "normal modes" of the hybrid system and their minimum energy separation is typically called Rabi splitting. So far, many studies have employed Fabry-Perot resonators, whispering gallery modes or photonic crystal cavities to sustain optical modes that interact with matter [12-16]. Achieving the strong coupling regime in these cavities is relatively easy due to their high quality factors and low damping rate in the optical domain.

Recently, the vibrational strong coupling between Fabry-Perot cavity photons and the vibration of specific molecular bonds has been investigated. The resulting vibro-polariton modes explored in various systems [12, 13, 17-19] promise to have several interesting applications. Indeed, the strong couplings between excitons (bound states of electrons and electron holes) and photons have already shown that, by proper manipulation of both the excitonic and the light part of the polariton, it is possible to realize Bose-Einstein condensates of polaritons [1, 2, 17, 20]. Furthermore, the vibrational strong coupling has also been found to lead to the modification of chemical reactions. Since the electromagnetic "environment" of a molecule can modify its vibrations, the strength of its chemical bonds can be altered and in turn, this can be used to control the rate of chemical reactions [12, 13, 21, 22].

Nowadays, nanocrystals have attracted considerable attention in the domain of quantum electrodynamics, due to their unique favorable features [23-28]. For example, semiconductor

nanocrystals can be used to make novel transistors working at room temperature while achieving better device mobility compared to conventional ones, as well as light-emitting diodes offering tunable color properties [23-28]. Phonons, being the main source of energy dissipation in solid-state systems, represent the ultimate bottleneck that limits the operation of functional nanomaterials [23, 29]. Therefore, phonon strong coupling could be an interesting route to modify phonon-related energy dissipation in nanomaterials. In addition, a recent study shows that molecules under vibrational strong coupling can efficiently emit infrared (IR) light [30]. We could thus similarly expect that phonon strong coupling could lead to novel devices for the emission of terahertz (THz) light. Driven by such motivation, we have selected to use as a testbed system cadmium sulfide (CdS) nanocrystals [31], since polar semiconducting nanoparticles [32] possess an intense optical phonon mode (Fröhlich (FR) phonon) laying in the THz region, which can be efficiently coupled to THz light. In this system, we will test whether the energy level of the FR phonon can be intrinsically modified, via strong coupling in a plasmonic nanocavity. Indeed, the nanoscale strong coupling of surface plasmon resonances and nanoparticles has become an attractive research topic in the visible and IR regions [1, 33-36]. Due to the intrinsic nature of surface plasmons, the light field component of a plasmonic resonance can be confined into dimensions much smaller than the free-space wavelength of the employed radiation [5, 37, 38]. A plasmonic cavity thus offers an appealing solution to investigate light-nanomatter interactions in the THz region, where the radiation wavelength is orders of magnitude larger than the size of the nanoparticles.

Summarizing, my Ph.D. project aims to realize a vibrational strong coupling system using THz plasmonic nanostructures and optical phonons of nanocrystals. This system represents a proof of principle platform to prove the possibility of modifying the phonon response of nanomaterials, in view of altering the energy dissipation mechanism in nanosystems. In addition, since phonons can find a novel route to decay through a radiative process under strong coupling, this could also lead to an innovative generation of THz emitters.

1.2 Light-Matter Interaction in Electromagnetic Wave Cavities

In 1946, Purcell revealed that by modifying the electromagnetic environment of an emitter, the spontaneous emission rate could be either enhanced or suppressed [9], and this phenomenon is called the **Purcell effect.** This epochmaking observation opened up a new route to study quantum dynamics, especially between light and matter, aiming at modulating the interaction by exploiting various photonic resonators [4].

An optical resonance is essentially a condition that enhances electromagnetic waves in cavities of various geometries, e.g., Fabry-Perot (usually two parallel mirrors), ring and photonic crystal -based resonators. The frequencies at which the maximum energy is stored in the optical cavity are named resonance frequencies. The inverse of the cavity lifetime (the latter being a time constant defining the decay of energy in the cavity) defines the damping factor (γ) of a specific resonator, which can be quantitatively extracted from calculating the full width at half maximum (FWHM), i.e., the linewidth of the resonance. The ratio between the resonance frequency and the linewidth is the quality factor "Q", a high quality factor value indicating a low rate of energy loss relative to the stored energy in an optical cavity. The dimensions of the optical cavity (such as the cavity length in a Fabry Perot geometry) determine the resonance frequency, while the radiative and non-radiative cavity loss determine the damping factor. In classical physics, the optical resonance can be understood as a dipole oscillation driven by an incident electromagnetic wave.

In quantum optics, the quantum harmonic oscillator model is informative to explain non-classical phenomena in modern scientific observations. In particular, via the quantum harmonic oscillator model, one can find that the zeroth state (ground state) of an oscillator has non-zero energy (unlike in the classical picture). Such energy is equal to $\hbar\omega/2$, where $\hbar$ is the reduced Planck constant and ω is the angular frequency of the oscillator. For a quantized electromagnetic field, this zero-point energy is associated with vacuum electric field fluctuations, namely the vacuum field, which is present everywhere even in a complete vacuum. This can also be seen as a direct consequence of the Heisenberg uncertainty principle between the position (Δx) and momentum (Δp_x) of a particle confined in a finite volume (i.e., the cavity volume): $\Delta x \Delta p_x \geq \hbar/2$. The amplitude of the **vacuum electric field** E_{vac} associated with the zero-point energy "$\hbar\omega/2$" can be shown to be equal to [39] [15, 40]:

$$\left|E_{\text{vac}}\right| = \sqrt{\frac{\hbar\omega}{2}\cdot\frac{1}{\varepsilon_0\varepsilon V_{\text{mod}}}}, \qquad \textbf{(1.1)}$$

where ε_0 is the vacuum permittivity (~8.85×10^{-12} F$\cdot$m^{-1}), ε is the relative permittivity of the eventual background, and V_{mod} is the cavity mode volume. As will be shown in details later in this thesis (see Section 3.8) in properly designed cavities, the mode volume can be shrunk down considerably by exploiting confinement strategies. From Equation (1.1), we see that a small mode volume gives rise to a high vacuum electric field. In light-matter interaction processes, the vacuum electric field is a determinant factor for quantifying the coupling between light and matter.

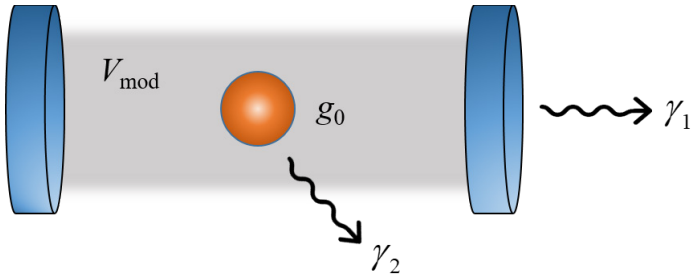

Figure 1.1 **An atom in a resonant cavity: V_{mod} is the mode volume, g_0 the coupling strength, γ_1 the cavity decay, and γ_2 the non-resonant atomic decay.**

Let us consider the simple case of an atom in a cavity. In the semi-classical approach, the interaction energy ($\hbar g_0$) between the atom and the cavity vacuum field can be written as: $\hbar g_0 = \mu_{12}\left|E_{\mathrm{vac}}\right|$ in which g_0 is the **coupling strength** (it has the same unit as the angular frequency ω), and μ_{12} is the dipole moment of the energy transition for the matter side (the subscript "12" indicates a transition from an initial state $|1\rangle$ to a final state $|2\rangle$). Using Equation (1.1), we can derive:

$$g_0 = \frac{\mu_{12}}{\hbar}\sqrt{\frac{\hbar\omega}{2}\cdot\frac{1}{\varepsilon_0\varepsilon V_{\mathrm{mod}}}} = \sqrt{\frac{\mu_{12}^2\omega}{2\varepsilon_0\varepsilon\hbar V_{\mathrm{mod}}}}. \qquad \textbf{(1.2)}$$

In free space, the coupling strength is typically weak due to a large mode volume. However, when a matter system is positioned in an optical cavity, the coupling strength can be greatly improved. As shown in Figure 1.1, in an atom-cavity coupling system, there are three factors that finally determine the interaction: i) the photon decay rate of the cavity γ_1; ii) the atomic decay rate γ_2 of the matter system; iii) and the coupling strength g_0 between the atom and the photons of the cavity. The coupling strength g_0 competes with the other two terms to define, whether the system is in the weak or strong coupling regime. In general, when $g_0 \ll (\gamma_1, \gamma_2)$, the interaction between the atom and cavity is in the regime of **weak coupling**; when $g_0 \gg (\gamma_1, \gamma_2)$, the interaction is classified in the regime of **strong coupling**. These conditions are sufficient but not necessary. In fact, when the coupling strength and the decay rates are comparable in specific systems, the individual decay rates may not be the main factor which determines the overall behavior of the system [1]. In the *weak coupling regime*, the emission of the photons from the interacting atom is an **irreversible process,** as in normal free-space spontaneous emission, but only the emission rate is affected by the cavity. Conversely, in the *strong coupling regime*, the cavity-atom energy

exchange rate is faster than the irreversible processes which dissipate photons out of the cavity. This guarantees that the atom emission becomes a quasi- **reversible process,** i.e., the emitted photons can be re-absorbed by the atom before they are lost from the cavity [39].

The Purcell effect is a characteristic interaction of light and matter in the weak coupling regime. The spontaneous emission rate of an atom in free space can be calculated, using **Fermi's golden rule** [39, 41, 42], as $W_{\text{free}} = \mu_{12}^2 \omega^3 / \left(3\pi\varepsilon_0 \varepsilon \hbar c^3\right)$, where c is the speed of light. In the same way, the spontaneous emission rate of an atom in a cavity is $W_{\text{cav}} = 2\mu_{12}^2 Q / \left(3\hbar\varepsilon_0 \varepsilon V_{\text{mod}}\right)$ - or, using the coupling strength, $W_{\text{cav}} = 4g_0^2 / \left(3\gamma_1\right)$, with γ_1 the damping factor of the resonator. Then, the Purcell factor is simply the ratio of such spontaneous emission rates:

$$F_{\text{P}} = \frac{W_{\text{cav}}}{W_{\text{free}}} = \frac{3}{4\pi^2}\left(\frac{\lambda}{n}\right)^3 \left(\frac{Q}{V_{\text{mod}}}\right), \tag{1.3}$$

where n is the refractive index of the medium inside the cavity (note: $\left(c/\omega\right)$ is replaced by $\left(\lambda/n\right)/\left(2\pi\right)$). A Purcell factor greater than one implies that the spontaneous emission rate is enhanced by the cavity, while a Purcell factor smaller than one implies that the cavity inhibits the emission. To increase the spontaneous emission rate, we can thus use cavities with high quality factors (Q) – i.e., a "temporal" enhancement, and/or small mode volumes (V_{mod}) – spatial enhancement. Q and V_{mod} are intrinsically related to the material properties and morphology of the cavity used.

As mentioned above, when the coupling rate g_0 is larger than the intrinsic atom/cavity decay rates, the system can be defined as *strongly coupled*. In such condition, the energy exchange between the atom and the cavity is thus faster than the irreversible processes characterizing the atom and cavity separately, and this reversible phenomenon is at the basis of **cavity quantum electrodynamics** (cavity QED). In 1963, Jaynes and Cummings developed a quantized model (which is now named after them) to explain a strong coupling interaction. Here, we summarize the main conclusions.

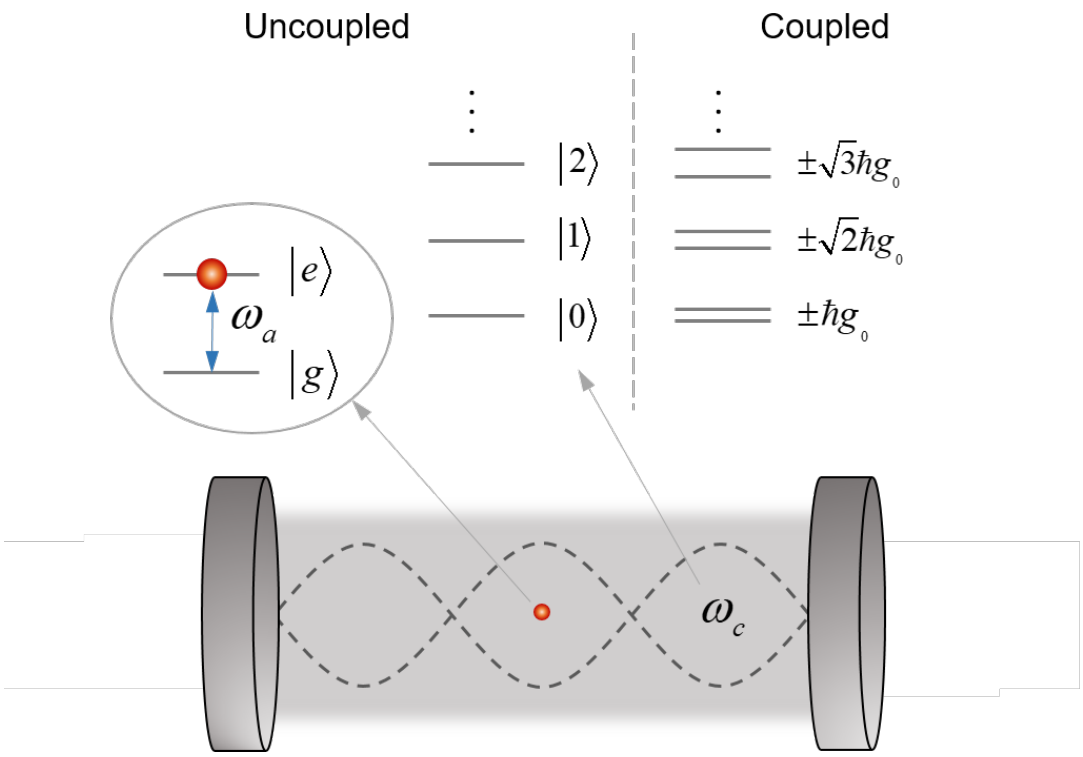

Figure 1.2 **Illustration of the Jaynes-Cumming model. When the photon number is "0", there is still a resonance splitting due to the vacuum field.**

In the case of a single atom coupled to a quantized field (see Figure 1.2), the Hamiltonian within the rotating wave approximation can be written as [43]:

$$H = \frac{1}{2}\hbar\omega_a\sigma_z + \hbar\omega_c\hat{a}^\dagger\hat{a} + \hbar g_0\left(\hat{a}\sigma_+ + \hat{a}^\dagger\sigma_-\right). \tag{1.4}$$

In this equation, $\omega_{a,c}$ is the atomic/cavity transition angular frequency; σ_z is the atomic inversion operator; g_0 is the coupling strength; $\hat{a}^\dagger$ and $\hat{a}$ are the creation and the annihilation operators, respectively; σ_+ and σ_- are raising and lowering operators, respectively. This Hamiltonian only couples the states $|e,n\rangle$ and $|g,n+1\rangle$, in which "e" and "g" in the kets denote the excited and ground states, while "n" refers to the photon number. On resonance, the eigenstates are:

$$\begin{aligned} |n,-\rangle &= \frac{1}{\sqrt{2}}\left[-|e,n\rangle + |g,n+1\rangle\right], \\ |n,+\rangle &= \frac{1}{\sqrt{2}}\left[|e,n\rangle + |g,n+1\rangle\right]. \end{aligned} \tag{1.5}$$

These atom-photon mixed states are called as **dressed states,** and we know that for each state the atom and the photon become inextricably connected. The eigenstates are equal to a superposition of the states $|e,n\rangle$ and $|g,n+1\rangle$. The corresponding eigenenergies are:

$$E_n^- = \hbar\left(n+\frac{1}{2}\right)\omega - \hbar g_0\sqrt{n+1},$$
$$E_n^+ = \hbar\left(n+\frac{1}{2}\right)\omega + \hbar g_0\sqrt{n+1}. \quad \textbf{(1.6)}$$

These half-matter and half-photon quasiparticles are named as **polaritons**. The splitting of energy states of these polaritons is the so-called **Rabi splitting** (exemplified in Figure 1.2):

$$\hbar\Omega_{\mathrm{R}} = E_n^+ - E_n^- = 2\hbar g_0\sqrt{n+1}. \quad \textbf{(1.7)}$$

Intriguingly, in contrast to the classical case, there is a splitting even for the case of $n=0$, which means these polaritons are mixed states between the excited atom and the vacuum field. This splitting is called the **vacuum Rabi splitting**, and its value is given by:

$$\hbar\Omega_{\mathrm{R}} = 2\hbar g_0. \quad \textbf{(1.8)}$$

In most cases, single atom systems are inefficient to strongly couple to a single-mode cavity. However, the situation improves by adding N atoms into the cavity. Thus, considering N atoms (all featuring a single two-level transition) in a single-mode cavity, the system can be described by the Tavis-Cummings Hamiltonian within the rotating wave approximation [1], whose solution leads to a vacuum Rabi splitting of:

$$\hbar\Omega_{\mathrm{R}} = 2\hbar g_N, \quad \textbf{(1.9)}$$

where the overall coupling strength $g_N = \sqrt{N}g_0$ for N atoms or other many-body cases. In terms of Equation (1.2), we know that the energy of interaction complies the relation:

$$\hbar g_N = \sqrt{N}\mu_{12}\left|E_{\mathrm{vac}}\right| = \sqrt{N}\mu_{12}\sqrt{\frac{\hbar\omega}{2}\cdot\frac{1}{\varepsilon_0\varepsilon V_{\mathrm{mod}}}}. \quad \textbf{(1.10)}$$

Very recently, the **ultrastrong** and **deep couplings** between light and matter have passed from theoretical predictions to experimental reality (see a recent review in ref [4]). The coupling strength in these regimes is comparable to the transition frequencies, so that it becomes possible to modify the very nature of the light and matter degrees of freedom [4]. In general, the

Hamiltonian for describing a system beyond strong coupling cannot employ the rotating-wave approximation. Thus, compared to Equation (1.4), the Hamiltonian is of the form:

$$H = \frac{1}{2}\hbar\omega_a\sigma_z + \hbar\omega_c\hat{a}^\dagger\hat{a} + \hbar g_0\left(\hat{a}+\hat{a}^\dagger\right)\left(\sigma_+ + \sigma_-\right). \quad \textbf{(1.11)}$$

This is the quantum Rabi model for the 1 atom case (as shown in Figure 1.3a). Regarding the N atoms case (Figure 1.3b), one should use the Dicke and Hopfield models to describe the problem [4]. It is important to be aware that the inclusion of the counter-rotating terms in the equation above may not be the only modification to consider when describing systems in the ultrastrong coupling regime, and other factors, depending on the specific system under study may have to be considered [1].

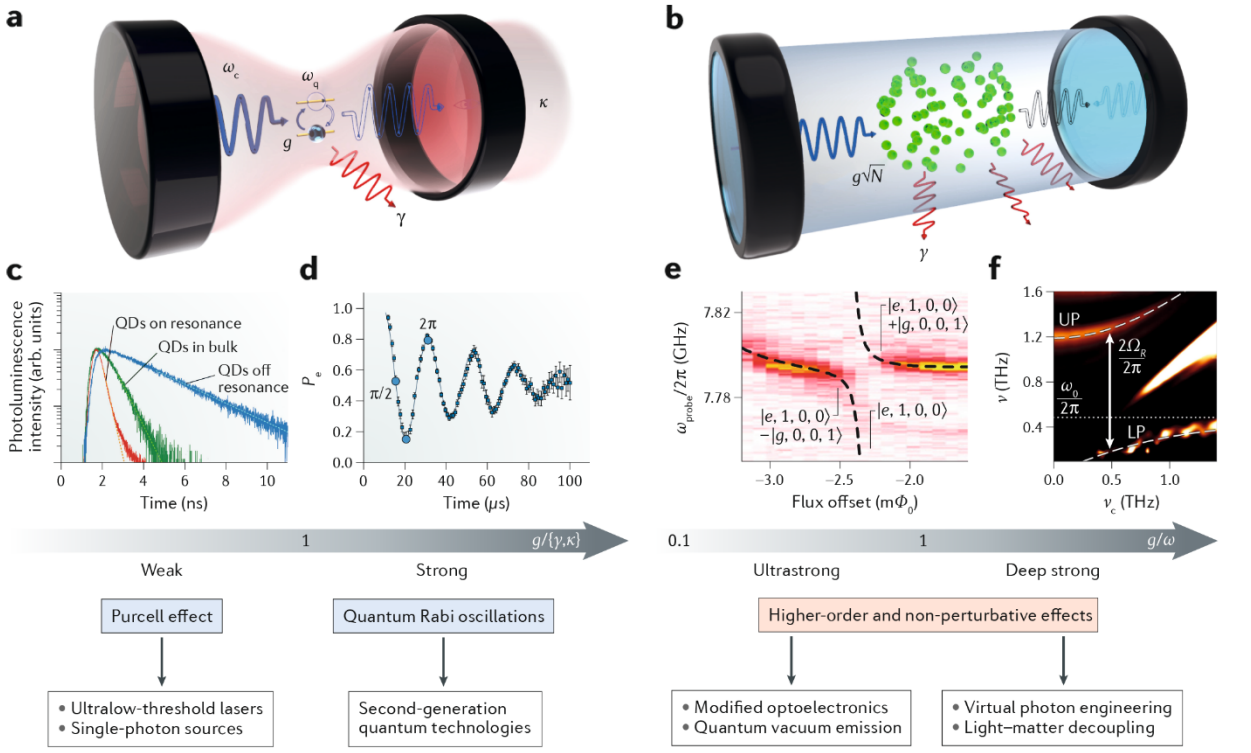

Figure 1.3 **(a) Sketch of a cavity QED system with a single two-level atom. (b) Sketch of an optical cavity coupled to many quantum emitters. (c) An example of weak coupling: the spontaneous-emission dynamics of single quantum dots can be controlled by a photonic- crystal nanocavity [44]. (d) An example of strong coupling: Rydberg atoms strongly coupled to a superconducting microwave Fabry–Perot resonator, displaying clear vacuum Rabi oscillations in time [27]. (e) An example of ultrastrong coupling: microwave spectroscopy of a system with a superconducting flux qubit coupled to a coplanar- waveguide resonator [45]. (f) An example of deep coupling: magneto- THz transmission measurements on a THz metamaterial coupled to the cyclotron resonance of a 2D electron gas [46]. All panels in this figure are reproduced with permission from Ref [4], Nature Publishing Group.**

The definitions of weak, strong, ultrastrong, and deep coupling regimes (see Figure 1.3c-f for some practical examples) are all directly connected to the coupling strength. Weak coupling and

strong coupling depend, as mentioned above, on whether the coupling g is larger than the losses of the system [27, 44]. In contrast, ultrastrong and deep coupling conditions relate to the unperturbed oscillator energies and not their damping factors. In particular, we can define a normalized coupling strength "η" – the ratio between the coupling strength "g" and the bare frequency of the excitation "ω". When η is greater than 0.1, the system is considered to enter the **ultrastrong coupling regime** [45], while if it is greater than 1, it is in the **deep coupling regime** [46]. As mention under Figure 1.3e and Figure 1.3f, the ultrastrong and deep couplings provide higher-order and non-perturbative effects, which can lead to interesting applications, such as modified optoelectronics, quantum vacuum emission, virtual photon engineering, and light-matter decoupling (see [4] and references therein for more details).

1.3 Strong Coupling Experiments: from Fabry-Perot Cavities to Plasmonic Nanoresonators and from Electronic Transitions to Phonons

In 1983, Haroche et al. reported, for the first time, experimental evidence of strong coupling using a collection of atoms and a high-*Q* microwave cavity [11]. In particular, they were able to directly observe an oscillatory exchange of energy between radiation and matter in time, which is known as vacuum Rabi oscillations. Later in 1985, a one-atom maser was realized by strongly coupling single-atoms to a microwave cavity [47]. In 1992, individual atoms were found to be strongly coupled in an optical cavity [48]. In this work, Thompson et al. injected a cesium atomic beam into a Fabry-Perot cavity and, under weak excitation, observed *vacuum* Rabi splittings with a mean number of atoms ranging from N = ~1 to 10. As shown in Figure 1.4, by only changing the average number of atoms in the cavity, a transition of the D_2 line of cesium was split, with a separation between the newly-formed, hybridized resonance peaks growing as $\sqrt{N}$. The splitting was clearly observable even for the 1 atom case, although the coupling strength g_0 was only marginally larger than the damping factors γ_1 and γ_2 in this case.

Moving towards condensed-matter excitations, **excitons** (atomic-like excitations that exist at low temperatures in many semiconductors) are known to form due to the electron-hole interaction that can lead to a concentration of oscillator strength from the continuum of electron-hole unbound states into hydrogen-like bound levels [49, 50]. Exploiting this, again in 1992, exciton-photon strong coupling was observed in a semiconductor microcavity [51]. In this work, Weisbuch et al. arranged a solid-state experiment by putting GaAs quantum wells in between a Fabry-Perot cavity made of GaAlAs/AlAs layers (working as Bragg reflectors). The 2D quantum well resonance

(exciton) was split into two bands, as presented in Figure 1.4d and the “polariton traces” (which follow the energy dispersion of the newly formed light-matter hybrid states) were shown in Figure 1.4e. It is important to notice the clear “anti-crossing behavior” of such traces in correspondence of the unperturbed exciton resonance, which is a distinctive feature of strong coupling. The authors of this work clearly underlined the importance of translating strong coupling experiments into condensed-matter systems, suggesting that the modification of the quantum well properties in such a regime could greatly improve the figures of merit of solid-states devices.

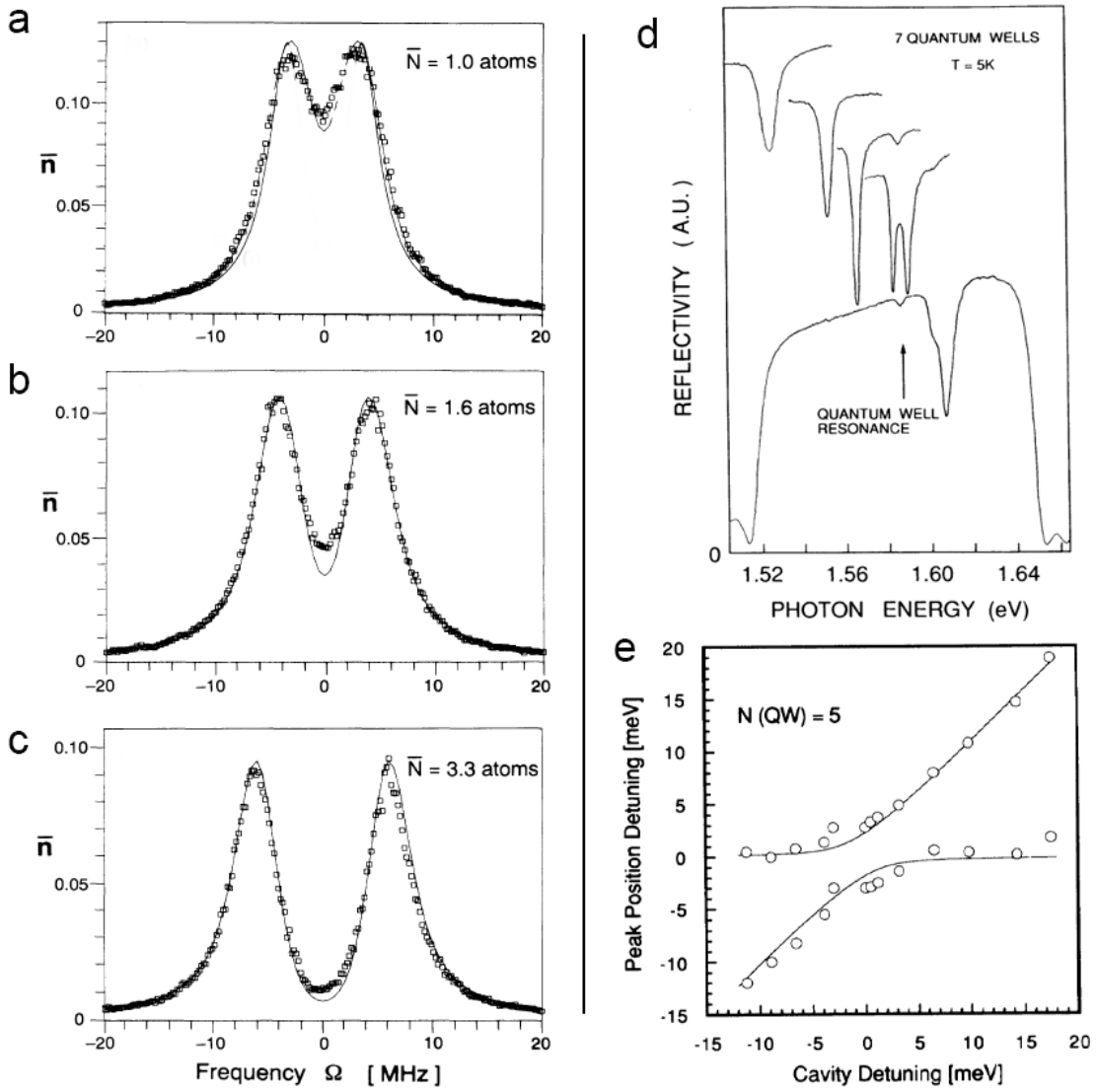

Figure 1.4 **(a)-(c) Observation of the vacuum Rabi splittings when cesium atoms are in a Fabry-Perot cavity (as can be seen, the intra-cavity photon number $\overline{N}$ is well below 1, confirming weak excitation conditions). (d)-(e) Observation of the exciton-photon strong coupling in a semiconductor microcavity. (d) Reflection spectra in a microcavity structure (measured at the temperature of 5K) for various detuning conditions. (e) Splitting peak positions as a function of cavity mode detuning. Panels (a)-(c) and (d)-(e) are reproduced with permission from Ref [48] and Ref [51], American Physical Society.**

The half-matter half-light nature of polaritons makes polariton lasers promising since they are expected to have extremely low threshold energy [20, 52-55], offering a unique testbed for many-body theories and cavity QEDs. In 2003, the polariton lasing effect was found in a semiconductor microcavity similar to the one employed in the previous work (GaAs quantum wells layers sandwiched between GaAl/AlAs Bragg reflectors) by Deng et al. [52]. In 2006, Kasprzak et al. realized Bose-Einstein condensation (a particular condition in which all particles – or quasiparticles - occupy the lowest quantum state) of exciton polaritons in a CdTe/CdMgTe microcavity [20]. Following these (and others, not mentioned for brevity) pioneering experiments, cavity QED has been developed and adapted, also using a variety of different emitters, such as quantum dots, J-aggregates, and dye molecules [1, 4].

On the other hand, advanced photonic cavities beyond traditional Fabry-Perot resonators have been employed in strong coupling experiments. An interesting example is represented by photonic crystals. They are periodic structures that support a so-called “photonic bandgap”. In a bulk photonic crystal, light is forbidden to propagate in the frequency range of the photonic bandgap. However, if part of the perfect periodicity is broken (e.g., a point or a line defect), the light will be confined and enhanced at the defect area, which can be used to build a high quality factor cavity with low mode volume. Placing quantum dots (zero-dimensional nanomaterials exploiting quantum confinement for tunable light emission properties) into photonic crystal cavities was found to be an efficient strategy to strongly couple light and matter. In 2004, the signature of vacuum Rabi splitting was observed by putting a single quantum dot in a photonic crystal cavity [15]. The authors, considering the compact size of the photonic crystal cavity, envisioned the possibility of realizing a quantum network using such system that would be able to store, process and distribute quantum information.

In recent years, plasmonic-based modes supported by metallic nanostructures have also been explored for strong coupling investigations [1]. Under appropriate conditions, electromagnetic waves can interact with free electrons at the surface of a metal to form a combined electron-light oscillation mode. These quasiparticles are known as **surface plasmon polaritons**. **Resonant** (plasmonic) **modes** can also be sustained by finite-sized metallic nanostructures, such as nanospheres, nanorods, as well as different forms of so-called “nanoantennas” [56]. By shaping the geometry of these structures and their characteristic dimensions, it is possible to obtain nanoantenna resonances over an extremely wide range of frequencies (from the UV to the THz range [56-58]). When the incident light frequency corresponds to one of such modes, the electromagnetic energy results to be coupled to the

plasmonic resonator. Since the electric field associated with the plasmonic resonance is confined in the vicinity of the nanostructure extremities, typically on a size scale comparable to the local radius of curvature of the nanostructure, light can be concentrated into extremely sub-wavelength volumes (see Chapter 4 for details regarding THz nanoantennas).

In 2016, by exploiting plasmonic nanocavities, strong coupling was achieved at room temperature [59]. In this work, the 1000-times enhanced electric field could be squeezed into a mode volume as small as 40 nm^3, leading to resonance hybridization down to a single dye molecule. The authors used a nanoparticle-on-mirror geometry for this investigation. The detailed structure is shown in Figure 1.5a, where isolated methylene-blue molecules (the Dye in the figure) were placed between the gap of gold nanoparticles and a gold mirror underneath. The size of the gold nanoparticles was 40 nm, and the thickness of the gold mirror was 70 nm. A gap with a size of 0.9 nm was obtained with a molecular spacer. Since the investigated molecular transition of the methylene blue (dye) molecules is at 665 nm, the size of the gold nanoparticle was fine-tuned to align its resonance to this transition.

As shown in Figure 1.5b, the authors conducted dark-field scattering measurements to examine the strong coupling feature of their designed system, with the transition dipole moment of the dye molecules (estimated as 100 molecules) oriented perpendicular (top) and parallel (bottom) to the plasmonic cavity electric field (for technical details regarding the procedure to align the molecules within the cavity, see Ref [59]). In the former case, the resonant scattering plasmonic peak at ω_0 was identical to the bare response without any emitters; when instead the molecular dipole moment was aligned to the cavity electric field, the spectrum showed two split peaks (ω_+ and ω_-) resulting from the strong coupling between the emitters and the plasmonic cavity. To confirm this splitting feature, the authors conducted many on-resonance-position experiments on several plasmonic cavities (see Figure 1.5c), presenting an averaged Rabi frequency as wide as 380 meV. Figure 1.5d further shows a clear anti-crossing behavior of the plasmon-exciton polariton branches. Finally, as summarized in Figure 1.5e (the mean number of the in-cavity molecules was tuned from single to a few), the Rabi splitting followed the expected scaling of $\sqrt{N}$, where N is the number of coupled molecules. This work for the first time realized room temperature strong coupling in a plasmonic nanocavity down to the single molecule, by utilizing the ultra-small mode volume featured by properly designed nanoresonators.

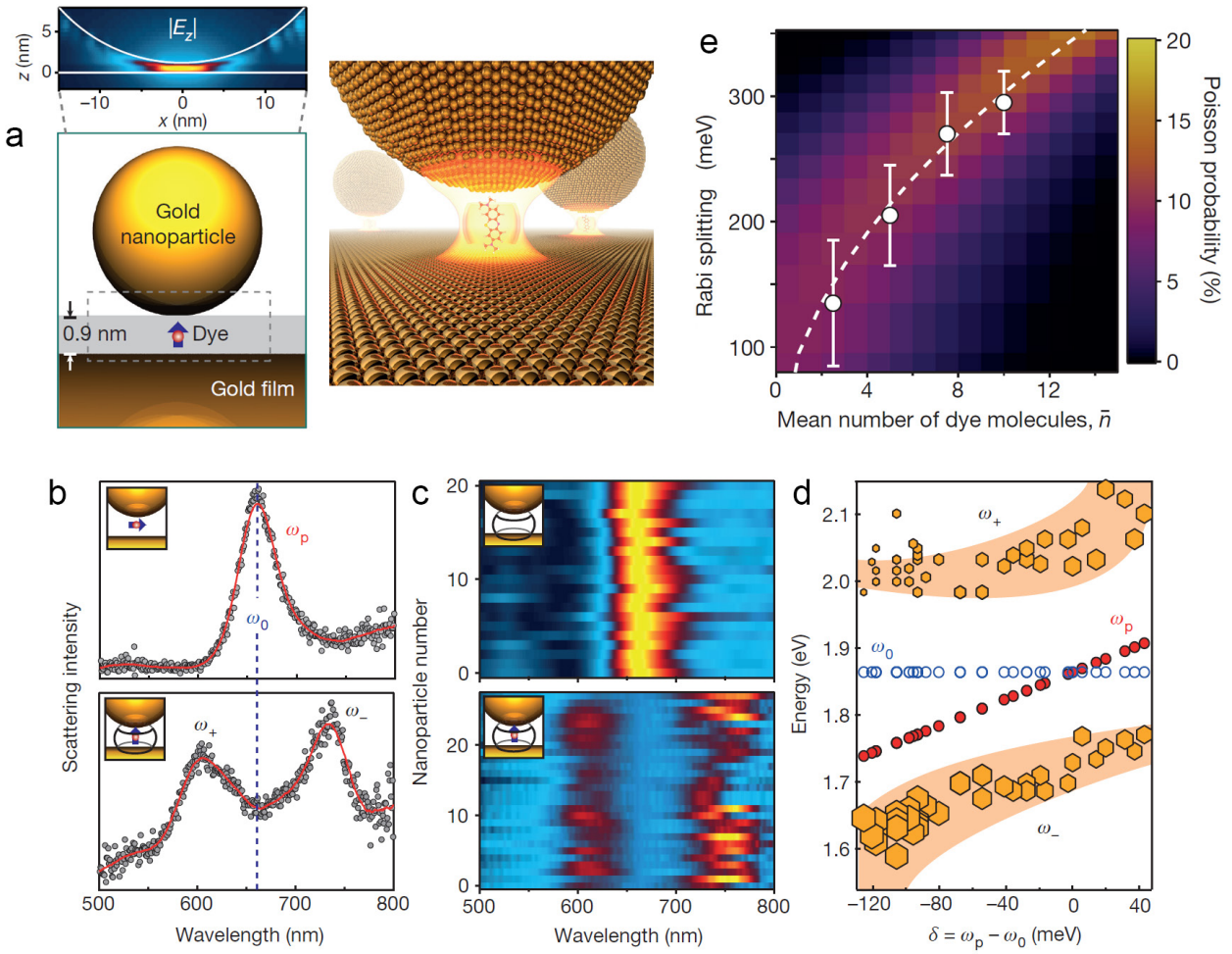

Figure 1.5 **(a) Sketch of the involved structure. The blue arrow in the gap between the nanoparticle and the mirror locates the transition dipole moment of the emitter. The inset above shows the simulated local field of the plasmonic response in the cavity, with maximum electric field enhancement of about 400, and field oriented vertically (in the z-direction). (b) Scattering spectra resulting from isolated samples according to the orientation of the emitter. (c) Comparison of scattering spectra from different samples. (d) Resonant positions of methylene-blue (ω_0), plasmon (ω_p) and hybrid modes (ω_+ and ω_-) as a function of extracted detuning. For the measurements conducted in panels (b), (c) and (d), the number of molecules in each cavity was estimated as 100. (e) Energy of Rabi oscillations versus mean number of dye molecules. All panels in this figure are reproduced with permission from Ref [59], Nature Publishing Group.**

Besides strong light-matter interactions involving electronic matter transitions, in recent years also vibrational modes were found to strongly couple to the electromagnetic field in optical cavities, realizing what was named as **vibrational strong coupling** [12, 18, 21, 22, 30, 60, 61]. The resulting dressed states in this kind of interaction are usually called vibro-polaritons. In a set of significant investigations, specific vibrational states of individual molecules were studied, showing that this type of strong coupling can lead to important applications. For example, it was shown that it could enhance the Raman signal of the vibro-polariton resonances [61], support IR

light emission [30], and also have the potential to modify the chemical reaction rate of the involved molecules [21, 22].

Raman spectroscopy is one of the essential methods to characterize a matter system and its chemical composition. It indeed offers a “fingerprint” test on a targeted material, making it useful for a wide range of applications in research and industry. The operating principle of a Raman measurement is based on the inelastic scattering of light [18]. In a typical spontaneous Raman interaction (see the left part of the energy diagram in Figure 1.6a), the scattered photons are shifted to: $\omega_{sc} = \omega_{ex} - \omega_V$, with respect to the frequency of the incident light excitation ω_{ex} , where ω_V is the Raman shift corresponding to a (Raman-allowed) vibrational transition. In 2015, Shalabney et al. found that a specific molecular vibration of a Polyvinyl acetate (PVAc) layer can be strongly hybridized by means of the vacuum field of a cavity optical mode in the infrared region, resulting in two new vibro-polariton states observable also in Raman measurements [61]. Figure 1.6a shows the energy diagram of the overall system, and also explains the mechanism of the Raman scattering process under a vacuum Rabi splitting condition. The (off-resonant) light used to retrieve the Raman response, instead of inelastically scattering via the original molecular vibration mode, can find two channels to relax within the cavity, corresponding to the new hybridized vibrational resonances. In Figure 1.6b, the schematic of the Fabry-Perot cavity (with Ag mirrors) filled with PVAc molecules is presented. The cavity resonance was tuned to match the vibrational mode of the C=O bond of the PVAc molecules (at 1740 cm^{-1}, see the red curve in Figure 1.6c). The Raman spectra were measured in reflection, by using a micro-Raman system with excitation light at 514 nm and an objective with numerical aperture of 0.7. When the system was tuned to off-resonance (i.e., the cavity mode is away from the vibrational mode), as shown in Figure 1.6c (direct infrared spectroscopy) and Figure 1.6d (Raman), there was no detectable new feature in both measurements when compared to the reference (PVAc film with no cavity). In stark contrast, when the system was tuned on-resonance (cavity mode aligned to the vibrational resonance) as shown in Figure 1.6e and Figure 1.6f, both IR and Raman measurements showed the clear emergence of upper and lower vibro-polariton bands (VP- and VP+ in Figure). Intriguingly, the Raman signal corresponding to the polariton peaks was found to be enhanced by two to three orders of magnitude when compared to the pristine vibrational transition. Only the hybridized resonance was affected by this enhancement, the origin of which is still a matter of debate from a theoretical perspective [17-19]. The authors also found, in their specific experimental conditions, that the splitting size extracted from the Raman spectrum was about twice larger than the one extracted from the IR transmission spectrum. The direct observation of

the Rabi splitting in Raman measurements represents an elegant demonstration of vibrational strong coupling directly driven by the vacuum electric field of the IR cavity, hinting at the possibility of directly modifying the intrinsic vibrational properties of molecules.

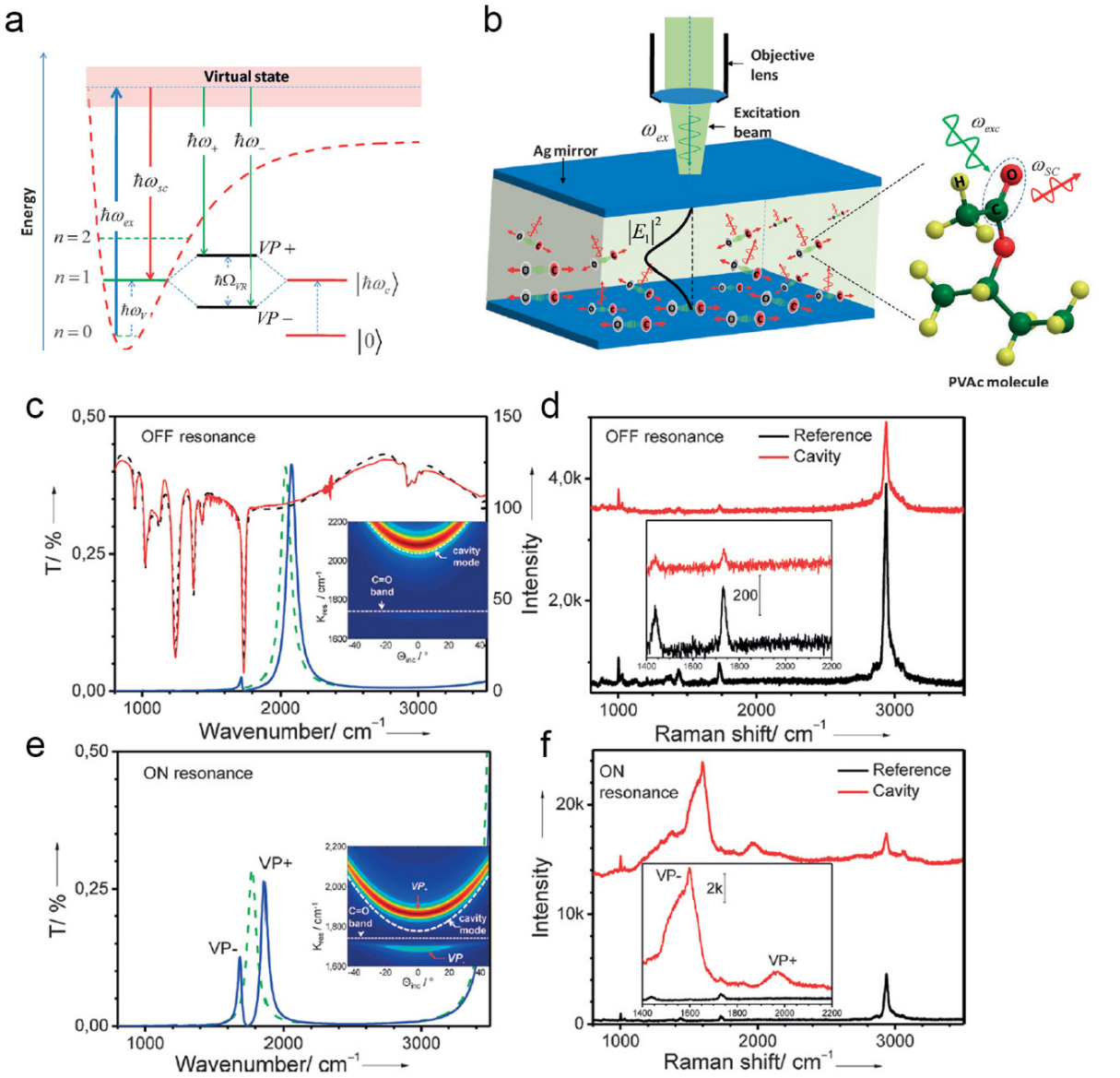

Figure 1.6 **(a) Energy-level diagram representing Raman scattering under vibrational strong coupling. (b) Schematic description of the Fabry-Perot cavity used in the experiment, which is composed of two thin Ag mirrors spaced by a Polyvinyl acetate (PVAc) layer. (c) Transmission spectra of a thin PVAc film (red and dashed black curves, measured and calculated, respectively), a bare cavity detuned from the vibrational transition (dashed green), and the same cavity filled with molecules (blue). The inset shows the C=O band and uncoupled cavity mode dispersion. (d) Off-resonance Raman scattering measurement on the cavity (red) compared to a reference molecule film. (e) On-resonance transmission measurements of a bare cavity (dashed green) and of the same cavity filled with molecules (solid blue). (f) On-resonance Raman measurement. Upper (VP+) and lower (VP-) polaritons were observed with significant Raman enhancement. All panels in this figure are reproduced with permission from Ref [61], Wiley-VCH.**

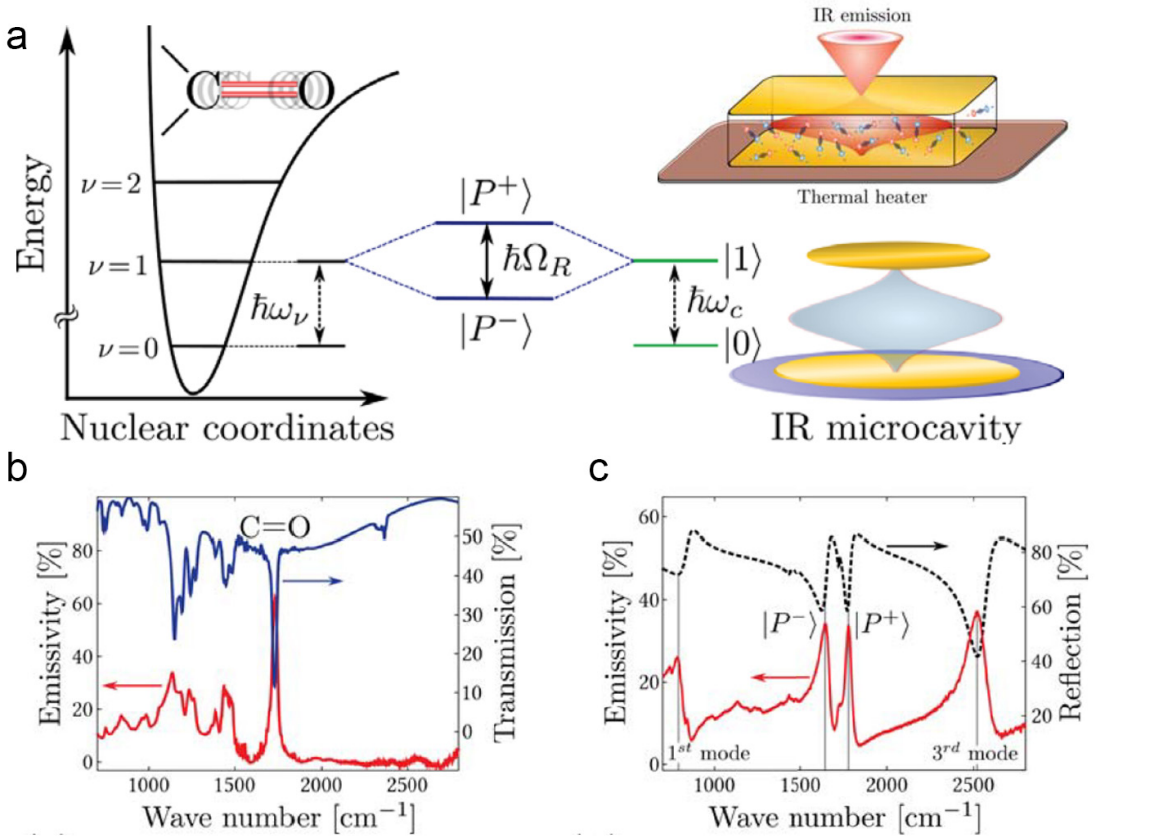

Figure 1.7 **(a) Energy level sketch of the vibrational strong coupling system for IR emission. A thermal heater is placed beneath the Fabry-Perot microcavity (left). (b) Emissivity spectrum of a 4 μm thick film of PMMA at 100 °C (red curve) and transmission spectrum of PMMA (blue curve). (c) Emissivity (red curve) and simulated cavity reflection (black dashed curve) spectra of the strongly coupled cavity at 100 °C. All panels in this figure are reproduced with permission from Ref [30], ACS.**

Vibrational strong couplings can also lead to light emission via the vibro-polaritonic transitions. In 2017, Chervy et al. achieved a new IR source by heating a vibro-polaritonic system [30]. The energy diagram and device setup are shown in Figure 1.7a. A common organic polymer (poly(methyl methacrylate), PMMA) layer was embedded in a Fabry-Perot microcavity with gold mirrors. By tuning the cavity mode to a vibrational transition related to the C=O bond of PMMA, the pristine mode of PMMA splits into two vibro-polariton states $\left|P^+\right\rangle$ and $\left|P^-\right\rangle$. After examining the splitting features by means of IR transmission measurement, the authors heated the sample up to 100 ºC to check the emission of IR light. The original emissivity spectrum of a 4 μm thick film of PMMA at 100 °C (red curve) and the corresponding PMMA transmission spectrum (blue curve) are shown in Figure 1.7b. After embedding this PMMA layer into the Fabry-Perot cavity, the emissivity (red curve) and simulated cavity reflection spectrum (black dashed curve) of the strongly coupled system at 100 °C are shown in Figure 1.7c. As can be seen, the authors in this study observed comparable emissivity from both the upper and lower vibro-polaritonic states. As

it is evident from this figure, the expected vibro-polariton branches dispersion in this type of cavity can be clearly identified also in the emission response of the system. The stronger emission appears to originate from the lower polariton branch $|P^-\rangle$ for small in-plane wavevector values. Though still a very first investigation, this work suggests the possibility of using vibro-polaritons for new long-wavelength light sources, possibly following the path of what has been achieved on polaritonic light emission from hybridized electronic transition [20, 52-55].

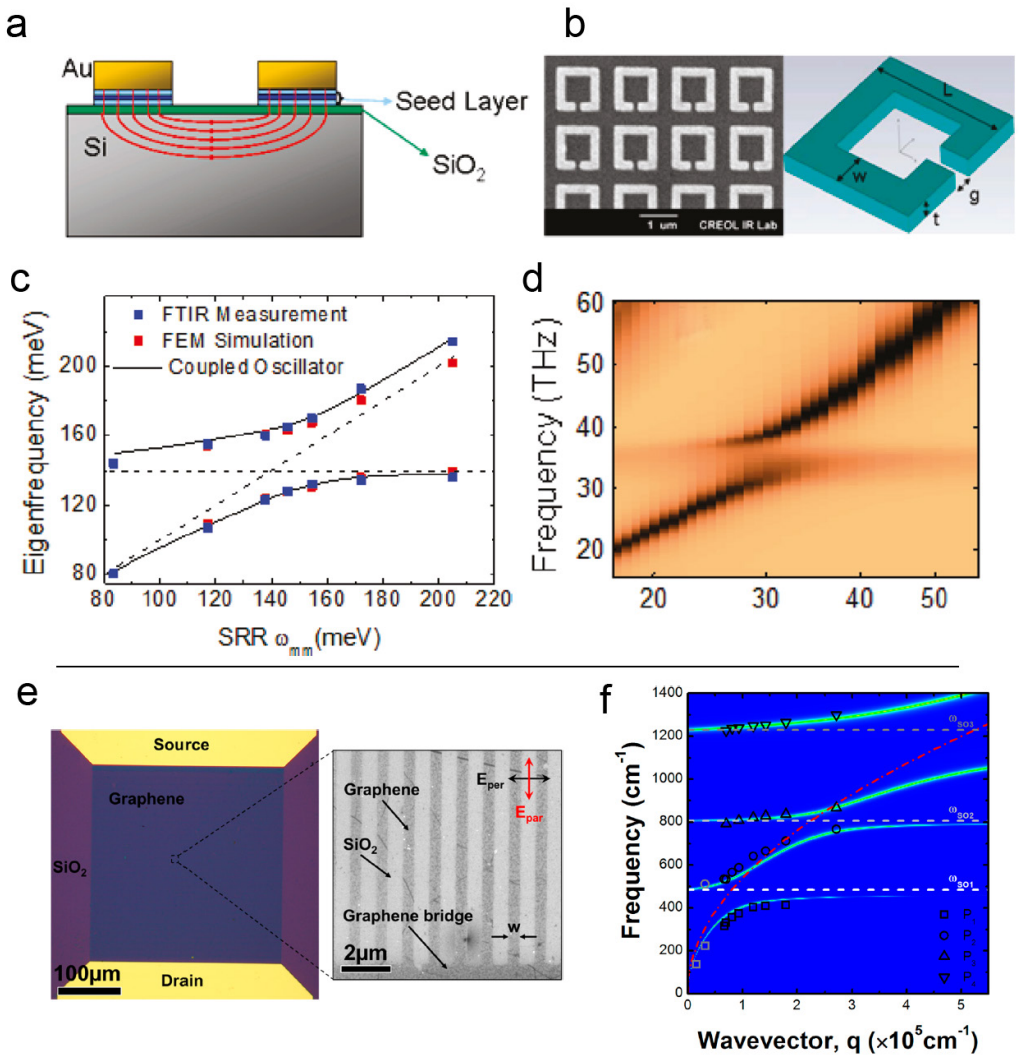

Figure 1.8 **(a) Schematic cross-section showing the interface between a metallic split-ring structure and a silica layer on top of a silicon substrate. (b) Schematic detail of the split-ring resonator array. (c) Measured (blue) and simulated (red) resonant frequencies of the coupled system, compared to the analytical model for two coupled oscillators (black line). (d) Simulated normal mode splitting when the metasurface is directly in contact with the silica substrate. (e) Optical (left) and scanning electron microscope (right) images of the graphene nanoribbon array device. (f) Calculated loss plot with extracted peak frequencies overlaid. The red dashed line shows the calculated dispersion of the uncoupled graphene plasmon. The white, light grey and grey dashed lines show the calculated frequency of the three surface optical phonons. Panels from (a) to (d) in this figure are reproduced with permission from Ref [33], ACS. Panels (e) and (f) in this figure are reproduced with permission from Ref [35], ACS.**

The above-mentioned pioneering works on vibrational strong coupling all involved IR light and vibrations characteristic of individual molecules, and were performed utilizing Fabry-Perot cavities filled with a large number of molecules. This thesis (as it will be largely discussed in the following Chapters) instead focuses on the THz spectral region and collective vibrations (phonons) in nanomaterials, and will make use of plasmonic nanoresonators coupled to a small number of nanocrystals.

Regarding the plasmonic coupling to collective vibrations, several recent works have investigated the interaction between plasmonic structures and surface phonons [33, 35, 36]. For instance, as shown in Figure 1.8a-d, the strong coupling between split-ring resonators and infrared active phonons for a SiO_2 underlayer was observed [33]. The phonon absorption of the silica thin film (10 nm thick) is located at around 9 µm (33 THz). By tuning the plasmonic resonance of split-ring metasurfaces (see Figure 1.8b) across this phonon mode, the authors observed a Rabi splitting of ~40 meV. As shown in Figure 1.8c, the two polariton branches were retrieved through experimental IR measurements and numerical simulations. The normal mode splitting from the simulated spectra shown in Figure 1.8d clearly highlights the polariton branch separation beyond the finite linewidths of the resonant modes.

Plasmon-phonon strong coupling was also realized between the plasmon resonance of graphene nanoribbons and several surface optical phonons of silica [35]. As shown in Figure 1.8e, the authors fabricated a graphene monolayer on a 300-nm-thick silica film (overall substrate: silicon). Through electron beam lithography, nanoribbons of graphene were prepared with widths ranging from 150 nm to 500 nm, in such a way to tune their plasmon resonances over the three surface phonon modes (485 cm^{-1}, 806 cm^{-1}, 1229 cm^{-1}) of the silica film. As presented in Figure 1.8f, the multiple Rabi splittings were clearly observed in IR transmission measurements, when the graphene nanoribbons were resonantly excited (IR light polarization perpendicular to the ribbons).

Compared to previous works involving phonon strong coupling with plasmonic resonant structures, the investigation presented in this thesis focuses on nanocavities resonating in the THz frequency range and coupled to few nano-objects. It furthermore studies such interaction not only via direct THz resonant illumination of an ensemble of nanocavities, but also in the so-called “dark conditions”, i.e., employing non-resonant (visible) radiation, by means of micro-Raman spectroscopy. The latter gives access to the characterization of vacuum-field-driven phonon resonance hybridization performed on individual plasmonic nanocavities.

1.4 Thesis Organization and Achievements

In Chapter 1, I present the motivation and the objective of this doctoral research, as well as giving a brief introduction of strong light-matter interaction in electromagnetic wave cavities. Then, I introduce the formalism to describe two/three-level coupled oscillators from the classical and quantum point of view in Chapter 2. The prerequisites of designing plasmon-phonon coupling systems in the THz regime are elaborated in Chapter 3, where the detailed steps of building numerical models and some analytical tools are introduced. By utilizing all the information that I presented from Chapters 1 to 3, in Chapter 4, I successfully designed end-to-end nanoantenna arrays whose resonance is strongly coupled to the optical phonon mode of CdS nanocrystals. Through direct THz illumination, we measure clear Rabi splittings that confirm the implementation of a strongly coupled system between nanoantenna resonance and phonons. In addition, by micro-Raman measurements, we show that the intrinsic FR phono response of the CdS nanocrystals can even be modified without any THz illumination. Indeed, the plasmonic nanocavity alone can get the nanocrystals strongly coupled without a resonant illumination, thanks to the extremely high cavity vacuum electric field. In Chapter 5, a moon-shaped nanoantenna array is designed to further improve the coupling strength in such a THz-plasmon and FR-phonon strongly coupled system. This particular improvement was made by optimizing the moon structure to reduce the ohmic loss and scattering, which can lead to a higher field enhancement, a smaller mode volume, as well as a narrower line-width of the plasmon response to make it more comparable to the phononic counterpart. This new design has proved its effectiveness by means of direct THz illumination and micro-Raman measurements, offering a new playground to conduct intriguing investigations in nonlinear optics, strong-coupling driven THz light emission. In Chapter 6, a summary of this thesis work and some perspectives are given.

2 Theoretical Description of a Light-Matter Coupling System

The interaction between light and matter can be essentially explained as a process in which two oscillators exchange energy under a variety of coupling conditions [1, 4]. Building appropriate physical models for the targeted systems can help to gain an intuitive understanding of strong coupling and thus facilitate the structural design and parametric optimization, as well as reproduce the experimental/numerical results. In this chapter, theoretical approaches will be presented in a general way. In the beginning, a mechanical analog shows that the motions of two independent oscillating objects are intensively influenced by a connecting spring (when it ensures enough coupling strength). Then classical coupled-oscillator models offer a tool to understand the energy dissipation in such strongly coupled systems. In the end, phenomenological quantum models are also presented, which will be later used for fitting the retrieved polariton traces in Chapter 4 and Chapter 5.

2.1 Classical Coupled-Oscillator Models

2.1.1 An Analogy - Mechanical Model

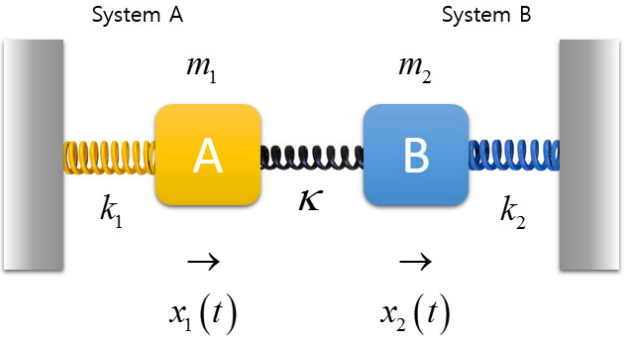

Figure 2.1 Mechanical analog of a coupled system

Coupled harmonic oscillators are an intuitive and popular model for many phenomena [62-64]. In the mechanical model shown in Figure 2.1, if the "black spring" in the middle is absent (i.e., the coupling: $\kappa = 0$), object A and B will oscillate around their equilibrium positions independently. The motions of A (x_1) and B (x_2) will only depend on their masses (m_1 and m_2) and spring constants (k_1 and k_2) respectively:

$$\begin{aligned} m_1\ddot{x}_1 + k_1 x_1 &= 0 \\ m_2\ddot{x}_2 + k_2 x_2 &= 0. \end{aligned} \tag{2.1}$$

By taking the Fourier transformation:

$$\begin{aligned} x &= Ae^{-i\omega t} \\ \dot{x} &= -i\omega \cdot Ae^{-i\omega t} = -i\omega x \\ \ddot{x} &= -\omega^2 \cdot Ae^{-i\omega t} = -\omega^2 x, \end{aligned} \tag{2.2}$$

the eigenfrequencies of these two independent oscillators are $\omega_1^0 = \sqrt{k_1 / m_1}$ and $\omega_2^0 = \sqrt{k_2 / m_2}$ respectively. We now connect these two objects through a black spring (i.e., in the presence of coupling: $\kappa \neq 0$) as in Figure 2.1, the motions of A and B become:

$$\begin{aligned} m_1\ddot{x}_1 + \left(k_1 + \kappa\right)x_1 - \kappa x_2 &= 0 \\ m_2\ddot{x}_2 + \left(k_2 + \kappa\right)x_2 - \kappa x_1 &= 0. \end{aligned} \tag{2.3}$$

From these equations, we know that the motions are not independent anymore, because each oscillator is influenced by the other through the coupling κ. Since it is reasonable to assume that the resulting motions of A and B have an oscillatory behavior, we can substitute the following trial solutions $x_1(t) = A_1 e^{-i\omega t}$ and $x_2(t) = A_2 e^{-i\omega t}$ into Equation (2.3). Thus the overall motions of this coupled system can be simplified by the following matrix.

$$\begin{pmatrix} k_1 + \kappa - \omega^2 m_1 & -\kappa \\ -\kappa & k_2 + \kappa - \omega^2 m_2 \end{pmatrix} \begin{pmatrix} x_1 \\ x_2 \end{pmatrix} = 0$$

$$\downarrow \tag{2.4}$$

$$\begin{pmatrix} \dfrac{k_1 + \kappa}{m_1} - \omega^2 & \dfrac{-\kappa}{m_1} \\ \dfrac{-\kappa}{m_2} & \dfrac{k_2 + \kappa}{m_2} - \omega^2 \end{pmatrix} \begin{pmatrix} x_1 \\ x_2 \end{pmatrix} = 0.$$

In order to retrieve a nontrivial solution in the frequency domain, the determinant of the above matrix should be zero,

$$\begin{vmatrix} \dfrac{k_1 + \kappa}{m_1} - \omega^2 & \dfrac{-\kappa}{m_1} \\ \dfrac{-\kappa}{m_2} & \dfrac{k_2 + \kappa}{m_2} - \omega^2 \end{vmatrix} = 0. \tag{2.5}$$

By solving this equation, we have the eigenfrequencies (dressed modes):

$$\omega_{\pm}^2 = \frac{1}{2}\left(\omega_1^2 + \omega_2^2\right) \pm \frac{1}{2}\sqrt{4\Gamma^2 + \left(\omega_1^2 - \omega_2^2\right)^2}, \tag{2.6}$$

where

$$\omega_1 = \sqrt{\frac{k_1 + \kappa}{m_1}},\ \omega_2 = \sqrt{\frac{k_2 + \kappa}{m_2}},\ \Gamma = \frac{\kappa}{\sqrt{m_1 m_2}}. \tag{2.7}$$

We discard the negative frequencies from taking the square root of $\omega_{\pm}^2$, and can have two pairs of eigenvalues and eigenvectors as: ω_- for $\begin{pmatrix} x_1^- \\ x_2^- \end{pmatrix}$ and ω_+ for $\begin{pmatrix} x_1^+ \\ x_2^+ \end{pmatrix}$. Through separately studying the amplitude contributions of each eigenvalue, we can easily reconstruct the time-dependent displacements of objects A and B in the coupled system. For the case of the first eigenvalue and eigenvector:

$$\begin{pmatrix} \frac{k_1 + \kappa}{m_1} & \frac{-\kappa}{m_1} \\ \frac{-\kappa}{m_2} & \frac{k_2 + \kappa}{m_2} \end{pmatrix} \begin{pmatrix} x_1^- \\ x_2^- \end{pmatrix} = \begin{pmatrix} \omega_-^2 & 0 \\ 0 & \omega_-^2 \end{pmatrix} \begin{pmatrix} x_1^- \\ x_2^- \end{pmatrix}, \tag{2.8}$$

we know that the first dressed mode determines the amplitude contributions to both objects A and B as follows,

$$\begin{aligned} A_1^- &= x_1^- A \\ A_2^- &= x_2^- A. \end{aligned} \tag{2.9}$$

Thus the displacements (for both A and B) in time are,

$$\begin{aligned} x_1^-(t) &= x_1^- A \exp\left(-i\omega_- t\right) \\ x_2^-(t) &= x_2^- A \exp\left(-i\omega_- t\right). \end{aligned} \tag{2.10}$$

(note: $x_1^-(t)$ is the displacement function over time, while x_1^- is the value from the eigenvector)

For the case of the second eigenvalue and eigenvector:

$$\begin{pmatrix} \frac{k_1 + \kappa}{m_1} & \frac{-\kappa}{m_1} \\ \frac{-\kappa}{m_2} & \frac{k_2 + \kappa}{m_2} \end{pmatrix} \begin{pmatrix} x_1^+ \\ x_2^+ \end{pmatrix} = \begin{pmatrix} \omega_+^2 & 0 \\ 0 & \omega_+^2 \end{pmatrix} \begin{pmatrix} x_1^+ \\ x_2^+ \end{pmatrix}, \tag{2.11}$$

the second dressed mode determines the amplitude contributions to both objects A and B as follows,

$$A_1^+ = x_1^+ A$$
$$A_2^+ = x_2^+ A. \tag{2.12}$$

Thus the displacements (for both A and B) in time are,

$$x_1^+(t) = x_1^+ A\exp(-i\omega_+ t)$$
$$x_2^+(t) = x_2^+ A\exp(-i\omega_+ t). \tag{2.13}$$

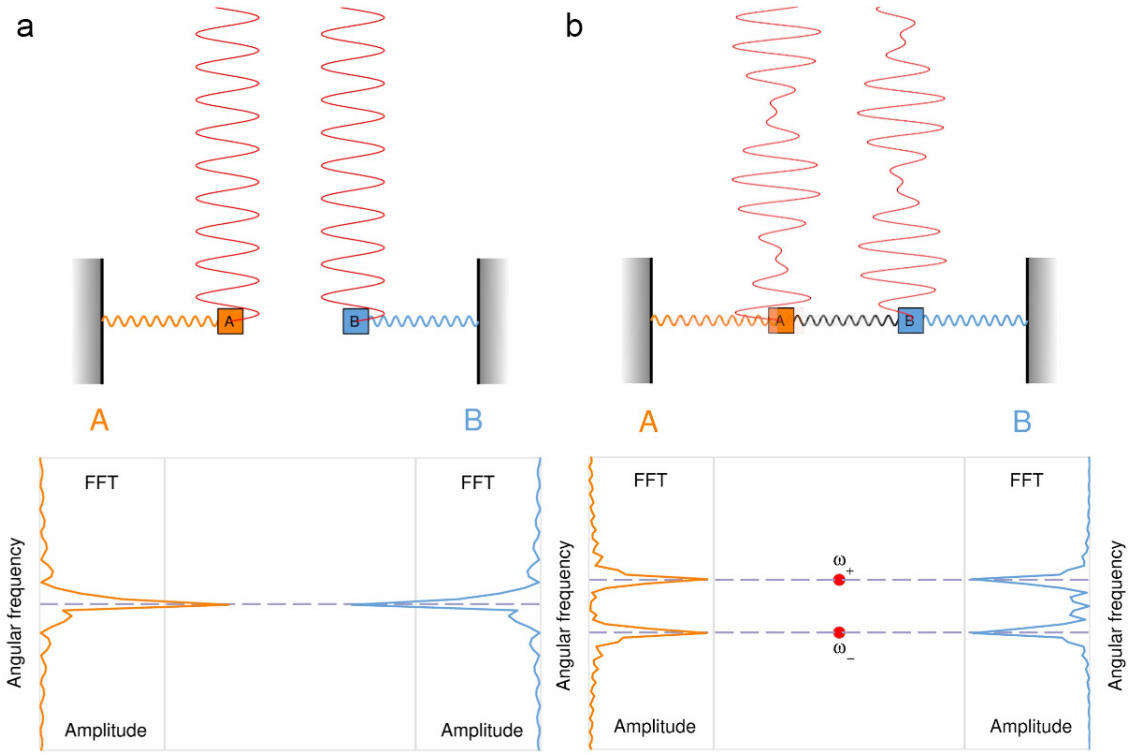

Figure 2.2 Motion and frequency analysis of two uncoupled (a) and coupled (b) oscillators.

In the end, the movement of object 'A' can be described as a sum of the movement contribution from both the dressed modes:

$$x_1(t) = x_1^-(t) + x_1^+(t)$$
$$= x_1^- A\exp(-i\omega_- t) + x_1^+ A\exp(-i\omega_+ t). \tag{2.14}$$

Meanwhile, the movement of object 'B' can be described in the same way:

$$x_2(t) = x_2^-(t) + x_2^+(t)$$
$$= x_2^- A\exp(-i\omega_- t) + x_2^+ A\exp(-i\omega_+ t). \tag{2.15}$$

The motions of uncoupled and coupled spring systems are plotted in Figure 2.2. By adding a coupling strength (the black spring in Figure 2.2b) between two independent oscillators, the motions of these two objects A and B become inevitably connected, with a periodic exchange of energy between the two oscillators (Figure 2.2b). In the frequency domain, we can also see two normal modes of the coupled system.

2.1.2 Two-Coupled-Oscillator Model

More generally, in a classical undamped system, one can describe two coupled harmonic oscillators with the following physical model [65].

$$\begin{aligned} \ddot{x}_1 + \omega_1^2 x_1 + g^2 x_2 &= 0 \\ \ddot{x}_2 + \omega_2^2 x_2 + g^2 x_1 &= 0, \end{aligned} \tag{2.16}$$

in which g is the coupling between the two oscillators. By substituting the trial solutions:

$$\begin{aligned} x_1(t) &= A_1 e^{-i\omega t} \\ x_2(t) &= A_2 e^{-i\omega t}. \end{aligned} \tag{2.17}$$

One can solve the equations as follows:

$$\begin{cases} -\omega^2 x_1 + \omega_1^2 x_1 + g^2 x_2 = 0 \\ -\omega^2 x_2 + \omega_2^2 x_2 + g^2 x_1 = 0 \end{cases}$$
$$\downarrow$$
$$\begin{pmatrix} \omega_1^2 - \omega^2 & g^2 \\ g^2 & \omega_2^2 - \omega^2 \end{pmatrix} \begin{pmatrix} x_1 \\ x_2 \end{pmatrix} = 0 \tag{2.18}$$
$$\downarrow$$
$$\begin{vmatrix} \omega_1^2 - \omega^2 & g^2 \\ g^2 & \omega_2^2 - \omega^2 \end{vmatrix} = 0.$$

The dressed states are:

$$\omega_{\pm}^2 = \frac{1}{2}\left(\omega_1^2 + \omega_2^2\right) \pm \frac{1}{2}\sqrt{4g^4 + \left(\omega_1^2 - \omega_2^2\right)^2}. \tag{2.19}$$

By introducing the damping factors for both oscillators, the equations of motion become [5, 65, 66]:

$$\begin{aligned}\ddot{x}_1+\gamma_1\dot{x}_1+\omega_1^2x_1+g^2x_2=0\\ \ddot{x}_2+\gamma_2\dot{x}_2+\omega_2^2x_2+g^2x_1=0.\end{aligned} \tag{2.20}$$

After Fourier transformation, we have

$$\begin{cases}-\omega^2x_1-i\omega\gamma_1+\omega_1^2x_1+g^2x_2=0\\ -\omega^2x_2-i\omega\gamma_2+\omega_2^2x_2+g^2x_1=0\end{cases}$$
$$\downarrow$$
$$\begin{pmatrix}\omega_1^2-i\omega\gamma_1-\omega^2 & g^2\\ g^2 & \omega_2^2-i\omega\gamma_2-\omega^2\end{pmatrix}\begin{pmatrix}x_1\\ x_2\end{pmatrix}=0 \tag{2.21}$$
$$\downarrow$$
$$\begin{vmatrix}\omega_1^2-i\omega\gamma_1-\omega^2 & g^2\\ g^2 & \omega_2^2-i\omega\gamma_2-\omega^2\end{vmatrix}=0.$$

The determinant can be arranged as a quartic equation

$$\omega^4+i\left(\gamma_1+\gamma_2\right)\omega^3-\left(\omega_1^2+\omega_2^2+\gamma_1\gamma_2\right)\omega^2-i\left(\gamma_2\omega_1^2+\gamma_1\omega_2^2\right)\omega+\omega_1^2\omega_2^2-g^4=0. \tag{2.22}$$

This equation has four roots. By discarding the negatives, one can obtain the dressed modes $\omega_{\pm}$.

2.1.3 Power Dissipation in the Damped Model

With a driving force applied, we can describe the two coupled oscillators as follows [5, 66-68].

$$\begin{cases}\ddot{x}_1 + \gamma_1\dot{x}_1 + \omega_1^2x_1 + g^2x_2 = f\\ \text{kinetic force} + \text{damping} + \text{restoring force} + \text{coupling} = \text{driving force},\\ \ddot{x}_2 + \gamma_2\dot{x}_2 + \omega_2^2x_2 + g^2x_1 = 0\end{cases} \tag{2.23}$$

in which $x_{1,2}$, $\gamma_{1,2}$, and $\omega_{1,2}$ are the displacement, the damping, and the resonance frequency of two oscillators respectively. The constant g is the coupling between two oscillators as in the last section and $f=Fe^{-i\omega t}$ is the driving force applied to the first oscillator.

After Fourier transformation, we can write Equation (2.23) as,

$$\begin{cases}\left(\omega_1^2-i\gamma_1\omega-\omega^2\right)\tilde{A}_1+g^2\tilde{A}_2=F\\ g^2\tilde{A}_1+\left(\omega_2^2-i\gamma_2\omega-\omega^2\right)\tilde{A}_2=0.\end{cases} \tag{2.24}$$

By solving these equations, the two complex amplitudes now can be written as,

$$\begin{aligned}\tilde{A}_1 &= \tilde{\chi}_1 F \\ \tilde{A}_2 &= \tilde{\chi}_2 F,\end{aligned} \tag{2.25}$$

in which,

$$\begin{aligned}\tilde{\chi}_1 &= \frac{\left(\omega_2^2 - i\gamma_2\omega - \omega^2\right)}{\left(\omega_1^2 - i\gamma_1\omega - \omega^2\right)\left(\omega_2^2 - i\gamma_2\omega - \omega^2\right) - g^4} \\ \tilde{\chi}_2 &= \frac{-g^2}{\left(\omega_1^2 - i\gamma_1\omega - \omega^2\right)\left(\omega_2^2 - i\gamma_2\omega - \omega^2\right) - g^4}.\end{aligned} \tag{2.26}$$

On the first oscillator, the transient power is,

$$p(t) = \mathrm{Re}\left[f(t)\right]\mathrm{Re}\left[\dot{x}_1\right]. \tag{2.27}$$

The work done by the driving force in one period can be presented as [69],

$$W = \int_0^T \mathrm{Re}\left[f(t)\right]\mathrm{Re}\left[\dot{x}_1\right]dt, \tag{2.28}$$

where $T = 2\pi/\omega$. Then the dissipated power of driving force is,

$$\left\langle p(t)\right\rangle = \frac{1}{T}\int_0^T \mathrm{Re}\left[f(t)\right]\mathrm{Re}\left[\dot{x}_1\right]dt. \tag{2.29}$$

After a series of calculation (see the details in Appendix 1), we can have the dissipated power from the driving force as:

$$P_{\text{dissipate}} = \left\langle p(t)\right\rangle = \mathrm{Re}\left[\frac{-i\omega\tilde{\chi}_1 F^2}{2}\right]. \tag{2.30}$$

2.1.4 Splitting Spectrum of Unevenly-Damped Oscillators

In most of the strong coupling studies, the interaction is phenomenologically described either by a classical two-coupled-oscillator model (see Subsection 2.1.2) or a two-level quantum system (see Subsection 2.2.2 below). Both in classical [1] and quantum [2] descriptions, the frequencies of the resulting two hybridized resonances are typically extracted through the calculation of the normal modes of the coupled system:

$$\omega_\pm = \omega_1 + \omega_2 - i\left(\gamma_1 + \gamma_2\right)/4 \pm \sqrt{g_{\text{eff}}^2 - \left(\gamma_1 - \gamma_2\right)^2/16}. \tag{2.31}$$

The parameter g_{eff} is the effective coupling constant, and $g_{\text{eff}} = g^2/(2\bar{\omega})$ where $\bar{\omega} = (\omega_1 + \omega_2)/2$ as in Reference [66]. Thus the Rabi splitting $(\omega_+ - \omega_-)$ is:

$$\Omega_R = 2\sqrt{g_{\text{eff}}^2 - (\gamma_1 - \gamma_2)^2/16}. \quad \textbf{(2.32)}$$

Conventionally, the Rabi splitting in a damped system will be clearly visible if the splitting is larger than the resonance widths of the new hybridized modes $\Omega_R > \frac{\gamma_1}{2} + \frac{\gamma_2}{2}$. This is the most commonly used rule of thumb that defines the onset of strong coupling. Therefore, from Equation (2.32), the coupling constant should satisfy the following restriction:

$$4g_{\text{eff}}^2 > \frac{\gamma_1^2}{2} + \frac{\gamma_2^2}{2} \quad \textbf{(2.33)}$$

However, this should be understood more like a rule of thumb, and the measured splittings can indeed be also smaller than the average resonance width [1].

In general, Equation (2.32) well describes the spectrally observed splitting when the damping factors of the two oscillators are comparable. However, when one of the damping factors is much larger than the other, Equation (2.32) fails to predict the peak positions of the hybridized resonance of a strongly coupled system. For example, in the plasmon-phonon interaction at THz frequencies that will be described in Chapter 4, the damping factor of the plasmonic resonators is significantly larger than the one associated with the phonon resonance of the employed nanocrystals, preventing Equation (2.32) from accurately describing the experimentally observed Rabi splittings. Here, I show that the energy dissipation spectra directly calculated from the two-coupled-oscillator model can better predict the splitting feature of a strongly coupled system. As an example, we consider the damping factor of one oscillator to be two times larger than the one of the other (i.e., $\gamma_1 > 2\gamma_2$). Overall, the parameters were chosen as: $\omega_1 = \omega_2 = 8$, $\gamma_1 = 2$, $\gamma_2 = 0.5$, $g = 5$ (all in THz), and the comparison of the splitting is shown in Figure 2.3. One can find that the splitting derived from the power dissipation (blue curve in Figure 2.3b) shows a significantly earlier peak separation under a relatively weak coupling strength, and generally a larger splitting for the considered parameter space. Therefore, the calculation of the dissipated power (using Equation (2.30)) is a useful tool for the investigation of the spectral response of a strongly coupled system.

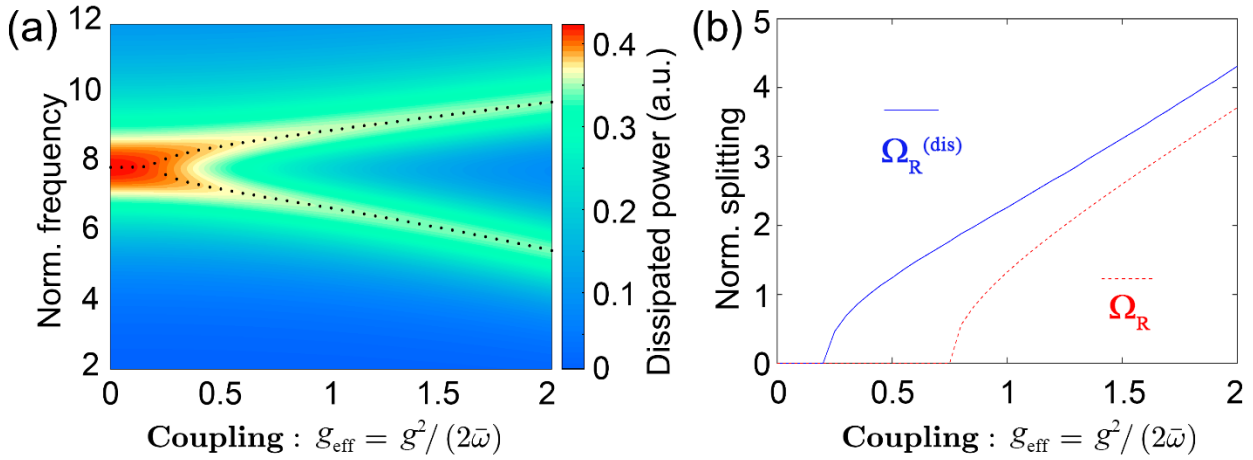

Figure 2.3 **(a) Dissipated power spectrum as a function of the coupling strength *V*. (b) Rabi splitting as a function of coupling strength. $\Omega_R^{(\text{dis})}$ (blue) is the Rabi splitting extracted from the curve of dissipated power described by Equation (2.30), and Ω_R (red) is the Rabi splitting calculated from Equation (2.32).**

2.1.5 Power Dissipation in the Damped Three-Coupled-Oscillator Model

A Three-coupled-oscillator model is advantageous when the influence of a third oscillator is not negligible. For example, in Chapter 4, we will show that an additional resonant mode of the nanoantenna array (a "lattice mode") is close to the antenna response and clearly visible on the far-field spectra. Similar to the two-coupled-oscillator case, the three-coupled-oscillator system driven by a force f can be described with the following equations of motion,

$$\begin{cases} \ddot{x}_1 + \gamma_1\dot{x}_1 + \omega_1^2 x_1 + g_{12}^2 x_2 + g_{13}^2 x_3 = f \\ \ddot{x}_2 + \gamma_2\dot{x}_2 + \omega_2^2 x_2 + g_{12}^2 x_1 = 0, \\ \ddot{x}_3 + \gamma_3\dot{x}_3 + \omega_3^2 x_3 + g_{13}^2 x_1 = 0 \end{cases} \tag{2.34}$$

in which $x_3(t) = A_3 e^{-i\omega t}$ is the motion of the third oscillator. The parameter g_{12} is the coupling constant between the first and the second oscillators, while g_{13} is the coupling constant between the first and the third oscillators. In the frequency domain:

$$\begin{cases} \left(\omega_1^2 - i\gamma_1\omega - \omega^2\right)\tilde{A}_1 + g_{12}^2\tilde{A}_2 + g_{13}^2\tilde{A}_3 = F \\ g_{12}^2\tilde{A}_1 + \left(\omega_2^2 - i\gamma_2\omega - \omega^2\right)\tilde{A}_2 = 0 \\ g_{13}^2\tilde{A}_1 + \left(\omega_2^2 - i\gamma_2\omega - \omega^2\right)\tilde{A}_3 = 0 \end{cases}. \tag{2.35}$$

For simplicity, we define:

$$
\begin{aligned}
A &= \omega_1^2 - i\gamma_1\omega - \omega^2 \\
B &= \omega_2^2 - i\gamma_2\omega - \omega^2 \\
C &= \omega_3^2 - i\gamma_3\omega - \omega^2 \\
D &= ABC - g_{12}^4 C - g_{13}^4 B.
\end{aligned}
\tag{2.36}
$$

Thus the three complex amplitudes can be written as:

$$
\begin{aligned}
\tilde{A}_1 &= \tilde{\chi}_1 F = \frac{BC}{D} \cdot F \\
\tilde{A}_2 &= \tilde{\chi}_2 F = \frac{-g_{12}^2 C}{D} \cdot F \\
\tilde{A}_3 &= \tilde{\chi}_3 F = \frac{-g_{13}^2 B}{D} \cdot F.
\end{aligned}
\tag{2.37}
$$

Since there is only one driving force applied to the first oscillator, the expression of the dissipated power of the system is the same as Equation (2.30), which is $P_{\text{dissipate}} = \left\langle p(t) \right\rangle = \text{Re}\left[\frac{-i\omega\tilde{\chi}_1 F^2}{2}\right]$.

2.2 Phenomenological Quantum Models

2.2.1 Two-Level Coupling System

A phenomenological quantum model can be very useful to reproduce the energy dispersion of the polaritons branches without considering the detailed quantum mechanisms [1, 2, 4]. A two-by-two interaction Hamiltonian can describe the interaction as follows:

$$
\begin{pmatrix} E_{\text{p}} & E_g \\ E_g & E_1 \end{pmatrix} \begin{pmatrix} \alpha \\ \beta \end{pmatrix} = \mathbf{E} \begin{pmatrix} \alpha \\ \beta \end{pmatrix},
\tag{2.38}
$$

in which E_{p} and E_1 are the unperturbed energy levels of the first (light) and the second (matter) oscillators, and E_g is the coupling constant accountable for the energy exchange rate. α and β represent the coefficients of the basis functions for the two oscillators. We can rewrite Equation (2.38) as follows:

$$
\begin{pmatrix} E_{\text{p}} - E & E_g \\ E_g & E_1 - E \end{pmatrix} \begin{pmatrix} \alpha \\ \beta \end{pmatrix} = 0.
\tag{2.39}
$$

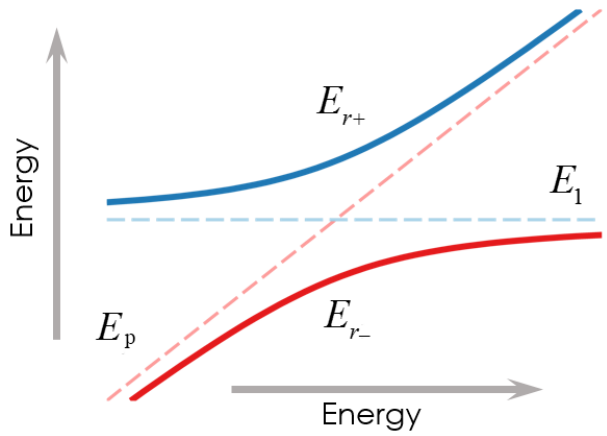

Figure 2.4 **Two-coupled-oscillator model.**

By solving its determinant equation:

$$\begin{vmatrix} E_p - E & E_g \\ E_g & E_1 - E \end{vmatrix} = 0, \tag{2.40}$$

we find that the solutions are the roots of the following equation:

$$\left(E_1 E_p - E_g^2\right) + \left(-E_1 - E_p\right)E + E^2 = 0, \tag{2.41}$$

and the roots are:

$$E_{r\pm} = \frac{E_1}{2} + \frac{E_p}{2} \pm \frac{1}{2}\sqrt{4E_g^2 + \left(E_1 - E_p\right)^2}. \tag{2.42}$$

When $E_1 = E_p$, the separation between the two polariton branches is,

$$\Omega_R = 2E_g. \tag{2.43}$$

In this two-level model, the Rabi splitting is thus just two times the coupling strength.

2.2.2 Damped Model for Two-Level coupling System

Here, we set the damping factor κ_p and κ_1 as half of the FWHM of the respective resonances γ_p and γ_1. The eigensystem can be then written as follows [2]:

$$\begin{pmatrix} E_p & E_g \\ E_g & E_1 \end{pmatrix}\begin{pmatrix} \alpha \\ \beta \end{pmatrix} = \mathbf{E}\begin{pmatrix} \alpha \\ \beta \end{pmatrix} + \begin{pmatrix} i\kappa_p & 0 \\ 0 & i\kappa_1 \end{pmatrix}\begin{pmatrix} \alpha \\ \beta \end{pmatrix} \tag{2.44}$$

$$\begin{pmatrix} E_{\mathrm{p}} - i\kappa_{\mathrm{p}} - E & E_g \\ E_g & E_1 - i\kappa_1 - E \end{pmatrix} \begin{pmatrix} \alpha \\ \beta \end{pmatrix} = 0. \tag{2.45}$$

We can now solve the following determinant equation:

$$\begin{vmatrix} E_{\mathrm{p}} - i\kappa_{\mathrm{p}} - E & E_g \\ E_g & E_1 - i\kappa_1 - E \end{vmatrix} = 0. \tag{2.46}$$

Now the solutions are the roots of the following equation:

$$\left(E_1 E_{\mathrm{p}} - E_g^2 - iE_{\mathrm{p}}\kappa_1 - iE_1\kappa_{\mathrm{p}} - \kappa_1\kappa_{\mathrm{p}}\right) + \left(-E_1 - E_{\mathrm{p}} + i\kappa_1 + i\kappa_{\mathrm{p}}\right) z + z^2 = 0, \tag{2.47}$$

and the roots are:

$$E_{r\pm} = \frac{E_{\mathrm{p}}}{2} + \frac{E_1}{2} - i\frac{\kappa_{\mathrm{p}}}{2} - i\frac{\kappa_1}{2} \pm \frac{1}{2}\sqrt{4E_g^2 + \left(E_{\mathrm{p}} - E_1 - i\kappa_{\mathrm{p}} + i\kappa_1\right)^2}. \tag{2.48}$$

It is important to note that, despite the different symbolic expressions, Equation (2.48) and Equation (2.31) have the same form.

2.2.3 Three-Level Coupling System

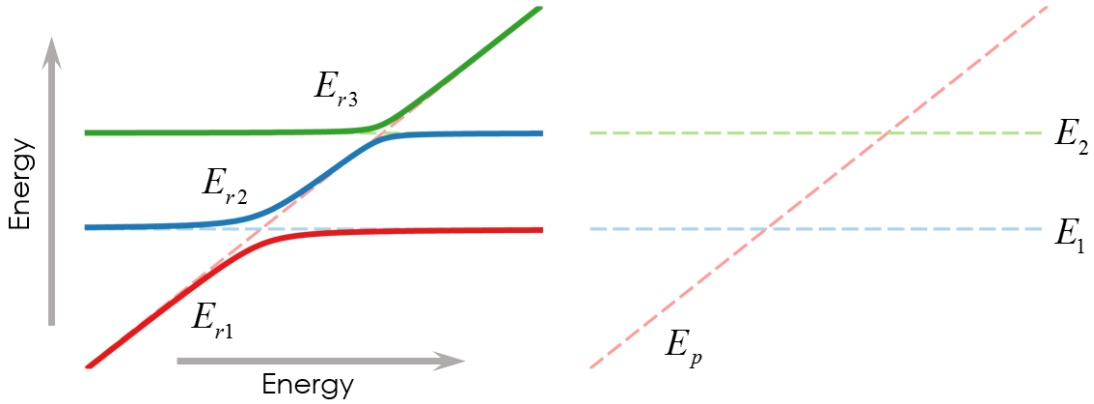

Figure 2.5 Three-coupled-oscillator model.

In some scenarios, a third mode also has to be included [70-72] (as it is also the case for the investigation described in Chapter 4). Therefore, we need to describe the system by using a three-by-three Hamiltonian, and the eigensystem of three-coupled oscillators is:

$$\begin{pmatrix} E_{\mathrm{p}} & E_{g1} & E_{g2} \\ E_{g1} & E_1 & 0 \\ E_{g2} & 0 & E_2 \end{pmatrix} \begin{pmatrix} \alpha \\ \beta \\ \gamma \end{pmatrix} = \mathbf{E} \begin{pmatrix} \alpha \\ \beta \\ \gamma \end{pmatrix}, \tag{2.49}$$

in which E_3 is the energy level of the third mode, and γ is the coefficient of the basis function of the third mode. Now E_{g1} is the coupling between mode 1 and 2, and E_{g2} the one between mode 1 and 3 (no coupling is considered here between mode 2 and 3, as it is not relevant for the interaction described in Chapter 4).

By solving this eigensystem,

$$\begin{pmatrix} E_{\mathrm{p}}-E & E_{g1} & E_{g2} \\ E_{g1} & E_1-E & 0 \\ E_{g2} & 0 & E_2-E \end{pmatrix}\begin{pmatrix} \alpha \\ \beta \\ \gamma \end{pmatrix}=0, \tag{2.50}$$

we can have the eigenvalues as:

$$\begin{aligned} E_{r3} &= A_1+A_6 \\ E_{r2} &= A_1-\frac{1}{2}A_6+i\frac{\sqrt{3}}{2}A_7 \\ E_{r1} &= A_1-\frac{1}{2}A_6-i\frac{\sqrt{3}}{2}A_7. \end{aligned} \tag{2.51}$$

Regarding the detailed derivation and parameter notations, see Appendix 2. When $E_{\mathrm{p}}=E_1$, the Rabi splitting between the first two branches (E_{r1} and E_{r2}) is:

$$\Omega_{\mathrm{R1}}=i\sqrt{3}A_7. \tag{2.52}$$

When $E_{\mathrm{p}}=E_2$, the Rabi splitting between the last two branches (E_{r2} and E_{r3}) is:

$$\Omega_{\mathrm{R2}}=\frac{1}{2}A_6-i\frac{\sqrt{3}}{2}A_7. \tag{2.53}$$

Because the parameters $A_1 \sim A_7$ are quite complicated and nested with each other, the direct relations between the Rabi splittings and coupling strengths cannot be immediately acquired by examining the equations above. Alternatively, the relations can be much clearer by directly solving the Equations (2.52) and (2.53). For example, when E_2 is far away enough from E_1 and E_{g2} is also small enough, The Rabi splitting between the first two branches can be still approximately $\Omega_{\mathrm{R1}}=2E_{g1}$ as in the two-level case. This behavior is also observed in our plasmon-phonon strong coupling system presented in Chapter 4, where the lattice diffraction mode participates weakly (see the detailed analysis in Subsection 4.5.3).

3 Designing a Plasmon-Phonon Coupling System: Basic Concepts

In this chapter, the basic tools to describe the investigated plasmon-phonon strong coupling system are presented. I start by introducing the models that account for the electromagnetic behavior of the involved materials. The Drude model can be used to extract the permittivity of gold in the THz region, according to the literature. Then the Lorentz model is also presented to describe polar semiconductors in the so-called "reststrahlen region." The Mie theory and quasistatic approximation are introduced for explaining the FR surface phonon mode of a single nanocrystal. By combining the Lorentz model with the Maxwell-Garnett Mixing rule, the permittivity of an ensemble of polar semiconducting nanocrystals can be well described for numerical simulations. To better reproduce the exact illumination conditions of the THz characterization experiments described in Chapter 4 and Chapter 5, I also present general Fresnel equations to set a specific combination of incident light polarization and angle of incidence. The method for locating the lattice modes of an array of scatterers is introduced as well, which is relevant for the discussion reported in Section 4.1.7. The calculation of absorption and scattering cross-sections for nanoantenna arrays is also presented. Finally, a method of extracting the mode volume from numerical simulations is given, which can estimate the cavity vacuum electric field of the nanocavities presented in Chapter 4 and Chapter 5.

3.1 Drude Model for Gold Thin Films in the THz Region

The optical properties of metals can be described by a "free electron model" [73, 74]. Without taking into account the lattice potential, and assuming that there is an effective optical mass m for each electron, then the motion ($\mathbf{x}$) of an electron (in the plasma sea) driven by an external electric field $\mathbf{E}$ can be written as:

$$m\ddot{\mathbf{x}} + m\gamma\dot{\mathbf{x}} = -e\mathbf{E}. \quad \textbf{(3.1)}$$

The right side of the above equation is the driving force, which is described as a multiplication of the elementary charge $-e$ and the electric field. The damping factor $\gamma = 1/\tau$ is caused by the electron collision during the oscillation, τ in turn being the relaxation time (or life time) of the free electron gas. Assuming that the driving field has a harmonic time dependence: $\mathbf{E}(t) = E_0 \mathrm{e}^{-i\omega t}$, a general solution of the equation of motion is $\mathbf{x}(t) = x_0 \mathrm{e}^{-i\omega t}$. After the Fourier transformation, we find:

$$\mathbf{x}(t) = \frac{e}{m\left(\omega^2 + i\gamma\omega\right)}\mathbf{E}(t). \tag{3.2}$$

We know that the displacement of the oscillating electrons contributes to the overall polarization $\mathbf{P}$ of the metal, with $\mathbf{P} = -ne\mathbf{x}$, where n is the number density of electrons. Thus we write the polarization as:

$$\mathbf{P} = -\frac{ne^2}{m\left(\omega^2 + i\gamma\omega\right)}\mathbf{E}. \tag{3.3}$$

We also apply the relation between the displacement field $\mathbf{D}$ and polarization: $\mathbf{D} = \varepsilon_0\mathbf{E} + \mathbf{P}$ (ε_0 is the electric permittivity of vacuum). Then, the direct relation between $\mathbf{D}$ and $\mathbf{E}$ becomes:

$$\mathbf{D} = \varepsilon_0\left(1 - \frac{\omega_\mathrm{p}^2}{\omega^2 + i\gamma\omega}\right)\mathbf{E}, \tag{3.4}$$

where $\omega_\mathrm{p}^2 = \frac{ne^2}{\varepsilon_0 m}$ is the square value of the plasma frequency of the free electron gas. Therefore, since we also know $\mathbf{D} = \varepsilon_0\varepsilon\mathbf{E}$, the complex permittivity is:

$$\varepsilon(\omega) = 1 - \frac{\omega_\mathrm{p}^2}{\omega^2 + i\gamma\omega}. \tag{3.5}$$

Equation (3.5) represents the key result of the so-called Drude model, proposed by Paul Drude in 1900 [75]. It works perfectly for describing the permittivities of metals in the THz region.

Gold as a noble metal represents a favorable choice that has been used in many optical and electronic devices due to its high electrical/thermal conductivity, high plasticity, and most importantly, high chemical stability. Other metals such as silver, copper, and aluminum also have prominent optical properties from the visible to the far-IR; however, they are all easy to oxidize under ambient conditions, which can cause an issue in experiments. Therefore, in our studies, we have selected gold as the material for making nanoantennas. In particular, since the nanoantennas are very thin (~ 60 to 100 nm), we have used values for the gold permittivity directly extracted from THz experiments on gold thin-films [76], which have returned values for the plasma frequency of $\omega_\mathrm{p}/2\pi = 2080$ THz and for the relaxation time of $\tau = 18$ fs. The plasma frequency of gold thin films is thus far above the THz region of interest for our investigation (~ 8 THz), so

there is no need to modify the Drude model and consider the contribution of the interband transition to the permittivity, which is instead important for the visible region [73].

3.2 Lorentz Model for Semiconductors

To describe the optical properties of semiconductors around their electron/phonon energy levels, we need to add a restoring force in the equation of motion. This extended equation of motion which in general describes a bound charge with a resonance frequency ω_0, presents more comprehensive optical properties for semiconductors, insulators, and even metals (the permittivities of metals at visible and ultraviolet regions). Such an expression for the permittivity can be derived via the Lorentz Model, also known as the Lorentz-Drude mode. Hendrik A. Lorentz extended the Drude Model in 1906 in his lecture notes (in Columbia University), and summarized the model in his book published in 1915 [77]. The equation of motion after adding a restoring force reads as follows:

$$m\ddot{\mathbf{x}} + m\gamma\dot{\mathbf{x}} + m\omega_0^2\mathbf{x} = -e\mathbf{E}. \tag{3.6}$$

This equation can, for example, describe the motion of an electron bound to an atomic nucleus, where the electron oscillates with a natural resonant frequency ω_0, and dissipates the energy with a friction term γ. We apply again the driving field as $\mathbf{E}(t) = E_0 \mathrm{e}^{-i\omega t}$, and consider a general solution of the form $\mathbf{x}(t) = x_0 \mathrm{e}^{-i\omega t}$, then the relation between electron movement and driving field is:

$$\mathbf{x}(t) = \frac{e}{m\left(\omega^2 - \omega_0^2 + i\gamma\omega\right)}\mathbf{E}(t). \tag{3.7}$$

Hence, the polarization is,

$$\mathbf{P} = -en\mathbf{x} = -\frac{ne^2}{m\left(\omega^2 - \omega_0^2 + i\gamma\omega\right)}\mathbf{E}, \tag{3.8}$$

as well as the displacement field:

$$\mathbf{D} = \varepsilon_0\left(1 - \frac{\omega_\mathrm{p}^2}{\omega^2 - \omega_0^2 + i\gamma\omega}\right)\mathbf{E}. \tag{3.9}$$

In the end, the permittivity derived from the Lorentz model is:

$$\varepsilon(\omega) = 1 - \chi(\omega) = 1 - \frac{\omega_p^2}{\omega^2 - \omega_0^2 + i\gamma\omega} \tag{3.10}$$

in which the term $-\frac{\omega_p^2}{\omega^2 - \omega_0^2 + i\gamma\omega}$ is the electric susceptibility $\chi(\omega)$. The real and imaginary parts of this permittivity function are:

$$\varepsilon_r(\omega) = 1 - \frac{\omega_p^2\left(\omega^2 - \omega_0^2\right)}{\left(\omega^2 - \omega_0^2\right)^2 + \gamma^2\omega^2}, \tag{3.11}$$

and

$$\varepsilon_i(\omega) = \frac{-\gamma\omega\omega_p^2}{\left(\omega^2 - \omega_0^2\right)^2 + \gamma^2\omega^2}, \tag{3.12}$$

respectively. From Equation (3.11), we know that when the frequency is extremely low ($\omega \to 0$), the real part of the permittivity will be static as $\varepsilon_s = 1 + \omega_p^2 / \omega_0^2$; while when the frequency is extremely high ($\omega \to \infty$), the permittivity will become $\varepsilon_\infty = 1$.

It is worth mentioning that, in real semiconductors (or metals), this high-frequency permittivity ε_∞ can be different from "1", when other higher frequency resonances are present for ($\omega > \omega_p$). In such cases, it is possible to introduce a residual polarization term $\mathbf{P}_\infty = \varepsilon_0\left(\varepsilon_\infty - 1\right)\mathbf{E}$ into $\mathbf{D} = \varepsilon_0\mathbf{E} + \mathbf{P}$, which leads to [73]:

$$\begin{aligned}\mathbf{D} &= \varepsilon_0\mathbf{E} + \mathbf{P} + \mathbf{P}_\infty \\ &= \left(\varepsilon_0 - \frac{\varepsilon_0\omega_p^2}{\omega^2 - \omega_0^2 + i\gamma\omega} + \varepsilon_0\varepsilon_\infty - \varepsilon_0\right)\mathbf{E} \\ &= \varepsilon_0\left(\varepsilon_\infty - \frac{\omega_p^2}{\omega^2 - \omega_0^2 + i\gamma\omega}\right)\mathbf{E}.\end{aligned} \tag{3.13}$$

Thus the permittivity is rewritten as,

$$\varepsilon(\omega) = \varepsilon_\infty + \frac{\omega_p^2}{\omega_0^2 - \omega^2 - i\gamma\omega}. \tag{3.14}$$

Typically, ε_∞ is in the range of ($1 \le \varepsilon_\infty \le 10$) [73]. The Drude and Lorentz models are the bricks to build more complicated models (sometimes being a sum of multiple oscillators) for describing the optical properties of various materials.

3.3 Surface Phonons of Semiconducting Nanocrystals

3.3.1 Bulk Permittivity of Polar Semiconductors in the Reststrahlen Region

In polar semiconductors (heteropolar semiconductors such as CdS, cadmium selenide, and lead sulfide), optical phonons are electric-dipole active, which means that the lattice vibrations (phonons) can couple with the electromagnetic waves (photons). This feature gives the potential to mix phonons and photons in the same system [78]. Instead, in homopolar semiconductors such as Si, Ge, and diamond, the fundamental vibration has no dipole moment and is IR inactive. In heteropolar semiconductors like CdS, the first order dipole moment triggers a very strong absorption which is due to the long-wavelength optical phonons [79]. This happens in the spectral region called the reststrahlen region. The reststrahlen region is located between two optical phonon modes: at low frequency, the transverse optical (TO) phonon mode; and at high frequency, the longitudinal optical (LO) phonon mode. As labeled by their names, the TO and LO phonon modes correspond to out-of-phase atomic lattice vibrations with the k-vectors aligned perpendicular and parallel to the incident light, respectively [80].

The interaction between the electromagnetic field and the TO phonon vibration can be treated as a collection of damped (damping factor γ) harmonic oscillators with a characteristic vibrational frequency ω_{TO}, in a manner equivalent to the Lorentz model introduced in the last section. The permittivity can be written as [81],

$$\varepsilon(\omega) = \varepsilon_\infty + \frac{S\omega_{\mathrm{TO}}^2}{\omega_{\mathrm{TO}}^2 - \omega^2 - i\omega\gamma}. \tag{3.15}$$

Compared to the Equation (3.14), we know that $\omega_{\mathrm{p}} = S\omega_{\mathrm{TO}}^2$. To define S, we introduce the LO phonon mode frequency ω_{LO} via the Lyddane-Sachs-Teller relation [82, 83]:

$$\frac{\omega_{\mathrm{LO}}^2}{\omega_{\mathrm{TO}}^2} = \frac{\varepsilon_{\mathrm{s}}}{\varepsilon_\infty}. \tag{3.16}$$

Knowing that ε_s is the static or extremely low-frequency permittivity as in Section 3.2, S in Equation (3.15) turns out to be $S = \varepsilon_s - \varepsilon_\infty$ (notice that S > 0, since ε_s is always greater than ε_∞ from Equation (3.16)). Thus, we can write the bulk permittivity of a polar semiconductor in the reststrahlen region in terms of the TO and LO phonon mode frequencies as follows [32, 79, 80]:

$$\varepsilon(\omega) = \varepsilon_\infty \left(1 + \frac{\omega_{LO}^2 - \omega_{TO}^2}{\omega_{TO}^2 - \omega^2 - i\omega\gamma}\right), \tag{3.17}$$

(that can also be written as $\varepsilon(\omega) = \varepsilon_\infty \left(1 + \frac{\omega_{LO}^2 - \omega^2 - i\omega\gamma}{\omega_{TO}^2 - \omega^2 - i\omega\gamma}\right)$)

Within the reststrahlen region, a specific bulk polar semiconductor is found to have high reflectivity and negative ε_r (real part), indicating that the semiconductor behaves similarly to metal in such region. Therefore, in analogy with metals supporting surface-plasmon polaritons [56, 84], polar semiconductors feature the so-called surface-phonon polaritons [32, 80].

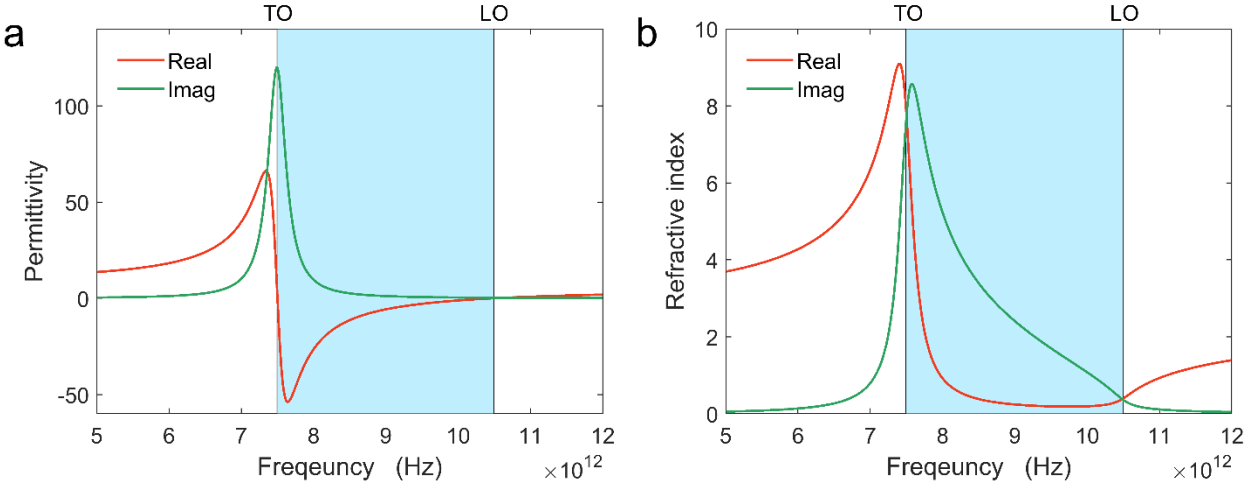

Figure 3.1 **Example of Permittivity (a) and refractive index (b) of a demonstrating material in the reststrahlen band.**

To get an insight into the optical properties of polar semiconductors around the reststrahlen region, I present the permittivity and refractive index of a demonstrating material as shown in Figure 3.1. The artificial parameters are chosen as: ε_∞ = 5, ω_{TO} = 250 cm^{-1} (~7.5 THz), ω_{LO} = 350 cm^{-1} (~10.5 THz), and γ = 10 cm^{-1}. In Figure 3.1a, we can see that the real part of the permittivity is negative in the reststrahlen region (light blue). The crossing points of the real and imaginary parts of the refractive index in Figure 3.1b indicate the boundaries of the reststrahlen region, i.e., the positions of TO and LO modes respectively.

3.3.2 Surface-Phonon Resonance of a Polar Semiconducting Nanocrystal

Once again in analogy with the metal case, where nanoparticles typically show surface plasmon resonances [56, 84], nanoparticles of polar semiconductors exhibit surface phonon resonances. Such surface resonance mode is located between ω_{TO} and ω_{LO}, the exact mode position being related to the nanoparticle morphology and the size, as well as the packing ratio if an ensemble of nanoparticles is considered. This surface optical phonon mode is the so-called FR optical phonon mode [32, 80].

Mie theory

The Mie theory, proposed by Gustav Mie in 1908, can analytically describe the incident, internal and scattered electromagnetic fields of a spherical nanoparticle by introducing a series of spherical harmonics [85]. The detailed derivation can be found in the Bohren and Huffman's book [83]. In general, all the far-field information can be described by the following scattering coefficients:

$$a_m = \frac{nS_m(nx)S_m'(x) - S_m(x)S_m'(nx)}{nS_m(nx)H_m'(x) - H_m(x)S_m'(nx)},$$
$$b_m = \frac{S_m(nx)S_m'(x) - nS_m(x)S_m'(nx)}{S_m(nx)H_m'(x) - nH_m(x)S_m'(nx)}. \quad \textbf{(3.18)}$$

These coefficients have been simplified by introducing the Riccati-Bessel functions: $S_m(x) = x \cdot j_m(x)$ and $H_m(x) = x \cdot h_m(x)$, in which $j_m(x)$ is the Bessel function of the first kind and $h_m(x)$ is the Hankel function (i.e., the Bessel function of the third kind). Here m denotes the order number. The size parameter x and the relative refractive index n are defined as follows:

$$x = \mathrm{k}(\lambda)r = \frac{2\pi n_{\mathrm{s}}(\lambda)r}{\lambda}, \quad n = \frac{\mathrm{k}_1(\lambda)}{\mathrm{k}(\lambda)} = \frac{n_{\mathrm{m}}(\lambda)}{n_{\mathrm{s}}(\lambda)}. \quad \textbf{(3.19)}$$

Here λ is the free-space wavelength of the incident wave, r is the radius of the sphere, k_1 and k are the internal and external wave numbers of the Mie sphere; n_{m} and n_{s} are the refractive indices of the Mie sphere and surrounding medium, respectively. One can easily retrieve the extinction, scattering, and absorption cross-sections by using the scattering coefficients a_m and b_m. A Mie calculator based on the Fortran code is available in Huffman's book [83], as well as a

Matlab version from Schäfer's doctoral thesis [86]. The response of a 10-nm spherical nanocrystal of the demonstrating material discussed in the previous subsection is calculated by using the Mie calculator. As shown in Figure 3.2a, the 10-nm nanocrystal has a (FR) optical surface phonon mode at 9.73 THz. The corresponding local electric field distribution at this frequency is also presented in Figure 3.2b. Similar to a metal nanoparticle case [84], one can see a dipole-like mode distribution around the polar nanocrystal.

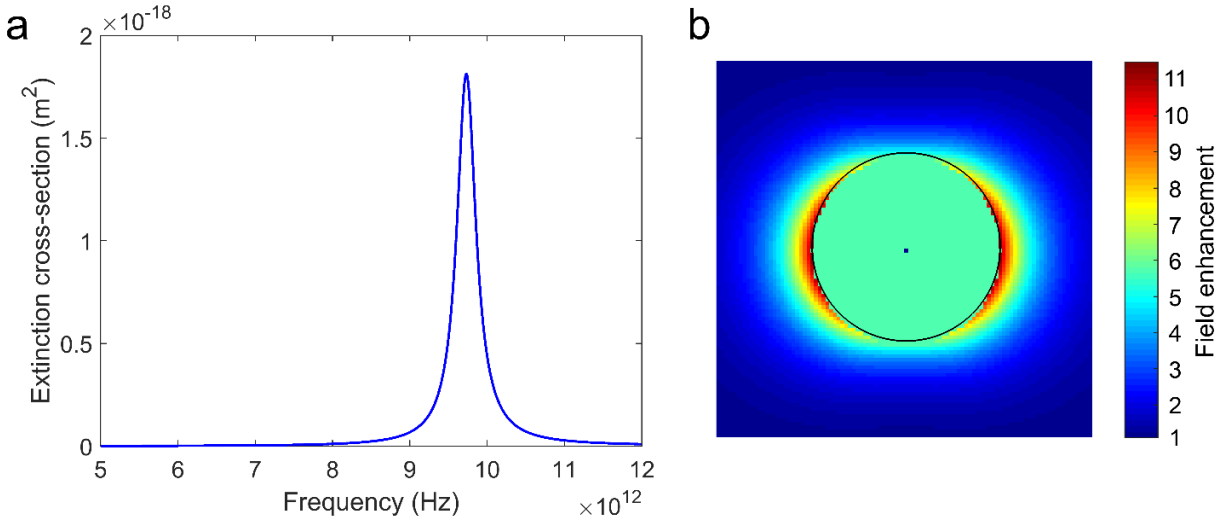

Figure 3.2 **(a) The FR phonon mode of a 10-nm nanoparticle made of the demonstrating material introduced in the previous paragraph and surrounded by air. (b) near field distribution at the peak frequency of 9.7 THz. The Mie calculations in (a) and (b) were fulfilled using the Matlab code.**

Quasi-static approximation

The Mie theory gives an exact solution for a spherical nanoparticle under electromagnetic plane-wave illumination. We can also use a much simpler approach, the so-called quasi-static approximation, to retrieve the same response. Indeed, when the size of the nanoparticle is less than ~1% of the incident light wavelength, it is found that such approximation well reproduces the exact solution from the Mie theory. In the quasi-static limit, the incident field is uniform across the spherical nanoparticle. This approximation is frequently used for the first-order resonance estimation of sub-wavelength spherical nanoparticles [87].

Under the quasistatic approximation (see page 211 in [87]), one can define the polarizability of a nanosphere as,

$$\alpha = \frac{\left(4\pi\varepsilon_0\varepsilon_\mathrm{b}\right)R^3\left(\varepsilon-\varepsilon_\mathrm{b}\right)}{\left(2\varepsilon_\mathrm{b}+\varepsilon\right)}, \tag{3.20}$$

where ε_b is the relative permittivity of the surrounding dielectric, ε is the complex relative permittivity of the polar semiconductor, and R is the radius of the nanosphere. A maximum in the polarizability corresponds to a nanosphere resonance. Therefore, to maximize the polarizability, one has to minimize the denominator of the equation above (notice that there is no size dependence under the approximation). We can thus obtain the resonance condition as:

$$\mathrm{Re}(\varepsilon) \approx -2\varepsilon_b, \tag{3.21}$$

which is the well-known FR condition for a metal nanoparticle surface plasmon resonance [73, 87]. We can check if this condition works well also with our example polar material. Considering air as the surrounding material, $\mathrm{Re}(\varepsilon)$ should be around -2 for the resonance condition. The resonance peak (9.73 THz) obtained from the Mie theory in Figure 3.2a, indeed corresponds to a complex permittivity "$-1.96+0.53i$" as can be extracted from data in Figure 3.1a. Therefore, we can conclude that the quasi-static approximation works very well in predicting the FR resonance of a spherical nanocrystal.

Moreover, this approximation can also estimate the on-resonance field enhancement of the spherical nanoparticle. When the real part of the permittivity $\mathrm{Re}(\varepsilon)$ is much greater than the imaginary part $\mathrm{Im}(\varepsilon)$, the field enhancement at the surface of the sphere becomes [87]:

$$F = \left|\frac{E_{\mathrm{res}}}{E_0}\right| \approx 3\left|\frac{\mathrm{Re}(\varepsilon)}{\mathrm{Im}(\varepsilon)}\right|. \tag{3.22}$$

Using the permittivity "$-1.96+0.53i$", we can estimate a field enhancement of "11.09", which is in an excellent agreement with the maximum value of "11" shown in Figure 3.2b.

3.3.3 An Effective Medium Theory – The Maxwell-Garnett Mixing Rule

If we consider an ensemble of nanoparticles, neither the original Mie theory nor the quasi-static approximation is capable of properly describing the overall electromagnetic response. To obtain an analytical solution of the multi-nanoparticle case, Xu and Gustafson developed a generalized multiparticle Mie-solution (GMM) [88]. Using GMM, one can extract the multi-nanoparticle response while considering the interaction among all involved particles. This means that all the contributing fields between the particles will be calculated. Therefore, such an approach can be quite time-consuming if the involved particles are many. Moreover, also in numerical simulations, considering each individual nanoparticle in a large ensemble quickly

becomes extremely memory consuming. To overcome this problem, we describe the permittivity of a large ensemble of nanoparticles within a background by an effective medium theory, instead of thoroughly considering the morphology of the inclusions [89],

$$\frac{\varepsilon_{\text{eff}} - \varepsilon_{\text{b}}}{\varepsilon_{\text{eff}} + 2\varepsilon_{\text{b}}} = f \frac{\varepsilon_{\text{bulk}} - \varepsilon_{\text{b}}}{\varepsilon_{\text{bulk}} + 2\varepsilon_{\text{b}}}, \tag{3.23}$$

where $\varepsilon_{\text{bulk}}$ is the bulk permittivity of the filling material. The filling factor f is a dimensionless quantity representing the filling ratio of the mixture. Equation (3.23) is called the Rayleigh mixing formula. It is worth to underline that if the particles of the inclusion are much smaller than the incident wavelength, their exact size does not affect the overall response. For spherical inclusions, the mixing rule takes the form:

$$\varepsilon_{\text{eff}} = \varepsilon_{\text{b}} + 3 f \varepsilon_{\text{b}} \frac{\varepsilon_{\text{bulk}} - \varepsilon_{\text{b}}}{\varepsilon_{\text{bulk}} + 2\varepsilon_{\text{b}} - f\left(\varepsilon_{\text{bulk}} - \varepsilon_{\text{b}}\right)}. \tag{3.24}$$

This formula, known as the Maxwell-Garnett formula, gives an explicit expression for the effective permittivity, and has been extensively used in different contexts. By varying the filling factor f, one can either obtain the bulk semiconductor response:

$$f \to 1 \;\Rightarrow\; \varepsilon_{\text{eff}} \to \varepsilon_{\text{bulk}}, \tag{3.25}$$

or just the background response:

$$f \to 0 \;\Rightarrow\; \varepsilon_{\text{eff}} \to \varepsilon_{\text{b}}. \tag{3.26}$$

By combining the polar semiconductor bulk permittivity (Equation (3.17)) and the Maxwell-Garnett mixing rule (Equation (3.24)), we can approximately describe the permittivity of a large ensemble of polar nanocrystals, as it will be shown in Chapter 4 and Chapter 5.

3.4 Locating the Lattice Modes: Wood-Rayleigh Anomalies

Lattice modes, also known as diffraction modes or Wood-Rayleigh anomalies, are inevitable grazing oscillations of electromagnetic waves in periodic structures [90, 91]. In the relevant case of plasmonic nanoantenna arrays (see Chapter 4), lattice modes are always present for a given ordered design. Manipulating the resonance position of these lattice modes is important, e.g., to improve the quality factor of specific plasmonic resonances [92-94], or to avoid unwanted interactions with the main plasmonic resonance (as it is the case for what is presented in Chapter 4).

In 1902, Wood observed a surprising phenomenon while he was studying metallic diffraction gratings, as he said: “I was astounded to find that under certain conditions, the drop from maximum illumination to minimum, a drop certainly of from 10 to 1, occurred within a range of wavelengths not greater than the distance between the sodium lines” [90]. However, he was unable to interpret the discovered phenomena at that moment, instead termed them as “singular anomalies.” Then in 1907, Rayleigh first theoretically gave an interpretation about these anomalies [91]. He found that the scattered or diffracted outgoing waves at some specific wavelengths emerge from the grating at a grazing angle. These particular wavelengths are so-called Rayleigh cutoff wavelengths, which are geometrically related to the periodicity, or spacing of the gratings. The modern analysis of Wood-Rayleigh anomalies started to thrive from the 1960s and 1970s, thanks to the invention of lasers which made the experimental verification much easier [95]. Nowadays, periodic arrangements of scatterers, such as nanoantenna arrays and metasurfaces, are of great interest to the scientific community [96-99]. Therefore, a renewed interest in lattice modes has arisen.

It is important to highlight that, in the case of scattering elements over a substrate, lattice modes at distinct frequencies exist both on the air side and on the substrate side of the lattice. The ones in the air always appearing at higher frequencies compared to the ones in the substrate.

In a rectangular lattice cell of a periodic structure, the wavenumber of a lattice resonance reads as follows:

$$k_{\mathrm{lat}} = \left|\mathbf{k} + \mathbf{G}\right|. \tag{3.27}$$

In this equation, $\mathbf{k} = \hat{\mathbf{e}}_{\mathbf{x}} k_x + \hat{\mathbf{e}}_y k_y$ is the wavevector of the incident electromagnetic wave, in which $\hat{\mathbf{e}}_{x,y}$ and $k_{x,y}$ are the unit vector and the wavenumber along the x or y-axis; the reciprocal lattice vector $\mathbf{G} = lG_x\hat{\mathbf{e}}_x + mG_y\hat{\mathbf{e}}_y$ is extracted as a combination (weighted by the mode orders l, m) of $G_{x,y} = \dfrac{2\pi}{g_{x,y}}$ where $g_{x,y}$ is the geometrical spacing between the scatterers. The wavenumber of a lattice resonance can be generally written as $k_{\mathrm{lat}} = n \cdot k_0$, where k_0 is the wavenumber in free space and n is the refractive index of the considered medium. Similarly to what will be presented in Section 3.6 for the illumination condition, we now decompose the wavevector $\mathbf{k}$ while considering its polar (θ) and azimuthal (φ) incident angles (see the schematic in Figure 3.4), and thus the x and y components of the incident wavevector can be written as:

$$k_x = k_0 \sin\theta\cos\varphi = A \cdot k_0$$
$$k_y = k_0 \sin\theta\sin\varphi = B \cdot k_0. \quad \textbf{(3.28)}$$

Here, for simplicity, we put the angle-related parameters as: $A = \sin\theta\cos\varphi$ and $B = \sin\theta\sin\varphi$. We substitute the decomposed values into Equation (3.27), and then we have a new equation as:

$$n^2 k_0^2 = \left(Ak_0 + lG_x\right)^2 + \left(Bk_0 + mG_y\right)^2. \quad \textbf{(3.29)}$$

This quadratic equation for k_0,

$$\left(A^2 + B^2 - n^2\right)k_0^2 + 2\left(AlG_x + BmG_y\right)k_0 + l^2G_x^2 + m^2G_y^2 = 0, \quad \textbf{(3.30)}$$

has a general solution:

$$k_0 = \frac{2\left(AlG_x + BmG_y\right) \pm \sqrt{4\left(AlG_x + BmG_y\right)^2 + 4\left(n^2 - A^2 - B^2\right)\left(l^2G_x^2 + m^2G_y^2\right)}}{2\left(n^2 - A^2 - B^2\right)}. \quad \textbf{(3.31)}$$

By discarding the unphysical solution with a negative sign, finally k_0 reads,

$$k_0 = \frac{2\left(AlG_x + BmG_y\right) + \sqrt{4\left(AlG_x + BmG_y\right)^2 + 4\left(n^2 - A^2 - B^2\right)\left(l^2G_x^2 + m^2G_y^2\right)}}{2\left(n^2 - A^2 - B^2\right)}. \quad \textbf{(3.32)}$$

The corresponding wavelength and frequency of the lattice mode are thus $\lambda_0 = \frac{2\pi}{k_0}$ and $f_0 = \frac{ck_0}{2\pi}$ respectively.

Now that we have successfully described the wavenumbers of lattice modes in Equation (3.32), we can sort out which combination of l and m in Figure 3.3 gives the lattice mode with the lowest frequency, which is of relevance for what will be discussed in the next Chapter. Through calculation, we know that if $g_x > g_y$, the first lattice mode in frequency needs $l = -1$ and $m = 0$. Indeed, the larger spacing always determines the lowest lattice mode. Symmetrically, if $g_x < g_y$, the first lattice mode in frequency needs $l = 0$ and $m = -1$, which is the case of the designed nanoantenna arrays in Chapter 4.

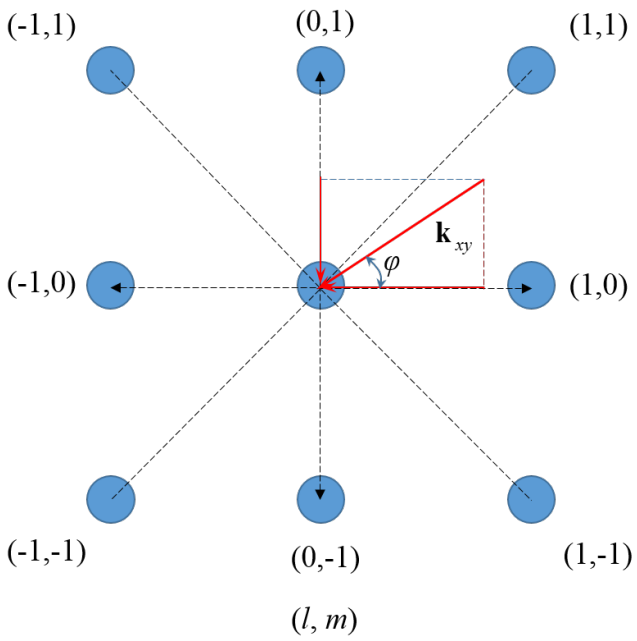

Figure 3.3 **The primary lattice modes in the reciprocal space when the order numbers l and m hold the value ±1 and 0. k_{xy} is the projection of wavevector $\mathbf{k}$ in the x-y plane.**

3.5 Numerical Simulation Environment

All the electromagnetic simulations that are presented in this thesis were performed by using a commercial finite-element-method (FEM) based software: COMSOL Multiphysics, optics module. The hardware for conducting the numerical simulations is based on a customized high-performance workstation, which in general has two 10-core Intel Xeon CPUs working at the frequency of 2.8 GHz, and 196 GB of RAM working at a frequency of 1600 MHz. In the following, I will briefly introduce the simulation environment and the operative steps to be taken for preparing the model. Starting with the COMSOL software wizard, one can open a blank model for the frequency domain solver. By assigning parameters in the "Global Definitions" of the "Model Builder," one can then start to build the geometry of the targeted design. In the "Materials" section, the optical properties of the involved materials can be assigned, making use of the permittivity models presented in the previous sections. In the "Definitions" section, the illumination condition can be defined by using the "Variables" options (as mentioned above, the details on how to mathematically describe the illumination condition will be presented in Section 3.6; the methods for extracting the absorption and scattering cross-sections of a given structure from the simulations are introduced in Section 3.7; while the calculation of the mode volumes is presented in Section 3.8). The top and bottom boundaries of the designed geometry are truncated by so-called "perfectly matched layers", which prevent any spurious reflection in the simulation

environment. The four remaining boundaries are finally defined by using Floquet periodic boundary conditions, to imitate an infinitely large array of periodic structures. A power detector is set beneath the calculation domain, for extracting the transmitted power. In the end, after meshing the geometry properly, the simulation model can be launched by setting the frequency (or a frequency band) of the illuminating plane wave. As an example, a scan of 100 frequency values can take from 7 to 36 hours, depending on the size of the meshing elements. The results can be exported and analyzed using postprocessing software like Matlab.

3.6 Setting the Illumination Condition

To extract the electromagnetic response of the designed geometry, we have to assign a proper background field. The background field is a pre-calculated electromagnetic field within the simulation environment before the scatterer is placed in the considered domain. The scattered light can be calculated from a subtraction between the full field (with scatterer) computed via the simulation software and the background field (without scatterer). The most straightforward way to set a background field in a homogeneous environment is to consider a plane wave: ($E_0 \exp\left(-i\mathbf{k}\cdot\mathbf{r}\right)$, where the wave vector $\mathbf{k}$ is also determined by the refractive index of the surrounding material (n_{sur}): $\mathbf{k} = \left(k_x, k_y, k_z\right)\cdot n_{\text{sur}}$). In most of our simulations, we have to consider the presence of a substrate, and the exact angle of incidence for the input field. Thus, one needs to properly calculate the background field at the substrate interface, considering the incident angle.

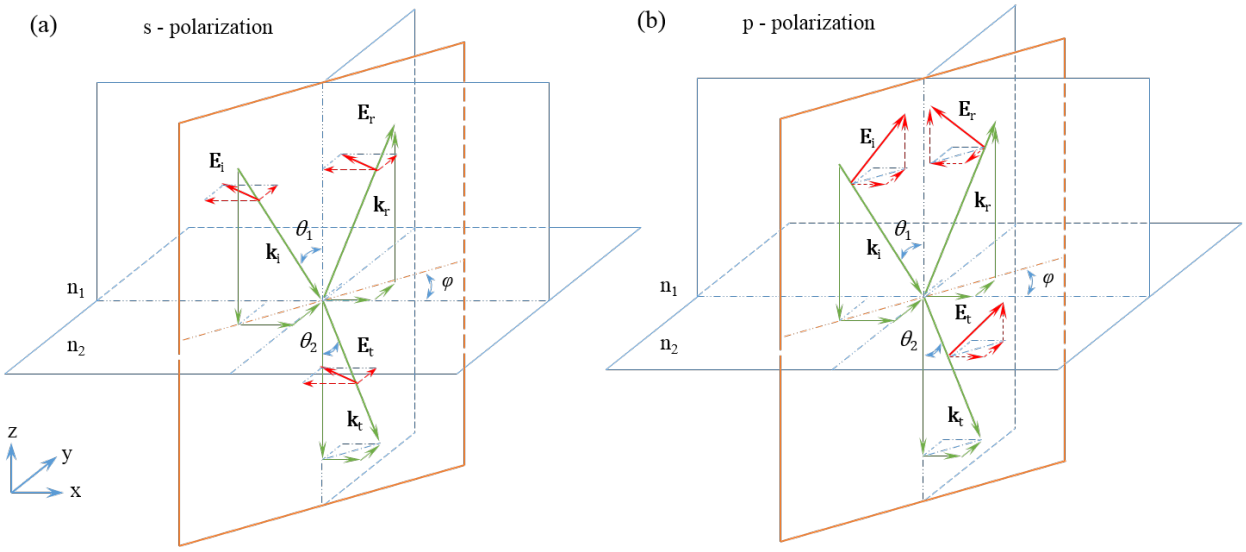

Figure 3.4 **The schematic of incident light with both s (a) and p (b) polarizations.**

As shown in Figure 3.4, when an arbitrarily polarized wave is impinging from one material (with index n_1) to another (with index n_2) with an incident angle θ_1 and an azimuthal angle φ, part of the light is reflected with a reflection angle θ_1, and part is refracted into the substrate with an angle θ_2. The wave can be decomposed into two perpendicular components: the *s*-polarized wave with polarization perpendicular to the plane of incidence and the *p*-polarized wave with polarization parallel to the same plane. The Fresnel equations of the reflection (*r*) and transmission (*t*) coefficients for both *s* and *p* – polarized waves are:

$$\begin{aligned} r_{\mathrm{s}} &= \frac{n_1\cos\theta_1 - n_2\cos\theta_2}{n_1\cos\theta_1 + n_2\cos\theta_2}, \\ t_{\mathrm{s}} &= \frac{2n_1\cos\theta_1}{n_1\cos\theta_1 + n_2\cos\theta_2}, \\ r_{\mathrm{p}} &= \frac{n_2\cos\theta_1 - n_1\cos\theta_2}{n_2\cos\theta_1 + n_1\cos\theta_2}, \\ t_{\mathrm{p}} &= \frac{2n_1\cos\theta_1}{n_2\cos\theta_1 + n_1\cos\theta_2}. \end{aligned} \tag{3.33}$$

We suppose that the incident electric field vector (with an amplitude E_0) forms an angle α with the incident plane, then its *s* and *p* components can be written as:

$$\begin{aligned} E_0^{\mathrm{s}} &= \sin\alpha E_0, \\ E_0^{\mathrm{p}} &= \cos\alpha E_0. \end{aligned} \tag{3.34}$$

As for the $\mathbf{k}$ vectors, we can write them down as follows (see Figure 3.4):

Incident:

$$\begin{aligned} k_x^i &= \cos\varphi\sin\theta_1 n_1 k_0, \\ k_y^i &= \sin\varphi\sin\theta_1 n_1 k_0, \\ k_z^i &= -\cos\theta_1 n_1 k_0. \end{aligned} \tag{3.35}$$

Reflected:

$$\begin{aligned} k_x^r &= \cos\varphi\sin\theta_1 n_1 k_0 = k_x^i, \\ k_y^r &= \sin\varphi\sin\theta_1 n_1 k_0 = k_y^i, \\ k_z^r &= \cos\theta_1 n_1 k_0 = -k_z^i. \end{aligned} \tag{3.36}$$

Transmitted:

$$\begin{aligned} k_x^t &= \cos\varphi \sin\theta_2 n_2 k_0 = k_x^i, \\ k_y^t &= \sin\varphi \sin\theta_2 n_2 k_0 = k_y^i, \\ k_z^t &= -\cos\theta_2 n_2 k_0. \end{aligned} \tag{3.37}$$

It is easy to notice that all the k_x and k_y components are the same after applying Snell's law $n_1 \sin\theta_1 = n_2 \sin\theta_2$. The detailed decomposition of the *s* and *p* – polarizations are presented in Appendix 3. In the end, we can adequately describe the general background field $\mathbf{E}_\mathrm{b}$ at a two-material interface. On and above the interface ($z \geq 0$), the background field in the air is:

$$\mathbf{E}_\mathrm{b}^{(\mathrm{up})}\left(\alpha, \theta_1, \varphi\right) = \left\{E_x^i + E_x^r; E_y^i + E_y^r; E_z^i + E_z^r\right\}. \tag{3.38}$$

Below the interface ($z < 0$), the background field in the substrate is:

$$\mathbf{E}_\mathrm{b}^{(\mathrm{down})}\left(\alpha, \theta_1, \varphi\right) = \left\{E_x^t; E_y^t; E_z^t\right\}. \tag{3.39}$$

3.7 Calculation of Absorption, Scattering, and Extinction Cross-Sections

In the following, I will present the methods to extract the far-field information in our numerical simulations. The volume and surface integrals reported below can be directly calculated by the COMSOL software.

Absorption cross-section:

$$\sigma_\mathrm{abs} = \frac{1}{I_0} \iiint_V Q_\mathrm{abs} \cdot dV, \tag{3.40}$$

where Q_abs is the power loss density in the material, and I_0 is the incident intensity.

Scattering cross-section:

$$\sigma_\mathrm{sca} = \frac{1}{I_0} \oiint_S \left(\mathbf{n} \cdot \mathbf{S}_\mathrm{sca}\right) \cdot dS, \tag{3.41}$$

Here $\mathbf{n}$ is the normal vector pointing outwards from the object surface, $\mathbf{S}_\mathrm{sca}$ is the scattered intensity (Poynting) vector.

Extinction cross-section:

$$\sigma_\mathrm{ext} = \sigma_\mathrm{sca} + \sigma_\mathrm{abs}. \tag{3.42}$$

Extinction efficiency:

$$\eta_{\text{ext}} = \frac{\sigma_{\text{ext}}}{\sigma_{\text{geo}}}, \tag{3.43}$$

where σ_{geo} is the geometrical cross-section of the tested object.

3.8 Calculation of the Mode Volume

As mentioned in the introduction of this thesis, the mode volume of a resonant structure is a key parameter to achieve the strong coupling condition in a light-matter interaction system. Indeed, this volume is directly connected to the vacuum electric field of the resonator, and thus ultimately to the coupling strength value (see Section 1.2). The mode volume is generally defined as the ratio between the overall energy density and the maximum energy density value in the whole physical domain. Thus it is written as [10]:

$$V_{\text{mod}} = \frac{\int \varepsilon(\mathbf{r})\left|E(\mathbf{r})\right|^2 d\mathbf{r}}{\max\left(\varepsilon(\mathbf{r})\left|E(\mathbf{r})\right|^2\right)}, \tag{3.44}$$

where $\varepsilon(\mathbf{r})\left|E(\mathbf{r})\right|^2$ is the energy density, while $\varepsilon(\mathbf{r})$ and $E(\mathbf{r})$ are the permittivity and electric field at the position. Equation (3.44) works well for the case of dielectric cavities, such as Fabry–Perot resonators and standard photonic crystals. However, for plasmonic cavities, Maier found that Equation (3.44) leads to unphysical values, due to the negative real part and large imaginary part of the permittivity that is typical of metals [100]. Alternatively, he suggested that the energy density in the metal domain should be adjusted as follows [10, 100, 101]: $\left(\varepsilon_{\text{r}}(\mathbf{r}) + 2\omega\varepsilon_{\text{i}}/\gamma\right)\left|E(\mathbf{r})\right|^2$, where ε_{r} and ε_{i} are the real and imaginary parts of the permittivity, respectively, ω is the angular frequency of the incident light, and γ is the metal damping factor as defined in the Drude model (see Section 1). The mode volumes for our plasmonic nanocavities were thus calculated by considering this correction and extracting the electric field domain values by means of the numerical simulations.

4 Phonon Resonance Modification of Nanocrystals inside a THz Plasmonic Nanocavity[1]

The interaction between low-frequency modes, such as phonons (collective vibrations) and plasmons (collective oscillations of electrons) in the THz region has fundamental implications including the opportunity of modifying material properties, thus opening exciting perspectives in material science and nanotechnology [1, 4, 74]. By judiciously designing plasmonic nanocavities, the free-space THz radiation can be concentrated into deeply sub-diffraction volumes, leading to an extremely high local field enhancement that can significantly improve the light-matter interaction. In 2015, this technique was first employed by our group to demonstrate Nanoantenna-Enhanced THz Spectroscopy [5], showing that the phonon mode of a monolayer of cadmium selenide quantum dots placed over the surface of nanoantenna arrays can be successfully detected. In 2018, my collaborators and I moved forward and showed that the optical phonon response of CdS nanocrystals could be drastically modified inside THz nanocavities, due to the strong coupling happening between the FR optical phonon mode of the nanocrystals and the nanoantenna plasmonic resonance [70]. As shown in Figure 4.1, the FR optical mode (ν_{FR}) of nanocrystals existing between the TO (ν_{TO}) and LO (ν_{LO}) phonon modes (see Section 3.3) will strongly hybridize with the plasmonic (ν_{PL}) mode of the nanocavity, resulting in the split lower (ν_{-}) and upper (ν_{+}) vibro-polaritons. In this chapter, I exploit all the concepts and methods presented in the previous chapters to properly design such hybridization, which is finally fabricated and experimentally validated. A comprehensive analysis of this strong coupling system is also given in the last section of this chapter.

[1] Copyright: The discussion presented in this chapter was adapted from:

[70] X. Jin, A. Cerea, G. C. Messina, A. Rovere, R. Piccoli, F. De Donato, F. Palazon, A. Perucchi, P. Di Pietro, R. Morandotti, S. Lupi, F. De Angelis, M. Prato, A. Toma, and L. Razzari, "Reshaping the Phonon Energy Landscape of Nanocrystals inside a Terahertz Plasmonic Nanocavity," *Nature Communications* **9**, 763 (2018).

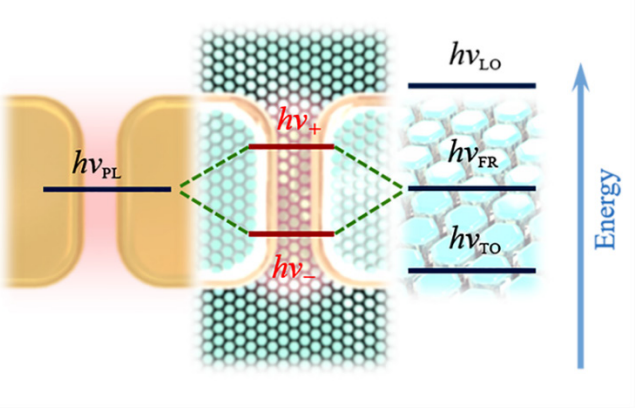

Figure 4.1 **Energy diagram exemplifying the plasmon–phonon resonance hybridization.**

4.1 Design of End-to-End Nanoantenna Arrays in Numerical Simulations

The precise design of plasmonic nanocavities and the examination of their corresponding electromagnetic response via numerical simulations are the essential steps to realize an effective platform for plasmon-phonon strong coupling, and also offer an in-depth insight into the underlying physical mechanism.

4.1.1 Simulation Platform and General Settings

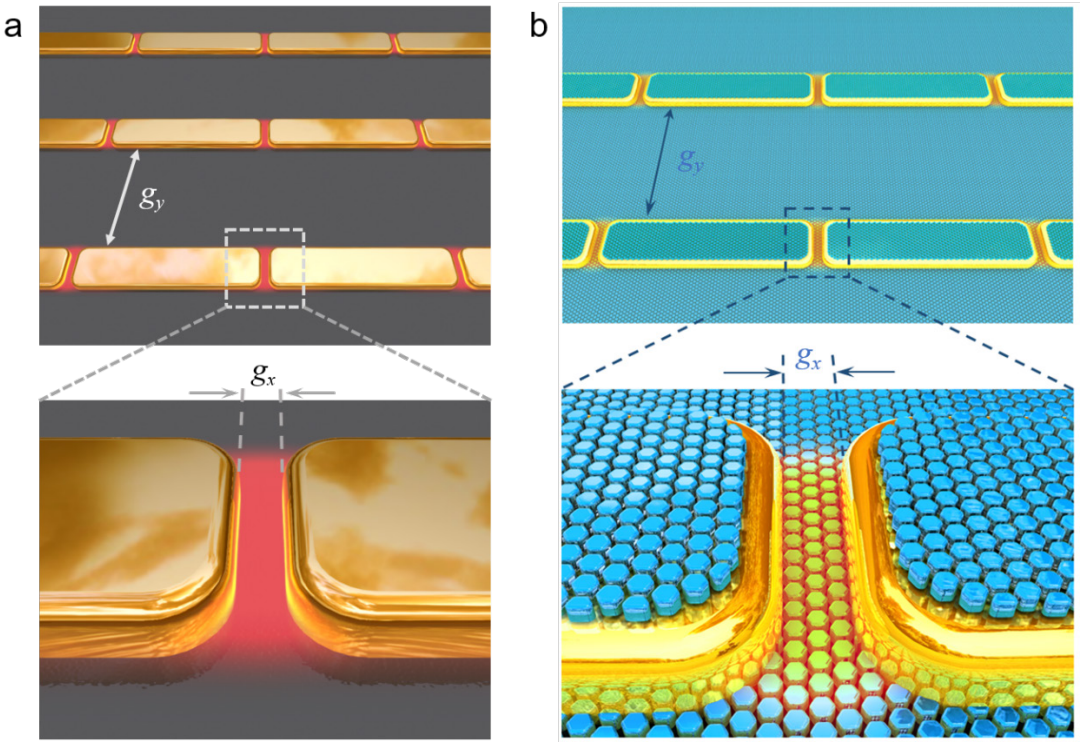

Figure 4.2 **(a) The schematic of an end-to-end nanoantenna array. (b) The graphical representation of a plasmonic nanoantenna array covered with a monolayer of CdS nanocrystals.**

As mentioned above, I used the software COMSOL Multiphysics to design and check the electromagnetic behavior of the target nanocavities. In particular, I focused on the design of a plasmon-phonon coupling system in which CdS nanocrystals are interacting strongly with the THz light in nanocavities. As shown in Figure 4.2a, I designed end-to-end nanoantenna arrays on a silicon substrate (refractive index n_{Si} = 3.42) with spacing g_x = 30 nm along the nanoantenna long axis (x-axis) and g_y = 8.5 μm in the perpendicular direction (y-axis). The nanoantenna width was set to 200 nm, the height to 55 nm. Regarding the antenna length, its first rough estimation was extracted by using the following equation $L = \lambda_{\mathrm{res}} / \left(2n_{\mathrm{Si}}\right)$, in which λ_{res} is the wavelength at which the resonance of a dipolar antenna occurs [57]. Since the phonon mode of our interest (see details in Subsection 4.1.3) is located around 8 THz (corresponding λ_{res}: 37.5 μm), the resonance of the nanoantennas needs to be tuned to the same location. Thus, by using the simple equation presented above, the first estimation of the antenna length is L = 5.5 μm. The nanoantenna length was then varied in the range 4 to 7 μm for the plasmon resonance to sweep across the phonon mode. Extensive numerical simulations were conducted to characterize the exact resonance properties of these nanoantenna arrays. In the simulation model, all the nanoantenna sharp edges were rounded with a radius of curvature of 20 nm, except the ones perpendicular to the substrate in correspondence of the nanocavities, where a curvature of 40 nm was introduced to better resemble the fabricated structures. To simulate the monolayer of CdS nanocrystals (see Figure 4.2b for a sketch), I then employed the "effective layer" strategy, as discussed in Section 3.3.

Finally, since the finite size of the nanoantenna array (200 × 200 μm^2) used in the experiments is smaller than the estimated area of the illuminating THz beam (diameter $D \approx 260$ μm, see Section 4.3 for the experimental details regarding this characterization), the transmission results of the simulations (assuming an infinite array) were normalized as $T'_{\mathrm{num}} = 0.76T_{\mathrm{num}} + 0.24T_{\mathrm{sub}}$, where T_{num} is the numerical transmission of an infinite nanoantenna array and T_{sub} is the transmission of a bare silicon substrate. The coefficient 0.76 takes into account the area of the THz spot effectively covered by the array. The relative transmittance was then obtained (as it is done in the measurements) as: $T_{\mathrm{rel}} = T'_{\mathrm{num}} / T_{\mathrm{sub}}$.

4.1.2 Setting the Background Field

For the input illumination conditions in the simulations, we employed a linearly polarized plane wave. To represent the illumination condition of the "Cassegrain objective" employed in the measurement (see Section 4.3) as shown in Figure 4.3, we need to adjust the general formula presented in Equation (3.38) properly. Since the direction of the polarization projection on the x-y plane is fixed in a reflective "Cassegrain objective" configuration, it means that for each azimuthal angle φ composing the overall Cassegrain illumination at the focal spot we have to find an appropriate α (the angle between the plane of incidence and electric field vector, see detailed relations in Figure 4.4b) to maintain the fixed direction of polarization projection on the x-y plane. In light of this concept, we can plot a schematic as in Figure 4.4, and find out the intrinsic relations between α and φ.

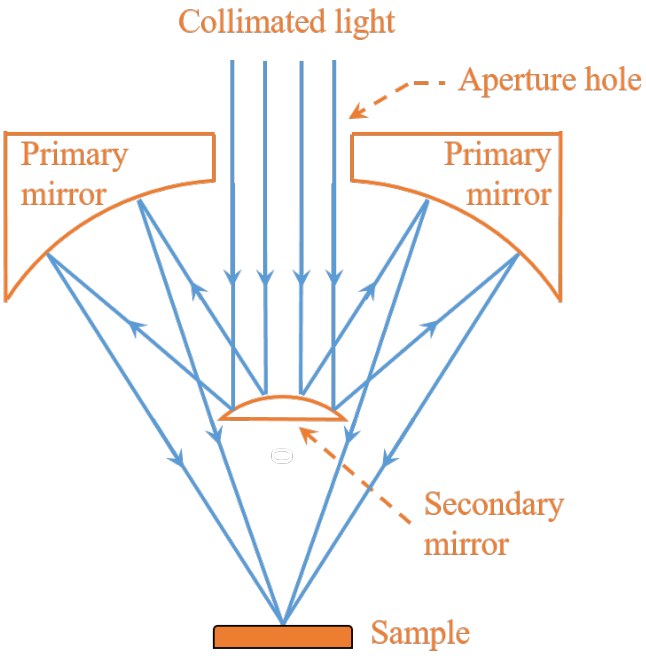

Figure 4.3 The sketch of a Cassegrain objective.

Figure 4.4 shows that $\mathbf{E}_0^{\mathrm{p}'}$ and $\mathbf{E}_0'$ are the projections of $\mathbf{E}_0^{\mathrm{p}}$ and $\mathbf{E}_0$ in the x-y plane, respectively. Therefore, α is the angle between $\mathbf{E}_0^{\mathrm{p}}$ and $\mathbf{E}_0$, and α' is the angle between $\mathbf{E}_0^{\mathrm{p}'}$ and $\mathbf{E}_0'$. We now have relations as follows:

$$E_0^{p'} = \cos\theta_1 E_0^{p},$$
$$\tan\alpha' = \frac{E_0^{s}}{E_0^{p'}} = \frac{\sin\alpha \cdot E_0}{\cos\theta_1 \cos\alpha \cdot E_0} = \frac{\tan\alpha}{\cos\theta_1}, \quad \textbf{(4.1)}$$
$$\alpha = \arctan\left(\tan\alpha' \cos\theta_1\right).$$

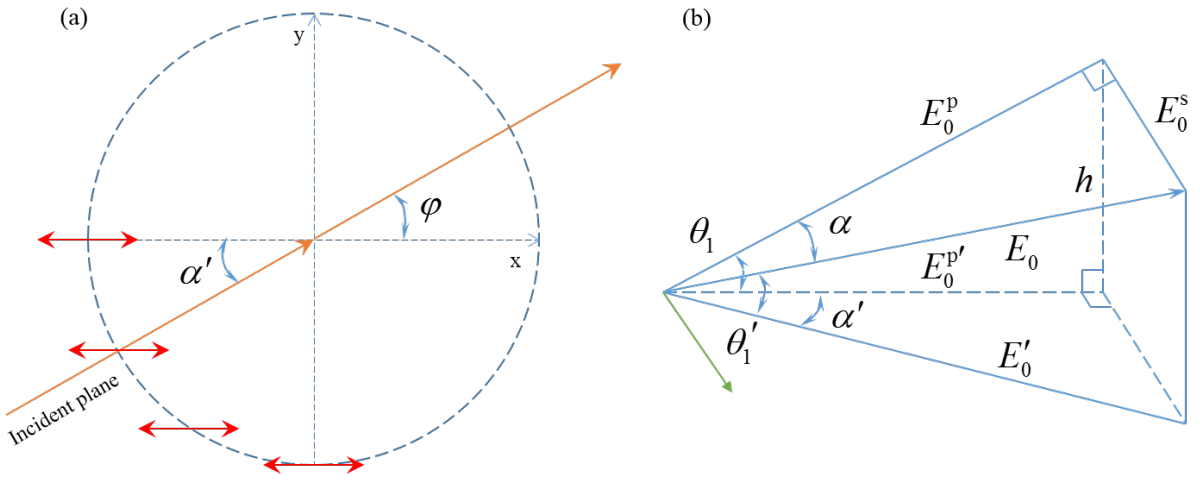

Figure 4.4 **(a) The wave vector (in orange) and polarization projections (red) on the x-y plane. (b) The schematic describing the relation between α and φ. The green arrow indicates the k-vector.**

By inspecting Figure 4.4 (a), we can find out that the azimuthal angle φ is always equal to $-\alpha'$. Therefore, as long as we set $\alpha' = -\varphi$, we can obtain a series of plane waves whose polarization projections on the x-y plane will always be aligned, for instance, along the x-axis. Hence, Equation (3.38) for the background field can be written in this case as:

$$\mathbf{E}_b(\theta_1, \varphi) = \mathbf{E}_b\left(\alpha = \arctan\left(\tan(-\varphi)\cos\theta_1\right), \theta_1, \varphi\right), \quad \textbf{(4.2)}$$

in which the background field now only depends on θ_1 and φ. Note that though φ has a range from 0° to 360°, a full description of the problem can be obtained by spanning only one-quarter of this range (i.e., 0° to 90°). Considering that the specific "Cassegrain objective" used in the measurements has an average incident angle as 18°, in all the following simulations we set θ_1 to this value in the background field expression $\mathbf{E}_b(\theta_1, \varphi)$. Furthermore, we found that setting φ = 45°, the illumination condition reproduces well the transmission response of the arrays when illuminated through the Cassegrain objective, as well as the measured lattice mode at around 9.8 THz (see discussion in Section 4.3 below).

4.1.3 Extracting the Permittivity of CdS Nanocrystals from the Experimental Results

To extract the dielectric properties of the layer of CdS nanocrystals, we employed the following procedure: a thick layer (2.5 μm) of nanocrystals (average size: 10 nm, see detailed description in what follows) was prepared over a silicon substrate and its THz transmission was measured (Figure 4.5a, blue circles). We then fitted this measurement (solid red line), considering an effective permittivity ε_{eff} for the nanocrystal layer, following the Maxwell-Garnett approximation for a mixture described in Subsection 3.3.3.

In the fitting procedure of the experimental data illustrated in Figure 4.5a, we used the following literature values relative to bulk crystalline CdS: ε_{∞} = 5.3, ω_{TO} = 240 cm^{-1}, ω_{LO} = 302 cm^{-1} [102]. We then tuned the filling factor to match the experimental resonance position at around 7.85 THz, obtaining f = 0.75, a value that is consistent with the densely packed arrangement of our CdS layer. Finally, we tuned the damping constant to reproduce the width of the resonance, which led to a value γ = 15 cm^{-1}.

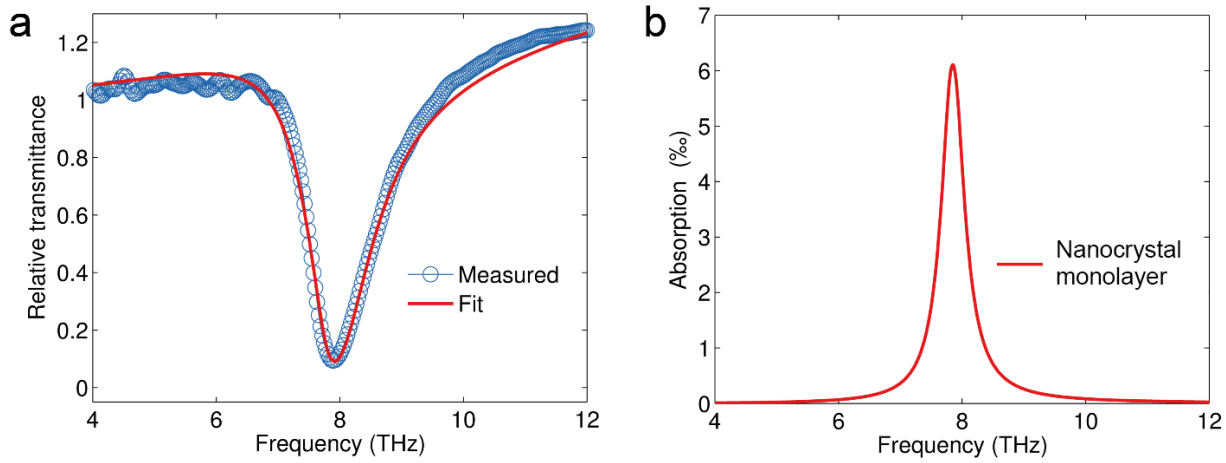

Figure 4.5 **(a) Relative transmittance spectrum (blue circles: experimental measurement, red line: fit with Equation (3.23)) of a 2.5-μm-thick CdS nanocrystal layer. The relative transmittance is obtained normalizing the sample transmission to the one of a bare silicon substrate. (b) The absorption spectrum of a monolayer of CdS nanocrystals, as obtained using Equation (3.23) and the parameters extracted from the fit in (a).**

The self-assembled nanocrystal layers that are the subjects of the experimental investigation presented in the following sections were then simulated by employing an equivalent layer with the aforementioned effective permittivity and appropriate thickness. This solution allowed us to drastically simplify the meshing requirements in the simulation domain and speed up the calculations. Figure 4.5b shows the absorption of a single layer of CdS nanocrystals (10 nm

thickness), obtained by adopting this procedure. From the result shown in Figure 4.5b, we can also extract the linewidth (i.e., the FWHM) of the absorption band of the monolayer, corresponding to ~ 0.45 THz.

4.1.4 Verifying the Appropriateness of the Effective Medium Theory to Describe Compact Layers of Nanocrystals

To clarify the validity of the effective medium theory in our simulations, we have performed a series of numerical simulations by ideally varying the morphology of the nanocrystals and retrieved the FR resonance peak of their ensembles in various conditions. The results of this investigation are summarized in the following figures. In Figure 4.6, it is clear that the changes in the shape of the individual nanocrystals, as well as in the two-dimensional lattice arrangement have basically no effect on the FR resonance as long as the filling factor is fixed. The resonance positions and the line widths are in agreement with Figure 4.5b, where the effective medium approximation was employed.

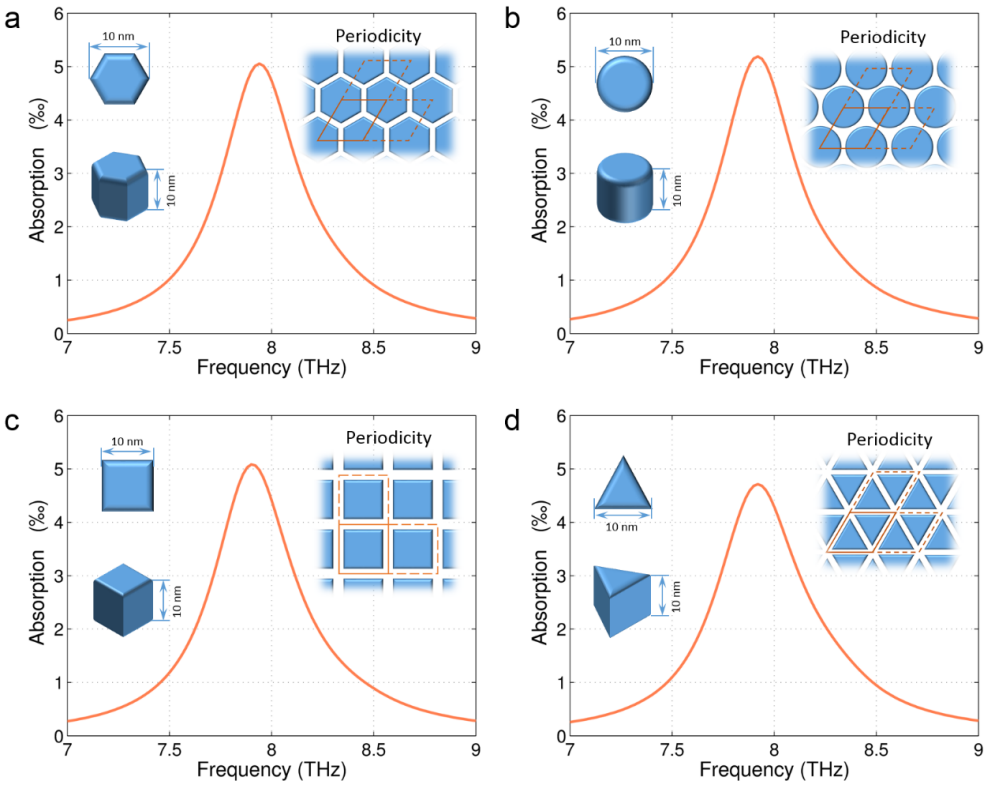

Figure 4.6 **FR resonance absorption peak retrieved by means of numerical simulations for different nanocrystal shapes and lattice arrangements (filling factor f = 0.75). The CdS nanoparticles are on a silicon substrate. All narrow separations (<1 nm) were meshed at least by 4 grids.**

Moreover, Figure 4.7 also shows that the shape and spectral position of the FR phonon resonance does not change when different layer numbers are considered (see the relevant cases

of N = 1, 1.5, 2, and 3 layers in Figure 4.7a), or the input polarization is modified (Figure 4.7b). Furthermore, significant changes in the size of the individual nanocrystals do not shift or perturb the FR resonance (Figure 4.8a). Only changes in the filling factor f of the layers cause a rigid shift of the FR resonance (Figure 4.8b). However, a small shift of 0.2 THz is observed for a significant change of f from 0.7 to 0.8. As mentioned above, the filling factor of our CdS nanocrystals is experimentally determined as f = 0.75, according to the fit shown in Figure 4.5. The resulting value of the FR resonance peak position ($\nu_{FR} \approx$ 7.85 THz) for this f value also agrees remarkably well with the anti-resonant peak position observed in our THz transmission measurements when the nanoantenna arrays are covered with the nanocrystal layers (See Figure 4.20b in Section 4.3 below). We can thus safely employ the Maxwell-Garnett mixing rule in our numerical models, which drastically reduces the computational power otherwise required to simulate the individual nanocrystals composing the layers.

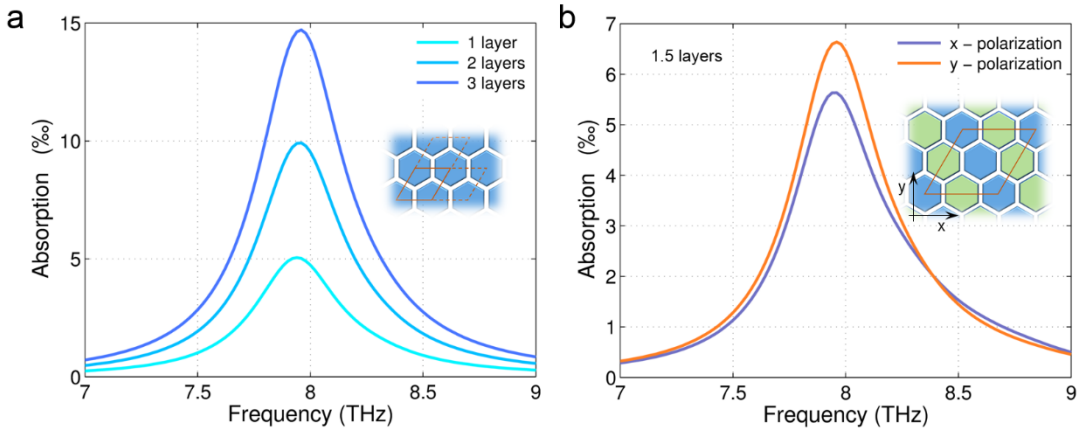

Figure 4.7 **FR resonance for different number of nanocrystal layers (a) and input polarization orientation (b)**

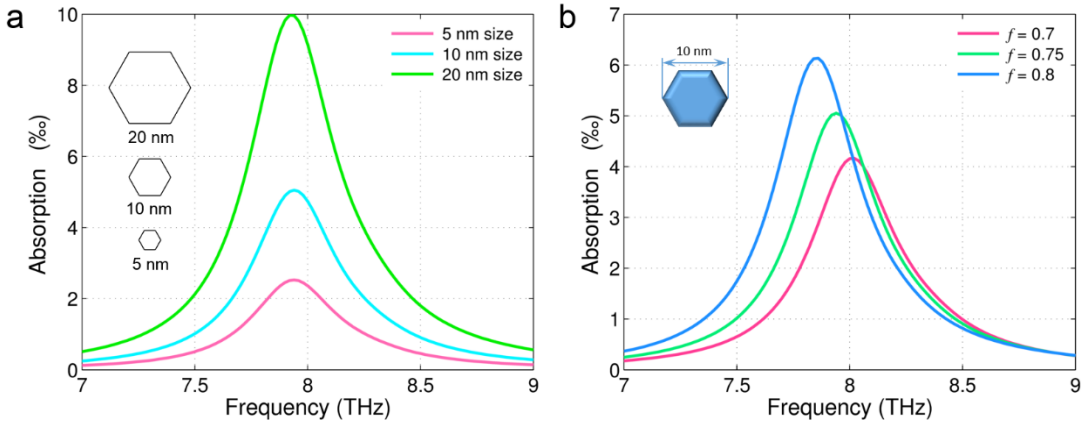

Figure 4.8 **FR resonance for different nanocrystal sizes (a) and different filling factors (b).**

4.1.5 Simulated Array Response with and without CdS Nanocrystals

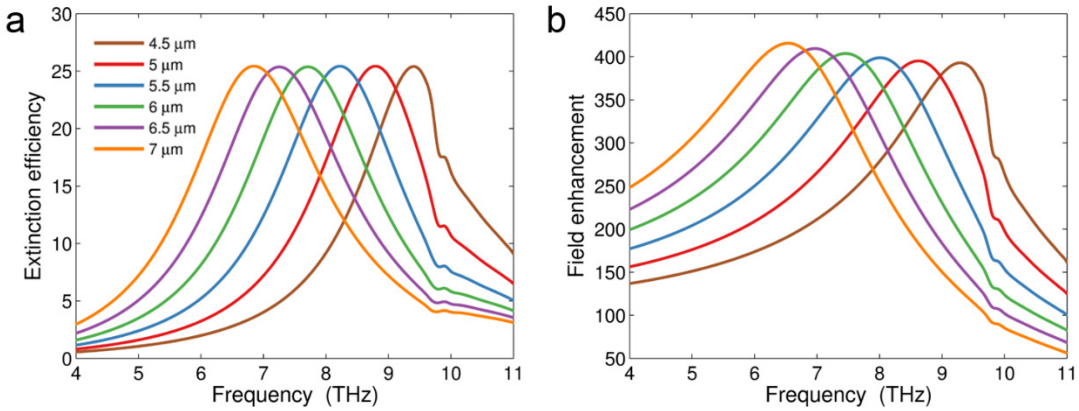

Figure 4.9 **(a) Extinction efficiency for six different nanoantenna lengths. (b) Corresponding field enhancement values, estimated in the center of the nanocavity.**

Figure 4.9a shows the nanoantenna extinction efficiency (the ratio of the extinction cross-section to the nanoantenna geometrical cross-section, see Equation (3.43) in Section 3.7) for arrays with different nanoantenna lengths as a function of frequency. Figure 4.9b shows the dispersion of the near field enhancement value (the ratio of the local electric field to the background field) at the center of the nanocavities. In both figures, the presence of a lattice mode at around 9.8 THz is clearly visible. The details about this lattice mode will be discussed in Subsection 4.1.7.

The 2D maps of the extinction (simply one minus the transmittance, in correspondence with the measured extinctions) as a function of frequency and nanoantenna length are shown in Figure 4.10a and Figure 4.10b, where the bare arrays (a) and the arrays covered with a single effective layer of CdS nanocrystals (b) are presented respectively. Here the effective layer thickness is 10 nm, which corresponds to the particle size of our synthesized CdS nanocrystals. A clear anti-crossing behavior in correspondence of the CdS FR phonon resonance is visible in Figure 4.10b. The geometrical arrangement of the CdS layer in the simulations and the field distribution in the nanocavity region are shown in Figure 4.10c and Figure 4.10d, respectively.

Finally, the simulated transmission spectra of the bare nanoantenna arrays, as well as of the arrays covered with 1, 2, and 3 CdS nanocrystal layers are plotted in Figure 4.11a, b, c, and d, respectively. As we can clearly see in this figure, the resonance of the nanoantenna array splits into two bands (i.e., the two new hybridized states) when the surface is covered with CdS nanocrystal layers. Moreover, by increasing the number of layers, the Rabi splitting (i.e., the separation in frequency between the newly formed resonance bands; see Figure 4.26 for clearer

splitting size increase) also increases as predicted by Equation (1.9) and Equation (1.10) (see the relation between the number of matter oscillators and the coupling strength in Section 1.2).

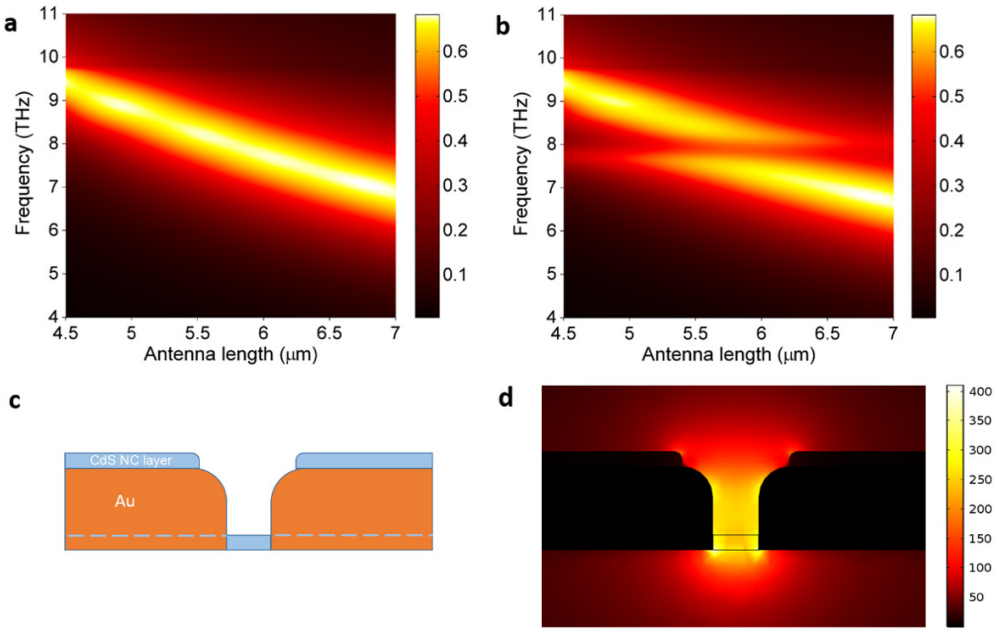

Figure 4.10 **(a) 2D map showing the extinction spectrum for different nanoantenna lengths, in the case of the bare arrays. (b) Same as in (a), when the arrays are covered with a 10-nm-thick "effective" layer of CdS nanocrystals. (c) Lateral view of the geometrical arrangement adopted in the simulations for the CdS nanocrystal layer. (d) Corresponding electric field distribution (frequency: 8 THz, nanoantenna length: 5.75 μm).**

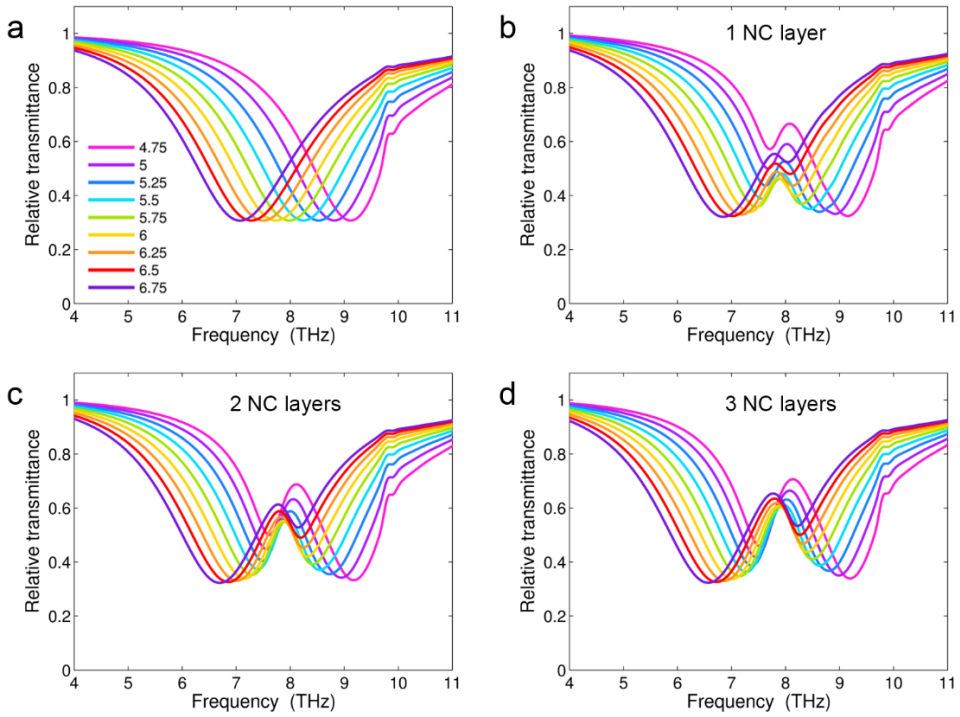

Figure 4.11 **Simulated transmission spectra for bare arrays (a), and arrays covered with 1 (b), 2 (c), and 3 (d) CdS nanocrystal layers. The antenna lengths are from 4.75 to 6.75 μm.**

4.1.6 Estimation of the Mode Volume and the THz Vacuum Electric Field

Figure 4.12 shows the electric field distribution in a nanocavity area at resonance, on the planes perpendicular to the main simulation axes. Starting from the distribution of the local electric field in the 3D space, one can estimate the mode volume of the plasmonic nanocavity using Equation (3.44). As elaborated in Section 3.8, the numerator of this equation can be interpreted as the full domain integral of the energy density, and the denominator as the maximum value of the energy density extracted within the same domain. Considering the case of the array with nanoantenna length of 5.75 μm (corresponding to an array resonance centered at around 8 THz, well aligned to the nanocrystal phonon resonance), we obtain a mode volume at resonance as small as V_{mod} = 1.43 × 10^6 nm^3 (which is smaller than $\lambda^3/10^7$ compared to the incident THz light). Compared to the geometrical volume of the nanocavity ($V_{\mathrm{geo}} \approx$ 200 × 30 × 55 nm^3 = 0.33 × 10^6 nm^3), the mode volume is thus just ~4.3 times larger. Pictorial comparison of these two volumes is given in Figure 4.13, in which the effective squeezing of the radiation in the nanocavity region becomes evident. Having an estimate of the mode volume, we can also evaluate the THz vacuum electric field within the cavity using Equation (1.1). We find that the vacuum electric field is $\left|E_{\mathrm{vac}}\right| = 4.6\times10^5$ V·m^{-1} in air, a value that guarantees a significant coupling strength in our system.

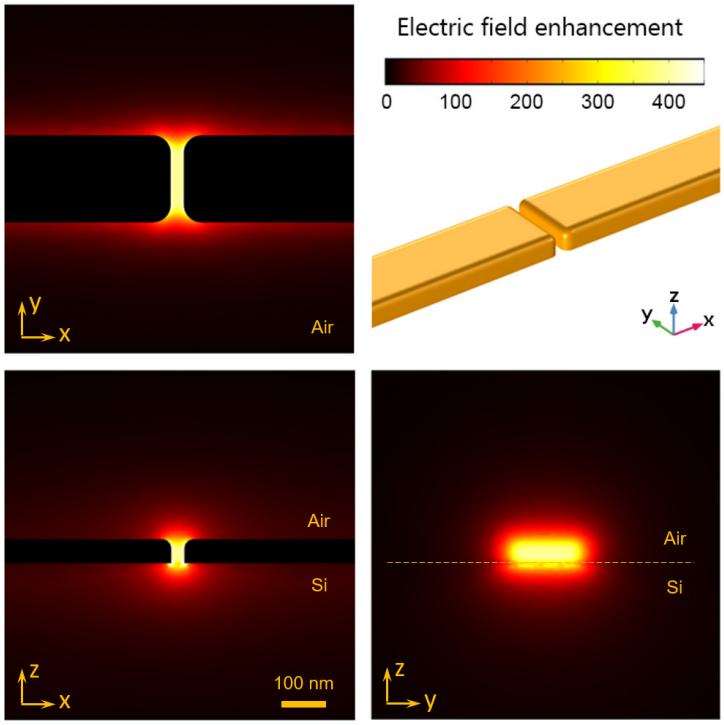

Figure 4.12 **The local electric field distribution in the area of a nanocavity. All the 2D projections are taken on a plane passing through the nanocavity geometrical center. Picked frequency: 8 THz; nanoantenna length: 5.75 μm**

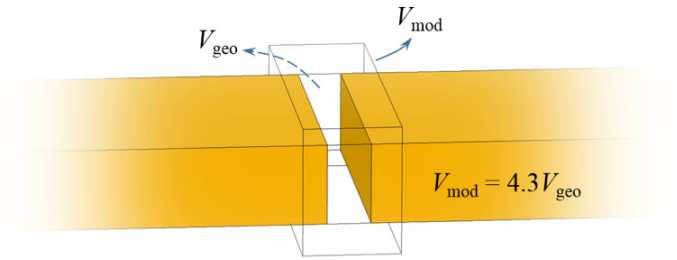

Figure 4.13 **Size comparison between the geometrical nanocavity volume and the mode volume.**

4.1.7 Lattice Mode Calculation for the Nanoantenna Arrays

A detailed explanation regarding the origin of lattice modes (i.e., Wood-Rayleigh anomalies) has been given in Section 3.4. We have used Equation (3.32) in our design to place the first appearing lattice mode for the nanoantenna arrays at a frequency higher than their fundamental resonance mode. In this way, the lattice mode does not significantly influence the nanoantenna resonance, especially when the latter is located in the relevant spectral region around 8 THz. We recall here that, in our specific configuration: i) the incident light is considered with an incident polar angle of 18° and an azimuthal angle of 45°; ii) the nanoantenna spacing along y-axis (g_y = 8.5 μm) is always greater than the one along x-axis (g_x: equal to the antenna length plus the nanogap size). We can thus extract the exact values of the parameters A and B in Equation (3.32) by setting the lattice orders $l = 0$ and $m = -1$, in order to calculate the lowest-frequency lattice mode, which satisfies the following relation:

$$k_{sub}^2 = k_x^2 + \left(k_y - G_y\right)^2, \tag{4.3}$$

where $k_{sub} = k_0 n_{sub} = \dfrac{2\pi \nu_0 n_{sub}}{c}$ is the absolute value of the wavenumber in the array substrate, $k_x = \sin\theta\cos\varphi \cdot k_0 = A \cdot k_0$ and $k_y = \sin\theta\sin\varphi \cdot k_0 = B \cdot k_0$ are the *x* and *y* in-plane components of the incident wave vector (with φ the angle formed by the plane of incidence with the long axis of the nanoantennas and θ the angle of incidence within this plane), while $G_y = \dfrac{2\pi}{g_y}$ is the reciprocal lattice vector in the *y*-direction. The variable ν_0 is the frequency of the first lattice mode that we want to retrieve. For our specific system, we can now write the wavenumber of the first lattice mode as:

$$k_0 = \frac{-B + \sqrt{n_{\text{sub}}^2 - A^2}}{n_{\text{sub}}^2 - \left(A^2 + B^2\right)} G_y$$

$$k_0 = \frac{-\sin\theta\sin\varphi + \sqrt{n_{\text{sub}}^2 - \sin^2\theta\cos^2\varphi}}{n_{\text{sub}}^2 - \sin^2\theta} G_y. \quad \textbf{(4.4)}$$

The corresponding frequency of the first lattice mode is:

$$\nu_0 = \frac{-\sin\theta\sin\varphi + \sqrt{n_{\text{sub}}^2 - \sin^2\theta\cos^2\varphi}}{n_{\text{sub}}^2 - \sin^2\theta} \cdot \frac{c}{g_y}. \quad \textbf{(4.5)}$$

Consequently, the wavelength of the first lattice mode in free space can be written as:

$$\lambda_0 = \frac{n_{\text{sub}}^2 - \sin^2\theta}{-\sin\theta\sin\varphi + \sqrt{n_{\text{sub}}^2 - \sin^2\theta\cos^2\varphi}} g_y. \quad \textbf{(4.6)}$$

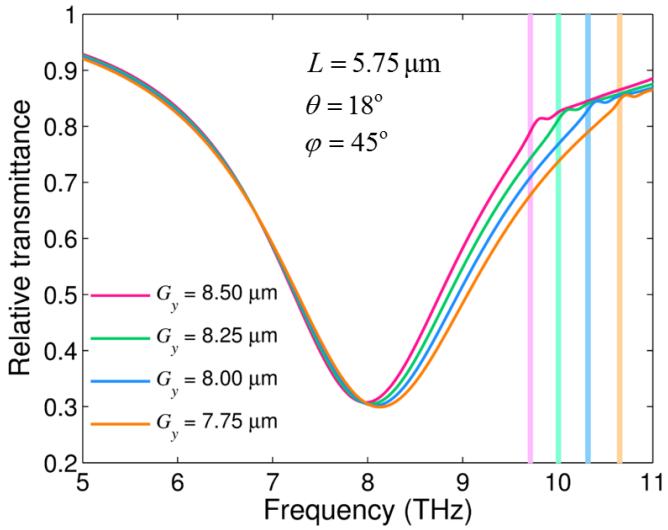

Figure 4.14 **Lattice mode dependence on the array spacing, estimated for a fixed antenna length of 5.75 µm. The colored curves are the simulated transmission spectra, while the corresponding vertical lines indicate the lattice resonance positions calculated using Equation (4.5).**

Figure 4.14 shows how the lattice mode can be straightforwardly tuned by changing the spacing g_y of the array, and also evidences the good agreement between the lattice resonance positions that can be estimated using Equation (4.5) (vertical lines, evaluated using the parameters of our investigation, i.e. $n_{\text{sub}} = 3.42$, $\varphi = 45°$, $\theta = 18°$) and the ones visible in the electromagnetic simulations (colored curves). Notice that for the y-direction spacing selected fo sample fabrication (g_y = 8.5 µm), the first lattice mode is located at 9.8 THz (as can also be seen

in the simulations shown in Figure 4.9 and Figure 4.11 above, where the near and far-field response of the arrays are presented).

4.2 Nanoantenna Fabrication and Nanocrystal Synthesis

4.2.1 Fabrication of Gold Nanoantenna Arrays

The design of the nanoantenna arrays was sent to our collaborators at the Italian Institute of Technology – IIT – in Genoa (Italy) for fabrication. The nanoantenna chains were prepared using the electron beam lithography (EBL) technique (for technical details, see Supplementary Information of [70]). Each fabricated two-dimensional array covered an area of 200 × 200 μm^2.

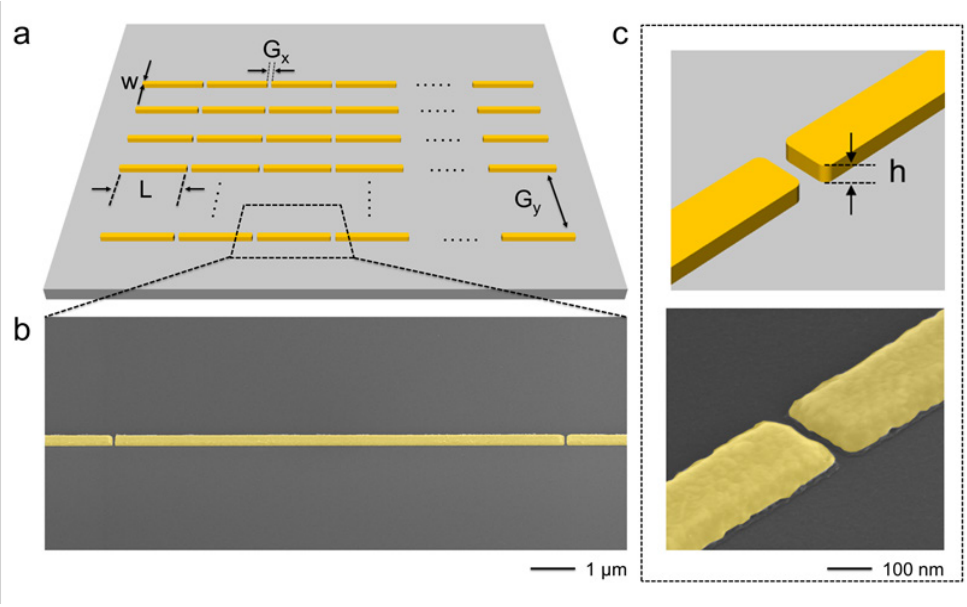

Figure 4.15 **(a) Schematic view of THz antennas on the Si substrate. (b) SEM image of a nanoantenna chain in false colors. (c) Sketch showing the details of the gap between two nanoantennas (upper panel) and corresponding SEM picture (lower panel).**

A schematic view of a THz nanoantenna array, together with two representative scanning electron microscope (SEM) images, are presented in Figure 4.15. Arrays with different nanoantenna length L, ranging from 4 to 7 μm, in accordance with the results of our design, were fabricated on a single silicon substrate, in order to tune their plasmonic resonances in the THz frequency band comprising the FR optical phonon mode of the CdS nanocrystals.

4.2.2 Synthesis of CdS Nanocrystals

The synthesis of the CdS nanocrystals was also performed at IIT in Italy. The nanocrystals used in the present study were synthesized using a two-steps protocol, in which a CdS shell of

desired thickness was grown on pre-synthesized CdS cores, following the procedure reported in Ref. [103] for CdSe/CdS giant-shell nanocrystals. For a detailed characterization of the synthesized nanocrystals see Supplementary Information of [70].

Figure 4.16 shows Transmission Electron Microscope (TEM) images for the CdS cores (panels a) and the CdS@CdS giant nanocrystals (panels b). As evident from TEM characterizations, the two samples are quite monodisperse, with an average size of (5.6 ± 0.4) nm and (10.2 ± 0.6) nm for the CdS cores and the CdS@CdS giant nanocrystals, respectively. X-ray diffraction (XRD) patterns (reported in Supplementary Information file of [70]) confirm the crystallinity of both samples, showing an excellent match with a hexagonal wurtzite structure. Moreover, such XRD measurements also confirm the absence of other phases and precursors' residues, certifying the high purity of the used nanocrystal samples.

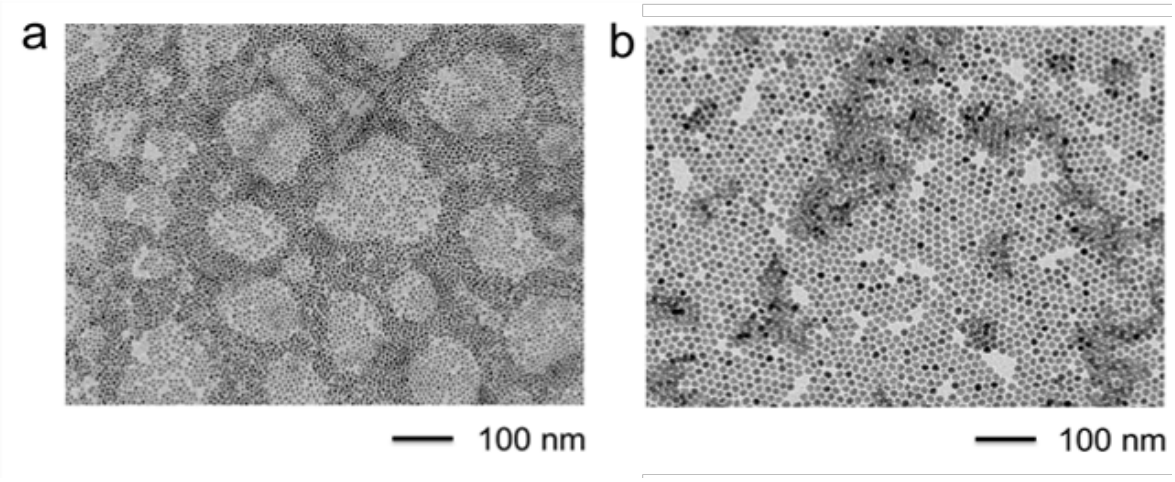

Figure 4.16 **TEM images of CdS cores (a) and CdS@CdS giant nanocrystals (b).**

4.2.3 CdS@CdS Giant Nanocrystal Layer Preparation on THz Gold Nanoantenna Arrays

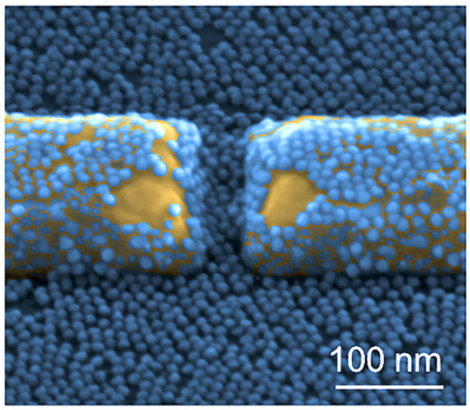

Figure 4.17 **Pseudo-colored SEM picture: A monolayer of CdS nanocrystals (10 nm in size) covers a THz nanoantenna cavity area.**

The deposition of the CdS@CdS giant shell nanocrystals on the THz gold nanoantenna arrays was carried out *via* spin coating under ambient conditions and at room temperature. Specifically, the obtained solution was diluted to a final nanocrystals concentration of 1 μM. Then, 20 μL of the diluted solution was spin-cast onto the patterned substrate at 2000 rpm for 60 s (acceleration of 1000 rpm·s^{-1}). The procedure resulted in the deposition of a uniform monolayer of CdS@CdS giant nanocrystals. An SEM picture of a nanocavity covered with such monolayer is shown in Figure 4.17. Thicker layers were obtained through multi-step layer-by-layer spin-coating deposition; to avoid complete re-dissolution of the already deposited nanocrystals, spin coating steps were interspersed with exposure of the sample to 20 μL of tetrabutylammonium iodide solution in methanol (10 mg·mL^{-1}) for 30 s, followed by three rinse-spin steps with methanol, as described in Ref. [104].

4.2.4 Estimation of the Number of Nanocrystal Layers

The estimation of the average number of nanocrystal layers over the sample surface was done by directly counting in the SEM images the number of nanocrystals inside the nanocavities (where the THz electric field mainly concentrates over the sample surface, thus representing the key locations of the electromagnetic interaction) and averaging these values for around twenty-thirty nanogaps. An example of this procedure, shown for a nanocavity covered with a single layer of nanocrystals, is presented in Figure 4.18.

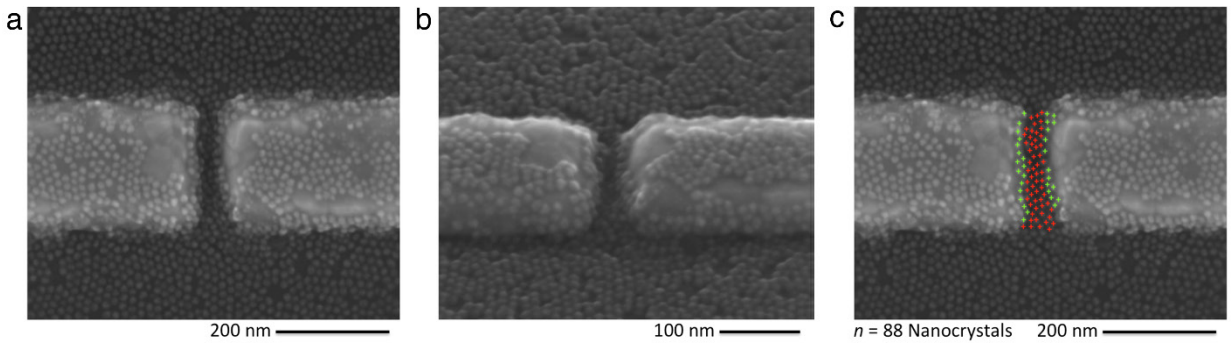

Figure 4.18 **Example of the visual estimate of the number of nanocrystals in a plasmonic nanocavity; (a) SEM top view. (b) Tilted view, allowing to appreciate further details of the nanocrystals positioning within the cavity. (c) Actual counting over the top view (red crosses: nanocrystals at the bottom of the cavity; green crosses: nanocrystals on the cavity sidewalls).**

For each nanocavity, several SEM images taken with different tilt angles were considered, to confirm the positioning of the nanocrystals in the nanocavity and also evaluate their stacking in the case of multiple layers. From the average number of nanocrystals obtained for the case of the monolayer n^1_{avg}, we then estimated the number of layers N_{EST} as $N_{\mathrm{EST}} = n_{\mathrm{avg}} / n^1_{\mathrm{avg}}$, where n_{avg} is

the average number of nanocrystals evaluated for the three different sample covering conditions of interest for our work. The obtained values for N_{EST} are summarized in the third column of Table 4.1.

Table 4.1 Estimation of the nanocrystal layer number

N	n_{avg}	N_{EST}	N_{EDX}
1.0	86.4±8.7	1.00±0.14	1.00±0.14
1.5	130.1±11.4	1.51±0.20	1.49±0.26
2	205.7±10.4	2.38±0.28	2.21±0.29

To confirm these estimates with an independent technique, we also performed Electron Dispersive X-Ray (EDX) measurements, by employing an FEI Helios Nanolab 650 microscope working at an accelerating voltage V = 5 kV, current I = 0.4 nA and acquisition time t = 120 s. SEM images of the nanogaps were collected with 250.000× magnification, in order to include in the images the CdS nanocrystals as well as the edges of the gold nanocavities. The relative atomic fractions of Cd and Au extracted from the EDX measurements taken in such a configuration were then used to estimate the equivalent number of nanocrystal layers, by fixing as a reference (N_{EDX} = 1) the case of a monolayer of nanocrystals. As can be seen in Table 4.1 (fourth column), the EDX estimate returns values for the effective number of layers in good agreement with the visual estimate described above.

As for the case of the micro-Raman measurements performed on individual nanocavity areas, which are described later on in this Chapter (see Section 4.4), the number of layers N refers to the actual number of nanocrystals n contained in the specific nanogap under measurement, estimated by directly counting the nanocrystals in the SEM image of that specific nanocavity ($N = n / n^{1}_{avg}$).

4.3 THz Characterization – Synchrotron Measurements

THz transmission spectra were collected at the high-brightness synchrotron IR source SISSI@Elettra. THz radiation is generated at the bending magnet 9.1 and propagated in ultra-high-vacuum to the SISSI laboratory, where the radiation enters a Bruker 70v Fourier Transform IR (FTIR) spectrometer equipped with a Si beam-splitter, and is then coupled to a Hyperion IR microscope. The microscope is provided with an external detector port allowing to install a He-cooled Si bolometer. Thanks to the high brightness of synchrotron light, this set-up allowed

performing polarized THz microscopy with good signal-to-noise performance on each individual array that was fabricated (see Figure 4.19).

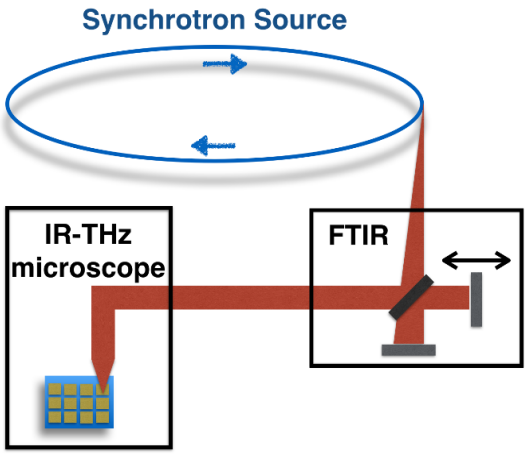

Figure 4.19 **Schematic layout of the experimental laboratory at the SISSI beamline: a Bruker 70v FTIR spectrometer is directly coupled to the synchrotron source, and then a Hyperion IR microscope is used to perform THz transmission measurements.**

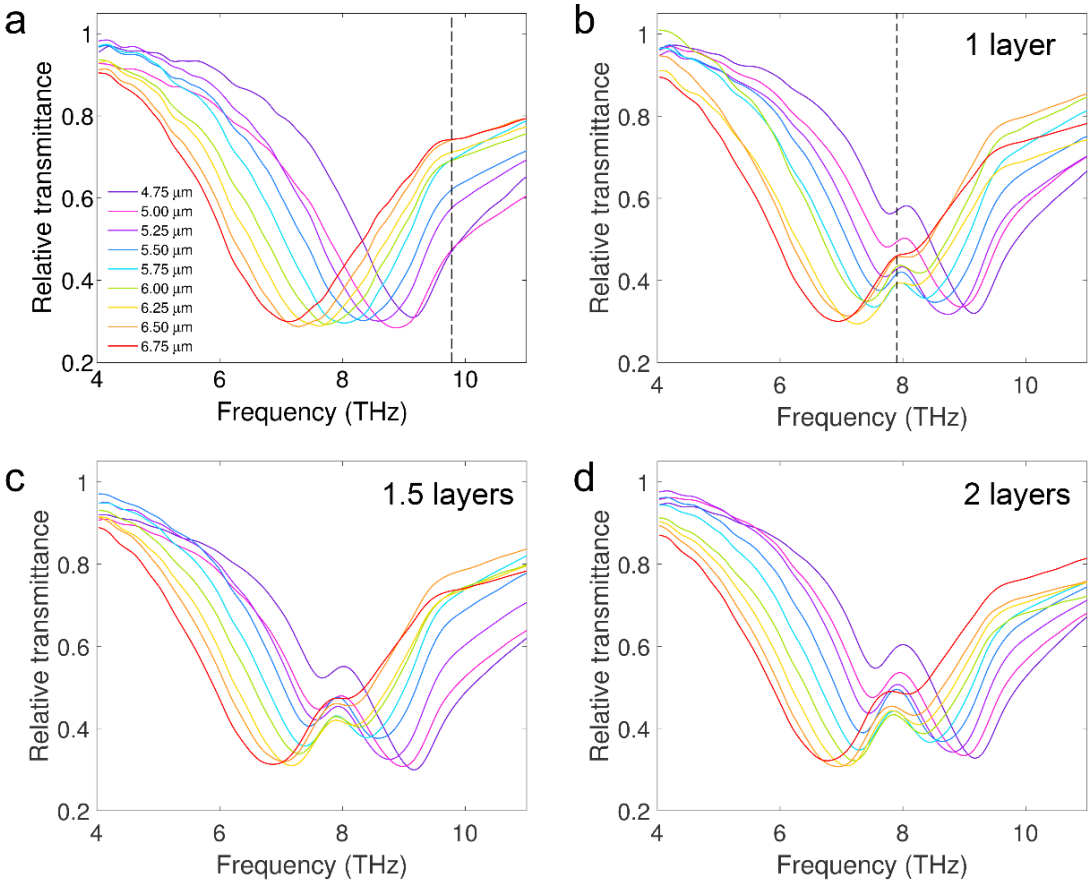

Figure 4.20 **Measured transmission spectra for bare arrays (a), and arrays covered with 1 (b), 1.5 (c), and 2 (d) CdS nanocrystal layers. The antenna lengths are from 4.75 to 6.75 µm. The dash lines in (a) and (b) are the lattice mode and FR phonon mode, respectively.**

A grating polyethylene polarizer was positioned at the entrance of the microscope, oriented along the main linear polarization axis of synchrotron radiation, corresponding to the electron's orbit plane. Polarized transmittance measurements were conducted by orienting the sample mounted on a goniometer, in such a way that the long nanoantenna axes were set parallel to the main polarization axis of the synchrotron beam. As mentioned above, a Cassegrain objective (15×, mean incidence angle: 18°) was used to focus THz light onto the sample, while an aperture was employed to limit the focal spot size to a diameter of approximately 260 μm. Data were acquired by averaging 512 scans with a resolution of 4 cm^{-1}. The measured transmission spectra are shown in Figure 4.20. We can see that they are in good agreement with the simulated transmission spectra (see Figure 4.11). Notice that the dashed line in Figure 4.20a indicates the lattice mode position, which can be observed both in the simulations and THz transmission measurements. The dashed line in Figure 4.20b marks the FR resonance of the CdS nanocrystals instead. Regarding the exact sizes of the Rabi splittings, see the extracted values in Figure 4.26.

4.4 Raman Measurements

All Raman measurements were conducted by our collaborators at IIT in Italy. We then contributed to data treatment and interpretation. Raman spectroscopy, by simply monitoring the frequency of visible light inelastically scattered by the sample under investigation, represents an interesting alternative tool to retrieve the phonon response of our system without recurring to direct THz illumination. In brief, the Raman investigation was performed in a backscattering configuration using a micro-spectrometer system (Renishaw inVia) equipped with a 150× LEICA PL APO objective (numerical aperture *NA* = 0.95) and a thermo-electrically cooled CCD as a detector (working temperature -60°C). Spectra were collected exciting the system with a He:Ne laser (λ = 632.8 nm). The wavelength was chosen after optimizing the experimental conditions in terms of scattering efficiency, suppression of fluorescence emission from the CdS nanocrystals (bandgap ~2.4 eV), and beam size at the diffraction limit. The laser power was fixed at 1.7 mW with an integration time of 10 seconds. The scans along the nanoantennas were performed using an XYZ motorized stage with a nominal 0.01 μm step. The polarization of the exciting laser source was set by means of a half waveplate.

Figure 4.21 shows examples of Raman spectra acquired on a resonant plasmonic nanocavity covered with CdS nanocrystals using different laser illumination powers (100% power level corresponds to 1.7 mW on the sample surface). The dashed lines indicate mode frequencies as follows: ν_{TO} ≈ 6.9 THz, ν_{LO} ≈ 9.1 THz, ν_{FR} ≈ 7.85 THz. As can be seen, apart from differences

in the signal-to-noise ratio, no power dependence is observed for the spectral positions of the lower (ν_-) and upper (ν_+) vibro-polariton frequencies related with the FR phonon resonance (ν_{FR}) hybridization (for a comprehensive description of the Raman spectral features observed in these measurements, see Section 4.5 below). For power levels below 85%, the two hybridized peaks cannot be distinguished anymore in the Raman spectra.

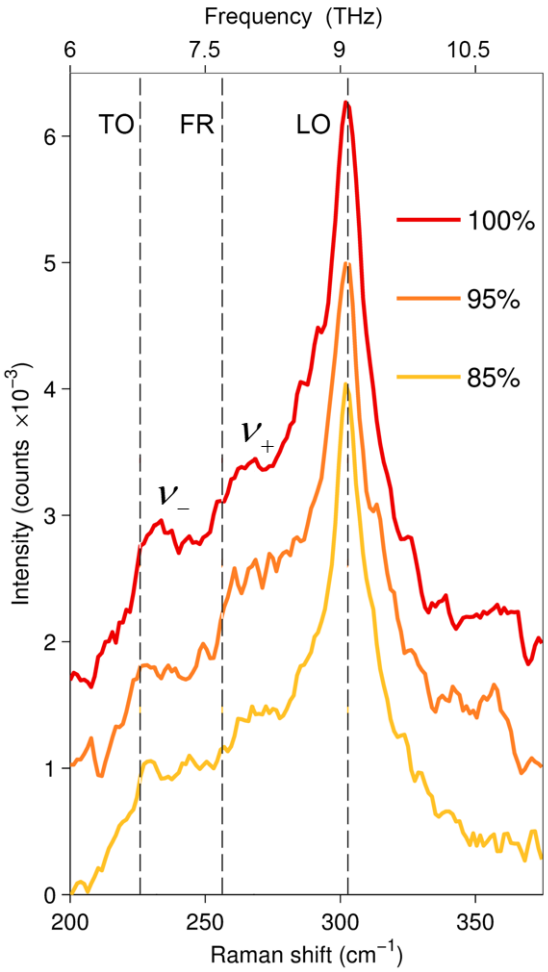

Figure 4.21 **Raman spectra taken at different laser power levels on a nanocavity featuring a number of nanocrystal layers $N \approx 1.5$. *v-* and *v+* are the frequency of lower and upper vibro-polaritons, respectively. The spectra are vertically shifted for clarity.**

4.4.1 Evaluation of the Rabi Splitting from the Raman Spectra

Raman measurements were acquired illuminating a sampling area of ~1.39 μm^2. Rabi splitting values were calculated from the measured spectra using the following procedure. A spectrum of interest (collected in a nanocavity region) was corrected through the subtraction of a reference spectrum for the CdS nanocrystals (acquired just outside the cavity region over the silicon substrate). In this way, the contributions deriving from the TO, LO and uncoupled FR

phonon modes, as well as from the gold nanoantenna luminescence background, were removed from the spectral data. On the resulting signals (see examples in Figure 4.22), a deconvolution in the region 200-300 cm^{-1} (6 – 9 THz) was operated, by fitting the peaks with two Lorentzian curves, and thus extracting the hybridized resonance positions.

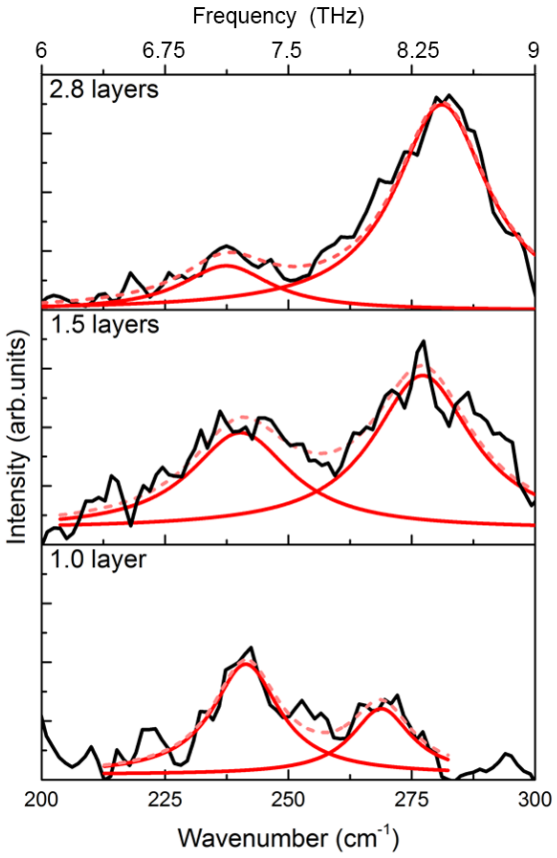

Figure 4.22 **Examples of the fitting procedure of the Raman spectra described above.**

4.4.2 Polarization Properties of Raman Spectra

As can be clearly seen in Figure 4.27b in Section 4.5.2, by comparing the spectra taken on the gold nanoantennas (black curves) with the one measured on the silicon substrate (blue curve), no enhancement of the intensity of Raman scattering associated with the gold nanostructures was observed for the pristine phonon modes of the CdS nanocrystals. This behavior can be explained considering that THz nanoantennas are far out of resonance for the exciting visible radiation (λ = 632.8 nm), and thus do not show any sizable antenna-assisted surface-enhanced-Raman-scattering (SERS) effect [105]. In order to further corroborate this result, additional Raman measurements were taken on a nanocavity covered with CdS nanocrystals, to compare spectra

where the polarization of the exciting visible laser was set either parallel (red line in Figure 4.23) or perpendicular (blue line) to the long axis of the antennas.

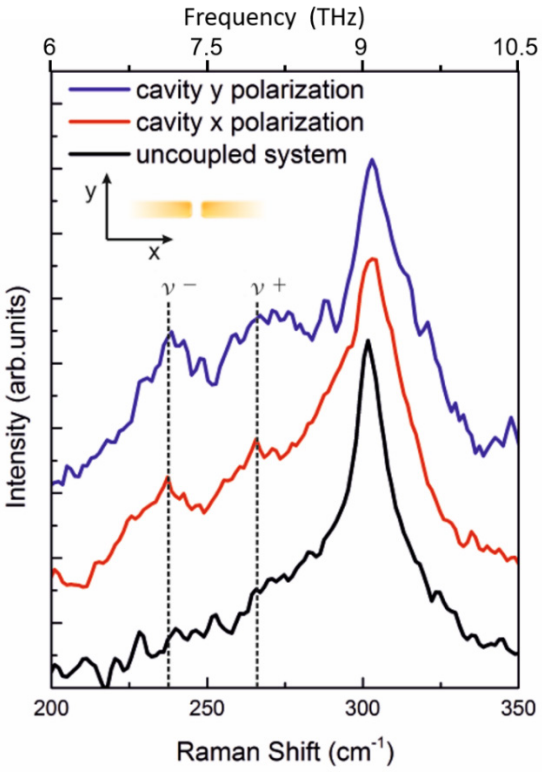

Figure 4.23 **Raman spectra collected in the same nanocavity with the polarization of the exciting laser source set parallel (red line) and perpendicular (blue line) to the long axis of the antennas. A spectrum collected just outside the gap region (black line) is also shown as a reference.**

As shown in Figure 4.23, in both cases, no sign of SERS enhancement was retrieved. Additionally, no significant differences in the hybridized peak positions and amplitudes were found, confirming that the phonon hybridization observed in Raman measurements does not depend on the polarization properties of the exciting visible laser.

Besides this, further Raman measurements were taken on resonant plasmonic nanocavities, by placing an output polarizer (analyzer) in the path of the scattered light collected from the sample. As can be seen in Figure 4.24, by increasing the angle formed by the main axis of the output analyzer relative to one of the input polarizer, a progressive reduction of the intensity of the Raman response is observed for both the main LO peak and the hybridized FR peaks. The input polarizer is set either along the long (Figure 4.24a) or short (Figure 4.24b) axis of the nanoantennas in these measurements. The overall Raman response of CdS nanocrystals eventually disappears when the main axis of the output analyzer is set perpendicular to the input polarization state. Indeed, the LO phonon resonance of CdS nanocrystals is known to show a negligible degree of depolarization in Raman measurements, since the symmetric A1(LO) phonon

mode is dominant [106]. These results thus seem to evidence, at least within our experimental configuration, a similar phonon symmetry between the hybridized FR response of our strongly coupled system and the LO mode of the nanocrystals.

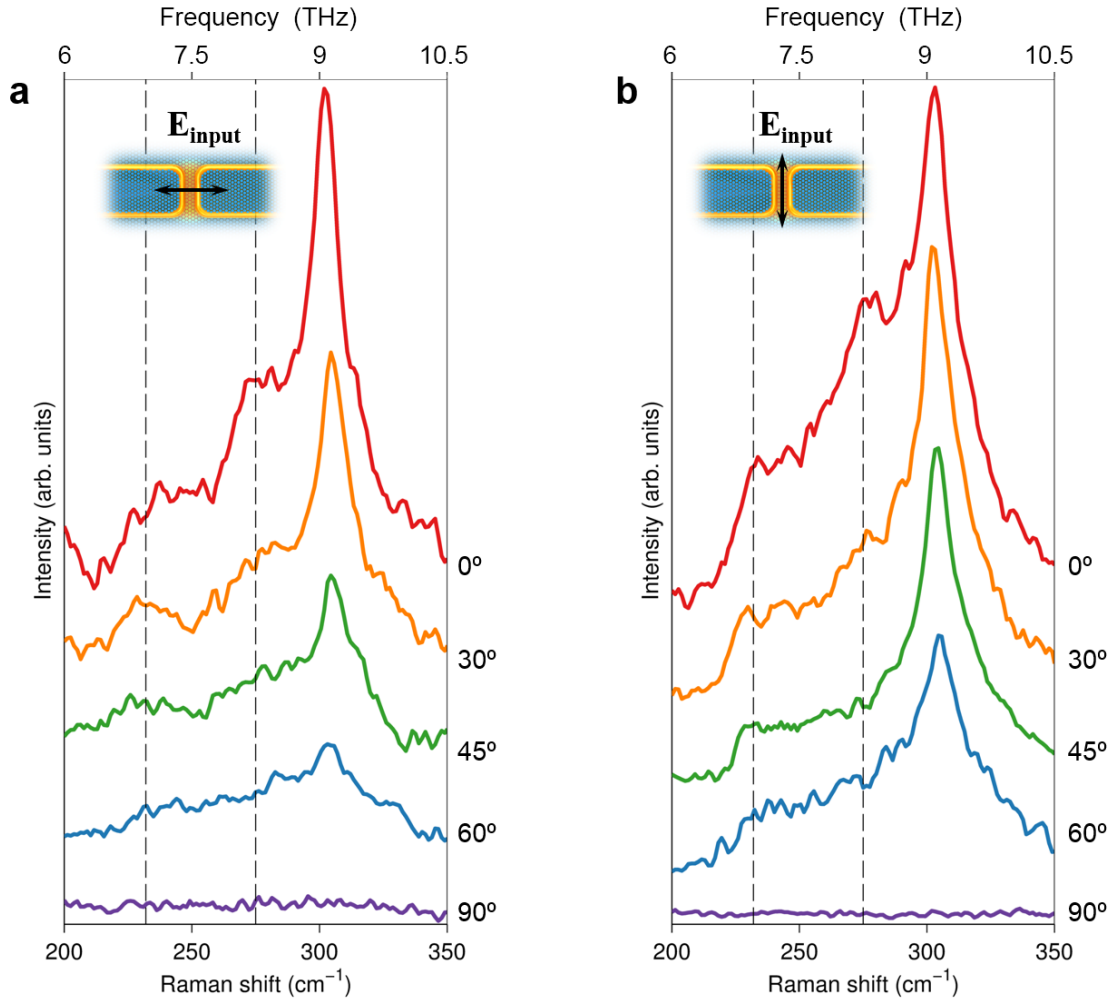

Figure 4.24 **Polarized Raman spectra taken with the input polarization set either along the long (a) or short (b) axis of the nanoantennas and the analyzer set at the angle reported in the figure legend. The measurements in (a) and (b) were performed on two nanocavities with a similar number of nanocrystal layers $N \approx 2.3$.**

4.4.3 Estimation of the Raman signal enhancement for the hybridized resonance

As discussed above, there is no evidence of SERS enhancement in our Raman measurements. Conversely, a different type of Raman signal enhancement, already reported in [61] and affecting only the hybridized resonance peaks, can be inferred from our experimental spectra, considering that the illuminating spot size of the micro-Raman system is more than 200 times larger than a nanocavity area. To extract an estimate of such an enhancement, we employed the following procedure:

We can consider the measured Raman signal $R_{\mathrm{MEAS}}(\nu)$ in a nanocavity region as the weighted average of the Raman response inside the nanocavity $R_{\mathrm{IN}}(\nu)$ and the one outside the nanocavity $R_{\mathrm{OUT}}(\nu)$, according to the following equation:

$$R_{\mathrm{MEAS}}(\nu) = \frac{B-A}{B} R_{\mathrm{OUT}}(\nu) + \frac{A}{B} R_{\mathrm{IN}}(\nu), \tag{4.7}$$

where $A = 0.006$ μm^2 (i.e., 30 nm × 200 nm) is the area of a nanocavity and $B = 1.39$ μm^2 is the spot size of the micro-Raman excitation laser on the sample. Using Equation (4.7), we can then estimate the Raman signal enhancement of the hybridized Raman peaks $K_{\nu\pm}$ as: $K_{\nu\pm} = \frac{R_{\mathrm{IN}}(\nu\pm)}{R_{\mathrm{OUT}}(\nu_{\mathrm{FR}})}$. The table below summarizes the enhancement values (spanning the range ~ 100 - 400), as extracted from the data presented in Figure 4.28 in Section 4.5.2. We note that the values in this table are consistent with the enhanced values reported by the first vibro-polaritonic Raman enhancement in a Fabry-Perot microcavity [61], where the Raman signals were also enhanced by about 2 orders of magnitude. It is important to note that this enhancement, unlike the traditional surface-enhanced Raman scattering mechanism [105], affects only the hybridized phonon resonance and leaves the rest of the Raman spectrum unaltered.

Table 4.2 **Enhancement values for the hybridized Raman peaks in Figure 4.28a**

N	$K_{\nu-}$	$K_{\nu+}$
1.0	185	90
1.5	262	380
2.8	101	384

4.5 Discussion

4.5.1 Phonon Resonance Hybridization in a THz Plasmonic Nanocavity

The schematic in Figure 4.25a summarizes the idea of creating a hybrid state at the nanoscale, by exploiting the strong coupling between a nanoantenna cavity resonance and the FR optical phonon mode of CdS nanocrystals. This results in the formation of two vibro-polariton resonant features that have both light and matter characteristics. As elaborated in Section 3.3, the nanocrystals in this coupled system are endowed with three main phonon lines: the TO and

LO phonon modes, which are also characteristic of bulk crystalline CdS, as well as a FR optical phonon resonance, typical of nanoparticles [32], which lies between the TO and LO lines. These three lines are identified once again here for clarity in Figure 4.25b, over the Raman spectrum of a single layer of CdS nanocrystals deposited on a silicon substrate. As can be seen in such spectrum, the FR mode is located in the low-frequency tail region of the main nanocrystal peak (LO phonon mode) in Raman measurements. Conversely, as shown in Figure 4.25c, the FR mode is the only relevant feature in the THz absorption spectrum, due to its dipole-active nature. By properly tuning the length (L = 5.75 μm) of the nanoantennas, we can observe evidence of resonance splitting both in Raman spectroscopy and direct THz extinction measurements (red curves in Figure 4.25b and Figure 4.25c, respectively), as large as 0.8 THz (see the Rabi splitting estimation in the next section).

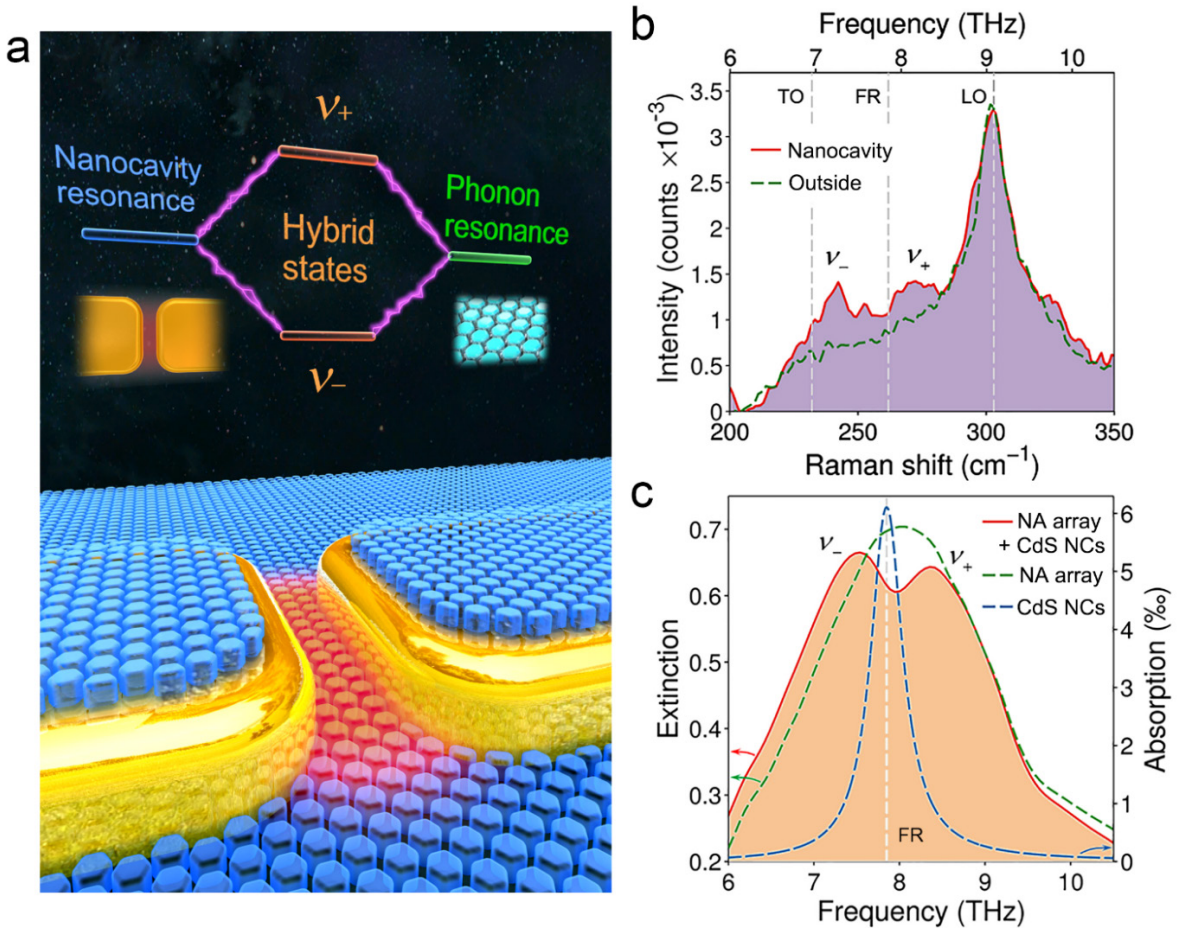

Figure 4.25 **(a) Sketch of the employed platform. (b) Raman spectra collected in a nanocavity region (solid red line) and just outside the nanocavity on the silicon substrate (green dashed line) for a sample covered with a nanocrystal monolayer; length of nanoantennas *L* = 5.75 μm. (c) Experimental THz extinction spectra of the array featuring nanoantennas of length *L* = 5.75 μm with (solid red line) and without (green dashed line) a nanocrystal monolayer on its surface; blue dashed line: absorption spectrum of a single layer of nanocrystals. The extinction is extracted from one minus the transmittance.**

4.5.2 Scaling of the Rabi Splitting with the Number of Nanocrystal Layers: THz Spectroscopy and Raman Measurements

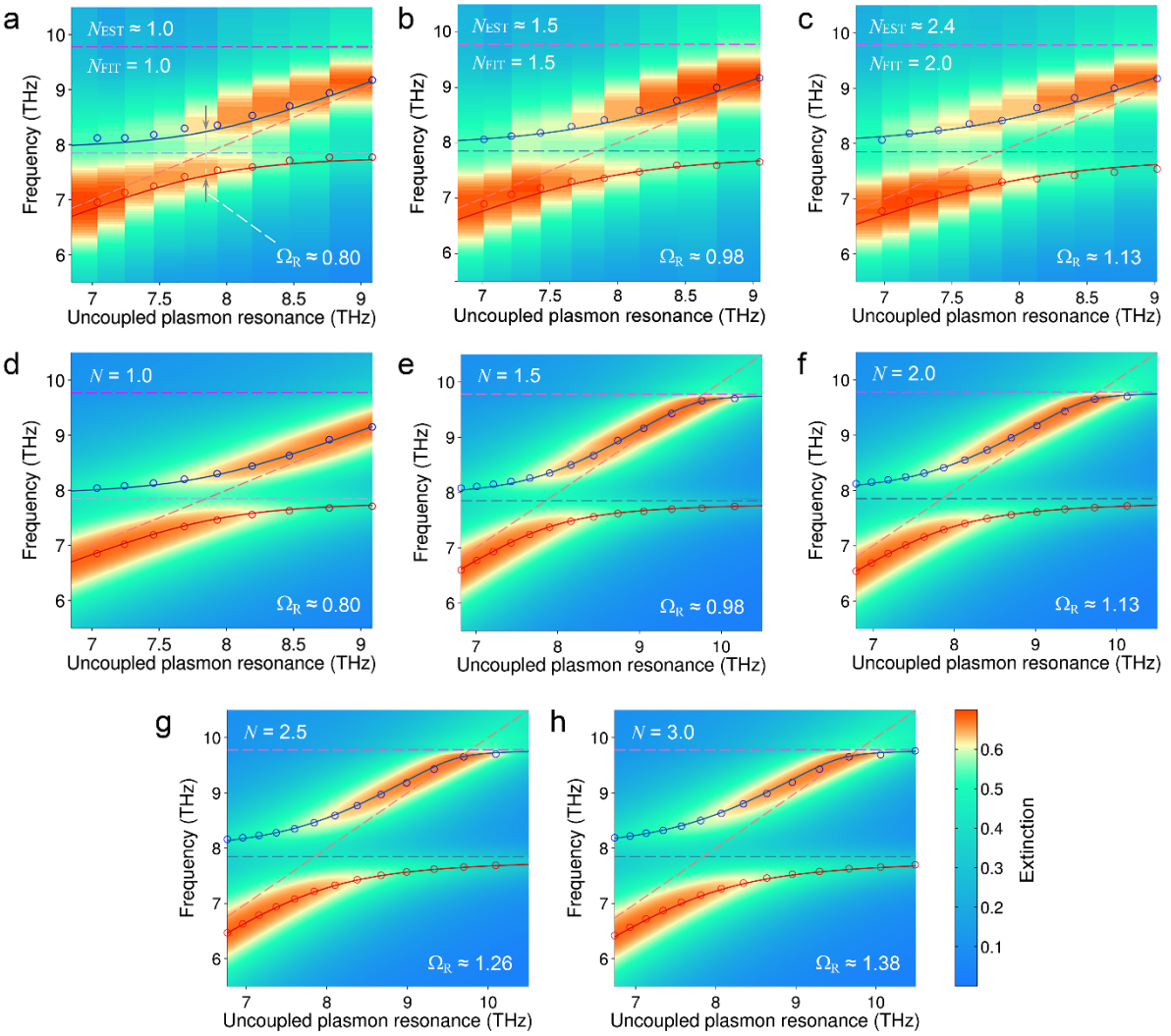

Figure 4.26 **Rabi splitting vs. number of nanocrystal layers. Experimental (a–c) and numerical (d–h) 2D maps of the polariton branches dispersion for different values of nanocrystal layer number N. As a reference for the experimental data, N_{EST} = 1 corresponds to an average number of nanocrystals inside a nanocavity of around 86 (see Section 4.2.4). The red (low-energy polariton) and blue (high-energy polariton) lines are the best fit with a three-coupled-oscillator model (see discussion in Section 4.5.3). The purple dashed line is the location of the first lattice mode of the arrays.**

In this section, we discuss how the plasmon-phonon coupling is affected by the number of nanocrystal layers. To increase the number of nanocrystals over the sample surface, we applied a specific protocol to stratify additional layers, as discussed in Subsection 4.2.3. Figure 4.26 shows the dispersion of the two polariton branches for different layer numbers, in both simulations and experiments. The Rabi splitting of the hybridized resonance can be extracted as the separation of the two branches when the uncoupled plasmon (nanoantenna) resonance is aligned

to the uncoupled FR mode. Using these extinction maps and fitting the peaks of the polariton traces by means of a three-coupled-oscillator model (see next section for details), we estimated (both from the simulation and experiment, Figure 4.26a and d) a Rabi splitting Ω_R of about 0.8 THz for the monolayer case, corresponding to approximately 10% of the uncoupled FR resonance frequency.

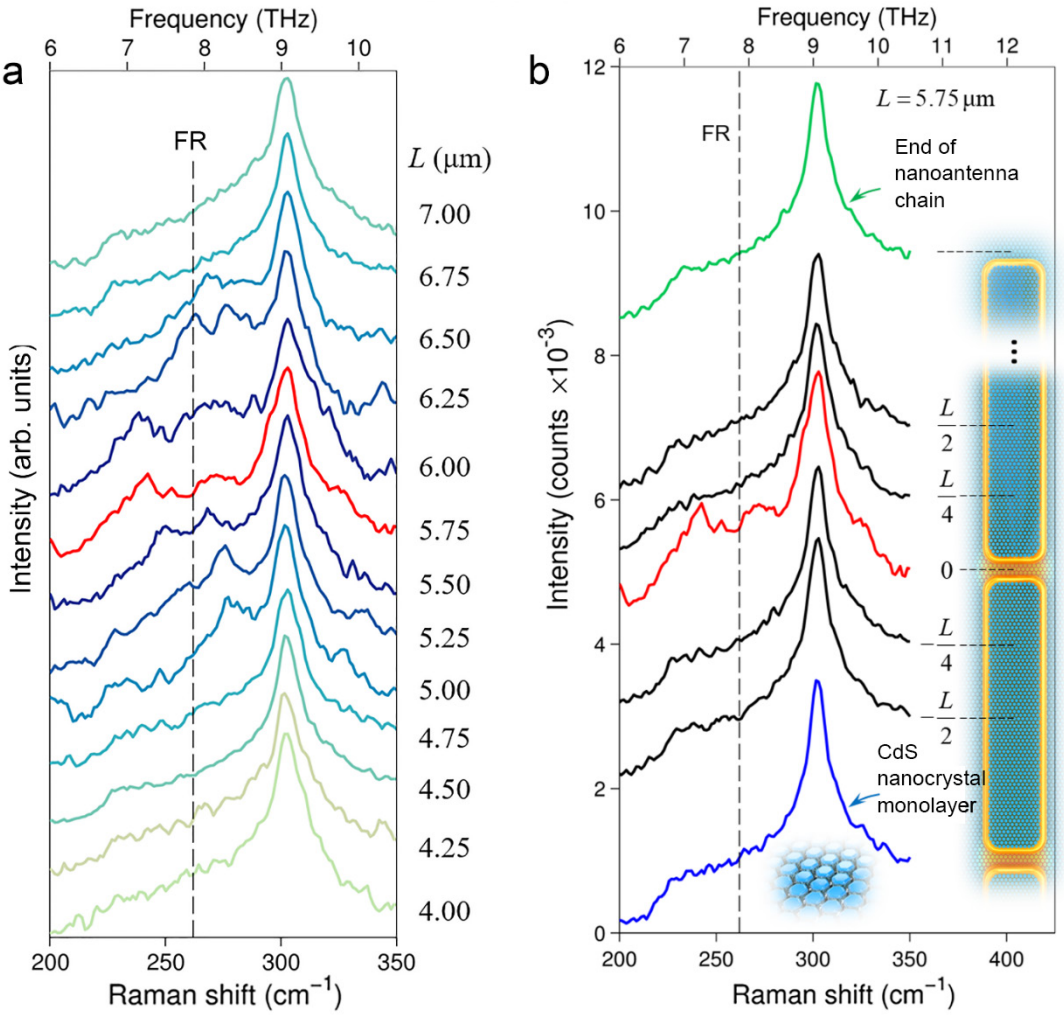

Figure 4.27 **(a) Raman spectra of the nanocrystals taken in a nanocavity region for different values of *L*. (b) Raman spectra of the nanocrystals taken on an array with *L* = 5.75 μm: in different positions along the nanoantennas composing a nanocavity (black lines), in the nanocavity region (red line), at the end of one nanoantenna chain (green line), and just outside the cavity on the silicon substrate (blue line). The spectra are vertically shifted for clarity.**

Figure 4.27 presents the micro-Raman characterization of a sample covered with a monolayer of nanocrystals. From this experimental evidence, we can infer that the phonon response of CdS nanocrystals is modified just within the nanocavity areas, and only when the nanoantenna length L is tuned to approximately match the plasmon resonance of the nanoantennas to the FR phonon mode of the nanocrystals. These specific conditions are the key

factors that allow the hybridization to occur. If the resonance of the nanoantenna arrays is detuned away from the FR mode, the two hybridized peaks in the Raman spectra eventually fade away (see Figure 4.27a). Figure 4.27b shows Raman spectra taken in different positions over the sample surface, in the case of an array with antenna length tuned to match the FR mode (L = 5.75 μm). If the nanocrystals are not located in the nanocavities, their Raman spectrum does not show any sign of FR phonon resonance hybridization.

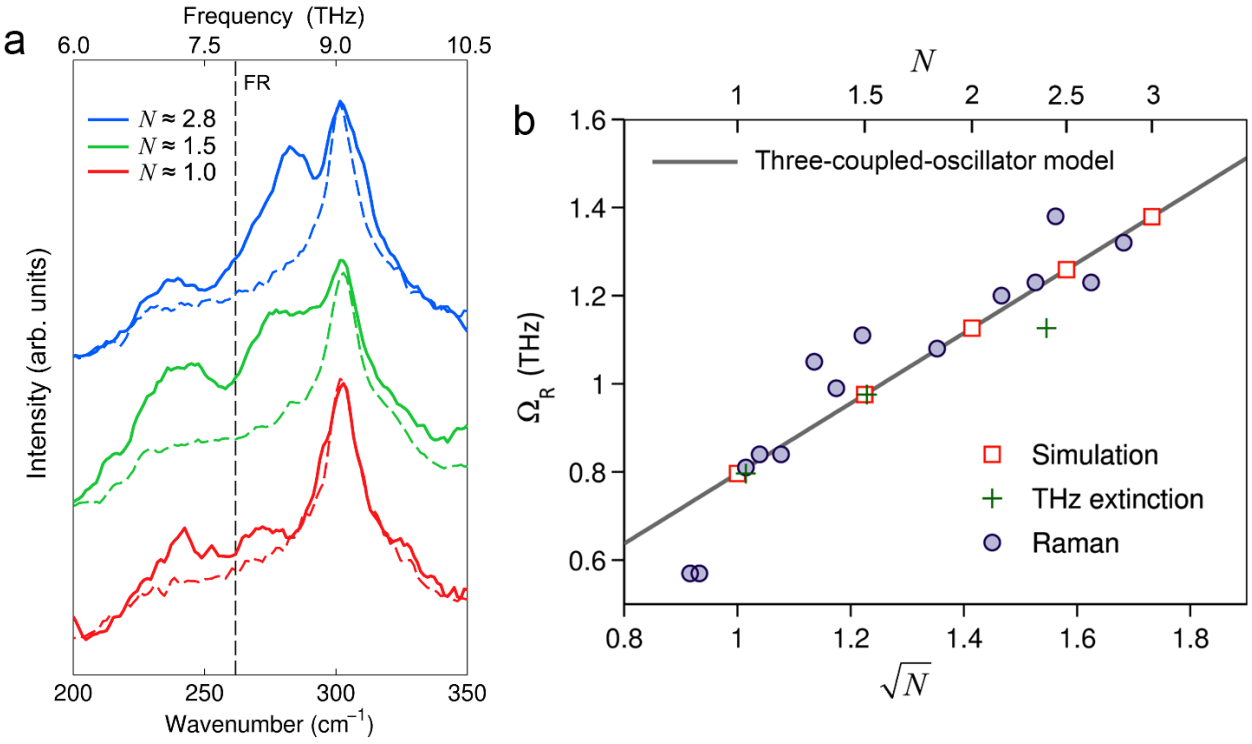

Figure 4.28 **(a) Raman spectra for L = 5.75 μm and three different values of nanocrystal layer number *N*. Solid lines indicate spectra taken in a nanocavity region and dashed lines indicate spectra taken just outside the respective cavity (using the same experimental parameters) on the silicon substrate. (b) Rabi splitting Ω_R as a function of $\sqrt{N}$, extracted from: the three-coupled-oscillator model (black line), numerical simulations (red bordered squares), THz extinction (green crosses), and Raman measurements (purple circles). For each Raman data point, *N* is evaluated considering the number of nanocrystals contained inside the specific nanocavity under measurement (see Section 4.2.4).**

In the case of multilayers, the Raman spectra for three different layer number N are given in Figure 4.28a, which clearly highlights the significant modification of the Raman response induced by the additional nanocrystals in a nanocavity region. Considering again the THz extinction maps shown in Figure 4.26, we can observe that, by adding more nanocrystal layers, the Rabi splitting increases. This trend is also confirmed by the Raman measurement, as suggested by the spectra in Figure 4.28a. For an immediate comparison of the Rabi splittings acquired from the extinction measurements (green crosses), numerical simulations (red bordered squares) and Raman measurements (purple circles), we can refer to Figure 4.28b. As can be seen, all results follow

the expected scaling widths, as also predicted by the three-coupled-oscillator model described in detail in the next section.

4.5.3 Fitting the Vibro-polariton Traces by Means of the Three-Coupled-Oscillator Model

As we can see from the spectra reported in Figure 4.26, due to the presence of a lattice mode at around 9.8 THz, our overall system in the THz transmission measurements is better described by a three-coupled oscillator model [71, 72]. The mathematical description of this model has been introduced in Section 2.2.3. The following matrix equation can be used to retrieve the characteristic frequency dispersion of the investigated interaction:

$$\begin{pmatrix} \nu_{\mathrm{pl}} - \nu & g_{\text{pl-ph}} & g_{\text{pl-lat}} \\ g_{\text{pl-ph}} & \nu_{\mathrm{ph}} - \nu & 0 \\ g_{\text{pl-lat}} & 0 & \nu_{\mathrm{lat}} - \nu \end{pmatrix} \begin{pmatrix} \alpha \\ \beta \\ \gamma \end{pmatrix} = 0, \tag{4.8}$$

where ν_{pl}, ν_{ph}, and ν_{lat} are the frequencies of the noninteracting plasmon, phonon, and lattice modes, respectively, while ν are the eigenfrequencies of the coupled system. $g_{\text{pl-ph}}$ ($g_{\text{pl-lat}}$) is the coupling constant between the plasmon and the phonon (lattice) modes. Finally, α, β and γ represent the coefficients of the basis functions of the bare plasmon, phonon and lattice modes, respectively. By diagonalizing this matrix, the dispersion of the hybrid eigenfrequencies can be directly evaluated. While this model does not include damping, it is worth underlining that such an idealized picture has proven to be successful in describing experimental systems with finite linewidths, as shown in a variety of studies, for both two- [59, 107] and three- [71, 72] coupled-oscillator interactions. From an operative point of view, a real system with finite resonance linewidths can be considered as strongly coupled whenever the two hybridized resonances are clearly visible in the response spectrum (see, for example, [108, 109]). This is evidently the case of our plasmon-phonon interaction, since the double peak formation can be distinctly seen not only in the direct THz extinction response, but also in the Raman measurements, with no THz illumination. Such splitting is indeed an intrinsic characteristic of the coupling between the matter transition and the cavity vacuum-field, and thus it manifests itself in any optical property of the system.

In order to compare the above model to our numerical and experimental results, the uncoupled plasmon resonance frequency needs to be estimated. The resonance wavelength λ_{Res}

of nanorod-shaped plasmonic nanoantennas typically obeys the following relation: $\lambda_{\mathrm{Res}} \approx 2n_{\mathrm{eff}}L$ [57, 110], where n_{eff} is the effective index of the nanorod surface mode. While this equation well describes the behavior of an isolated nanoantenna in the THz range, an additional parameter needs to be added in the case of an array of interacting nanoantennas: $\lambda_{\mathrm{Res}} = 2n_{\mathrm{eff}}L + S,$ to also take into account the expected red-shift of the resonance induced by the near-field coupling between the nanostructures [111]. In particular, by fitting the resonance wavelength dependence on the nanoantenna length for the case of bare nanoantenna arrays with the above formula (far from the lattice mode), we then obtain $n_{\mathrm{eff}}^{0} = 2.375$ and $S = 10.2$ μm (see red circles and related fit in Figure 4.29). The uncoupled plasmon resonance frequency in our system can be thus written as:

$$\nu_{\mathrm{pl}} = \frac{c}{2n_{\mathrm{eff}}L + S}. \tag{4.9}$$

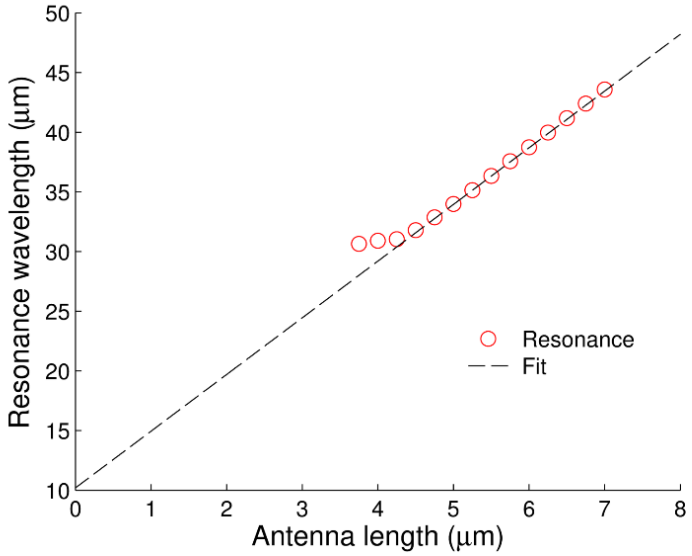

Figure 4.29 Resonance wavelength as a function of the antenna length for bare arrays.

The above relation in Equation (4.9) has been used to fit the numerical and experimental polariton dispersion curves with the model expressed in Equation (4.8). The results of these fittings are all reported in Figure 4.26 on page 75. Figure 4.30 shows again here the result of such procedure on the numerical data regarding a monolayer of nanocrystals.

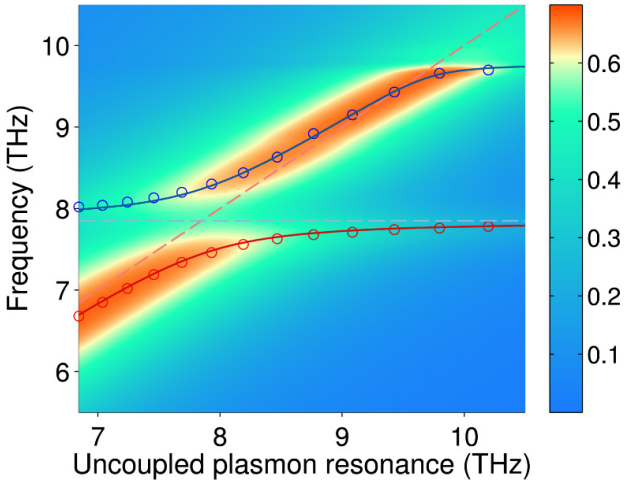

Figure 4.30 **Polariton trace fit of the simulation results for the case of 1 nanocrystal layer (compared to Figure 4.26d, here the axes are extended to frequency values above 10 THz). The red dashed line marks the uncoupled plasmon resonance position.**

From these fits, we can also extract the quantities $|\alpha|^2$, $|\beta|^2$ and $|\gamma|^2$, which can be used to estimate the relative contribution of the plasmon, phonon, and lattice modes to the overall hybridized state. As can be seen from Figure 4.31 below, at the FR resonance frequency an essentially complete hybridization of the plasmon-phonon modes occurs (i.e., $|\alpha|^2$, $|\beta|^2 \approx 0.5$) for both the polariton branches, while the contribution of the lattice mode is negligible.

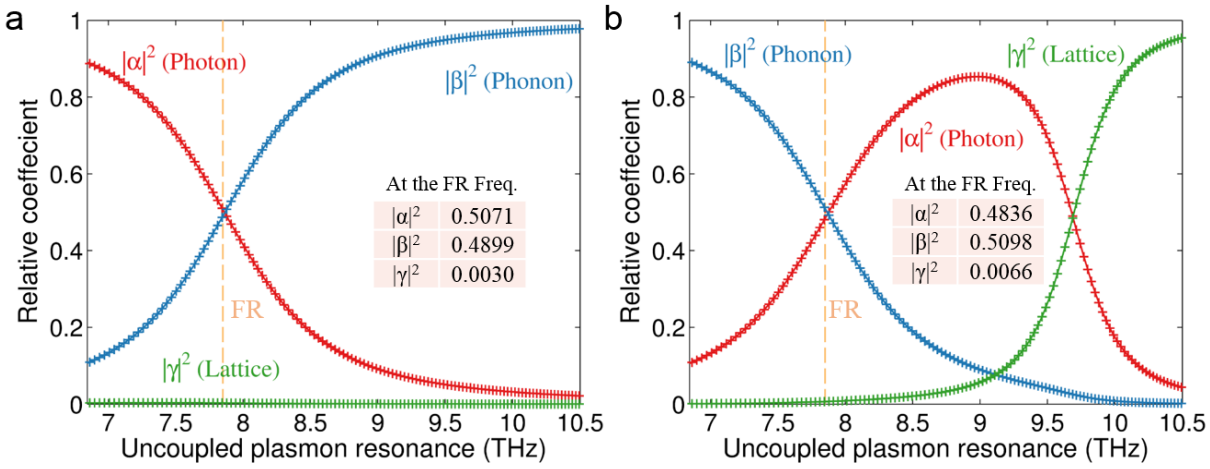

Figure 4.31 **(a) Relative coefficients for the low-energy polariton branch, in the case of 1 nanocrystal layer. (b) Same as in (a), for the high-energy polariton branch.**

Table 4.3 (for the simulations) and Table 4.4 (for the experiments) below summarize all the parameters used in the fitting procedure and also include the root-mean-square error (RMSE) analysis for the two polariton branches: $RMSE = \sqrt{\frac{1}{m}\sum_{j=1}^{m}\left(y_j - \hat{y}_j\right)^2}$ where y_j are the analytical

model estimates for the polariton branch positions and $\hat{y}_j$ the *m* experimental or simulation points. As can be seen, in both simulations and experiments, and for the different numbers of nanocrystal layers considered in our investigation, the following parameters were kept as constants in the fitting procedure: $\nu_{ph} = 7.85$ THz, $\nu_{lat} = 9.78$ THz, $S = 10.2$ μm, $g_{pl\text{-}lat} = 0.18$ THz. The plasmon-phonon coupling constant was considered to obey the relation [112]: $g_{pl\text{-}ph} = g^1_{pl\text{-}ph}\sqrt{N}$, where $g^1_{pl\text{-}ph}$ is the value of this coupling parameter for one layer of nanocrystals and *N* is the number of layers. Interestingly, we found that for the best fit of both the experimental and numerical data, the effective index n_{eff} needs to be slightly increased when adding the nanocrystal layers, according to the empirical rule: $n_{eff} = \gamma_{eff} N + n^0_{eff}$, with $\gamma_{eff} = 0.025$. This behavior is consistent with the increase in the average permittivity around the nanoantennas induced by the presence of the nanocrystal layers. For both the experimental and simulation polariton traces, the RMSE values associated with the fitting curves are of the order of some tens of GHz, well below the Rabi splitting values (≥ 800 GHz) extracted from our THz measurement data.

Table 4.3 Fitting coefficients for the simulated polariton traces

	1 layer	1.5 layers	2 layers	2.5 layers	3 layers	Units
$g_{pl\text{-}ph}$	0.40	0.49	0.57	0.63	0.69	THz
$g_{pl\text{-}lat}$	0.18	0.18	0.18	0.18	0.18	THz
ν_{ph}	7.85	7.85	7.85	7.85	7.85	THz
ν_{lat}	9.78	9.78	9.78	9.78	9.78	THz
n_{eff}	2.400	2.413	2.425	2.438	2.450	/
S	10.2	10.2	10.2	10.2	10.2	μm
$RMSE\ (\nu_+)$	0.025	0.025	0.019	0.020	0.024	THz
$RMSE\ (\nu_-)$	0.016	0.009	0.004	0.009	0.018	THz

Table 4.4 Fitting coefficients for the experimental polariton traces

	1 layer	~1.5 layers	~2 layers	Units
$g_{pl\text{-}ph}$	0.40	0.49	0.57	THz
$g_{pl\text{-}lat}$	0.18	0.18	0.18	THz
ν_{ph}	7.85	7.85	7.85	THz
ν_{lat}	9.78	9.78	9.78	THz
n_{eff}	2.400	2.413	2.425	/
S	10.2	10.2	10.2	μm
$RMSE\ (\nu_+)$	0.085	0.035	0.053	THz
$RMSE\ (\nu_-)$	0.065	0.049	0.069	THz

4.5.4 The Extinction Spectrum Evaluated using the Dissipated Power Model

Here, we briefly use the dissipated power model presented in Section 2.1.5 to reproduce the extinction response of the investigated coupled system. In such a model, the damping factors of all the involved oscillators are considered. Figure 4.32 presents the extinction spectra retrieved from the dissipated power model (blue curve), numerical simulations (red curve), and THz measurements (green curve), respectively, for the case of a single layer of nanocrystals and antenna array resonance aligned to the CdS FR phonon mode. We can see that the dissipated power calculation well predicts the resonance splitting and overall behavior of the extinction spectrum observed in the experiments/simulations (for the exact parameters used for this fitting procedure, see table below).

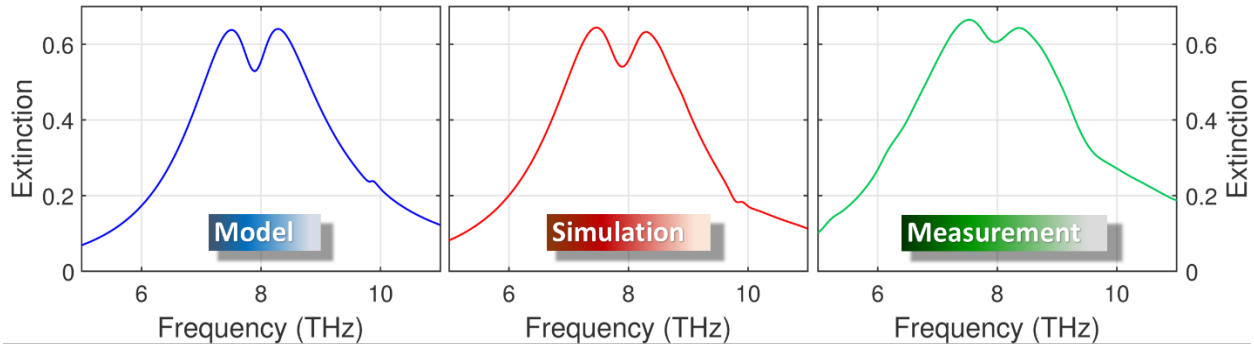

Fitting parameters

ω_1	ω_2	ω_3	γ_1	γ_2	γ_3	g_{12}	g_{13}	F
7.9	7.9	9.85	2.4	0.45	0.15	2.2	1.2	1.85

Figure 4.32 **Extinction spectra comparison among the dissipated power model, numerical simulations, and THz measurements. In this system, the damping factor (γ_1) associated with the nanoantenna resonance is about 5 times larger than the one (γ_2) of the CdS FR optical phonons mode. All the fitting parameters reported in the table above are in units of THz, except "*F* " that has no units (see Section 2.2 for details regarding the model).**

4.5.5 Chapter Summary and Impact

The work presented in this chapter has targeted a novel way to modify the optical phonon response of nanomaterials, just by exploiting the unique properties of THz plasmonic nanocavities. In our proof of principle study, we have found that, even without a direct THz excitation, the phonon spectrum of CdS nanocrystals can be significantly altered inside the nanocavities. This is due to an extremely high cavity vacuum electric field that reshapes the dipole-active phonon resonance of the nanocrystals into two new "vibro-polariton" bands. These hybridized resonances have both light and matter characters and show thus potential to modify the (typically non-radiative) phonon decay. For instance, the new hybrid states can find a novel

route to decay through a radiative process, which in turn could open up a novel class of nano-sources emitting THz radiation.

The design of the nanocavities is crucial to ensure the strong coupling (and thus the resonance hybridization) between their plasmonic resonance and the targeted phonon mode. Our array of end-to-end coupled gold nanoantennas is capable of squeezing THz radiation into extremely subwavelength cavity mode volumes (smaller than $\lambda^3/10^7$), thus ensuring very high THz vacuum electric fields up to 4.6×10^5 $V\cdot m^{-1}$ in air. To observe the effect of such high vacuum field on the nanocrystal phonon spectrum, we employed micro-Raman spectroscopy, focusing our investigation on individual nanocavities. We found that the two new hybrid states enhance Raman scattering by about two orders of magnitude. This allows us to clearly observe them in Raman spectroscopy measurements, even if the nanocavity area is 200 times smaller than the surface probed by the micro-Raman system. The evidence of phonon mode splitting without the need of any direct THz illumination represents the clear signature of the phonon strong coupling condition and confirms the possibility of altering the intrinsic phonon response of a nanomaterial using properly tailored nanoresonators.

The results presented in this chapter, besides representing a new playground for THz science and technology, suggest a potentially novel strategy to modify optical phonon-related energy dissipation and thus improve the electrical/optical performance of nanodevices.

5 Novel Nanocavity Design: Moon-Shaped Nanoantennas[1]

Here, a novel moon-shaped THz plasmonic nanoresonator is proposed for improving the interaction with the CdS FR phonon mode. Compared to the end-to-end nanoantenna cavity, the new design is endowed with a narrower resonance line width, a significantly reduced mode volume, a higher THz local field enhancement. The proposed geometry is inspired by the strategy of tapering metallic nanostructures to reduce plasmonic loss [113]. Therefore, in contrast to conventional split-ring resonators [114-117], a crescent-moon structure with a nanocavity between the tips is found to provide a noticeable improvement in THz field localization, thus promoting the coupling strength in the interaction with the nanocrystals. The design, fabrication, and characterization of this novel structure are presented in the following Sections.

5.1 Design of the Moon-Shaped Nanoantenna Array

5.1.1 Inspiration

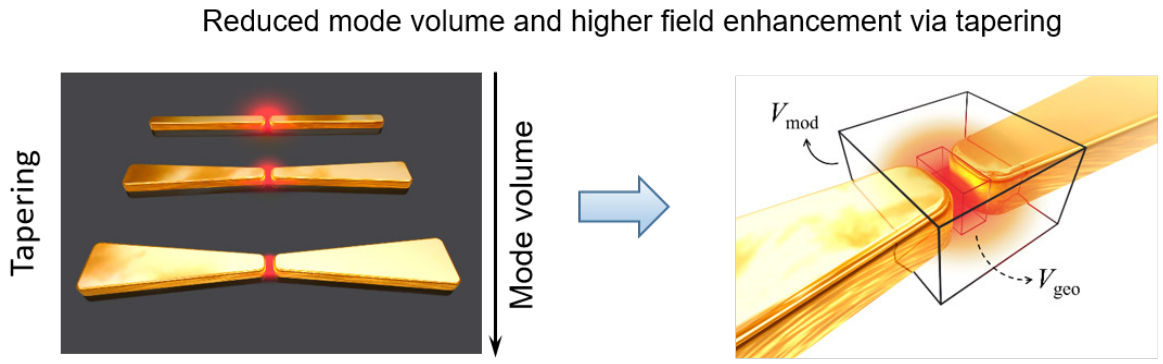

Figure 5.1 Inspiration: tapering straight nanoantennas for an improved field localization [113].

As mentioned above, the moon-shaped nanoantenna geometry is inspired by a recent work of our group on the tapering of straight THz nanoantennas [113]. By properly tuning the tapering angle, the ohmic loss associated with the surface mode responsible for the nanoantenna resonance can be reduced, resulting in a reduced mode volume and higher field enhancement (see pictorial representation in Figure 5.1). Starting from this result, we tested and compared several structures to further reduce the mode volume and thus increase the cavity vacuum electric field (see Figure 5.2). In general, split-ring resonators are known to have a narrow resonance

[1] This chapter is based on an ongoing work that is in preparation for submission to a refereed scientific journal.

linewidth as a result of a low scattering (radiative) loss [115, 116]. However, in the case of small lateral cross-sections (which is relevant to create nanoscale cavities between the split ring tips), they suffer from high ohmic losses, leading to low field enhancement and poor field localization. We could also envision the use of shuttle-shaped nanoantennas, following the tapering strategy mentioned above and maintaining nanoscale extremities on both sides of the nanoantenna, but this lead to broad resonances due to increased scattering. The moon-shaped resonator practically merges these two conceptual designs, promising to offer, at the same time, low ohmic and scattering loss with an extremely reduced mode volume within the so-constructed nanocavity. The geometrical design of the moon-shaped nanoantennas will be presented in the next subsection.

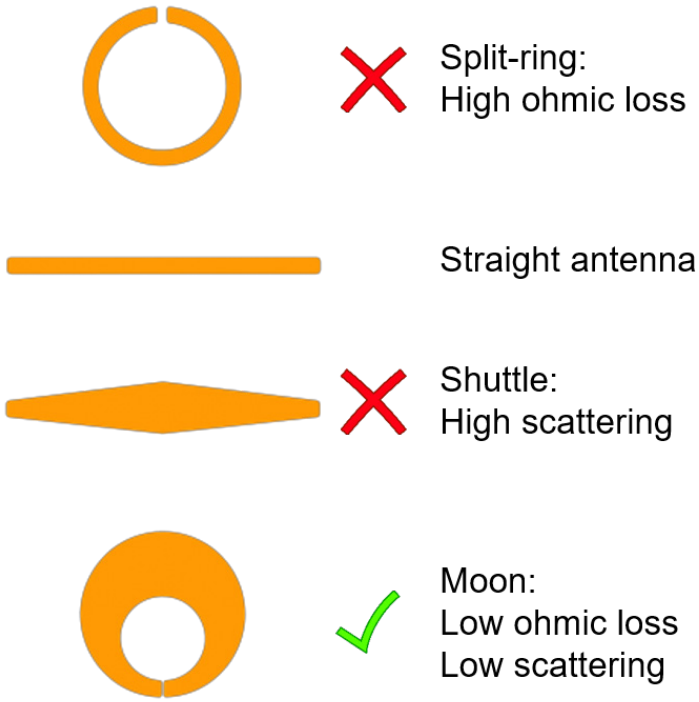

Figure 5.2 Selection of the appropriate geometry.

5.1.2 Geometrical Tuning of the Moon-Shaped Nanoantennas

The design and numerical tuning of the structure are once again realized with COMSOL Multiphysics. As shown in Figure 5.3, the gold moons (with a thickness of 100 nm) are laying on top of a silicon substrate with a fixed periodicity $g_x = g_y$ = 9 µm (chosen to locate the first lattice mode at a frequency higher than the relevant plasmonic resonance peaks). A detailed sketch of the individual moon structure is presented in Figure 5.4. The nanogap size and the antenna tip-

width are fixed at $w_{\text{gap}} = 20\,\text{nm}$ and $w_1 = 200\,\text{nm}$ respectively. We define the "length" (L) of the moon-shaped nanoantenna as the circumference ($L = 2\pi r$) of the central circle, whose center is at $o(0,0)$ and has a radius r. The inner and outer boundaries of the moon are delimited by two circles with radii $r_1 = r - w_1/2 - h/2$ and $r_2 = r + w_1/2 + h/2$, in which $h = (w_2 - w_1)/2$. Meanwhile, the center of these inner and outer circles are shifted according to $o_1 = h/2$ and $o_2 = -h/2$. In order to quantify the moon tapering, we define a "moon factor" f_{m} as the ratio between the larger waist width and the tip width of the moon, i.e., $f_{\text{m}} = w_2 / w_1$. We then use the antenna length L and the moon factor f_{m} to tune the resonance position and quality factor (the ratio between the resonance frequency and bandwidth) of the nanoresonator. Notably, the moon factor has to be optimized for a specific antenna length, to obtain a moon-shaped antenna with minimum ohmic loss.

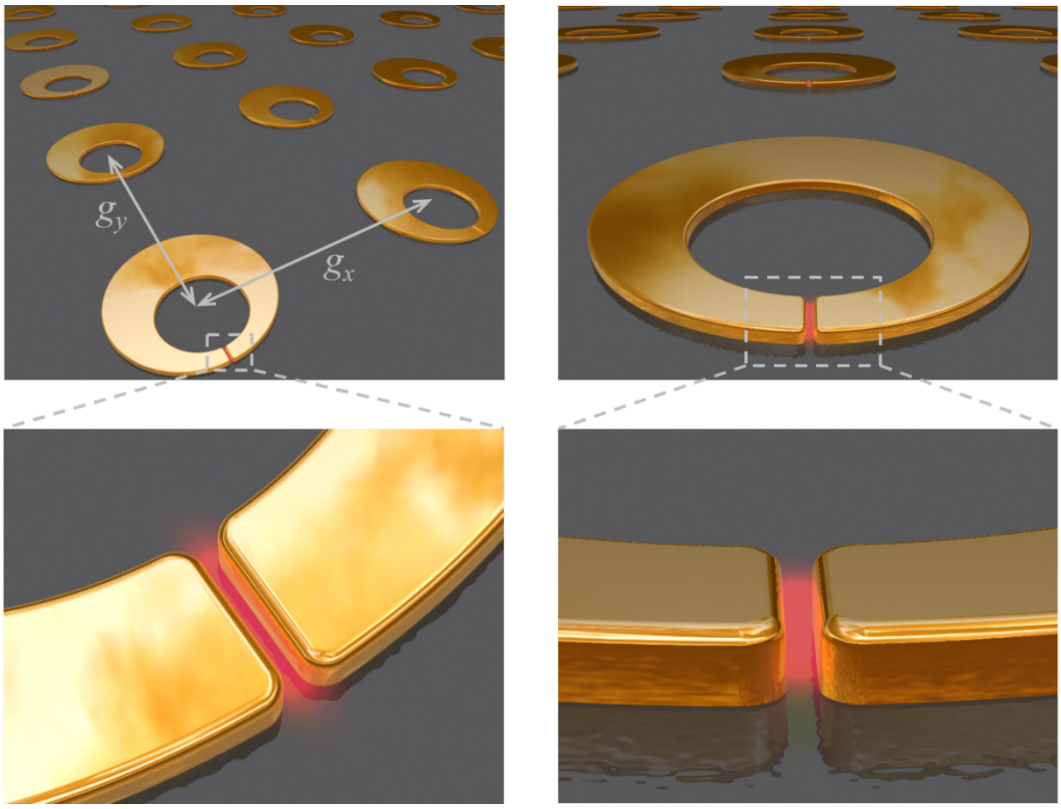

Figure 5.3 **Schematic of a moon-shaped nanoantenna array. The periodicity of our design is g_x = g_y = 9 μm, while the thickness of gold nanoantennas is 100 nm.**

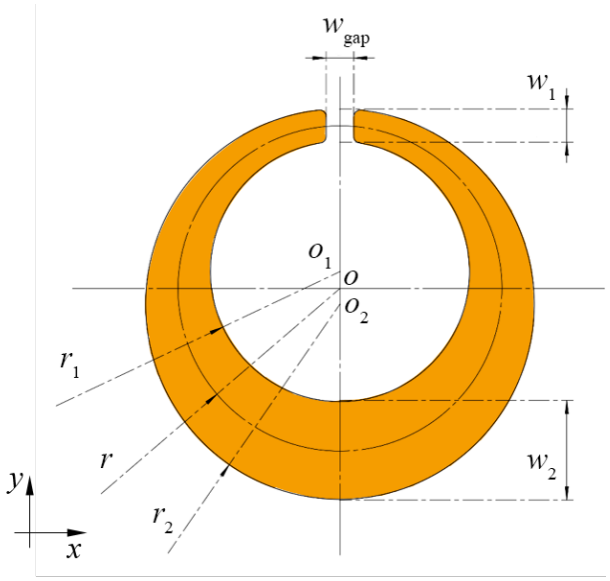

Figure 5.4 **Schematic of an individual moon.**

The physical settings and illumination conditions in the simulations are the same as in Chapter 4. The polarization projection in the x-y plane (see the coordinates in Figure 5.4) is always set along the x-axis, so to effectively localize the radiation in the nanogap. In Figure 5.5, we show the effect of varying the moon factor for a fixed antenna length L = 8 μm. As can be seen in Fig. 5.5a, for this parameter choice there is a maximum field enhancement for the resonance position of ~7.8 THz (very close to the FR optical phonon mode of CdS nanocrystals) when the moon factor is f_m = 6. The corresponding relative transmittances are presented in Figure 5.5b. According to these results, the moon factor in this study is from now on fixed at 6. Notice that the moon-shaped nanoantenna resonance is extremely sharp, with a FWHM of ~0.5 THz (for f_m = 6), which corresponds to ~1/5 of the linewidth of the straight nanoantenna case (see Chapter 4).

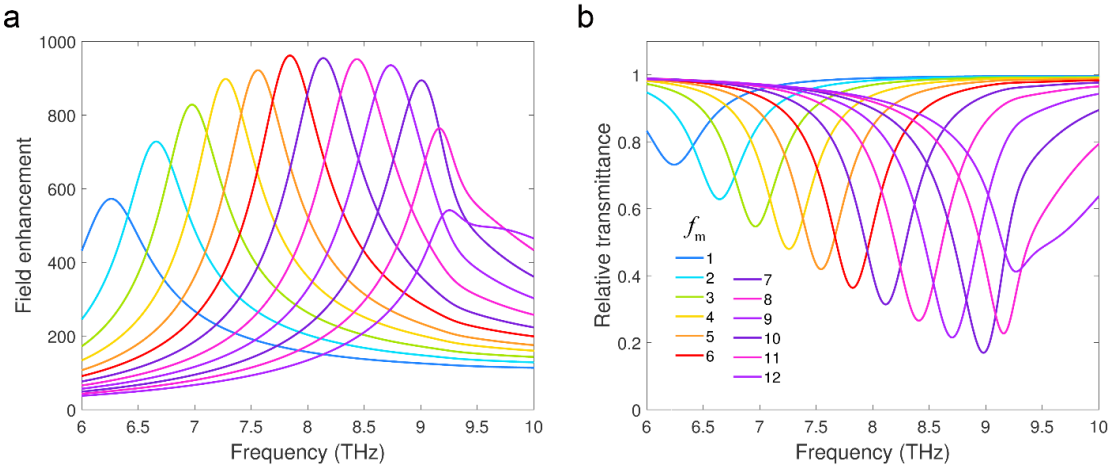

Figure 5.5 **(a) Field enhancement at the center of the nanogap of the moon-shaped nanoantennas, for moon factor values f_m varying from 1 to 12 and for a fixed nanoantenna length L = 8 μm. (b) The corresponding relative transmittance.**

5.1.3 Extracting the THz Response of a Monolayer of CdS Nanocrystals

The new batch of CdS nanocrystals (once again, with an average size of 10 nm) was independently investigated, to look for any deviation in their THz response compared to the ones characterized in Chapter 4. In this regard, THz measurements on a monolayer of CdS nanocrystals placed on top of a silicon substrate were conducted at the SISSI beamline in Trieste in Trieste (Italy), using the THz microscope described above. Three data sets for the monolayer relative transmittance are shown in Figure 5.6 (colored circles). Using a COMSOL simulation model incorporating the Maxwell-Garnett mixing formula, we then reproduced this response to extract the filling factor. As shown in Figure 5.6, such model (red curve) fits well the measured data when the filling factor f is set as 0.81 (in reasonable agreement with what obtained in our previous investigation). This value will be thus used in the rest of this Chapter. The FR optical phonon position corresponding to this filling factor is 7.73 THz. The linewidth (i.e., the FWHM) of the monolayer is about 0.45 THz.

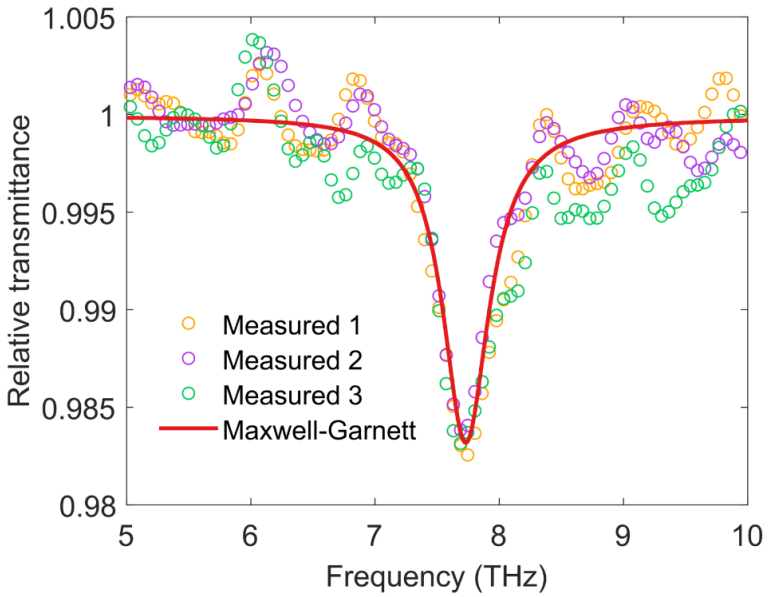

Figure 5.6 **Measured (open circles) and simulated (red line, for a filling factor of 0.81) transmittance of a monolayer of the new batch of CdS nanocrystals over a silicon substrate.**

5.1.4 Moon-shaped Nanoantenna Array Response with and without CdS Nanocrystals

The simulated transmission spectra of the bare nanoantenna arrays for *L* spanning from 7 to 9 μm, as well as of such arrays covered with 1, 2, and 3 CdS nanocrystal layers are plotted in Figure 5.7a, b, c, and d, respectively. From Figure 5.7a, as mentioned in the geometrical tuning subsection above, we can clearly observe that the resonance linewidth (FWHM) of the bare moon-

shaped antennas is much narrower than the one of the end-to-end nanoantennas in Chapter 4 (~2.3 THz). Such linewidth is indeed about 0.5 THz, now being thus comparable to the FR phonon linewidth of CdS nanocrystals. This contributed to the fact that, when the arrays are covered with CdS nanocrystals, the resonance splitting becomes more evident than in the case of the end-to-end antenna arrays, especially for the monolayer case. The corresponding field enhancement and extinction cross-section of the bare moon-shaped antennas are shown in Figure 5.8, respectively, for the different nanoantenna lengths. These results show that, with the selected moon factor, we can achieve a uniform field enhancement value of about 1000 in the nanocavities and also maintain a similar level for the far-field extinction in the considered range of nanoantenna lengths.

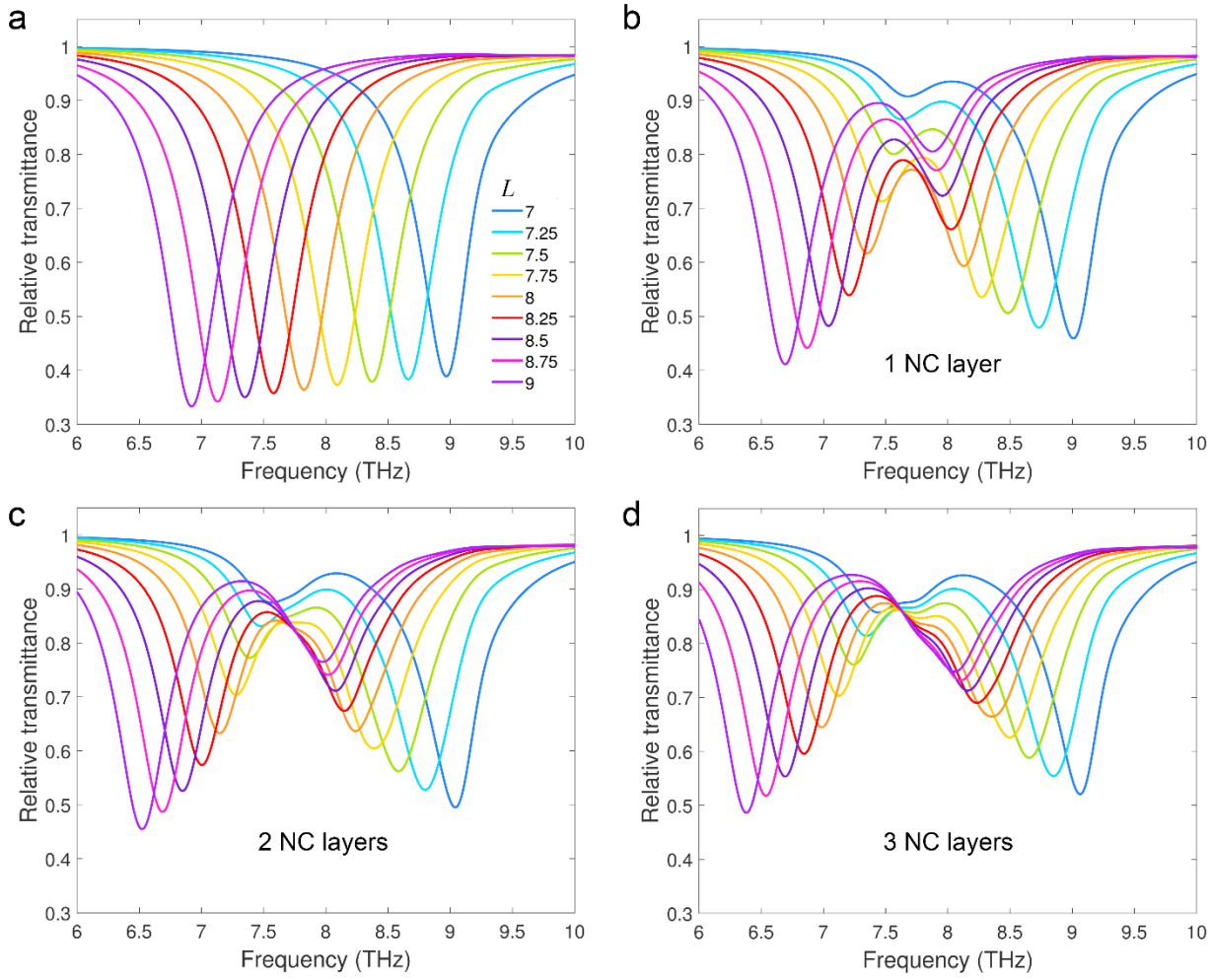

Figure 5.7 **Simulated transmission spectra for bare moon-shaped nanoantenna arrays (a), and arrays covered with 1 (b), 2 (c), and 3 (d) CdS nanocrystal layers. The antenna lengths are from 7 to 9 μm.**

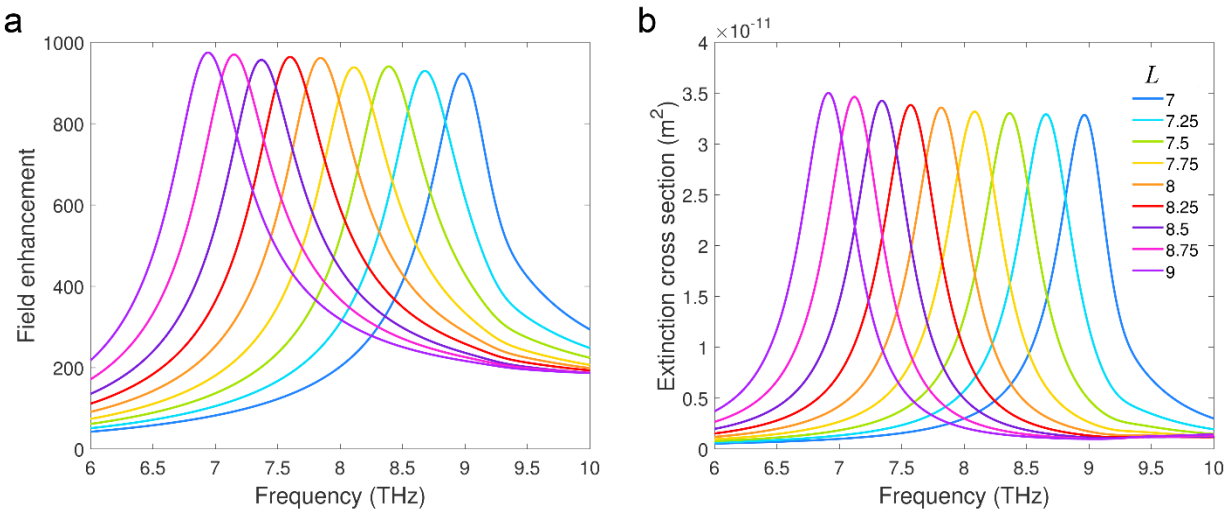

Figure 5.8 **(a) Field enhancement for the nanoantenna lengths considered in the previous figure. The values are estimated in the center of the nanocavity (b) Corresponding extinction cross-section.**

5.1.5 THz Absorption of CdS Nanocrystals in the Gap of a Moon-Shaped Nanoantenna

In our simulations, it is possible to extract the absorption at the nanocrystal monolayer center in the nanogaps. For comparison, I first checked the absorption at the center of a CdS nanocrystal monolayer (the monolayer is placed on top of a silicon substrate without moon-shaped nanoantennas) as shown in Figure 5.9a. The absorption point probe at the bare monolayer center shows an absorption peak corresponding to the FR optical phonon mode (~7.73 THz). In contrast, the local absorption rate of the monolayer in the center of a moon antenna nanocavity can reach a maximum value 120,000 times greater than the one without nanocavity (see the orange line in Figure 5.9b, for L = 8 μm, i.e., the non-detuning case). In addition, instead of a single peak, the nanocrystal monolayer in the plasmonic nanocavity starts to show two absorption peaks due to the arising of the FR resonance hybridization. Adding more layers in the nanocavity, e.g., two (Figure 5.9c) or three layers (Figure 5.9d), lead to a more pronounced splitting. In Figure 5.10, I also present the 2D map of the THz absorption at the center point of the nanocrystal layers for the 2 layer case. As can be clearly seen, a polariton anti-crossing behavior is evident also for this local absorption map.

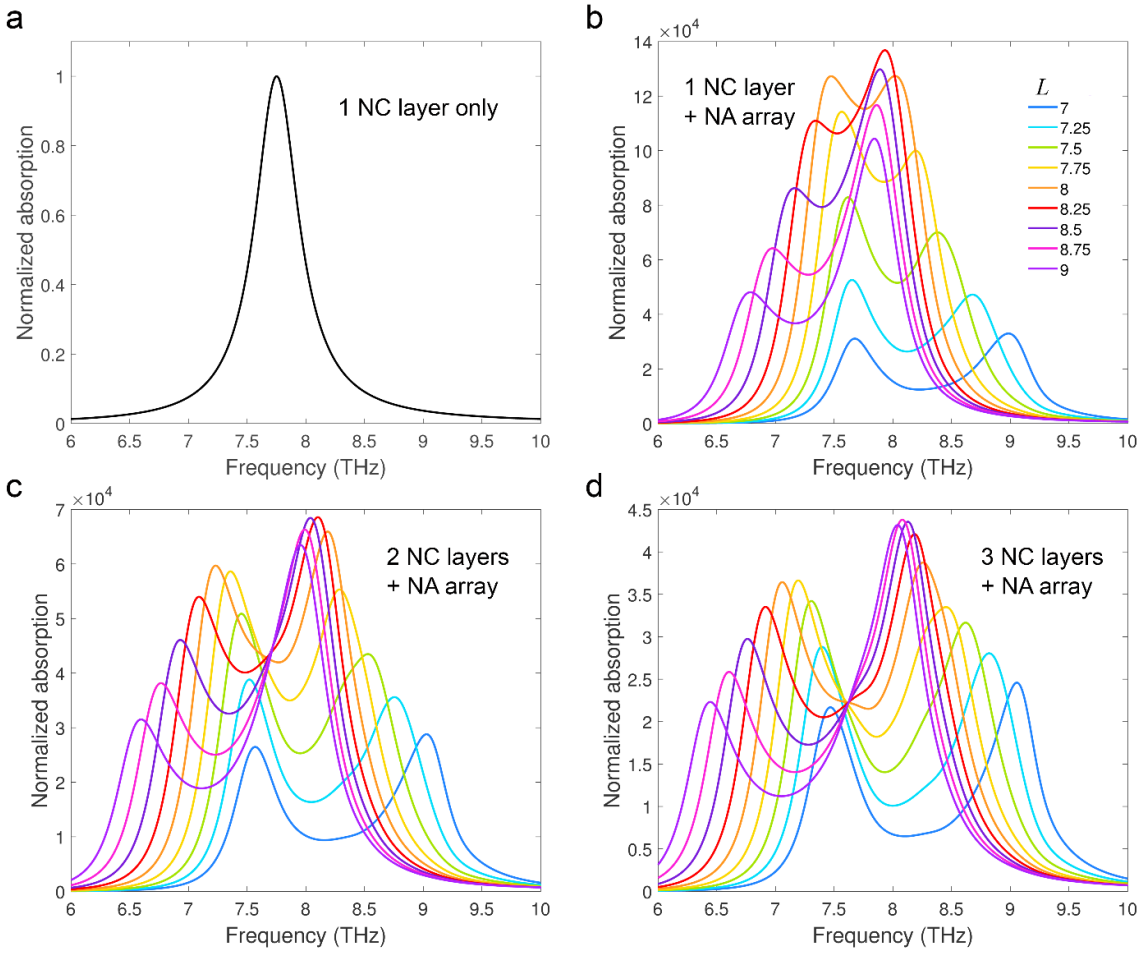

Figure 5.9 **Simulated absorption rate at the layer center point. A bare CdS nanocrystal monolayer on top of a silicon substrate (a); 1 (b), 2 (c), and 3 (d) CdS nanocrystal layers covering moon-shaped nanoantenna array. For (b), (c), and (d), the point probes are placed at the nanocavity centers. The antenna lengths vary from 7 to 9 μm. All the absorption spectra are normalized by the maximum value of the bare monolayer case.**

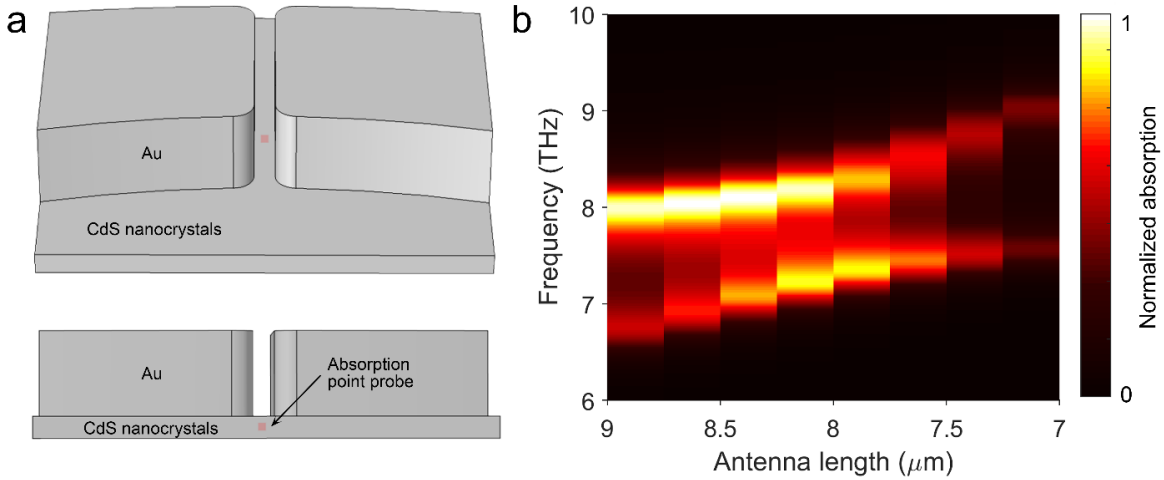

Figure 5.10 **Absorption splitting at the center point of the nanocavity within the CdS nanocrystal layers. (a) The sketch indicating the location of the point probe. (b) The point absorption 2D map as a function of antenna length and frequency. The values were extracted from the simulation model of nanoantenna arrays covered with 2 layers of CdS nanocrystals.**

5.1.6 Estimation of the Mode Volume and THz Vacuum Electric Field for Nanocavities of Moon-Shaped Nanoantennas

As seen above, moon-shaped nanoantenna arrays show very pronounced resonance splittings when covered with CdS nanocrystals. Here, as presented in the previous chapters, we quantitively estimate the vacuum electric field (directly connected with the coupling strength of the interaction) by calculating the resonator mode volume. In the case of antenna length equal to 8 µm (featuring a resonance at around 7.8 THz), the corresponding field enhancement distribution is shown in Figure 5.11. Using Equation (3.44), we obtain a mode volume V_{mod} = 2.16 × 10^5 nm^3. The geometrical volume of the nanocavity is in this case V_{geo} ≈ 200 × 20 × 100 nm^3 = 4 × 10^5 nm^3. Thus the volume ratio ($R_{\mathrm{vol}} = V_{\mathrm{mod}} / V_{\mathrm{geo}}$ = 0.54) is in this case smaller than 1. This means that the moon structure can squeeze the radiation into a volume that is even smaller than its nanogap. Compared to the end-to-end nanoantennas (featuring a volume ratio of ~4.3, see Subsection 4.1.6), the moon-shaped structure thus shows a more efficient radiation localization.

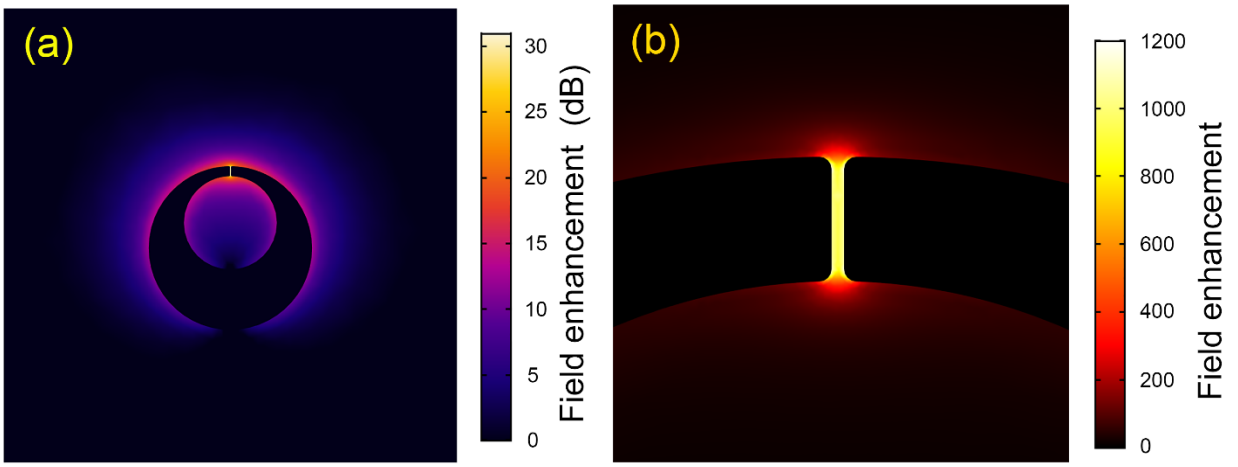

Figure 5.11 **Electric field enhancement distribution of a bare nanoantenna array with L = 8 µm, f_m = 6. (a) The field enhancement at resonance (~7.8 THz) shown in dB (10*log$_{10}$(E/E$_0$), E: full field; E$_0$: background field). (b) same as in (a) but in linear scale (magnified map of the nanocavity region).**

By plotting the volume ratio as a function of frequency, as shown in Figure 5.12a, we can confirm that the parameter combination of L = 8 µm and f_{m} = 6 offers the minimum mode volume (i.e., the best confinement) among the tested geometries. By fixing the moon factor at 6 (Figure 5.12b), and sweeping the resonance frequencies by tuning the antenna lengths, we can still maintain extremely low mode volume values.

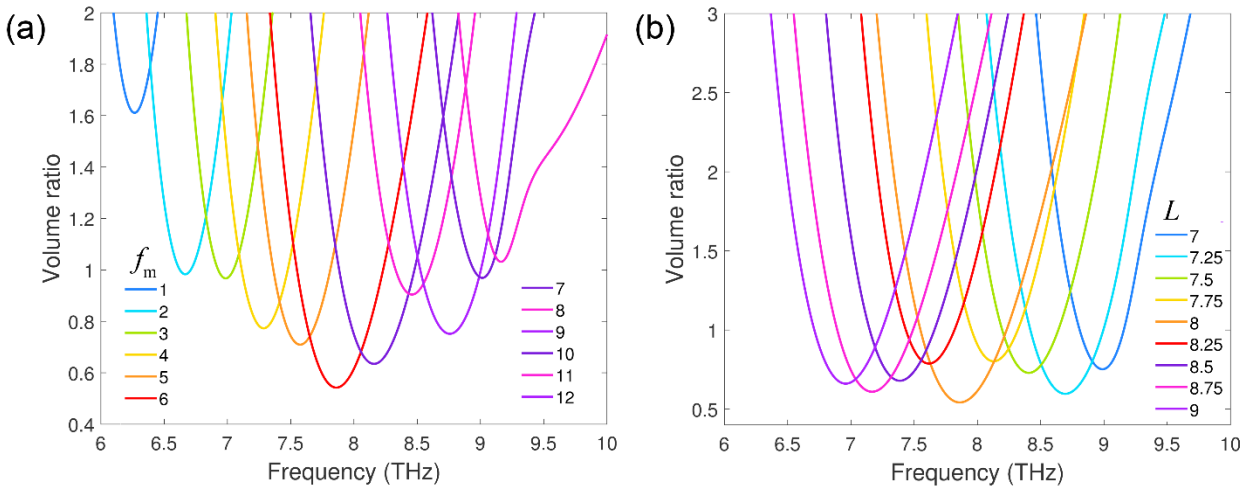

Figure 5.12 **Volume ratio of the moon-shaped nanoantenna arrays for (a) fixed antenna length L = 8 µm and moon factors from 1 to 12, and for (b) fixed moon factor f_m = 6, and antenna lengths from 7 to 9 µm.**

Using the calculated mode volume, we can now evaluate the THz vacuum electric field within the cavity at resonance, using Equation (1.1). We find $|E_{vac}| = 1.17 \times 10^6$ V·m^{-1} in air, which is more than two times higher than the one estimated in Chapter 4 for the end-to-end nanoantennas.

5.1.7 Lattice Modes for the Moon-Shaped Nanoantenna Arrays

The illumination condition in this study is the same as the one described in Chapter 4, i.e., the illuminating light has an incident polar angle of 18° and an azimuthal angle of 45°. The lattice spacing is set, as mentioned above, as g_x = g_y = 9 µm for all the arrays. Therefore, by using the same considerations presented in Subsection 4.1.7, we locate the first two lattice modes in frequency at 9.17 THz and 10.43 THz. Consequently, the resonance of our moon-shaped nanoantennas, when tuned across the phonon mode of the nanocrystals, is not significantly perturbed by the presence of these lattice modes.

5.1.8 Comparison between Simulation and Dissipated Power Calculation

Since the first lattice mode is at 9.17 THz, sufficiently far away from the FR mode of the nanocrystals at 7.73 THz, and considering the narrow resonance linewidth of the moon-shaped nanoantennas, we can neglect the influence of the lattice mode when we consider the case of array resonance aligned to the FR frequency. Therefore, the extinction spectrum of this moon-shaped nanoantenna array covered by a layer (or layers) of CdS nanocrystals can be described by the two-coupled-oscillator model (see Subsection 2.1.3). As shown in Figure 5.13 for the case

of a monolayer, the dissipated power model reproduces with remarkable accuracy the hybridization described by the numerical simulations.

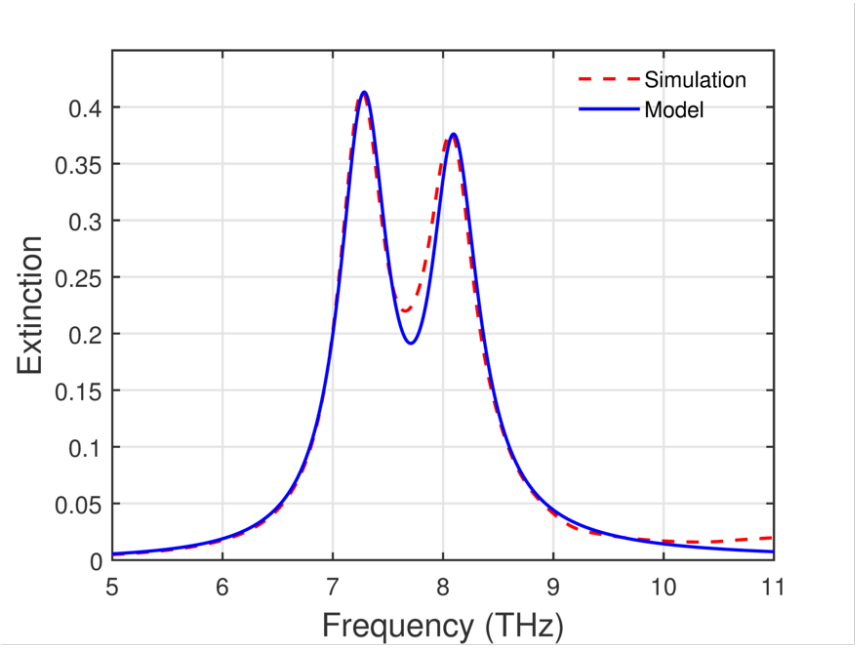

Fitting parameters

ω_1	ω_2	γ_1	γ_2	g	F
7.67	7.73	0.60	0.45	2.48	0.88

Figure 5.13 **Extinction spectrum comparison between simulation and dissipated power model. All the fitting parameters are in units of THz, except "*F* " that has no units. The simulated extinction is extracted from a nanoantenna array (L = 8 μm) covered with a monolayer of CdS nanocrystals.**

5.2 Fabrication and THz Characterization

The procedure for preparing the THz moon-shaped nanoantenna arrays and the CdS nanocrystal layers are the same as the ones described in Chapter 4. Also for this project, fabrication and Raman measurements were performed at IIT, while the THz characterization was done at the Synchrotron Radiation Source in Trieste.

An example of the fabricated arrays can be visualized in the SEM picture reported in Figure 5.14a. The overall array area is about 225 μm × 225 μm, and contains 625 (25 × 25) moons. From the magnified image of a nanogap region (Figure 5.14b), we can notice that the gap width of the fabricated structures is consistent with the design parameter of 20 nm.

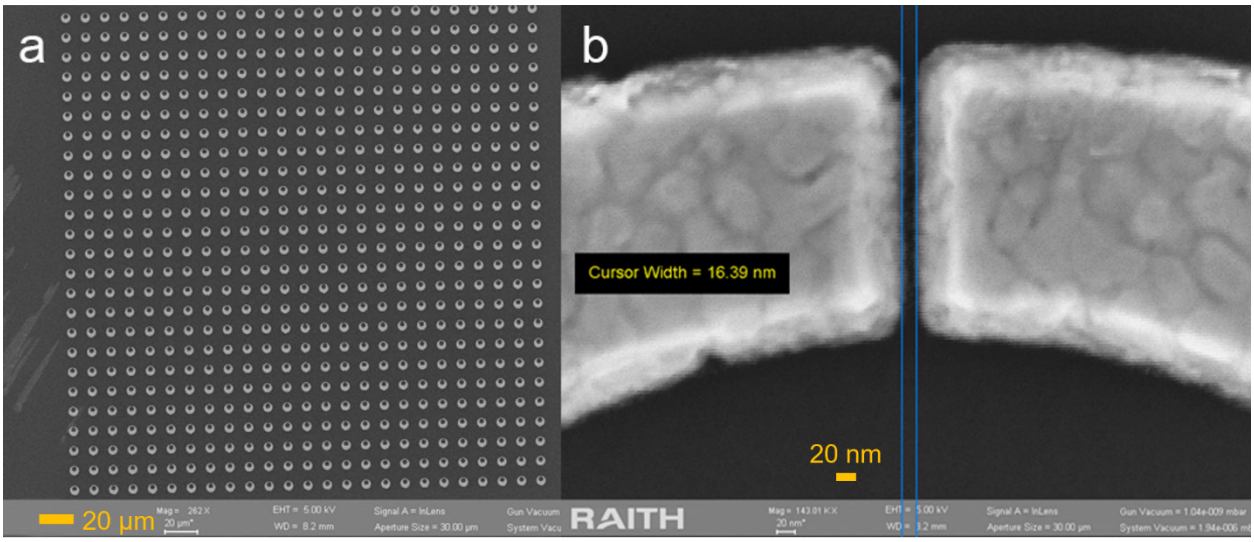

Figure 5.14 **(a) An SEM picture of a fabricated moon-shaped nanoantenna array. (b) A zoomed-in SEM image of a nanogap.**

We also used the spin-coating method to cover with a monolayer/multilayers of CdS nanocrystals the moon-shaped nanoantennas. An SEM picture of a CdS-nanocrystal-covered moon-shaped nanoantenna can be seen in Figure 5.15a. The zoomed-in image of a covered nanocavity is also presented in Figure 5.15b, showing tens of CdS nanocrystals within the nanocavity.

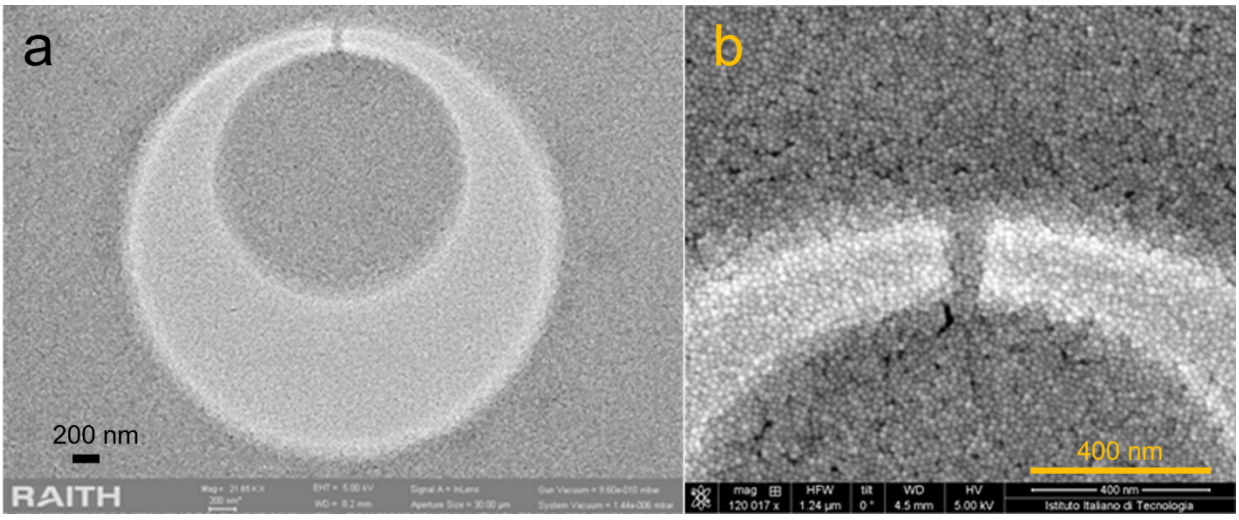

Figure 5.15 **(a) An SEM picture of a CdS-nanocrystal-covered (1.5 layer) moon-shaped nanoantenna. (b) The zoomed-in SEM image of (a).**

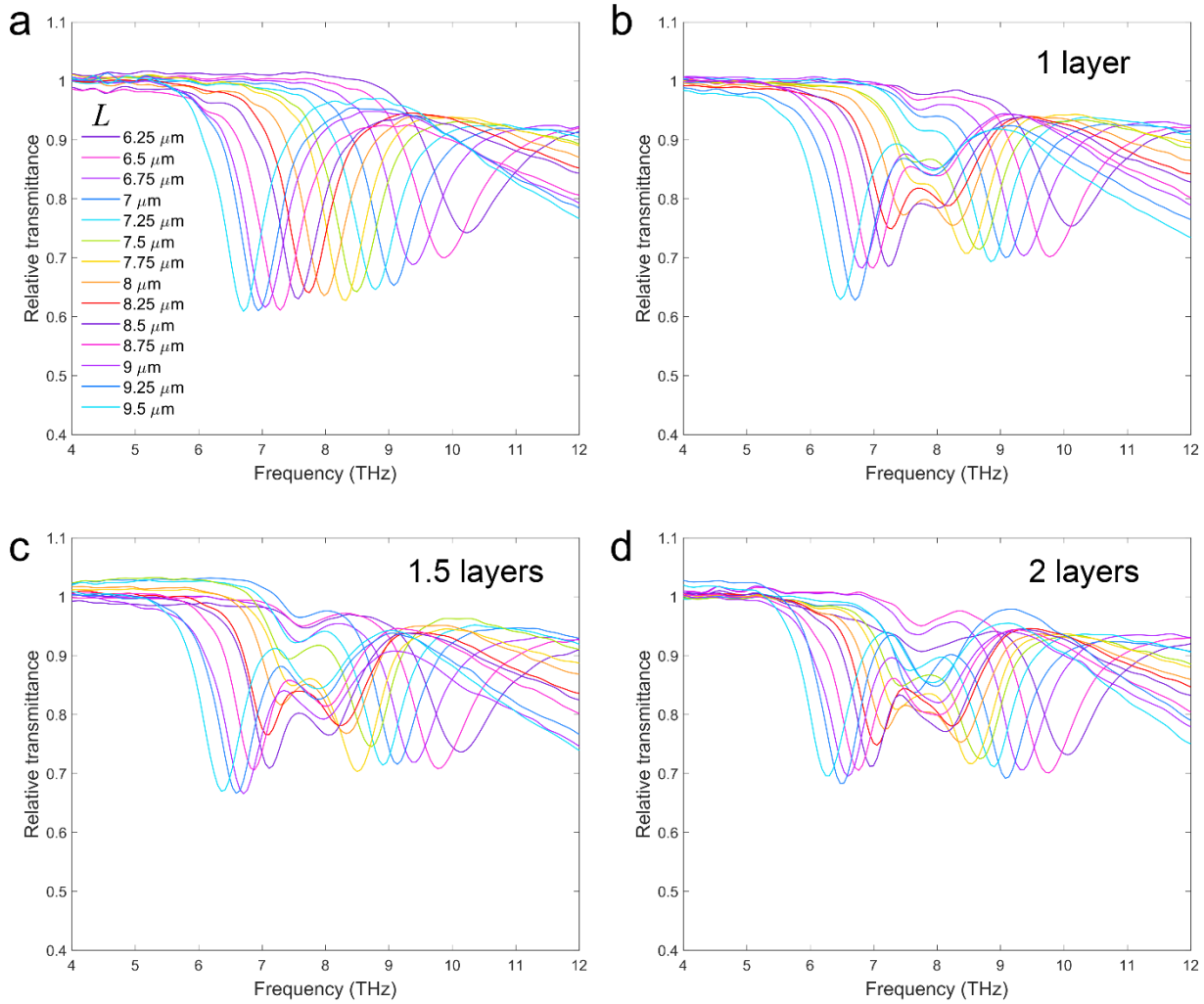

Figure 5.16 **Measured transmission spectra for bare arrays (a), and arrays covered with 1 (b), 1.5 (c), and 2 (d) CdS nanocrystal layers. The antenna lengths are from 6.25 to 9.5 μm. To avoid complete re-dissolution of the already deposited nanocrystals, in the 2 layers case (d), 1-nm alumina separator was disposed on top of the first layer.**

THz transmission spectra were again collected using a Cassegrain objective (15×, mean incidence angle: 18°) and are shown in Figure 5.16. We can see that they are in good agreement with the simulated transmission spectra presented in Figure 5.7. Since the simulated spectra shown in Figure 5.7 are not corrected by considering the spot size in this case, the minimum transmittance values in the simulations curves are overall lower than the experimental ones. Nevertheless, the hybridized peaks location and separation in the experiments match well with the simulation results.

5.3 Discussion

The measured extinction 2D map of the bare moon-shaped nanoantenna arrays (as a function of frequency and antenna length) is illustrated in Figure 5.17a. By covering the bare array with one or multiple layers of CdS nanocrystals, we can observe the formation and increase of the Rabi splitting (Figure 5.17b, c, and d). It is worth to mention that the nanogap area in a moon-shaped nanoantenna is 20×200 nm^2, which is 2/3 of the one previously employed in the end-to-end nanoantenna chain structure (30×200 nm^2). This means that the number of nanocrystals within a nanocavity is in general smaller in the moon array case for the same number of layers. Notwithstanding this, the Rabi splittings obtained with the moon structure are overall larger than the ones measured for the end-to-end structure (see estimates in the legend of Figure 5.17), as a result of an improved coupling. Such pronounced Rabi splitting has also been recently confirmed by micro-Raman measurements (see an example for the 2 layers case in Figure 5.18), which were performed on the moon-shaped structures following the same procedure described in Section 4.4. In this case, the Raman signal enhancement for the vibro-polariton peaks also seems more significant than the one observed previously on the end-to-end antenna arrays.

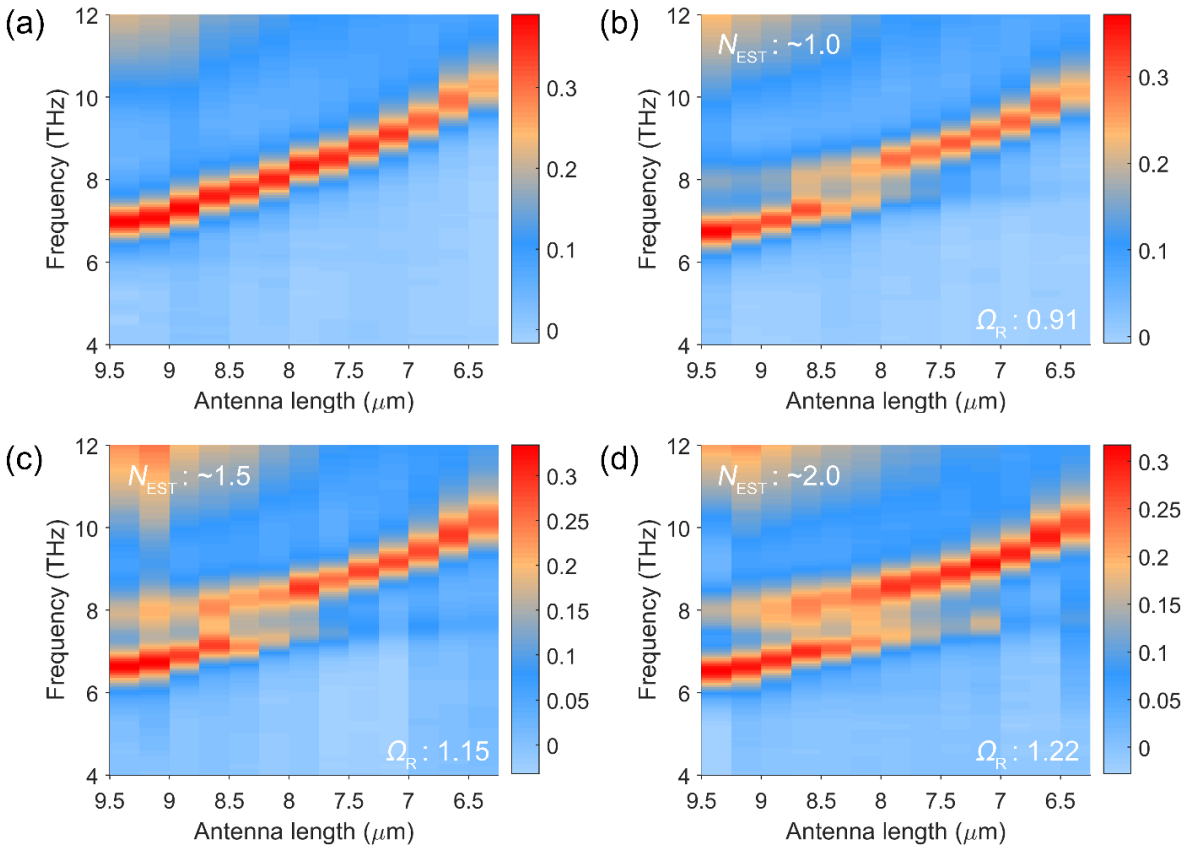

Figure 5.17 **Measured extinction 2D maps of bare moon-shaped nanoantenna arrays (a), and the same arrays covered with 1 (b), 1.5 (c), and 2 layers of CdS nanocrystals.**

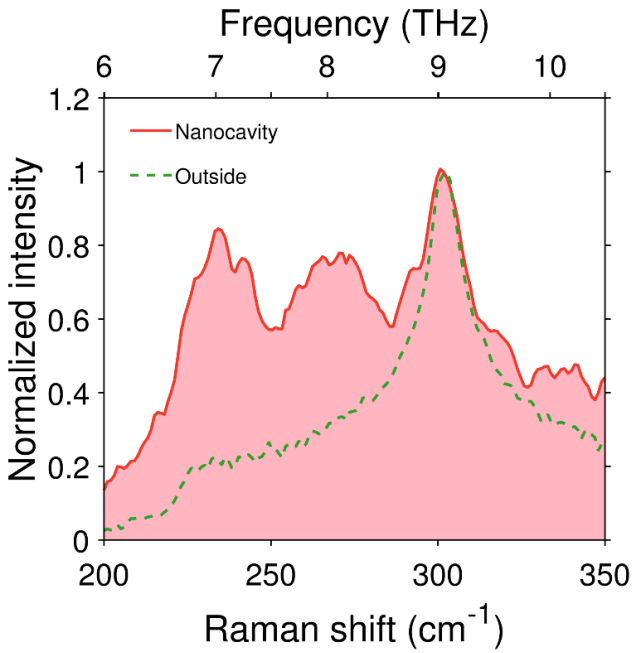

Figure 5.18 **Raman spectrum for a moon-shaped nanoantenna with *L* = 8 μm and covered by 2 layers of CdS nanocrystals. The solid line indicates the spectrum taken in a nanocavity region, and the dashed line corresponds to the spectrum taken just outside the same nanocavity.**

To conclude, we want to mention that, by adding more nanocrystals in a moon-shaped nanocavity (> 3 layers), our system can enter the so-called ultrastrong coupling regime [4], i.e., the coupling strength greater than 0.1 of the uncoupled central frequency, in which the coupling strength is a sizable fraction (typically large than 10%) of the natural frequencies of the noninteracting oscillators. Such exotic regime is promising for investigating a myriad of applications, e.g., in nonlinear optics, quantum optomechanics, quantum plasmonics, and quantum vacuum emission [4]. The moon-shaped nanoantennas that I have designed and validated in this chapter can thus be a perfect candidate platform to explore these extremely intriguing research fields.

6 Conclusion and Future Works

The main focus of this Ph.D. thesis has been to investigate THz light-nanomatter interaction under strong coupling conditions. This has been achieved in a test-bed system by employing resonant THz plasmonic nanostructures coupled to a dipole-active phonon mode of polar nanocrystals. In particular, I have contributed to conceiving two plasmonic nanocavity platforms to modify the FR optical phonon response of CdS nanocrystals: i) end-to-end nanoantenna chain arrays; ii) moon-shaped nanoantenna arrays. At first, I tested and verified the effectiveness of these two platforms by means of numerical simulations. Fabrication and THz/Raman characterizations have then been conducted at the Italian Institute of Technology (IIT, Italy) and at Elettra Synchrotron facility in Trieste (Italy). Finally, I carried out data analysis and post-processing, as well as theoretical modeling for a proper description of our experimental observations. More specifically, the key steps of my thesis work are listed as follows:

1. I have contributed to identifying, via a comprehensive literature study, a test-bed system to achieve nanoscale plasmon-phonon hybridization in the THz region. As mentioned above, this system exploits a surface phonon mode (FR optical phonon mode) of CdS nanocrystals and THz nanoantenna cavities. The latter ones (nanocavities) are indeed crucial for nano-vibrational strong coupling because they represent an effective way to confine the long-wavelength THz radiation effectively within tiny volumes. In turns, this guarantees extremely high values for the cavity vacuum electric field. In this regard, I have carefully developed tools and methods to optimize the geometry of the nanoantenna resonators in order to reduce their characteristic mode volume. I have also accurately implemented two-/three-coupled-oscillator models to fit the dispersion of the polariton branches obtained from the experimental extinction spectra, thus leading to an in-depth insight into the underlying physical mechanism.

2. In order to numerically simulate the investigated system, I have described the optical properties of the materials involved as follows: the permittivity of gold in the THz range was set using a standard Drude model and parameters retrieved from the literature, while the permittivity of the CdS nanocrystals was directly extracted by proper fitting of THz transmission measurements on a thick nanocrystal layer. To overcome the need of numerically simulating the individual nanocrystals within the layers, I used the Lorentz model in the reststrahlen region for CdS combined with the Maxwell-Garnett mixing rule. In this way, the finite-element-method based numerical simulations converged to a solution much faster, yet showing a very good agreement with the experimental results.

3. Following the definition of the permittivities, I have designed infinite gold nanoantenna-chain arrays by deploying the Floquet periodic boundary conditions. The incident THz wave in the semi-infinite air domain can impinge on the gold nanoantenna array from the top and its transmission is then evaluated through the semi-infinite silicon substrate below. Finally, the nanoantenna arrays were covered with a 10-nm-thick CdS nanocrystal layer and the transmission spectra were recorded for different nanoantenna lengths so that the plasmonic resonance was spanning across the CdS phonon resonance. The anti-crossing behavior typical of the strong coupling regime was clearly observed.

4. The designed samples were fabricated at the Italian Institute of Technology (IIT), Italy (our international collaborator). Their transmission characterization was performed at the Elettra facility in Trieste (Italy) by means of THz synchrotron radiation. The experimental results showed an excellent agreement with the numerical simulations.

5. The same samples were investigated through micro-Raman spectroscopy. Remarkably, we observed the strong coupling signature (Rabi splitting) even in the Raman spectra, thus further proving the nature of the coupling process. Indeed, in true strong coupling conditions, the hybridization also occurs without the need of any THz illumination, with the two oscillations that are coupled strongly just by means of the cavity vacuum electric field.

6. We also found that the Raman signature of the hybridized phonon resonance within the cavity is enhanced by about two orders of magnitude. Compared to conventional SERS, this polariton-induced enhancement affects only the hybridized transition and leaves the rest of the Raman spectrum unaltered.

7. Inspired by a recent investigation of our group regarding nanoantenna tapering to relax the ohmic loss of plasmonic nanoresonators, I have designed a moon-shaped nanoantenna structure. This new design can further reduce the mode volume (well below the geometrical cavity volume) and increase the local THz field enhancement. Such moon-shaped nanoantennas have been fabricated and characterized, in a manner similar to the previous end-to-end nanoantenna design. Both with and without direct THz illumination, we found that this new geometry gives larger Rabi splittings, even if the nanocavities are narrower and thus the number of nanocrystals involved in the interaction is lower than in the end-to-end nanoantenna chain case.

On the one hand, the findings presented in this thesis could open novel avenues for engineering the phonon response of functional nanomaterials, in order to improve their light-emission or charge transport properties, due to the decisive role played by electron-phonon

interactions in such systems [30, 60, 118, 119]. On the other hand, nanoscale plasmon–phonon strong coupling can offer an innovative platform for THz technology, for example, for the exploration of enhanced and localized nonlinear phenomena [120-122], as well as for the generation of coherent radiation [123-127]. The concepts and discoveries of this work can be transferred to a wide variety of platforms. For instance, a future direction that we are planning to investigate relates with the realization of a plasmon-phonon strong coupling system using 2D materials, such as transition metal dichalcogenides (TMDs) [128-131], in view of improving the optical/electrical response of TMDs via surface phonon hybridization, which could be of relevance for next-generation nano- and opto-electronics. Plasmon-phonon strong coupling may also help to design novel “topological states” [132-135]. Nanoscale vibrational strong coupling thus promises to be a valuable tool for the realization of a large variety of novel photonic/phononic nanodevices with distinctive properties.

BIBLIOGRAPHY

[1] P. Törmä, and W. L. Barnes, "Strong Coupling between Surface Plasmon Polaritons and Emitters: A Review," *Reports on Progress in Physics* **78**, 013901 (2015).

[2] M. Aspelmeyer, T. J. Kippenberg, and F. Marquardt, "Cavity Optomechanics," *Reviews of Modern Physics* **86**, 1391 (2014).

[3] H. Deng, H. Haug, and Y. Yamamoto, "Exciton-Polariton Bose-Einstein Condensation," *Reviews of Modern Physics* **82**, 1489 (2010).

[4] A. F. Kockum, A. Miranowicz, S. De Liberato, S. Savasta, and F. Nori, "Ultrastrong Coupling between Light and Matter," *Nature Reviews Physics* **1**, 19 (2019).

[5] A. Toma, S. Tuccio, M. Prato, F. De Donato, A. Perucchi, P. Di Pietro, S. Marras, C. Liberale, R. Proietti Zaccaria, and F. De Angelis, "Squeezing Terahertz Light into Nanovolumes: Nanoantenna Enhanced Terahertz Spectroscopy (NETS) of Semiconductor Quantum Dots," *Nano Letters* **15**, 386-391 (2014).

[6] F. P. Laussy, E. Del Valle, and C. Tejedor, "Luminescence Spectra of Quantum Dots in Microcavities. I. Bosons," *Physical Review B* **79**, 235325 (2009).

[7] E. Del Valle, F. P. Laussy, and C. Tejedor, "Luminescence Spectra of Quantum Dots in Microcavities. II. Fermions," *Physical Review B* **79**, 235326 (2009).

[8] S. Savasta, R. Saija, A. Ridolfo, O. Di Stefano, P. Denti, and F. Borghese, "Nanopolaritons: Vacuum Rabi Splitting with a Single Quantum Dot in the Center of a Dimer Nanoantenna," *ACS Nano* **4**, 6369-6376 (2010).

[9] E. M. Purcell, "Spontaneous Emission Probabilities at Radio Frequencies," *Physical Review* **69**, 681 (1946).

[10] A. F. Koenderink, "On the Use of Purcell Factors for Plasmon Antennas," *Optics Letters* **35**, 4208-4210 (2010).

[11] Y. Kaluzny, P. Goy, M. Gross, J. Raimond, and S. Haroche, "Observation of Self-Induced Rabi Oscillations in Two-Level Atoms Excited inside a Resonant Cavity: The Ringing Regime of Superradiance," *Physical Review Letters* **51**, 1175 (1983).

[12] A. Thomas, J. George, A. Shalabney, M. Dryzhakov, S. J. Varma, J. Moran, T. Chervy, X. Zhong, E. Devaux, and C. Genet, "Ground-State Chemical Reactivity under Vibrational Coupling to the Vacuum Electromagnetic Field," *Angewandte Chemie* **128**, 11634-11638 (2016).

[13] A. Shalabney, J. George, J. Hutchison, G. Pupillo, C. Genet, and T. W. Ebbesen, "Coherent Coupling of Molecular Resonators with a Microcavity Mode," *Nature Communications* **6** (2015).

[14] J. Reithmaier, G. Sęk, A. Löffler, C. Hofmann, S. Kuhn, S. Reitzenstein, L. Keldysh, V. Kulakovskii, T. Reinecke, and A. Forchel, "Strong Coupling in a Single Quantum Dot–Semiconductor Microcavity System," *Nature* **432**, 197-200 (2004).

[15] T. Yoshie, A. Scherer, J. Hendrickson, G. Khitrova, H. Gibbs, G. Rupper, C. Ell, O. Shchekin, and D. Deppe, "Vacuum Rabi Splitting with a Single Quantum Dot in a Photonic Crystal Nanocavity," *Nature* **432**, 200 (2004).

[16] C. Junge, D. O'Shea, J. Volz, and A. Rauschenbeutel, "Strong Coupling between Single Atoms and Nontransversal Photons," *Physical Review Letters* **110**, 213604 (2013).

[17] J. del Pino, J. Feist, and F. J. Garcia-Vidal, "Quantum Theory of Collective Strong Coupling of Molecular Vibrations with a Microcavity Mode," *New Journal of Physics* **17**, 053040 (2015).

[18] J. del Pino, J. Feist, and F. J. Garcia-Vidal, "Signatures of Vibrational Strong Coupling in Raman Scattering," *The Journal of Physical Chemistry C* **119**, 29132-29137 (2015).

[19] A. Strashko, and J. Keeling, "Raman Scattering with Strongly Coupled Vibron-Polaritons," *Physical Review A* **94**, 023843 (2016).

[20] J. Kasprzak, M. Richard, S. Kundermann, A. Baas, P. Jeambrun, J. Keeling, F. Marchetti, M. Szymańska, R. Andre, and J. Staehli, "Bose–Einstein Condensation of Exciton Polaritons," *Nature* **443**, 409-414 (2006).

[21] J. A. Hutchison, T. Schwartz, C. Genet, E. Devaux, and T. W. Ebbesen, "Modifying Chemical Landscapes by Coupling to Vacuum Fields," *Angewandte Chemie International Edition* **51**, 1592-1596 (2012).

[22] A. Thomas, L. Lethuillier-Karl, K. Nagarajan, R. M. Vergauwe, J. George, T. Chervy, A. Shalabney, E. Devaux, C. Genet, and J. Moran, "Tilting a Ground-State Reactivity Landscape by Vibrational Strong Coupling," *Science* **363**, 615-619 (2019).

[23] M. G. Panthani, and B. A. Korgel, "Nanocrystals for Electronics," *Annual Review of Chemical and Biomolecular Engineering* **3**, 287-311 (2012).

[24] A. Beveratos, R. Brouri, T. Gacoin, J.-P. Poizat, and P. Grangier, "Nonclassical Radiation from Diamond Nanocrystals," *Physical Review A* **64**, 061802 (2001).

[25] Y.-S. Park, A. K. Cook, and H. Wang, "Cavity QED with Diamond Nanocrystals and Silica Microspheres," *Nano Letters* **6**, 2075-2079 (2006).

[26] N. Le Thomas, U. Woggon, O. Schöps, M. Artemyev, M. Kazes, and U. Banin, "Cavity QED with Semiconductor Nanocrystals," *Nano Letters* **6**, 557-561 (2006).

[27] J.-M. Raimond, M. Brune, and S. Haroche, "Manipulating Quantum Entanglement with Atoms and Photons in a Cavity," *Reviews of Modern Physics* **73**, 565 (2001).

[28] K. Hennessy, A. Badolato, M. Winger, D. Gerace, M. Atatüre, S. Gulde, S. Fält, E. L. Hu, and A. Imamoğlu, "Quantum Nature of a Strongly Coupled Single Quantum Dot – Cavity System," *Nature* **445**, 896 (2007).

[29] M. Razeghi, *Fundamentals of Solid State Engineering* (Springer, 2006).

[30] T. Chervy, A. Thomas, E. Akiki, R. M. Vergauwe, A. Shalabney, J. George, E. Devaux, J. A. Hutchison, C. Genet, and T. W. Ebbesen, "Vibro-Polaritonic IR Emission in the Strong Coupling Regime," *ACS Photonics* **5**, 217-224 (2017).

[31] D. V. Talapin, J.-S. Lee, M. V. Kovalenko, and E. V. Shevchenko, "Prospects of Colloidal Nanocrystals for Electronic and Optoelectronic Applications," *Chemical Reviews* **110**, 389-458 (2009).

[32] G. Irmer, J. Monecke, and P. Verma, "Light Scattering of Semiconducting Nanoparticles," in *Encyclopedia of Nanoscience and Nanotechnology*(American Scientific Publishers Valencia, California, 2004), pp. 561-586.

[33] D. J. Shelton, I. Brener, J. C. Ginn, M. B. Sinclair, D. W. Peters, K. R. Coffey, and G. D. Boreman, "Strong Coupling between Nanoscale Metamaterials and Phonons," *Nano Letters* **11**, 2104-2108 (2011).

[34] R. Marty, A. Mlayah, A. Arbouet, C. Girard, and S. Tripathy, "Plasphonics: Local Hybridization of Plasmons and Phonons," *Optics Express* **21**, 4551-4559 (2013).

[35] I. J. Luxmoore, C. H. Gan, P. Q. Liu, F. Valmorra, P. Li, J. r. m. Faist, and G. R. Nash, "Strong Coupling in the Far-Infrared between Graphene Plasmons and the Surface Optical Phonons of Silicon Dioxide," *ACS Photonics* **1**, 1151-1155 (2014).

[36] Y. Jia, H. Zhao, Q. Guo, X. Wang, H. Wang, and F. Xia, "Tunable Plasmon–Phonon Polaritons in Layered Graphene–Hexagonal Boron Nitride Heterostructures," *ACS Photonics* **2**, 907-912 (2015).

[37] S. Tuccio, L. Razzari, A. Alabastri, A. Toma, C. Liberale, F. De Angelis, P. Candeloro, G. Das, A. Giugni, and E. Di Fabrizio, "Direct Determination of the Resonance Properties of Metallic Conical Nanoantennas," *Optics Letters* **39**, 571-573 (2014).

[38] R. Piccoli, A. Rovere, A. Toma, R. Morandotti, and L. Razzari, "Terahertz Nanoantennas for Enhanced Spectroscopy," *Terahertz Spectroscopy: A Cutting Edge Technology*, 21 (2017).

[39] M. Fox, *Quantum Optics: an Introduction* (OUP Oxford, 2006).

[40] Z.-J. Yang, T. J. Antosiewicz, and T. Shegai, "Role of Material Loss and Mode Volume of Plasmonic Nanocavities for Strong Plasmon-Exciton Interactions," *Optics Express* **24**, 20373-20381 (2016).

[41] P. A. M. Dirac, "The Quantum Theory of the Emission and Absorption of Radiation," *Proceedings of the Royal Society of London. Series A, Containing Papers of a Mathematical and Physical Character* **114**, 243-265 (1927).

[42] E. Fermi, *Nuclear Physics: a Course Given by Enrico Fermi at the University of Chicago* (University of Chicago Press, 1950).

[43] E. T. Jaynes, and F. W. Cummings, "Comparison of Quantum and Semiclassical Radiation Theories with Application to the Beam Maser," *Proceedings of the IEEE* **51**, 89-109 (1963).

[44] W.-H. Chang, W.-Y. Chen, H.-S. Chang, T.-P. Hsieh, J.-I. Chyi, and T.-M. Hsu, "Efficient Single-Photon Sources based on Low-Density Quantum Dots in Photonic-Crystal Nanocavities," *Physical Review Letters* **96**, 117401 (2006).

[45] T. Niemczyk, F. Deppe, H. Huebl, E. Menzel, F. Hocke, M. Schwarz, J. Garcia-Ripoll, D. Zueco, T. Hümmer, and E. Solano, "Circuit Quantum Electrodynamics in the Ultrastrong-Coupling Regime," *Nature Physics* **6**, 772 (2010).

[46] A. Bayer, M. Pozimski, S. Schambeck, D. Schuh, R. Huber, D. Bougeard, and C. Lange, "Terahertz Light–Matter Interaction beyond Unity Coupling Strength," *Nano Letters* **17**, 6340-6344 (2017).

[47] D. Meschede, H. Walther, and G. Müller, "One-Atom Maser," *Physical Review Letters* **54**, 551 (1985).

[48] R. Thompson, G. Rempe, and H. Kimble, "Observation of Normal-Mode Splitting for an Atom in an Optical Cavity," *Physical Review Letters* **68**, 1132 (1992).

[49] R. S. Knox, "Theory of Excitons," *Solid State Phys.* **5** (1963).

[50] R. K. Willardson, and A. C. Beer, *Semiconductors and Semimetals* (Academic Press, 1977).

[51] C. Weisbuch, M. Nishioka, A. Ishikawa, and Y. Arakawa, "Observation of the Coupled Exciton-Photon Mode Splitting in a Semiconductor Quantum Microcavity," *Physical Review Letters* **69**, 3314 (1992).

[52] H. Deng, G. Weihs, D. Snoke, J. Bloch, and Y. Yamamoto, "Polariton Lasing vs. Photon Lasing in a Semiconductor Microcavity," *Proceedings of the National Academy of Sciences* **100**, 15318-15323 (2003).

[53] S. Azzini, D. Gerace, M. Galli, I. Sagnes, R. Braive, A. Lemaître, J. Bloch, and D. Bajoni, "Ultra-Low Threshold Polariton Lasing in Photonic Crystal Cavities," *Applied Physics Letters* **99**, 111106 (2011).

[54] M. Wei, S. K. Rajendran, H. Ohadi, L. Tropf, M. C. Gather, G. A. Turnbull, and I. D. Samuel, "Low-Threshold Polariton Lasing in a Highly Disordered Conjugated Polymer," *Optica* **6**, 1124-1129 (2019).

[55] S. K. Rajendran, M. Wei, H. Ohadi, A. Ruseckas, G. A. Turnbull, and I. D. Samuel, "Low Threshold Polariton Lasing from a Solution-Processed Organic Semiconductor in a Planar Microcavity," *Advanced Optical Materials*, 1801791 (2019).

[56] V. Giannini, A. I. Fernández-Domínguez, S. C. Heck, and S. A. Maier, "Plasmonic Nanoantennas: Fundamentals and their Use in Controlling the Radiative Properties of Nanoemitters," *Chemical Reviews* **111**, 3888-3912 (2011).

[57] L. Razzari, A. Toma, M. Clerici, M. Shalaby, G. Das, C. Liberale, M. Chirumamilla, R. P. Zaccaria, F. De Angelis, and M. Peccianti, "Terahertz Dipole Nanoantenna Arrays: Resonance Characteristics," *Plasmonics* **8**, 133-138 (2013).

[58] L. Razzari, A. Toma, M. Shalaby, M. Clerici, R. P. Zaccaria, C. Liberale, S. Marras, I. A. Al-Naib, G. Das, and F. De Angelis, "Extremely Large Extinction Efficiency and Field Enhancement in Terahertz Resonant Dipole Nanoantennas," *Optics Express* **19**, 26088-26094 (2011).

[59] R. Chikkaraddy, B. De Nijs, F. Benz, S. J. Barrow, O. A. Scherman, E. Rosta, A. Demetriadou, P. Fox, O. Hess, and J. J. Baumberg, "Single-Molecule Strong Coupling at Room Temperature in Plasmonic Nanocavities," *Nature* **535**, 127 (2016).

[60] A. A. Bakulin, R. Lovrincic, X. Yu, O. Selig, H. J. Bakker, Y. L. Rezus, P. K. Nayak, A. Fonari, V. Coropceanu, and J.-L. Brédas, "Mode-Selective Vibrational Modulation of Charge Transport in Organic Electronic Devices," *Nature Communications* **6**, 7880 (2015).

[61] A. Shalabney, J. George, H. Hiura, J. A. Hutchison, C. Genet, P. Hellwig, and T. W. Ebbesen, "Enhanced Raman Scattering from Vibro-Polariton Hybrid States," *Angewandte Chemie International Edition* **54**, 7971-7975 (2015).

[62] L. Novotny, "Strong Coupling, Energy Splitting, and Level Crossings: A Classical Perspective," *American Journal of Physics* **78**, 1199-1202 (2010).

[63] N. Liu, L. Langguth, T. Weiss, J. Kästel, M. Fleischhauer, T. Pfau, and H. Giessen, "Plasmonic Analogue of Electromagnetically Induced Transparency at the Drude Damping Limit," *Nature Materials* **8**, 758 (2009).

[64] R. Taubert, M. Hentschel, J. r. Kästel, and H. Giessen, "Classical Analog of Electromagnetically Induced Absorption in Plasmonics," *Nano Letters* **12**, 1367-1371 (2012).

[65] D. Cline, *Variational Principles in Classical Mechanics* (University of Rochester River Campus Librarie, 2017).

[66] S. R.-K. Rodriguez, "Classical and Quantum Distinctions between Weak and Strong Coupling," *European Journal of Physics* **37**, 025802 (2016).

[67] K. Santhosh, O. Bitton, L. Chuntonov, and G. Haran, "Vacuum Rabi Splitting in a Plasmonic Cavity at the Single Quantum Emitter Limit," *Nature Communications* **7**, ncomms11823 (2016).

[68] X. Wu, S. K. Gray, and M. Pelton, "Quantum-Dot-Induced Transparency in a Nanoscale Plasmonic Resonator," *Optics Express* **18**, 23633-23645 (2010).

[69] S. Rudin, and T. Reinecke, "Oscillator Model for Vacuum Rabi Splitting in Microcavities," *Physical Review B* **59**, 10227 (1999).

[70] X. Jin, A. Cerea, G. C. Messina, A. Rovere, R. Piccoli, F. De Donato, F. Palazon, A. Perucchi, P. Di Pietro, R. Morandotti, S. Lupi, F. De Angelis, M. Prato, A. Toma, and L. Razzari, "Reshaping the Phonon Energy Landscape of Nanocrystals inside a Terahertz Plasmonic Nanocavity," *Nature Communications* **9**, 763 (2018).

[71] D. G. Lidzey, D. D. Bradley, A. Armitage, S. Walker, and M. S. Skolnick, "Photon-Mediated Hybridization of Frenkel Excitons in Organic Semiconductor Microcavities," *Science* **288**, 1620-1623 (2000).

[72] A. Armitage, M. Skolnick, A. Kavokin, D. Whittaker, V. Astratov, G. Gehring, and J. Roberts, "Polariton-Induced Optical Asymmetry in Semiconductor Microcavities," *Physical Review B* **58**, 15367 (1998).

[73] S. A. Maier, *Plasmonics: Fundamentals and Applications* (Springer Science & Business Media, 2007).

[74] P. Biagioni, J.-S. Huang, and B. Hecht, "Nanoantennas for Visible and Infrared Radiation," *Reports on Progress in Physics* **75**, 024402 (2012).

[75] P. Drude, "Zur Elektronentheorie der Metalle," *Annalen der Physik* **306**, 566-613 (1900).

[76] M. Walther, D. Cooke, C. Sherstan, M. Hajar, M. Freeman, and F. Hegmann, "Terahertz Conductivity of Thin Gold Films at the Metal-Insulator Percolation Transition," *Physical Review B* **76**, 125408 (2007).

[77] H. A. Lorentz, *The Theory of Electrons and Its Applications to the Phenomena of Light and Radiant Heart: A Course of Lectures Delivered in Columbia University, New York in March and April, 1906* (Teubner, 1915).

[78] G. Grosso, and G. Parravicini, *Solid State Physics, 2nd Edition* (ELSEVIER, 2013).

[79] S. Adachi, *The Handbook on Optical Constants of Semiconductors: In Tables and Figures* (World Scientific, 2012).

[80] J. D. Caldwell, L. Lindsay, V. Giannini, I. Vurgaftman, T. L. Reinecke, S. A. Maier, and O. J. Glembocki, "Low-Loss, Infrared and Terahertz Nanophotonics using Surface Phonon Polaritons," *Nanophotonics* **4**, 44-68 (2015).

[81] M. Bass, E. W. Van Stryland, D. R. Williams, and W. L. Wolfe, *Handbook of Optics* (McGraw-Hill New York, 1995).

[82] P. Y. Yu, and M. Cardona, *Fundamentals of Semiconductors: Physics and Materials Properties* (Springer, 2010).

[83] C. F. Bohren, and D. R. Huffman, *Absorption and Scattering of Light by Small Particles* (John Wiley & Sons, 2008).

[84] V. Amendola, R. Pilot, M. Frasconi, O. M. Marago, and M. A. Iati, "Surface Plasmon Resonance in Gold Nanoparticles: a Review," *Journal of Physics: Condensed Matter* **29**, 203002 (2017).

[85] G. Mie, "Beiträge zur Optik trüber Medien, speziell kolloidaler Metallösungen," *Annalen der Physik* **330**, 377-445 (1908).

[86] J.-P. Schäfer, "Implementierung und Anwendung Analytischer und Numerischer Verfahren zur Lösung der Maxwellgleichungen für die Untersuchung der Lichtausbreitung in Biologischem Gewebe," (Verlag Nicht Ermittelbar, 2011).

[87] D. Sarid, and W. A. Challener, *Modern Introduction to Surface Plasmons: Theory, Mathematica Modeling, and Applications* (Cambridge University Press, 2010).

[88] Y.-l. Xu, and B. Å. Gustafson, "A Generalized Multiparticle Mie-Solution: Further Experimental Verification," *Journal of Quantitative Spectroscopy and Radiative Transfer* **70**, 395-419 (2001).

[89] A. Sihvola, "Mixing Rules with Complex Dielectric Coefficients," *Subsurface Sensing Technologies and Applications* **1**, 393-415 (2000).

[90] R. W. Wood, "On a Remarkable Case of Uneven Distribution of Light in a Diffraction Grating Spectrum," *Proceedings of the Physical Society of London* **18**, 269 (1902).

[91] L. Rayleigh, "On the Dynamical Theory of Gratings," *Proceedings of the Royal Society of London. Series A, Containing Papers of a Mathematical and Physical Character* **79**, 399-416 (1907).

[92] V. Kravets, F. Schedin, and A. Grigorenko, "Extremely Narrow Plasmon Resonances based on Diffraction Coupling of Localized Plasmons in Arrays of Metallic Nanoparticles," *Physical Review Letters* **101**, 087403 (2008).

[93] W. Zhou, and T. W. Odom, "Tunable Subradiant Lattice Plasmons by Out-of-Plane Dipolar Interactions," *Nature Nanotechnology* **6**, 423 (2011).

[94] S. Zou, N. Janel, and G. C. Schatz, "Silver Nanoparticle Array Structures that Produce Remarkably Narrow Plasmon Lineshapes," *The Journal of Chemical Physics* **120**, 10871-10875 (2004).

[95] D. Maystre, "Theory of Wood's Anomalies," in *Plasmonics* (Springer, 2012), pp. 39-83.

[96] P. Zilio, M. Malerba, A. Toma, R. P. Zaccaria, A. Jacassi, and F. D. Angelis, "Hybridization in Three Dimensions: A Novel Route Toward Plasmonic Metamolecules," *Nano Letters* **15**, 5200-5207 (2015).

[97] G. Vecchi, V. Giannini, and J. G. Rivas, "Shaping the Fluorescent Emission by Lattice Resonances in Plasmonic Crystals of Nanoantennas," *Physical Review Letters* **102**, 146807 (2009).

[98] A. Bitzer, J. Wallauer, H. Helm, H. Merbold, T. Feurer, and M. Walther, "Lattice Modes Mediate Radiative Coupling in Metamaterial Arrays," *Optics Express* **17**, 22108-22113 (2009).

[99] A. Väkeväinen, R. Moerland, H. Rekola, A.-P. Eskelinen, J.-P. Martikainen, D.-H. Kim, and P. Törmä, "Plasmonic Surface Lattice Resonances at the Strong Coupling Regime," *Nano Letters* **14**, 1721-1727 (2013).

[100] S. A. Maier, "Plasmonic Field Enhancement and SERS in the Effective Mode Volume Picture," *Optics Express* **14**, 1957-1964 (2006).

[101] R. Ruppin, "Electromagnetic Energy Density in a Dispersive and Absorptive Material," *Physics Letters A* **299**, 309-312 (2002).

[102] S. Adachi, *Optical Constants of Crystalline and Amorphous Semiconductors: Numerical Data and Graphical Information* (Springer Science & Business Media, 1999).

[103] S. Christodoulou, G. Vaccaro, V. Pinchetti, F. De Donato, J. Grim, A. Casu, A. Genovese, G. Vicidomini, A. Diaspro, and S. Brovelli, "Synthesis of Highly Luminescent Wurtzite CdSe/CdS Giant-Shell Nanocrystals using a Fast Continuous Injection Route," *Journal of Materials Chemistry C* **2**, 3439-3447 (2014).

[104] C.-H. M. Chuang, P. R. Brown, V. Bulović, and M. G. Bawendi, "Improved Performance and Stability in Quantum Dot Solar Cells through Band Alignment Engineering," *Nature Materials* **13**, 796 (2014).

[105] M. Moskovits, "Surface-Enhanced Spectroscopy," *Reviews of Modern Physics* **57**, 783 (1985).

[106] S. DEL GOBBO, "Cadmium Sulfide Quantum Dots: Growth and Optical Properties, p88," (2009).

[107] D. Gomez, K. Vernon, P. Mulvaney, and T. Davis, "Surface Plasmon Mediated Strong Exciton− Photon Coupling in Semiconductor Nanocrystals," *Nano Letters* **10**, 274-278 (2009).

[108] A. Trügler, and U. Hohenester, "Strong Coupling between a Metallic Nanoparticle and a Single Molecule," *Physical Review B* **77**, 115403 (2008).

[109] L. C. Andreani, G. Panzarini, and J.-M. Gérard, "Strong-Coupling Regime for Quantum Boxes in Pillar Microcavities: Theory," *Physical Review B* **60**, 13276 (1999).

[110] E. Cubukcu, and F. Capasso, "Optical Nanorod Antennas as Dispersive One-Dimensional Fabry–Pérot Resonators for Surface Plasmons," *Applied Physics Letters* **95**, 201101 (2009).

[111] H. Fischer, and O. J. Martin, "Engineering the Optical Response of Plasmonic Nanoantennas," *Optics Express* **16**, 9144-9154 (2008).

[112] Y. Yamamoto, F. Tassone, and H. Cao, *Semiconductor Cavity Quantum Electrodynamics* (Springer, 2003).

[113] V. Aglieri, X. Jin, A. Rovere, R. Piccoli, D. Caraffini, S. Tuccio, F. De Angelis, R. Morandotti, R. Macaluso, A. Toma, and L. Razzari, "Antenna Tapering Strategy for Near-field Enhancement Optimization in Terahertz Gold Nanocavities," *CLEO/EUROPE-EQEC 2019, Munich, Germany* (2019).

[114] A. Datta, Z. Zeng, and X. Xu, "Split Ring Resonator as a Nanoscale Optical Transducer for Heat-Assisted Magnetic Recording," *Optics Express* **27**, 28264-28278 (2019).

[115] T. Corrigan, P. Kolb, A. Sushkov, H. Drew, D. Schmadel, and R. Phaneuf, "Optical Plasmonic Resonances in Split-Ring Resonator Structures: an Improved LC Model," *Optics Express* **16**, 19850-19864 (2008).

[116] S. M. Hein, and H. Giessen, "Tailoring Magnetic Dipole Emission with Plasmonic Split-Ring Resonators," *Physical Review Letters* **111**, 026803 (2013).

[117] A. W. Clark, A. Glidle, D. R. Cumming, and J. M. Cooper, "Plasmonic Split-Ring Resonators as Dichroic Nanophotonic DNA Biosensors," *Journal of the American Chemical Society* **131**, 17615-17619 (2009).

[118] M. Steiner, M. Freitag, V. Perebeinos, J. C. Tsang, J. P. Small, M. Kinoshita, D. Yuan, J. Liu, and P. Avouris, "Phonon Populations and Electrical Power Dissipation in Carbon Nanotube Transistors," *Nature Nanotechnology* **4**, 320 (2009).

[119] D. Bozyigit, N. Yazdani, M. Yarema, O. Yarema, W. M. M. Lin, S. Volk, K. Vuttivorakulchai, M. Luisier, F. Juranyi, and V. Wood, "Soft Surfaces of Nanomaterials Enable Strong Phonon Interactions," *Nature* **531**, 618 (2016).

[120] A. F. Kockum, A. Miranowicz, V. Macrì, S. Savasta, and F. Nori, "Deterministic Quantum Nonlinear Optics with Single Atoms and Virtual Photons," *Physical Review A* **95**, 063849 (2017).

[121] E. Sánchez-Burillo, D. Zueco, J. Garcia-Ripoll, and L. Martin-Moreno, "Scattering in the Ultrastrong Regime: Nonlinear Optics with One Photon," *Physical Review Letters* **113**, 263604 (2014).

[122] R. Stassi, V. Macrì, A. F. Kockum, O. Di Stefano, A. Miranowicz, S. Savasta, and F. Nori, "Quantum Nonlinear Optics without Photons," *Physical Review A* **96**, 023818 (2017).

[123] S. De Liberato, C. Ciuti, and I. Carusotto, "Quantum Vacuum Radiation Spectra from a Semiconductor Microcavity with a Time-Modulated Vacuum Rabi Frequency," *Physical Review Letters* **98**, 103602 (2007).

[124] A. Ridolfo, S. Savasta, and M. J. Hartmann, "Nonclassical Radiation from Thermal Cavities in the Ultrastrong Coupling Regime," *Physical Review Letters* **110**, 163601 (2013).

[125] M. Cirio, K. Debnath, N. Lambert, and F. Nori, "Amplified Optomechanical Transduction of Virtual Radiation Pressure," *Physical Review Letters* **119**, 053601 (2017).

[126] S. De Liberato, D. Gerace, I. Carusotto, and C. Ciuti, "Extracavity Quantum Vacuum Radiation from a Single Qubit," *Physical Review A* **80**, 053810 (2009).

[127] L. Garziano, A. Ridolfo, R. Stassi, O. Di Stefano, and S. Savasta, "Switching On and Off of Ultrastrong Light-Matter Interaction: Photon Statistics of Quantum Vacuum Radiation," *Physical Review A* **88**, 063829 (2013).

[128] M.-E. Kleemann, R. Chikkaraddy, E. M. Alexeev, D. Kos, C. Carnegie, W. Deacon, A. C. de Pury, C. Große, B. de Nijs, and J. Mertens, "Strong-Coupling of WSe 2 in Ultra-Compact Plasmonic Nanocavities at Room Temperature," *Nature Communications* **8**, 1296 (2017).

[129] W. Liu, B. Lee, C. H. Naylor, H.-S. Ee, J. Park, A. C. Johnson, and R. Agarwal, "Strong Exciton–Plasmon Coupling in MoS2 Coupled with Plasmonic Lattice," *Nano Letters* **16**, 1262-1269 (2016).

[130] L. Liu, L. Y. Tobing, J. Tong, D. H. Zhang, F. J. Garcia-Vidal, and Y. Luo, "Room Temperature Strong Coupling of Monolayer WS2 with Gold Nanoantennae," in *2017 Progress in Electromagnetics Research Symposium-Fall (PIERS-FALL)*(IEEE, 2017), pp. 2578-2580.

[131] L. Zhang, R. Gogna, W. Burg, E. Tutuc, and H. Deng, "Photonic-Crystal Exciton-Polaritons in Monolayer Semiconductors," *Nature Communications* **9**, 713 (2018).

[132] T. Karzig, C.-E. Bardyn, N. H. Lindner, and G. Refael, "Topological Polaritons," *Physical Review X* **5**, 031001 (2015).

[133] C.-E. Bardyn, T. Karzig, G. Refael, and T. C. Liew, "Topological Polaritons and Excitons in Garden-Variety Systems," *Physical Review B* **91**, 161413 (2015).

[134] V. Peano, C. Brendel, M. Schmidt, and F. Marquardt, "Topological Phases of Sound and Light," *Physical Review X* **5**, 031011 (2015).

[135] M. Milićević, T. Ozawa, P. Andreakou, I. Carusotto, T. Jacqmin, E. Galopin, A. Lemaitre, L. Le Gratiet, I. Sagnes, and J. Bloch, "Edge States in Polariton Honeycomb Lattices," *2D Materials* **2**, 034012 (2015).

SOMMAIRE RÉCAPITULATIF (Summary in French)

1 Motivation et objectif

L'interaction lumière-matière dans les cavités résonantes a fait l'objet de nombreuses études au cours des quatre dernières décennies [1-4]. En particulier, les transitions électroniques dans les systèmes de matière condensée, tels les points quantiques et les nanocristaux, ont déjà été étudiées [1, 5-8]. Il est bien connu que de tels émetteurs peuvent modifier leur taux d'émission spontanée en adaptant les propriétés électromagnétiques de leur environnement (par exemple, en plaçant l'émetteur dans une cavité optique) [9, 10]. Cependant, la fréquence d'émission demeure inchangée dans ce cas. C'est ce qui se produit généralement lorsque l'interaction entre l'émetteur et la cavité est faible et que le taux d'échange d'énergie entre les deux résonances (matière et cavité) ne permet pas de surmonter la perte d'énergie des systèmes (c'est-à-dire dans le cas de régime de couplage faible). En revanche, lorsque l'interaction devient suffisamment forte (c'est-à-dire lorsque le taux d'échange d'énergie entre l'émetteur et la cavité devient – au moins – comparable aux pertes du système), le niveau d'énergie associé à la transition voulue est modifié et se divise explicitement en deux nouveaux états distincts [1, 11]. Cette condition est connue sous le nom de couplage fort. La signature de cette condition est le croisement évité des « modes normaux » du système hybride et leur séparation d'énergie minimale est appelée séparation de Rabi (*Rabi splitting*). Jusqu'à présent, de nombreuses études ont utilisé des résonateurs de Fabry-Pérot, des modes de galerie ou des cavités à cristaux photoniques pour supporter des modes optiques qui interagissent avec la matière [12-16]. Il est relativement facile de parvenir au régime de couplage fort dans ces cavités en raison de leur facteur de qualité élevé et de leur faible taux d'amortissement dans le domaine optique.

Récemment, le couplage fort vibrationnel entre les photons de cavité de Fabry-Pérot et la vibration de liaisons moléculaires spécifiques a été étudié. Les modes de vibro-polariton obtenus dans divers systèmes [12, 13, 17-19] laissent présager plusieurs applications intéressantes. En effet, les forts couplages entre les excitons (paires d'électron-trou dans un état lié) et les photons ont déjà montré qu'il est possible de réaliser des condensats de Bose-Einstein de polaritons en manipulant correctement les parties excitonique et lumière des polaritons [1, 2, 17, 20]. En outre, il a également été constaté que le couplage fort vibrationnel conduisait à la modification de réactions chimiques. Dans la mesure où « l'environnement » électromagnétique d'une molécule

peut modifier ses vibrations, la force de ses liaisons chimiques peut également être modifiée, ce qui peut ensuite être utilisé pour contrôler la vitesse des réactions chimiques [12, 13, 21, 22].

De nos jours, les nanocristaux attirent une attention considérable dans le domaine de l'électrodynamique quantique en raison de leurs caractéristiques favorables uniques [23-28]. Par exemple, les nanocristaux semi-conducteurs peuvent être utilisés pour fabriquer des transistors novateurs fonctionnant à température ambiante et assurant une meilleure mobilité des dispositifs par rapport aux dispositifs conventionnels, ainsi que des diodes électroluminescentes à couleurs accordables [23-28]. Les phonons, qui sont la principale source de dissipation d'énergie dans les systèmes à l'état solide, représentent l'ultime goulot d'étranglement qui limite le fonctionnement des nanomatériaux fonctionnels [23, 29]. Par conséquent, le couplage fort de phonons pourrait être une voie intéressante pour modifier la dissipation d'énergie liée aux phonons dans les nanomatériaux. En outre, une étude récente montre que les molécules soumises à un fort couplage vibrationnel peuvent efficacement émettre de la lumière infrarouge (IR) [30]. Nous pourrions donc également nous attendre à ce que le couplage fort de phonon conduise à de nouveaux dispositifs pour l'émission de lumière térahertz (THz). Poussés par cette motivation, nous avons choisi d'utiliser des nanocristaux de sulfure de cadmium (CdS) [31], comme système de banc d'essai, car les nanoparticules semi-conductrices polaires [32] possèdent un mode de phonon optique intense (phonon de Fröhlich (FR)) dans la région THz qui peut être efficacement couplé à la lumière THz. Dans ce système, nous testerons si le niveau d'énergie du phonon de FR peut être modifié de manière intrinsèque, via le couplage fort dans une nanocavité plasmonique. En effet, le couplage fort à l'échelle nanométrique des résonances de plasmon de surface et des nanoparticules est devenu un sujet de recherche intéressant dans les régions du visible et de l'IR [1, 33-36]. En raison de la nature intrinsèque des plasmons de surface, la composante du champ lumineux d'une résonance plasmonique peut être confinée dans des dimensions beaucoup plus petites que la longueur d'onde du rayonnement utilisé en espace libre [5, 37, 38]. Une cavité plasmonique offre donc une solution intéressante pour étudier les interactions lumière-matière à l'échelle nanométrique dans la région THz, où la longueur d'onde du rayonnement est supérieure de plusieurs ordres de grandeur à la taille des nanoparticules.

En résumé, mon projet de doctorat consiste à réaliser un système de couplage fort vibrationnel en utilisant des nanostructures plasmoniques THz et des phonons optiques de nanocristaux. Ce système représente une plateforme pour faire la preuve de principe de la possibilité de modifier la réponse phononique de nanomatériaux, en vue de modifier le mécanisme de dissipation d'énergie dans des nanosystèmes. De plus, étant donné que les

phonons peuvent trouver une nouvelle voie de désintégration par un processus radiatif sous couplage fort, cela pourrait également conduire à une génération innovante d'émetteurs THz.

2 Interaction lumière-matière dans les cavités électromagnétiques

En 1946, Purcell révèle qu'en modifiant l'environnement électromagnétique d'un émetteur, le taux d'émission spontanée peut être soit augmenté ou supprimé [9]. Ce phénomène est nommé **effet Purcell**. Cette observation-clé a ouvert une nouvelle voie pour l'étude de la dynamique quantique, en particulier l'interaction entre la lumière et la matière, visant à moduler l'interaction en exploitant divers résonateurs photoniques [4].

Une résonance optique est essentiellement une condition qui amplifie les ondes électromagnétiques dans des cavités de géométries variées. Les fréquences auxquelles l'énergie maximale est stockée dans une cavité optique sont appelées fréquences de résonance. L'inverse de la durée de vie de la cavité définit le facteur d'amortissement (γ) d'un résonateur spécifique, qui peut être extrait en calculant la largeur à mi-hauteur (*full width at half maximum* ou FWHM). Le rapport entre la fréquence de résonance et la FWHM est le facteur de qualité « Q », qui indique la capacité de stockage d'énergie d'un résonateur. En physique classique, la résonance optique peut être comprise comme une oscillation dipolaire induite par une onde électromagnétique incidente. En optique quantique, le modèle d'oscillateur harmonique quantique sert à expliquer les phénomènes non classiques dans les observations scientifiques modernes. En particulier, à partir du modèle d'oscillateur harmonique quantique, on trouve que l'état fondamental d'un oscillateur a une énergie non nulle, égale à $\hbar\omega/2$ ($\hbar$ est la constante de Planck réduite et ω est la fréquence angulaire). Pour un champ électromagnétique quantifié, cette énergie du point zéro est associée à des fluctuations du champ électrique du vide, à savoir le champ du vide, présent partout, même dans un vide complet. L'amplitude du **champ électrique du vide** E_{vac} associé à l'énergie du point zéro « $\hbar\omega/2$ » peut être définie comme étant égale à [39] [15, 40]: $\left|E_{\text{vac}}\right| = \sqrt{\hbar\omega/\left(2\varepsilon_0\varepsilon V_{\text{mod}}\right)}$, où ε_0 est la permittivité du vide, ε est la permittivité relative de l'environnement et V_{mod} est le volume modal de la cavité, qui peut être considérablement réduit en exploitant des stratégies de confinement. Dans les processus d'interaction lumière-matière, le champ électrique du vide est un facteur déterminant pour quantifier le couplage entre la lumière et la matière.

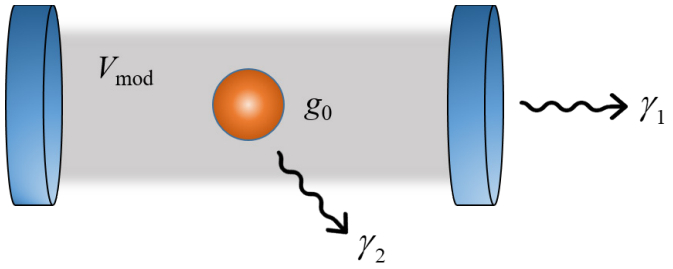

Fig. 1 **Un atome dans une cavité résonante: V_{mod} est le volume modal, g_0 la force de couplage, γ_1 le taux de décroissance de la cavité et γ_2 le taux de décroissance atomique en dehors de la résonance.**

Considérant le cas simple d'un atome dans une cavité, l'énergie d'interaction ($\hbar g_0$) entre l'atome et le champ du vide de la cavité peut s'écrire ainsi: $\hbar g_0 = \mu_{12}\left|E_{\mathrm{vac}}\right|$, où g_0 est la **force de couplage**, and μ_{12} le moment dipolaire de la transition d'énergie pour la partie matière (l'indice « 12 » indique une transition d'un état initial $\left|1\right\rangle$ à un état final $\left|2\right\rangle$). Ainsi, nous pouvons dériver l'équation suivante: $g_0 = \sqrt{\mu_{12}^2 \omega / \left(2\varepsilon_0 \varepsilon \hbar V_{\mathrm{mod}}\right)}$. En espace libre, la force de couplage est généralement faible en raison du volume modal important. Cependant, lorsqu'un système de matière est placé dans une cavité optique, la force de couplage peut être grandement améliorée. Comme le montre la figure 1, trois facteurs déterminent finalement l'interaction : i) le taux de décroissance des photons de la cavité γ_1; ii) le taux de décroissance atomique γ_2 du système de matière; iii) et la force de couplage g_0 entre l'atome et les photons de la cavité. La force de couplage g_0 entre en compétition avec les deux autres termes pour determiner si le système est dans le régime de couplage faible ou fort. En général, lorsque $g_0 \ll \left(\gamma_1, \gamma_2\right)$, l'interaction entre l'atome et la cavité se fait dans le régime de **couplage faible**; quand $g_0 \gg \left(\gamma_1, \gamma_2\right)$, l'interaction est classée dans le régime de **couplage fort**. Dans le *régime de couplage faible*, l'émission de photons par l'atome lors de l'interaction est **un processus irréversible**, comme dans l'émission spontanée normale en espace libre, mais seul le taux d'émission est affecté par la cavité. Inversement, dans le *régime de couplage fort*, le taux d'échange d'énergie entre la cavité et l'atome est plus rapide que pour les processus irréversibles, qui dissipent les photons hors de la cavité. Cela fait en sorte que l'émission d'atomes devient un **processus quasi-réversible**, c'est-à-dire que les photons émis peuvent être réabsorbés par l'atome avant d'être perdus hors de la cavité [39]. Ce phénomène réversible est à la base de **l'électrodynamique quantique en cavité** (*cavity quantum electrodynamics* ou QED en cavité). En 1963, Jaynes et Cummings développent

un modèle quantifié pour expliquer l'interaction de couplage forte. Ici, nous résumons les principales conclusions.

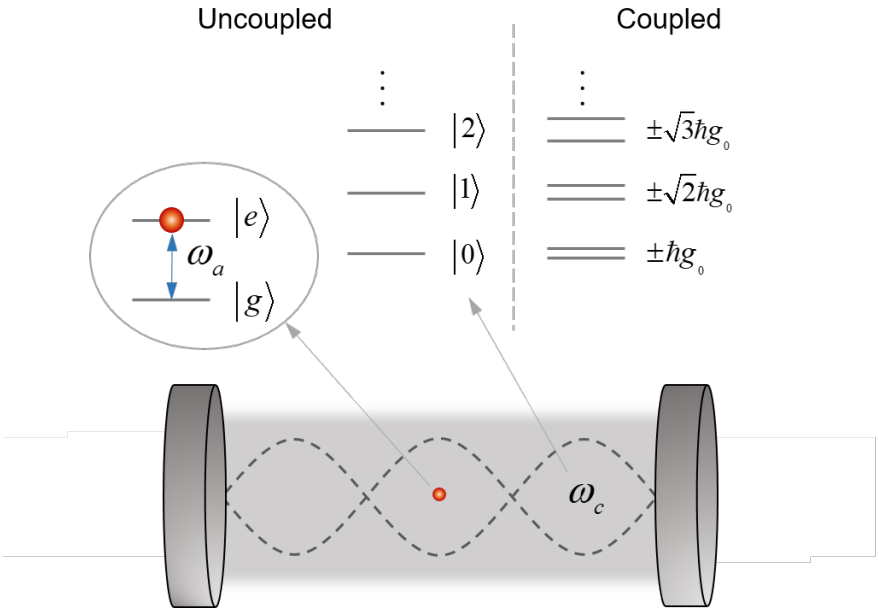

Fig. 2 **Illustration du modèle de Jaynes-Cumming. Quand le nombre de photon est « 0 », il y a tout de même une séparation de la résonance en raison du champ du vide.**

Dans le cas d'un seul atome couplé à un champ quantifié (voir la figure 2), l'hamiltonien dans l'approximation de l'onde tournante permet d'obtenir les niveaux d'énergie divisés qui ne peuvent être décrits que par des quasi-particules mi-matière et mi-photon, à savoir les **polaritons**. La séparation des états d'énergie de ces polaritons est dite **séparation de Rabi**: $\hbar\Omega_{\mathrm{R}} = 2\hbar g_0\sqrt{n+1}$, où « n » désigne le nombre de photons. Il est facile de montrer qu'il y a une séparation même dans le cas de $n = 0$, ce qui signifie que ces polaritons sont des états mixtes entre l'atome excité et le champ du vide. Cette séparation est appelée **séparation de Rabi dans le vide** (*vacuum Rabi splitting*) et sa valeur est donnée par: $\hbar\Omega_{\mathrm{R}} = 2\hbar g_0$. Dans la plupart des cas, les systèmes à un atome sont inefficaces pour obtenir un couplage fort dans une cavité monomode. Cependant, la situation s'améliore en ajoutant N atomes dans la cavité. Ainsi, en considérant N atomes dans une cavité monomode, le système peut être décrit par l'hamiltonien de Tavis-Cummings dans l'approximation de l'onde tournante [1], dont la solution conduit à une séparation de Rabi dans le vide de : $\hbar\Omega_{\mathrm{R}} = 2\hbar g_N$, où la force de couplage globale est $\hbar g_N = \sqrt{N}\,\mu_{12}\left|E_{\mathrm{vac}}\right|$ pour les cas de N atomes, avec $g_N = \sqrt{N}\,g_0$.

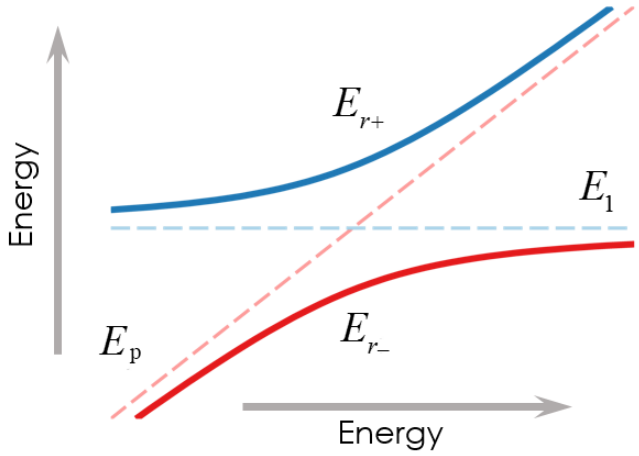

Fig. 3 Modèle à deux oscillateurs couplés.

Un modèle quantique phénoménologique peut être très utile pour reproduire la dispersion d'énergie des branches de polaritons (voir la figure 3) sans prendre en compte les mécanismes quantiques détaillés [1, 2, 4]. Ainsi, un système couplé à deux niveaux peut être généralisé par l'hamiltonien suivant $H = \begin{pmatrix} E_p & E_g \\ E_g & E_2 \end{pmatrix}$, où E_1 et E_2 sont respectivement le niveau d'énergie du premier oscillateur (lumière) et du deuxième oscillateur (matière) et E_g est la force de couplage. Les énergies propres du système sont $E_\pm = \frac{1}{2}\left(E_p + E_1\right) \pm \frac{1}{2}\sqrt{4E_g^2 + \left(E_p - E_1\right)^2}$, ce qui mène aux deux branches de polariton avec un croisement évité typique illustré à la figure 3. Lorsque $E_p = E_1$, la séparation de Rabi entre les deux branches de polariton est égale à $\Omega_R = 2E_g$. Dans certains scénarios, un troisième niveau d'énergie doit également être inclus [70-72]. Dans ce cas, le système couplé doit être décrit par un hamiltonien trois par trois (voir les détails dans le texte principal).

Très récemment, le couplage **ultra-fort** et le couplage **profond** entre la lumière et la matière sont passés de prédiction théorique à réalité expérimentale (voir l'article de revue de la réf. [4]). La force de couplage dans ces régimes est comparable aux fréquences de transition, de sorte qu'il devient possible de modifier la nature même des degrés de liberté entre lumière et matière [4]. En général, l'approximation de l'onde tournante ne peut pas être utilisée pour écrire l'hamiltonien décrivant un système au-delà du couplage fort. Contrairement aux couplages faibles et forts, les conditions de couplage ultra-fort et de couplage profond sont liées aux énergies de l'oscillateur non-perturbé plutôt qu'aux facteurs d'amortissement. En particulier, nous pouvons définir une force de couplage normalisée « η » – le rapport entre la force de couplage « g » et la

fréquence simple de l'excitation « ω ». Quand η est supérieur à 0.1, le système entre en **régime de couplage ultra-fort** [45], alors que s'il est supérieur à 1, il se trouve en **régime de couplage profond** [46]. Les couplages ultra-fort et profond donnent lieu à des effets d'ordre supérieur et non-perturbatifs pouvant mener à des applications intéressantes, telles qu'une optoélectronique modifiée, l'émission du vide quantique, l'ingénierie de photons virtuels et le découplage lumière-matière [4].

3 Modification de la résonance de phonon de nanocristaux dans une nanocavité plasmonique THz

L'interaction entre les modes à basse fréquence, tels que les phonons (vibrations collectives) et les plasmons (oscillations collectives d'électrons) dans la région THz a des implications fondamentales, notamment la possibilité de modifier les propriétés des matériaux, ouvrant ainsi des perspectives intéressantes pour la science des matériaux et la nanotechnologie [1, 4, 74]. En concevant judicieusement des nanocavités plasmoniques, le rayonnement THz en espace libre peut être concentré dans des volumes grandement inférieurs à la limite de diffraction, conduisant à une énorme augmentation du champ local ce qui peut améliorer de manière significative l'interaction lumière-matière. En 2015, cette technique a été utilisée pour la première fois par notre groupe pour démontrer la spectroscopie THz améliorée grâce à une nanoantenne [5], montrant que le mode de phonon d'une monocouche de points quantiques de séléniure de cadmium placés à la surface d'un réseau de nanoantennes peut être détecté avec succès. En 2018, mes collaborateurs et moi-même avons montré que la réponse phononique optique des nanocristaux CdS pouvait être modifiée de façon drastique dans des nanocavités THz, en raison du fort couplage entre le mode de phonon optique de FR des nanocristaux et la résonance plasmonique des nanoantennes [70]. Comme le montre la figure 4, le mode optique de FR (ν_{FR}) des nanocristaux, existant entre les modes de phonon TO (ν_{TO}) et LO (ν_{LO}) (voir la section 3.3 dans le texte principal), s'hybridera fortement avec le mode plasmonique (ν_{PL}) de la nanocavité, engendreant une séparation en un vibro-polariton inférieur (ν_{-}) et supérieur (ν_{+}).

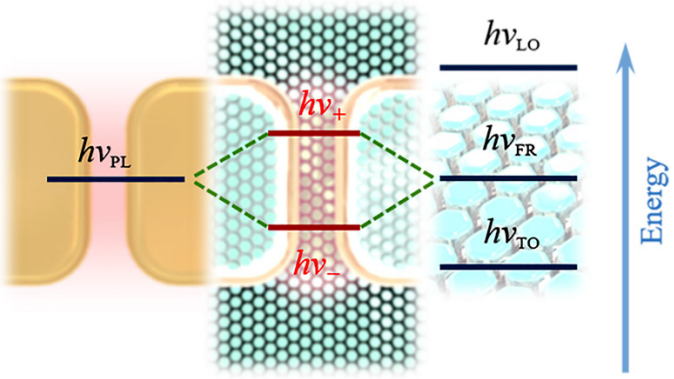

Fig. 4 Diagramme d'énergie montrant l'hybridation de la résonance plasmon–phonon.

Simulations numériques pour la conception de réseaux de nanoantennes bout à bout

La conception précise de nanocavités plasmoniques et l'étude de leur réponse électromagnétique au moyen de simulations numériques constituent des étapes essentielles dans la réalisation d'une plateforme efficace pour le couplage fort plasmon-phonon. Les simulations permettent également d'obtenir un aperçu plus en profondeur des mécanismes physiques sous-jacents. J'ai utilisé le logiciel COMSOL Multiphysics pour concevoir et valider le comportement électromagnétique des nanocavités visées. En particulier, je me suis concentré sur la conception d'un système de couplage plasmon-phonon dans lequel les nanocristaux de CdS interagissent fortement avec la lumière THz dans les nanocavités. Comme le montre la figure 5a, j'ai conçu des réseaux de nanoantennes bout à bout sur substrat de silicium (indice de réfraction n_{Si} = 3,42) avec un espacement g_x = 30 nm le long de l'axe longitudinal des nanoantennes (axe x) et g_y = 8,5 µm dans la direction perpendiculaire (axe y). La largeur de chaque nanoantenne a été fixée à 200 nm et la hauteur, à 55 nm. En ce qui concerne la longueur d'une antenne, la première estimation a été obtenue à l'aide de l'équation $L = \lambda_{\mathrm{res}} / \left(2n_{\mathrm{Si}}\right)$, dans laquelle λ_{res} est la longueur d'onde à laquelle se produit la résonance d'une antenne dipolaire [57]. Puisque le mode de phonon qui nous intéresse est situé autour de 8 THz (le mode de FR, avec λ_{res} correspondant égal à 37,5 µm), la résonance des nanoantennes doit être ajustée au même endroit. Ainsi, en utilisant l'équation simple présentée ci-dessus, la première estimation pour la longueur de l'antenne est L = 5,5 µm. La longueur de la nanoantenne a ensuite été variée entre 4 et 7 µm de façon à ce que la résonance plasmonique balaie tout le mode de phonon. Des simulations numériques poussées ont été effectuées pour caractériser les propriétés de résonance exactes de ces réseaux de nanoantennes. Pour simuler la monocouche de

nanocristaux de CdS (voir la figure 5b pour un schéma), j'ai ensuite utilisé la stratégie de « couche effective », qui décrit le comportement typique des cristaux polaires dans la région de Reststrahlen [79] en utilisant la règle des mélanges de Maxwell-Garnett [89].

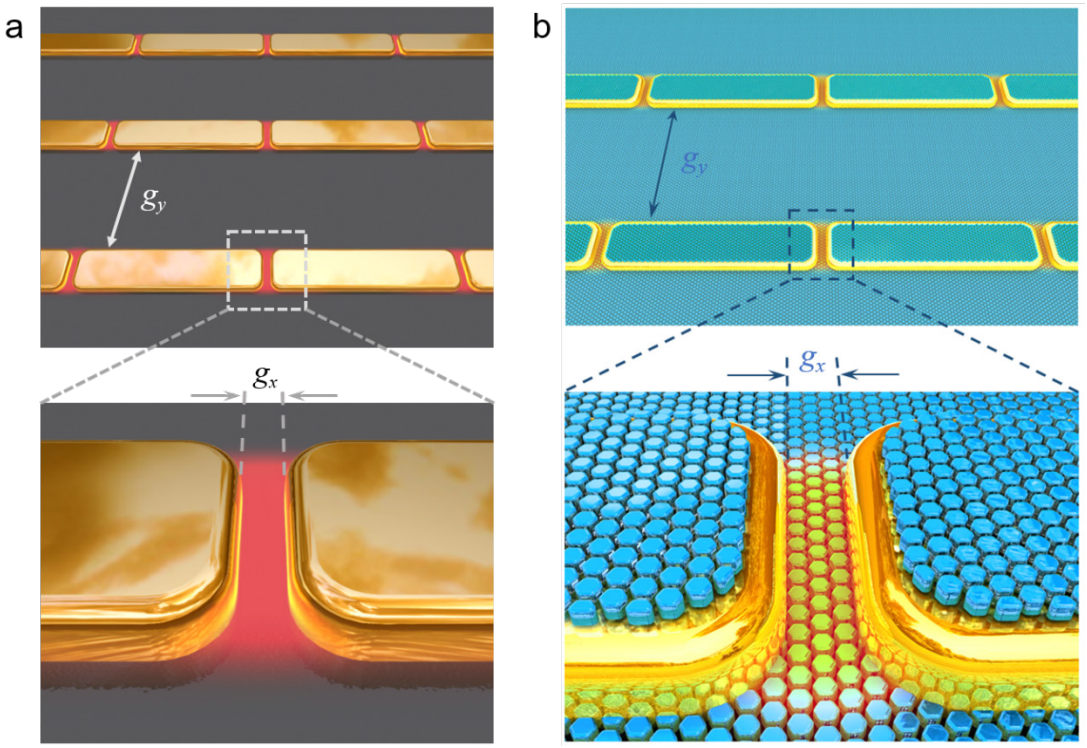

Fig. 5 **(a) Schéma d'un réseau de nanoantennes bout à bout. (b) Représentation graphique d'un réseau de nanoantennes plasmoniques couvert d'une monocouche de nanocristaux de CdS.**

Nous avons utilisé une onde plane polarisée linéairement comme condition d'entrée pour l'illumination dans les simulations. Le plan d'incidence était incliné de 45° par rapport à l'axe long de la nanoantenne, tandis que l'angle d'incidence dans ce plan était fixé à 18° (conformément à l'angle d'incidence moyen de l'objectif de Cassegrain utilisé dans les expériences). L'état de polarisation de l'onde a ensuite été défini en tenant compte de la polarisation d'entrée (parallèle à l'axe long de la nanoantenne) par rapport à l'objectif de Cassegrain. Nous avons constaté que ce type d'illumination reproduit bien la réponse à la transmission des réseaux de nanoantennes sous l'objectif de Cassegrain de même que la mesure expérimentale du premier mode du réseau autour de 9,8 THz.

Fabrication et synthèse

Le design des réseaux de nanoantennes a été envoyé à nos collaborateurs de l'Institut Italien de Technologie – IIT – à Gênes en Italie pour la fabrication. Les chaînes de nanoantennes ont été produites en utilisant la technique de la lithographie par faisceau d'électrons (*electron beam*

lithography ou EBL) (pour les détails techniques, voir la section Supplementary Information de [70]). Chaque réseau bidimensionnel fabriqué couvrait une surface de 200 × 200 μm^2.

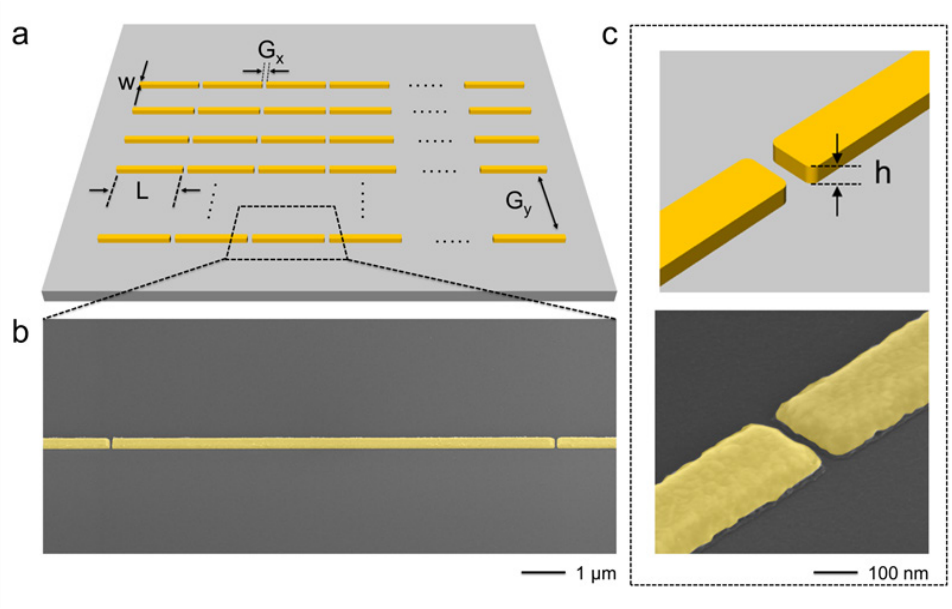

Fig. 6 **(a) Schéma d'antennes THz sur substrat de Si. (b) Image au MEB d'une chaîne de nanoantennes en fausses couleurs. (c) Schéma montrant l'écart entre deux nanoantennes (panneau supérieur) et l'image correspondante au MEB (panneau inférieur).**

La figure 6 présente une vue schématique d'un réseau de nanoantennes THz, ainsi que deux images au microscope électronique à balayage (MEB). Conformément aux résultats obtenus à la phase de conception, des réseaux avec différents longueurs *L* de nanoantennes, allant de 4 à 7 µm, ont été fabriqués sur un seul substrat de silicium, afin d'ajuster leurs résonances plasmoniques dans la bande de fréquences THz comprenant le mode phonon optique de FR des nanocristaux de CdS.

La synthèse des nanocristaux de CdS a également été réalisée à l'IIT en Italie. Les nanocristaux employés dans la présente étude ont été synthétisés en utilisant un protocole en deux étapes. Dans ce protocole, la croissance d'une coquille de CdS de l'épaisseur souhaitée a été faite sur des noyaux de CdS pré-synthétisés, en suivant la procédure décrite dans la réf. [103] pour les nanocristaux de CdSe/CdS à coquille géante. Pour une caractérisation détaillée des nanocristaux synthétisés, voir la section Supplementary Information de [70]. Les images au microscope électronique à transmission (MET) des noyaux de CdS (panneau a) et des nanocristaux géants CdS@CdS (panneau b) sont présentées à la figure 7. Comme le montrent les caractérisations au MET, les deux échantillons sont relativement monodispersés, avec une taille moyenne de (5,6 ± 0,4) nm et (10,2 ± 0,6) nm pour les noyaux de CdS et les nanocristaux géants CdS@CdS respectivement.

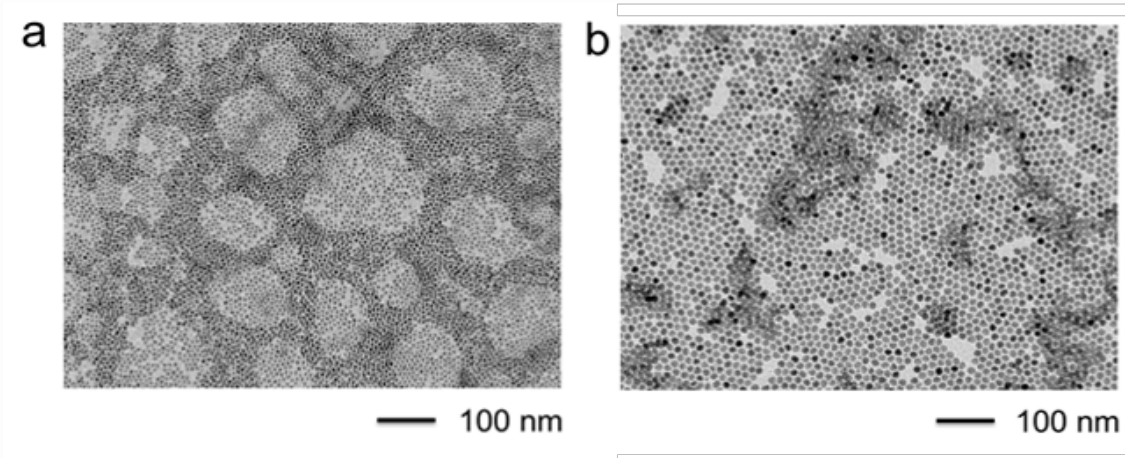

Fig. 7 Images au MET des noyaux de CdS (a) et des nanocristaux géants de CdS@CdS (b).

Le dépôt des nanocristaux à coquille géante CdS@CdS sur les réseaux de nanoantennes THz en or a été réalisé par enduction centrifuge dans des conditions ambiantes, à température ambiante. Plus précisément, la solution obtenue a été diluée jusqu'à obtenir une concentration finale de nanocristaux de 1 µM. Ensuite, 20 µL de la solution diluée ont été déposés par enduction centrifuge sur le substrat à motifs à une vitesse de 2000 tr/min pendant 60 s (accélération de 1000 tr/min·s-1). La procédure a abouti au dépôt d'une monocouche uniforme de nanocristaux géants CdS@CdS. Une image au MEB d'une nanocavité recouverte d'une telle monocouche est présentée à la figure 8. Des couches plus épaisses ont été obtenues en plusieurs étapes de dépôt par enduction centrifuge une couche à la fois. Pour éviter une re-dissolution complète des nanocristaux déjà déposés, les étapes de dépôt ont été entrecoupées à chaque fois par une exposition de l'échantillon à 20 µL de solution d'iodure de tétrabutylammonium dans du méthanol (10 mg·mL-1) pendant 30 s, suivie de trois étapes de rinçage au méthanol, tel que décrit dans la référence [104].

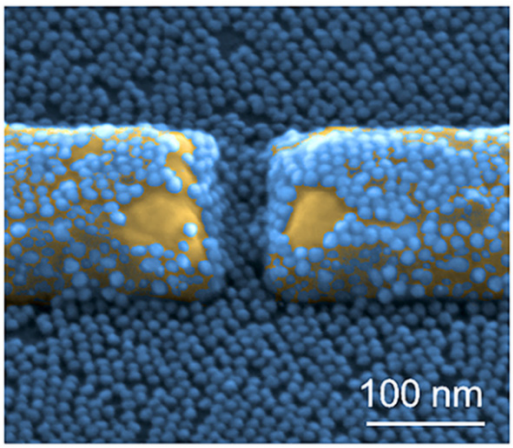

Fig. 8 Image au MEB en fausses couleurs : une monocouche de nanocristaux de CdS (grandeur de 10 nm) couvre la cavité d'une nanoantenne THz.

Mesures avec et sans illumination directe

Les spectres de transmission THz directe ont été mesurés à la source synchrotron IR haute luminosité SISSI@Elettra. Le rayonnement THz est généré au niveau de l'aimant courbé 9.1 et propagé sous vide ultra-poussé vers le laboratoire SISSI, où il entre dans un spectromètre IR à transformée de Fourier (Fourier Transform IR ou FTIR) Bruker 70v équipé d'une lame séparatrice de Si, puis est couplé à un microscope IR Hyperion. Le microscope est doté d'un port externe permettant d'installer un bolomètre de Si refroidi à l'hélium. Grâce à la luminosité élevée de la lumière synchrotron, cette configuration a permis de réaliser des mesures en microscopie THz polarisée avec un bon rapport signal/bruit sur chaque réseau fabriqué (voir figure 9).

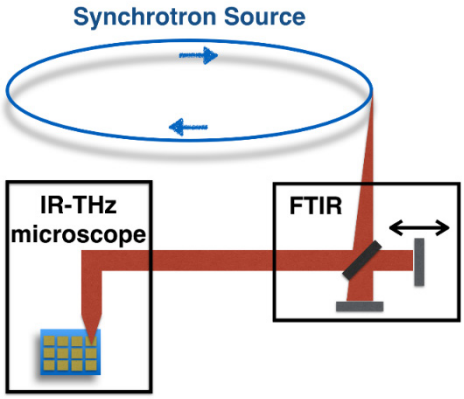

Fig. 9 Plan schématique du laboratoire expérimental au SISSI beamline.

Toutes les mesures Raman ont été effectuées par nos collaborateurs de l'IIT en Italie. Nous avons ensuite contribué au traitement et à l'interprétation de ces données. En mesurant simplement la fréquence de la lumière visible diffusée inélastiquement par l'échantillon à l'étude, la spectroscopie Raman représente une alternative intéressante pour déterminer la réponse phononique de notre système sans avoir à revenir à l'illumination THz directe. En bref, les mesures Raman ont été réalisées en rétrodiffusion à l'aide d'un microspectromètre (Renishaw inVia) équipé d'un objectif 150× LEICA PL APO (ouverture numérique NA = 0,95) et d'un détecteur CCD refroidi thermoélectriquement (température de travail de -60°C). Les spectres ont été recueillis en excitant le système avec un laser He:Ne (λ = 632,8 nm). La longueur d'onde a été choisie après optimisation des conditions expérimentales en termes d'efficacité de diffusion, de suppression de la fluorescence des nanocristaux de CdS (bande interdite ~ 2,4 eV) et de la taille du faisceau à la limite de diffraction. La puissance du laser était fixée à 1,7 mW avec un temps d'intégration de 10 secondes. Le balayage le long des nanoantennes a été effectué à l'aide d'une platine de translation XYZ motorisée avec un pas nominal de 0,01 µm. La polarisation de

la source d'excitation laser a été obtenue au moyen d'une lame demi-onde. Les mesures Raman ont été effectuées en éclairant une zone d'échantillonnage d'environ 1,39 μm^2 de nanocavités individuelles (dont l'aire est de 30 nm × 200 nm = 0,006 μm^2). Ainsi, l'aire de la zone illuminée du microsystème Raman est plus de 200 fois supérieure à celle d'une nanocavité.

Discussion des résultats

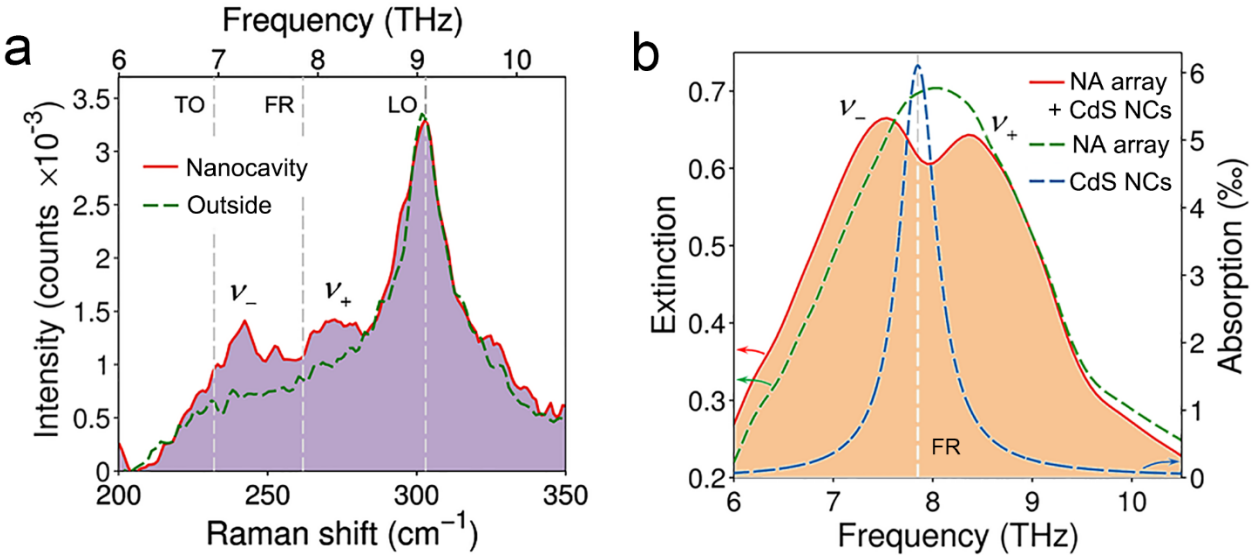

Fig. 10 **(a) Spectres Raman mesurés dans la région de la nanocavité (ligne rouge) et juste à l'extérieur de la nanocavité sur le substrat de silicium (ligne verte pointillée) pour un échantillon avec une monocouche; longueur des nanoantennes *L* = 5,75 µm. (b) Spectres d'extinction THz expérimentaux du réseau avec les nanoantennes de longueur *L* = 5,75 µm avec (ligne rouge) et sans (ligne verte pointillée) monocouche de nanocristaux à la surface du réseau; ligne bleue pointillée: spectre d'absorption d'une seule couche de nanocristaux. L'extinction est obtenue en calculant un moins la transmittance.**

La figure 10 résume l'idée de créer un état hybride à l'échelle nanométrique, en exploitant le couplage fort entre la résonance de la cavité d'une nanoantenne et le mode de phonon optique de FR des nanocristaux de CdS. Il en résulte la formation de deux vibro-polaritons résonants présentant à la fois des caractéristiques de la lumière et de la matière. Les nanocristaux de ce système couplé sont dotés de trois principales lignes de phonons : les modes de phonons TO et LO, qui sont également caractéristiques du CdS cristallin massif, ainsi qu'une résonance de phonon optique de FR, typique des nanoparticules [32], située entre les lignes de TO et de LO. À des fins de clarté, les trois lignes sont identifiées à la figure 10a, sur le spectre Raman d'une couche unique de nanocristaux de CdS déposée sur un substrat de silicium. Comme on peut le voir dans ce spectre, le mode de FR est situé dans la région des basses fréquences du pic principal des nanocristaux (mode de phonon LO) dans les mesures Raman. Inversement, comme le montre la figure 10b, le mode de FR est la seule caractéristique pertinente du spectre d'absorption THz en raison de sa nature dipolaire active. En réglant correctement la longueur (L

= 5,75 µm) des nanoantennes, nous pouvons observer des signes de séparation par résonance à la fois dans les mesures de spectroscopie Raman et celles d'extinction THz directe (courbes rouges des figures 10a et 10b, respectivement), jusqu'à 0,8 THz.

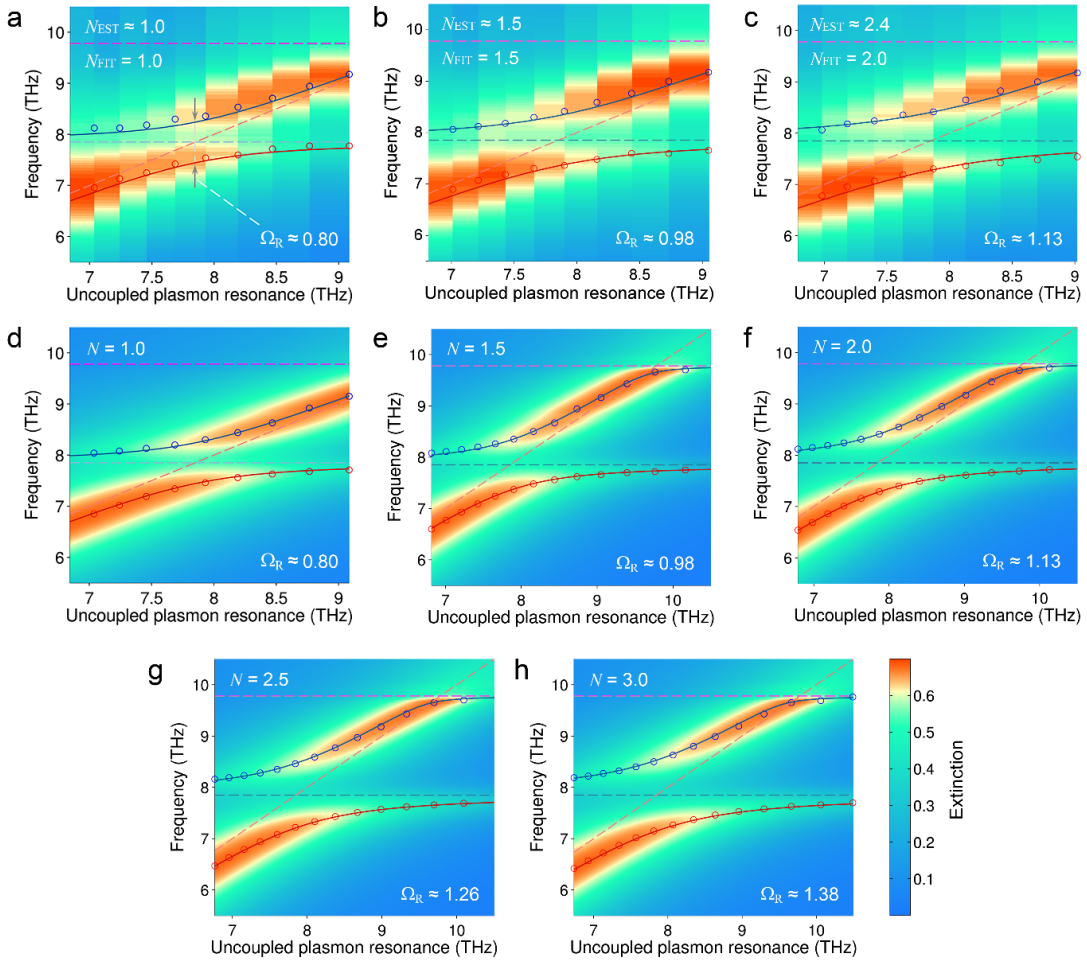

Fig. 11 Séparation de Rabi vs. nombre de couches de nanocristaux. Cartographie 2D expérimentale (a–c) et numérique (d–h) de la dispersion des branches de polariton pour différents nombres de couches de nanocristaux *N*.

Ici, nous discutons de la façon dont le couplage plasmon-phonon est affecté par le nombre de couches de nanocristaux. Pour augmenter le nombre de nanocristaux sur la surface de l'échantillon, nous avons appliqué un protocole spécifique pour ajouter des couches supplémentaires, tel qu'expliqué précédemment. La figure 11 montre la dispersion des deux branches de polariton pour différents nombres de couches, dans les simulations et les expériences. La séparation de Rabi de la résonance hybridée correspond à la séparation des deux branches lorsque la résonance du plasmon non-couplé (nanoantenne) est alignée sur le mode de FR non-couplé. En utilisant ces cartes d'extinction et en ajustant les pics des traces de polariton à l'aide d'un modèle à trois oscillateurs couplés, nous avons estimé (à partir de la

simulation et de l'expérience, figures 11a et d) une séparation de Rabi Ω_R d'environ 0,8 THz dans le cas d'une monocouche, correspondant à environ 10% de la fréquence de résonance de FR non-couplée.

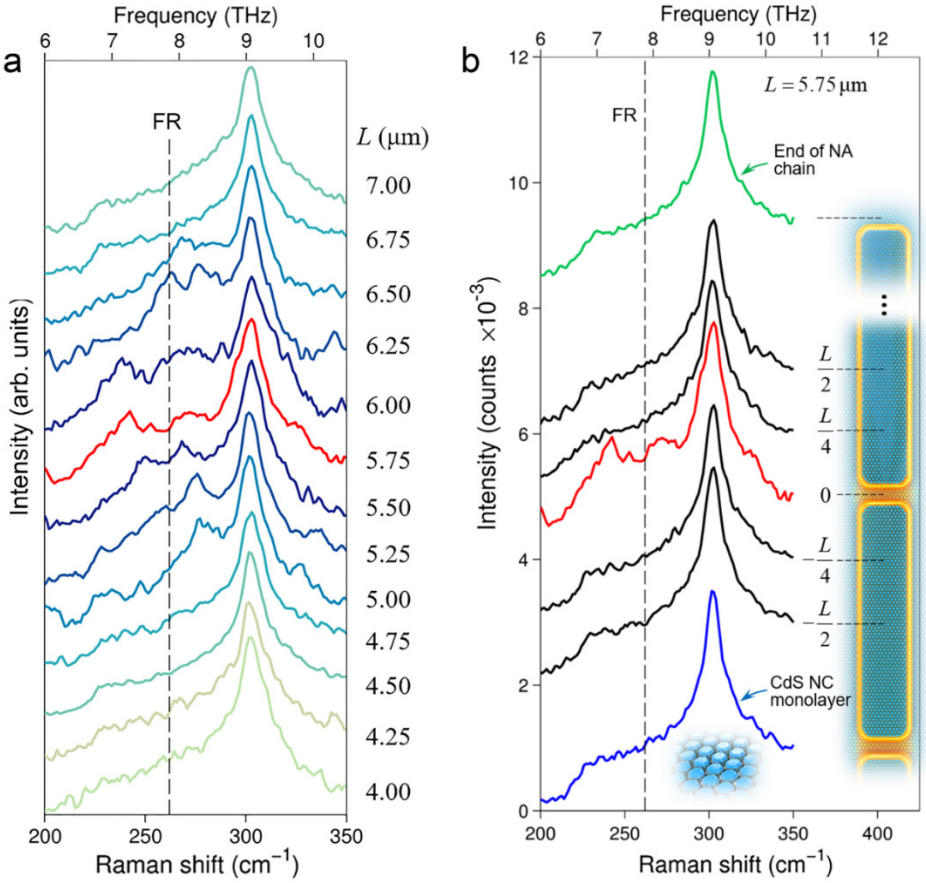

Fig. 12 **(a) Spectres Raman des nanocristaux mesurés dans une nanocavité pour différentes valeurs de L. (b) Spectres Raman des nanocristaux mesurés sur un réseau avec *L* = 5,75 µm : à différentes positions le long des nanoantennes formant une nanocavité (lignes noires), dans la région de la nanocavité (ligne rouge), à l'extrémité d'une chaîne de nanoantennes (ligne verte) et juste à l'extérieur d'une cavité sur le substrat de silicium (ligne bleue). Les spectres sont décalés verticalement pour plus de clarté.**

La figure 12 présente la caractérisation micro-Raman d'un échantillon recouvert d'une monocouche de nanocristaux. À partir de cette preuve expérimentale, nous pouvons déduire que la réponse phononique des nanocristaux de CdS est modifiée juste dans les nanocavités et seulement lorsque la longueur des nanoantennes est ajustée pour faire correspondre la résonance plasmonique des nanoantennes au mode de phonon de FR des nanocristaux. Ces conditions spécifiques sont les facteurs clés permettant l'hybridation. Si la résonance des réseaux de nanoantennes est « désaccordée » du mode de FR, les deux pics hybrides du spectre de Raman disparaissent éventuellement (voir figure 12a). La figure 12b montre des spectres Raman pris à différentes positions sur la surface de l'échantillon, dans le cas d'un réseau dont les antennes sont à une longueur ajustée pour correspondre au mode de FR (*L* = 5,75 µm). Si les

nanocristaux ne sont pas situés dans les nanocavités, leur spectre Raman ne montre aucun signe d'hybridation par résonance de phonon de FR.

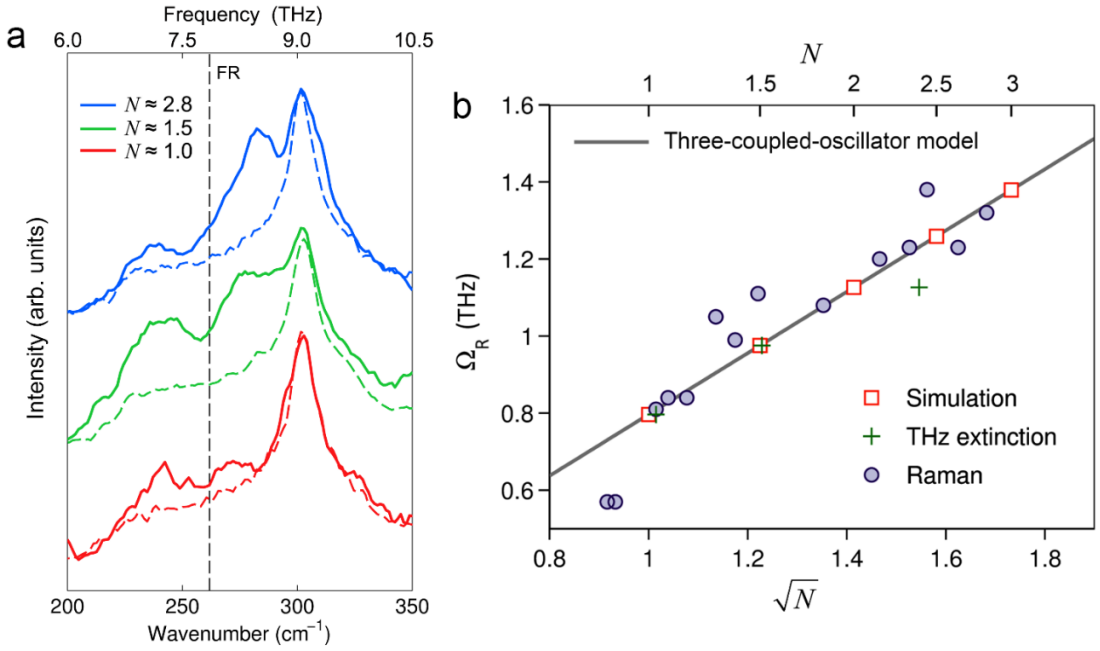

Fig. 13 **(a) Spectres Raman pour *L* = 5,75 µm et trois nombres différents de couches *N* de nanocristaux. Les lignes pleines correspondent aux spectres mesurés dans une nanocavité alors que les lignes pointillées sont associées aux spectres mesurés juste à l'extérieur de la cavité respective (avec les mêmes paramètres expérimentaux) sur le substrat de silicium. (b) Séparation de Rabi Ω_R en fonction de $\sqrt{N}$ obtenue par différentes méthodes : le modèle à trois oscillateurs couplés (ligne noire), les simulations numériques (carrés rouges), l'extinction THz (croix vertes) et les mesures Raman (cercles violets). Pour chaque point des mesures Raman, *N* est déterminé en considérant le nombre de nanocristaux contenus à l'intérieur de la nanocavité spécifique mesurée.**

Dans le cas de multicouches, les spectres Raman pour trois nombres différents de couches *N* sont présentés à la figure 13a, qui met clairement en évidence la modification significative de la réponse Raman induite par la présence de nanocristaux supplémentaires dans la nanocavité. Considérant que la taille de la zone d'illumination du système micro-Raman est plus de 200 fois supérieure à l'aire d'une nanocavité, nous notons également que l'amélioration de la réponse Raman dans notre système correspond aux valeurs accrues rapportées par la première amélioration vibro-polaritonique du signal Raman dans une microcavité de Fabry-Pérot [61], où le signal Raman a aussi été amplifié d'environ 2 ordres de grandeur. Il est important de noter que cette amélioration, contrairement au mécanisme traditionnel de diffusion Raman amélioré en surface [105], affecte uniquement la résonance de phonon hybridée, laissant le reste du spectre Raman inchangé. En considérant à nouveau les cartes d'extinction THz présentées à la figure 11, nous pouvons observer qu'en ajoutant davantage de couches de nanocristaux, la séparation de Rabi augmente. Cette tendance est également confirmée par les mesures Raman, comme le suggère le spectre de la figure 13a. Pour une comparaison immédiate des séparations de Rabi

obtenues à partir des mesures d'extinction (croix vertes), des simulations numériques (carrés rouges) et des mesures Raman (cercles violets), on peut se reporter à la figure 13b. Comme on peut le constater, tous les résultats suivent les échelles de grandeur attendues, comme prédit par le modèle à trois oscillateurs couplés.

Les travaux présentés dans ce chapitre ont défini une méthode novatrice pour modifier la réponse phononique optique des nanomatériaux, en exploitant simplement les propriétés uniques des nanocavités THz plasmoniques. Dans notre étude visant à établir une preuve de principe, nous avons constaté que, même sans excitation THz directe, le spectre de phonon des nanocristaux de CdS peut être modifié de manière significative à l'intérieur des nanocavités. Cela est dû à un champ électrique du vide extrêmement élevé dans la cavité qui transforme la résonance phononique dipolaire active des nanocristaux en deux nouvelles bandes de « vibro-polariton ». Ces résonances hybridées ont à la fois des caractéristiques de la lumière et de la matière et montrent ainsi un potentiel pour modifier la désintégration (généralement non-radiative) des phonons. Par exemple, les nouveaux états hybrides peuvent trouver une nouvelle voie pour se désintégrer à travers un processus radiatif, ce qui pourrait ouvrir la voie à une nouvelle classe de nanosources émettant un rayonnement THz. En plus de représenter un nouveau terrain de jeu pour la science et la technologie THz, nos découvertes mettent en lumière une stratégie potentiellement novatrice pour modifier la dissipation d'énergie liée aux phonons optiques et ainsi améliorer les performances électriques et optiques des nanodispositifs.

4 Une force de couplage améliorée dans les réseaux de nanoantennes en forme de lunes

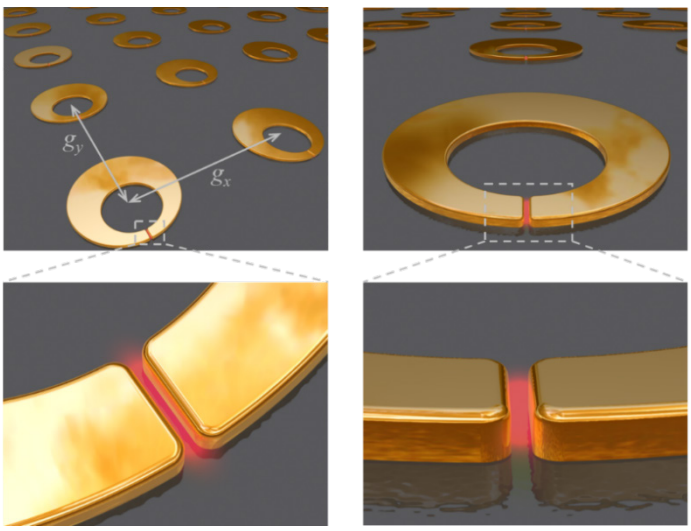

Fig. 14 Schéma d'un réseau de nanoantennes en forme de lunes. La taille d'une maille est $g_x = g_y = 9$ µm.

Ici, un nouveau nanorésonateur THz plasmonique en forme de lune est proposé pour améliorer l'interaction avec le mode de phonon de FR du CdS. Par rapport à la cavité de nanoantennes bout à bout, le nouveau design est doté d'une largeur de raie de résonance plus étroite, d'un volume modal considérablement réduit et d'une plus grande amélioration du champ THz local. La géométrie proposée s'inspire de la stratégie de réduction progressive des nanostructures métalliques pour réduire les pertes plasmoniques [113]. Par conséquent, contrairement aux résonateurs en anneau fendu conventionnels [114-117], une structure en croissant de lune (voir la figure 14) avec la nanocavité située entre les pointes du croissant apporte une amélioration notable de la localisation du champ THz, favorisant ainsi la force de couplage dans l'interaction avec les nanocristaux.

Nous définissons la « longueur » (L) de la nanoantenne en forme de lune comme étant la circonférence du cercle de référence central (voir le texte principal pour plus de détails) et un « facteur de lune » f_{m} comme le rapport entre la plus grande largeur du croissant et la largeur d'une extrémité pour quantifier l'amincissement de la lune. Nous fixons la longueur de l'antenne à 8 µm au début et trouvons qu'un facteur de lune de 6 permet d'atteindre l'amélioration maximale du champ (de l'ordre de 1000) à ~ 7,8 THz (très proche du mode de phonon optique de FR des nanocristaux de CdS). Les paramètres physiques et les conditions d'illumination dans les simulations sont les mêmes que dans le cas des nanoantennes droites (voir le chapitre précédent). La polarisation est toujours fixée le long de l'axe long des nanoantennes pour exciter une résonance dipolaire, afin de localiser efficacement le rayonnement dans le *nanogap*. La procédure de préparation des réseaux de nanoantennes THz en forme de lunes et des couches de nanocristaux de CdS est également identique à celle décrite dans le cas des antennes droites. Un exemple des réseaux fabriqués peut être visualisé dans l'image au MEB présentée à la figure 15a. La surface totale du réseau est d'environ 225 µm × 225 µm et contient 625 (25 × 25) lunes. À partir de l'image agrandie de la région d'un *nanogap* (figure 15b), nous pouvons remarquer que l'espacement sur les structures fabriquées correspond au paramètre de conception de 20 nm.

Nous avons également utilisé la méthode d'enduction centrifuge pour recouvrir de monocouche/multicouches de nanocristaux de CdS les nanoantennes en forme de lunes. La figure 16a montre une image au MEB d'un nanoantenne en forme de lune recouverte de nanocristaux de CdS. L'image agrandie d'une nanocavité couverte de CdS est également présentée à la figure 16b, montrant des dizaines de nanocristaux de CdS dans la nanocavité.

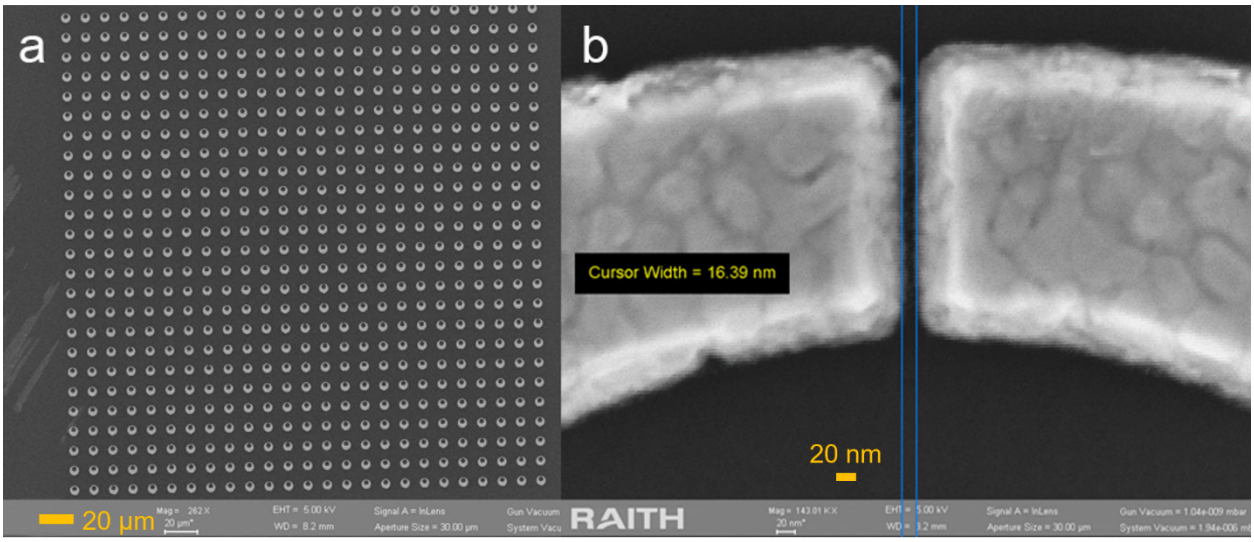

Fig. 15 **(a) Image au MEB d'un réseau fabriqué de nanoantennes en forme de lunes. (b) Agrandissement d'une image au MEB d'un nanogap.**

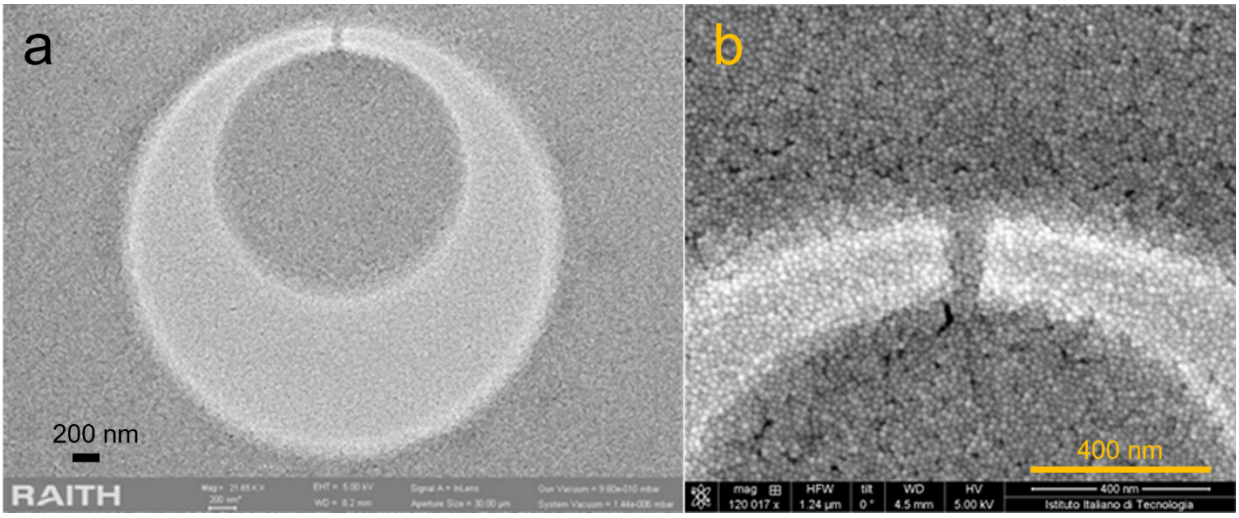

Fig. 16 **(a) Image au MEB d'une nanoantenne en forme de lune couverte de nanocristaux de CdS. (b) Agrandissement de l'image (a) au MEB.**

La carte 2D d'extinction mesurée pour les simples réseaux de nanoantennes en forme de lunes (en fonction de la fréquence et de la longueur de l'antenne) est montrée à la figure 17a. En recouvrant le réseau avec une ou plusieurs couches de nanocristaux de CdS, nous pouvons observer la formation et l'augmentation de la séparation de Rabi (figures 17b, c et d). Il est à noter que la surface du nanogap dans une nanoantenne en forme de lune est de 20×200 nm^2, ce qui correspond aux 2/3 de celle précédemment utilisée dans la structure de chaîne de nanoantennes bout à bout (30×200 nm^2). Cela signifie que le nombre de nanocristaux dans une nanocavité est généralement plus petit dans le cas du réseau avec nanoantennes en forme de lunes pour le même nombre de couches. Néanmoins, les séparations de Rabi obtenues avec la structure de

lune sont globalement plus grandes que celles mesurées pour la structure « bout à bout » (voir les estimations dans la légende de la figure 17), grâce à un couplage amélioré. Une telle séparation de Rabi prononcée a également été récemment confirmée par des mesures micro-Raman (voir un exemple pour le cas à 2 couches sur la figure 18), qui ont été effectuées sur les structures en forme de lunes en suivant la même procédure que celle décrite dans le cas des nanoantennes droites. Dans ce cas, l'amélioration du signal Raman pour les pics de vibro-polaritons semble également plus important que celle observée précédemment sur les réseaux d'antennes bout à bout.

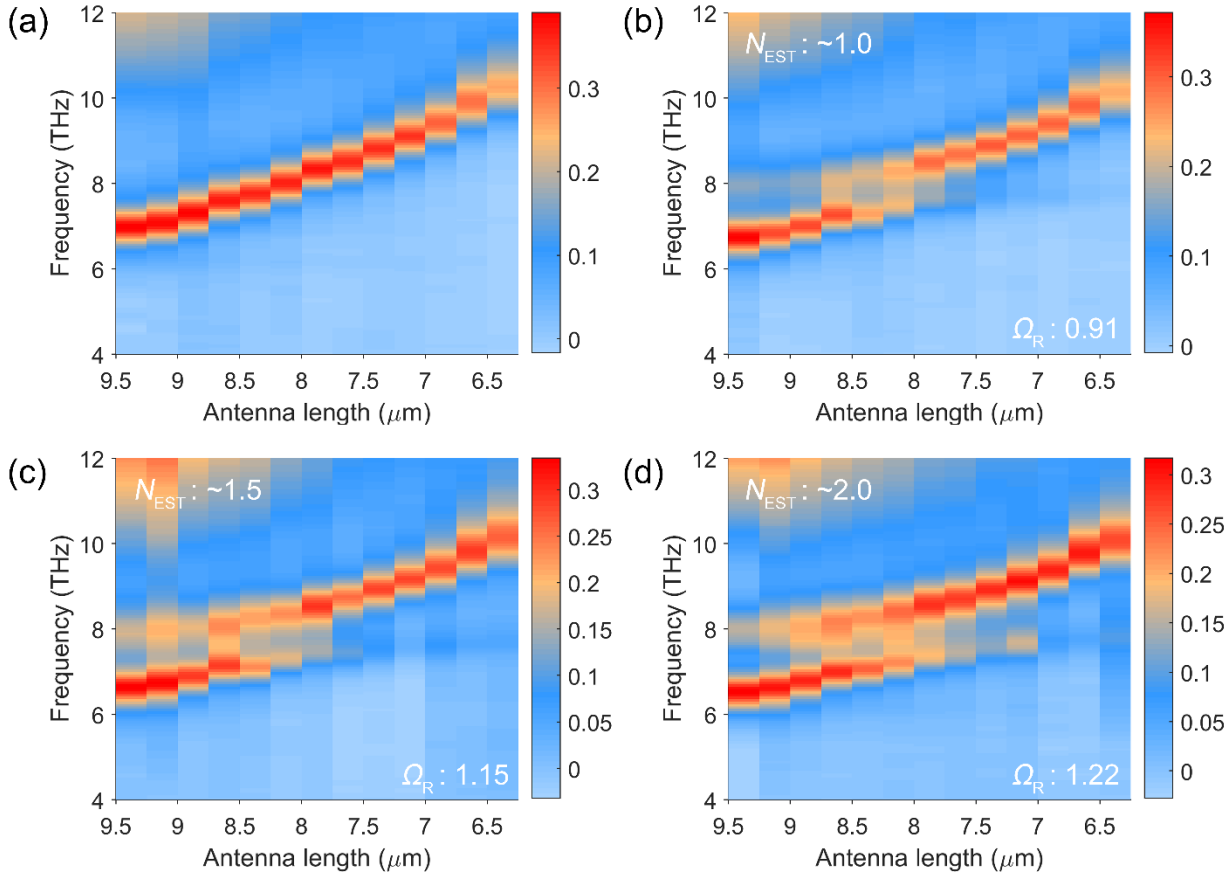

Fig. 17 Cartographie 2D de l'exctinction mesurée pour des réseaux simples de nanoantennes en forme de lunes (a) et pour les mêmes réseaux couverts par 1 (b), 1,5 (c) et 2 couches de nanocristaux de CdS.

Pour conclure, nous souhaitons mentionner qu'en ajoutant plus de nanocristaux dans une nanocavité en forme de lune (> 3 couches), notre système peut entrer dans le régime de couplage dit ultra-fort [4], c'est-à-dire que la force de couplage est supérieure de 0,1 à la fréquence centrale non-couplée, dans laquelle la force de couplage est une fraction non négligeable (typiquement supérieure à 10%) des fréquences propres des oscillateurs non interagissants. Un tel régime exotique est prometteur pour l'étude d'une multitude d'applications, par exemple en optique non-

linéaire, en optomécanique quantique, en plasmonique quantique et en émission du vide quantique [4]. Les nanoantennes en forme de lunes que j'ai conçues et dont j'ai validé le fonctionnement dans ce chapitre peuvent donc constituer une plateforme idéale pour explorer ces domaines de recherche extrêmement intrigants.

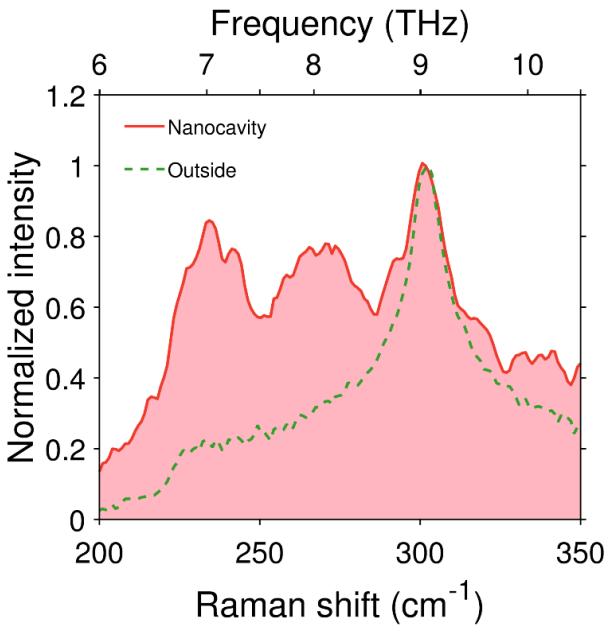

Fig. 18 **Spectre Raman pour une nanoantenne en forme de lune avec *L* = 8 µm et couverte par 2 couches de nanocristaux de CdS. La ligne pleine correspond au spectre mesuré dans la nanocavité tandis que la ligne pointillée est associée au spectre mesuré juste à l'extérieur de la même nanocavité.**

5 Conclusion et travaux futurs

L'objectif principal de cette thèse de doctorat était d'étudier l'interaction THz lumière-matière à l'échelle nanométrique dans des conditions de couplage fort. Cela a été réalisé dans un système de banc d'essai en utilisant des nanostructures plasmoniques THz résonantes couplées à un mode de phonon au dipôle actif de nanocristaux polaires. En particulier, j'ai contribué à la conception de deux plateformes de nanocavités plasmoniques pour modifier la réponse phononique optique de FR de nanocristaux de CdS : i) des réseaux de chaînes de nanoantennes bout à bout; ii) des réseaux de nanoantennes en forme de lunes. J'ai d'abord testé et vérifié l'efficacité de ces deux plateformes au moyen de simulations numériques. La fabrication et les caractérisations THz/Raman ont ensuite été réalisées à l'Institut Italien de Technologie (IIT, Italie) et à l'installation du synchrotron Elettra à Trieste (Italie). Enfin, j'ai effectué l'analyse et le post-traitement des données, ainsi que la modélisation théorique pour parvenir à une description juste de nos observations expérimentales. Plus précisément, les principales étapes de mon travail pendant cette thèse sont les suivantes :

1. J'ai contribué à l'identification, via une étude bibliographique exhaustive, d'un système de banc d'essai permettant de réaliser une hybridation nanométrique plasmon-phonon dans la région THz. Comme mentionné ci-dessus, ce système exploite un mode de phonon de surface (mode de phonon optique de FR) des nanocristaux de CdS et des cavités THz (nanoantennes). Ces dernières (nanocavités) sont vraiment cruciales pour le couplage fort nano-vibrationnel, car elles représentent un moyen efficace de confiner efficacement le rayonnement THz (longue longueur d'onde) dans de minuscules volumes. Cela garantit en retour des valeurs extrêmement élevées pour le champ électrique du vide dans la cavité. À cet égard, j'ai minutieusement développé des outils et des méthodes pour optimiser la géométrie des résonateurs (nanoantennes) afin de réduire leur volume modal caractéristique. J'ai également implémenté avec succès des modèles à deux et trois oscillateurs couplés pour trouver une correspondance avec la dispersion des branches de polariton obtenues à partir des spectres d'extinction expérimentaux, menant ainsi à une analyse approfondie des mécanismes physiques sous-jacents.

2. Afin de simuler numériquement le système étudié, j’ai décrit les propriétés optiques des matériaux utilisés : la permittivité de l’or dans la région THz a été définie à l’aide d’un modèle de Drude standard et de paramètres extraits de la littérature, tandis que la permittivité des nanocristaux de CdS a été directement extraite en ajustant la courbe (« fit ») des mesures de transmission THz sur une couche épaisse de nanocristaux. Pour éviter la simulation numérique des nanocristaux individuels dans les couches, j'ai utilisé le modèle de Lorentz dans la région de Reststrahlen pour le CdS, combiné à la règle des mélanges de Maxwell-Garnett. De cette manière, les simulations numériques basées sur la méthode des éléments finis ont convergé vers une solution beaucoup plus rapidement, tout en montrant un très bon accord avec les résultats expérimentaux.

3. Après avoir défini les permittivités, j'ai conçu des réseaux de chaînes infinies de nanoantennes d'or en appliquant les conditions limites périodiques de Floquet. L'onde THz incidente dans l’air (domaine semi-infini) peut toucher le réseau de nanoantennes en or par le haut et sa transmission est ensuite évaluée à travers le substrat de silicium semi-infini situé en dessous. Enfin, les réseaux de nanoantennes ont été recouverts d'une couche de nanocristaux de CdS de 10 nm d'épaisseur et les spectres de transmission ont été enregistrés pour différentes longueurs de nanoantennes, de sorte que la résonance plasmonique recouvrait la résonance de phonons du CdS. Le comportement de croisement évité typique du régime de couplage fort a été clairement observé.

4. Les échantillons conçus ont été fabriqués à l'Institut Italien de Technologie (IIT) en Italie (notre collaborateur international). La caractérisation de leur transmission a été réalisée à l'installation Elettra à Trieste (Italie) au moyen de rayonnement synchrotron THz. Les résultats expérimentaux ont montré un excellent accord avec les simulations numériques.

5. Les mêmes échantillons ont été étudiés par micro-spectroscopie Raman. Nous avons observé une signature de couplage fort (séparation de Rabi) remarquable même dans les spectres Raman, prouvant ainsi la nature du processus de couplage. En effet, dans de vraies conditions de couplage fort, l'hybridation se produit également sans qu'il soit nécessaire d'avoir une illumination THz, les deux oscillations étant couplées fortement au moyen du champ électrique du vide de la cavité.

6. Nous avons également constaté que la signature Raman de la résonance de phonon hybridée dans la cavité était améliorée d'environ deux ordres de grandeur. Comparé au SERS conventionnel, cette augmentation induite par un polariton n'affecte que la transition hybridée et le reste du spectre Raman demeure inchangé.

7. Inspiré par une étude récente de notre groupe concernant les nanoantennes rétrécies pour atténuer la perte ohmique des nanorésonateurs plasmoniques, j'ai conçu une structure de nanoantennes en forme de lune. Ce nouveau design peut réduire davantage le volume modal (bien en dessous du volume de la cavité géométrique) et favoriser encore plus l'augmentation du champ THz local. Ces nanoantennes en forme de lunes ont été fabriquées et caractérisées de manière similaire au design précédent de nanoantennes bout à bout. À la fois avec et sans illumination THz directe, nous avons constaté que cette nouvelle géométrie donnait des séparations de Rabi plus grandes, même si les nanocavités sont plus étroites et que le nombre de nanocristaux impliqués dans l'interaction est donc inférieur à celui dans la chaîne de nanoantennes bout à bout.

D'une part, les résultats présentés dans cette thèse pourraient ouvrir de nouvelles voies pour l'ingénierie de la réponse phononique des nanomatériaux fonctionnels, afin d'améliorer leurs propriétés d'émission de lumière ou de transport de charge, en raison du rôle crucial joué par les interactions électron-phonon dans de tels systèmes [30, 60, 118, 119]. D'autre part, le couplage fort nanométrique plasmon–phonon peut offrir une plateforme innovante pour la technologie THz, par exemple pour l'exploration de phénomènes non-linéaires améliorés et localisés [120-122], ainsi que pour la génération de rayonnement cohérent [123-127]. Les concepts et les découvertes de ce travail peuvent être transférés à une grande variété de plateformes. Par exemple, une avenue future que nous prévoyons explorer concerne la réalisation d'un système de couplage

fort plasmon-phonon utilisant des matériaux 2D, tels que les dichalcogénures de métaux de transition (TMD) [128-131], en vue d'améliorer la réponse optique/électrique des TMD par hybridation de phonon de surface, ce qui pourrait être pertinent pour l'avenir de la nano- et optoélectronique. Le couplage fort plasmon-phonon pourrait également aider à concevoir de nouveaux « états topologiques » [132-135]. Le couplage fort vibrationnel à l'échelle nanométrique s'annonce donc comme un outil précieux pour la réalisation d'une grande variété de nanodispositifs photoniques/phononiques novateurs aux propriétés uniques.

APPENDIX

1 Dissipated Power Calculation (Classical Two Coupled Oscillators)

Making use of the following relation:

$$\mathrm{Re}[\alpha]\mathrm{Re}[\beta]=\frac{1}{2}\mathrm{Re}[\alpha\beta]+\frac{1}{2}\mathrm{Re}[\alpha^{*}\beta]. \tag{A.1}$$

Considering the remaining non-zero term, we can have:

$$\begin{aligned}
&\frac{1}{T}\int_0^T \mathrm{Re}[f(t)]\mathrm{Re}[\dot{x}_1]dt \\
&=\frac{1}{2T}\int_0^T \mathrm{Re}[f(t)^{*}\cdot\dot{x}_1]dt \\
&=\frac{1}{2T}\int_0^T \mathrm{Re}\left[\left(Fe^{-i\omega t}\right)^{*}\cdot\left(-i\omega\tilde{\chi}_1 Fe^{-i\omega t}\right)\right]dt \\
&=\mathrm{Re}\left[-i\omega\tilde{\chi}_1F^2\right]\cdot\frac{1}{2T}\int_0^T \mathrm{Re}\left[e^{i\omega t}e^{-i\omega t}\right]dt \\
&=\mathrm{Re}\left[\frac{-i\omega\tilde{\chi}_1F^2}{2}\right].
\end{aligned} \tag{A.2}$$

Therefore the power dissipated by the driving force is:

$$P_{\mathrm{dissipate}}=\langle p(t)\rangle=\mathrm{Re}\left[\frac{-i\omega\tilde{\chi}_1F^2}{2}\right]. \tag{A.3}$$

Looking back at the equation of motion of the first oscillator, we can also extract the following power relations,

$$\begin{aligned}
&\frac{1}{T}\int_0^T \mathrm{Re}[\ddot{x}_1+\gamma_1\dot{x}_1+\omega_1^2x_1+g^2x_2]\cdot\mathrm{Re}[\dot{x}_1]dt=\frac{1}{T}\int_0^T \mathrm{Re}[f(t)]\cdot\mathrm{Re}[\dot{x}_1]dt \\
&\frac{1}{T}\int_0^T \mathrm{Re}[\ddot{x}_1]\cdot\mathrm{Re}[\dot{x}_1]dt+\frac{1}{T}\int_0^T \mathrm{Re}[\gamma_1\dot{x}_1]\cdot\mathrm{Re}[\dot{x}_1]dt+ \\
&\qquad P_{\mathrm{kinetic},1}=0 \qquad\qquad P_{\mathrm{damp},1}>0 \\
&\frac{1}{T}\int_0^T \mathrm{Re}[\omega_1^2x_1]\cdot\mathrm{Re}[\dot{x}_1]dt+\frac{1}{T}\int_0^T \mathrm{Re}[g^2x_2]\cdot\mathrm{Re}[\dot{x}_1]dt \\
&\qquad P_{\mathrm{restore},1}=0 \qquad\qquad P_{\mathrm{coupling},1}>0 \\
&=\frac{1}{T}\int_0^T \mathrm{Re}[f(t)]\cdot\mathrm{Re}[\dot{x}_1]dt \\
&\qquad P_{\mathrm{dissipate}}>0,
\end{aligned} \tag{A.4}$$

which gives,

$$P_{\text{damp},1} + P_{\text{coupling},1} = P_{\text{dissipate}}. \tag{A.5}$$

For the second oscillator, we also have the dissipated power relation:

$$\frac{1}{T}\int_0^T \text{Re}\left[\ddot{x}_2 + \gamma_2\dot{x}_2 + \omega_2^2 x_2 + g^2 x_1\right]\cdot\text{Re}\left[\dot{x}_2\right]dt = 0$$

$$\begin{aligned}
&\frac{1}{T}\int_0^T \text{Re}\left[\ddot{x}_2\right]\cdot\text{Re}\left[\dot{x}_2\right]dt + \frac{1}{T}\int_0^T \text{Re}\left[\gamma_2\dot{x}_2\right]\cdot\text{Re}\left[\dot{x}_2\right]dt + \\
&\qquad P_{\text{kinetic},2} = 0 \qquad\qquad P_{\text{damp},2} > 0 \\
&\frac{1}{T}\int_0^T \text{Re}\left[\omega_2^2 x_2\right]\cdot\text{Re}\left[\dot{x}_2\right]dt + \frac{1}{T}\int_0^T \text{Re}\left[g^2 x_1\right]\cdot\text{Re}\left[\dot{x}_2\right]dt = 0, \\
&\qquad P_{\text{restore},2} = 0 \qquad\qquad P_{\text{coupling},2} < 0
\end{aligned} \tag{A.6}$$

because such power is gained by the oscillator 2 through coupling

which gives a relation,

$$\begin{aligned}
&P_{\text{damp},2} + P_{\text{coupling},2} = 0 \\
&\text{or} \\
&P_{\text{damp},2} = -P_{\text{coupling},2}.
\end{aligned} \tag{A.7}$$

Through calculation, we also find $P_{\text{coupling},1} = -P_{\text{coupling},2}$, therefore from Equation (A.5) and Equation (A.7) we know that the total dissipated power from the driving force is, as trivially expected, equal to the sum of the damped power in the two oscillators:

$$P_{\text{damp},1} + P_{\text{damp},2} = P_{\text{dissipate}}. \tag{A.8}$$

In other words, to calculate the overall dissipated power in the coupled system (for only one driving force), one can simply use Equation (A.3) and the $\tilde{\chi}_1(\omega)$ of the first oscillator only, which the driving force is applied to.

2 Roots of the Three-level Coupling System (Phenomenological Quantum Model)

Solving the following determinant equation:

$$\begin{vmatrix} E_{\mathrm{p}}-E & E_{g1} & E_{g2} \\ E_{g1} & E_1-E & 0 \\ E_{g2} & 0 & E_2-E \end{vmatrix}=0, \tag{A.9}$$

is equivalent to solve:

$$\left(-E_1E_2E_{\mathrm{p}}+E_2E_{g1}^2+E_1E_{g2}^2\right)+\left(E_1E_2+E_1E_{\mathrm{p}}+E_2E_{\mathrm{p}}-E_{g1}^2-E_{g2}^2\right)z+\left(-E_1-E_2-E_{\mathrm{p}}\right)z^2+z^3=0. \tag{A.10}$$

The roots are:

$$\begin{aligned} E_{r3} &= A_1+A_6 \\ E_{r2} &= A_1-\frac{1}{2}A_6+i\frac{\sqrt{3}}{2}A_7 \\ E_{r1} &= A_1-\frac{1}{2}A_6-i\frac{\sqrt{3}}{2}A_7. \end{aligned} \tag{A.11}$$

in which the parameters from A_1 to A_7 are:

$$\begin{aligned} A_1 &= \frac{E_1+E_2+E_{\mathrm{p}}}{3} \\ A_2 &= \frac{\left(E_1+E_2+E_{\mathrm{p}}\right)^2}{9}+\frac{E_{g1}^2+E_{g2}^2-E_1E_2-E_1E_{\mathrm{p}}-E_2E_{\mathrm{p}}}{3} \\ A_3 &= \frac{\left(E_1+E_2+E_{\mathrm{p}}\right)\left(-E_{g1}^2-E_{g2}^2+E_1E_2+E_1E_{\mathrm{p}}+E_2E_{\mathrm{p}}\right)}{6} \\ A_4 &= \frac{E_1E_{g2}^2+E_2E_{g1}^2-E_1E_2E_{\mathrm{p}}}{2}-\frac{\left(E_1+E_2+E_{\mathrm{p}}\right)^3}{27}+A_3 \\ A_5 &= \left(\left(A_4^2-A_2^3\right)^{\frac{1}{2}}-A_4\right)^{\frac{1}{3}} \\ A_6 &= \frac{A_2}{A_5}+A_5 \\ A_7 &= \frac{A_2}{A_5}-A_5. \end{aligned} \tag{A.12}$$

3 Decomposition of the Illumination Condition

Starting from the *s* – polarization (see the schematic in Figure 3.4), we can simply describe all the magnitude components before considering the Fresnel coefficients as follows.

Incident:

$$\begin{aligned} E_{0x}^{\mathrm{s},i} &= -\sin\varphi E_0^{\mathrm{s}}, \\ E_{0y}^{\mathrm{s},i} &= \cos\varphi E_0^{\mathrm{s}}, \\ E_{0z}^{\mathrm{s},i} &= 0. \end{aligned} \tag{A.13}$$

Reflected:

$$\begin{aligned} E_{0x}^{\mathrm{s},r} &= -\sin\varphi E_0^{\mathrm{s}}, \\ E_{0y}^{\mathrm{s},r} &= \cos\varphi E_0^{\mathrm{s}}, \\ E_{0z}^{\mathrm{s},r} &= 0. \end{aligned} \tag{A.14}$$

Transmitted:

$$\begin{aligned} E_{0x}^{\mathrm{s},t} &= -\sin\varphi E_0^{\mathrm{s}}, \\ E_{0y}^{\mathrm{s},t} &= \cos\varphi E_0^{\mathrm{s}}, \\ E_{0z}^{\mathrm{s},t} &= 0. \end{aligned} \tag{A.15}$$

Meanwhile, for the *p* – polarization, we can describe all the components as follows.

Incident:

$$\begin{aligned} E_{0x}^{\mathrm{p},i} &= \cos\varphi\cos\theta_1 E_0^{\mathrm{p}}, \\ E_{0y}^{\mathrm{p},i} &= \sin\varphi\cos\theta_1 E_0^{\mathrm{p}}, \\ E_{0z}^{\mathrm{p},i} &= \sin\theta_1 E_0^{\mathrm{p}}. \end{aligned} \tag{A.16}$$

Reflected:

$$\begin{aligned} E_{0x}^{\mathrm{p},r} &= -\cos\varphi\cos\theta_1 E_0^{\mathrm{p}} = -E_{0x}^{\mathrm{p},i}, \\ E_{0y}^{\mathrm{p},r} &= -\sin\varphi\cos\theta_1 E_0^{\mathrm{p}} = -E_{0y}^{\mathrm{p},i}, \\ E_{0z}^{\mathrm{p},r} &= \sin\theta_1 E_0^{\mathrm{p}} = E_{0z}^{\mathrm{p},i}. \end{aligned} \tag{A.17}$$

Transmitted:

$$
\begin{aligned}
E_{0x}^{\mathrm{p},t} &= \cos\varphi\cos\theta_2 E_0^{\mathrm{p}},\\
E_{0y}^{\mathrm{p},t} &= \sin\varphi\cos\theta_2 E_0^{\mathrm{p}},\\
E_{0z}^{\mathrm{p},t} &= \sin\theta_2 E_0^{\mathrm{p}}.
\end{aligned}
\tag{A.18}
$$

Considering a plane wave $\mathbf{E} = \mathbf{E}_0 \exp\left(-i\mathbf{k}\cdot\mathbf{r}\right)$, we can decompose it in the following way:

$$
\begin{aligned}
E_x &= E_{0x}\exp\left(-i\left(k_x x + k_y y + k_z z\right)\right),\\
E_y &= E_{0y}\exp\left(-i\left(k_x x + k_y y + k_z z\right)\right),\\
E_z &= E_{0z}\exp\left(-i\left(k_x x + k_y y + k_z z\right)\right).
\end{aligned}
\tag{A.19}
$$

Now we can get the decomposed fields for *s* and *p* polarized wave.

s – polarization:

Incident:

$$
\begin{aligned}
E_x^{\mathrm{s},i} &= E_{0x}^{\mathrm{s},i}\exp\left(-i\left(k_x^i x + k_y^i y + k_z^i z\right)\right),\\
E_y^{\mathrm{s},i} &= E_{0y}^{\mathrm{s},i}\exp\left(-i\left(k_x^i x + k_y^i y + k_z^i z\right)\right),\\
E_z^{\mathrm{s},i} &= E_{0z}^{\mathrm{s},i}\exp\left(-i\left(k_x^i x + k_y^i y + k_z^i z\right)\right).
\end{aligned}
\tag{A.20}
$$

Reflected:

$$
\begin{aligned}
E_x^{\mathrm{s},r} &= r_{\mathrm{s}} E_{0x}^{\mathrm{s},r}\exp\left(-i\left(k_x^r x + k_y^r y + k_z^r z\right)\right),\\
E_y^{\mathrm{s},r} &= r_{\mathrm{s}} E_{0y}^{\mathrm{s},r}\exp\left(-i\left(k_x^r x + k_y^r y + k_z^r z\right)\right),\\
E_z^{\mathrm{s},r} &= r_{\mathrm{s}} E_{0z}^{\mathrm{s},r}\exp\left(-i\left(k_x^r x + k_y^r y + k_z^r z\right)\right).
\end{aligned}
\tag{A.21}
$$

Transmitted:

$$
\begin{aligned}
E_x^{\mathrm{s},t} &= t_{\mathrm{s}} E_{0x}^{\mathrm{s},t}\exp\left(-i\left(k_x^t x + k_y^t y + k_z^t z\right)\right),\\
E_y^{\mathrm{s},t} &= t_{\mathrm{s}} E_{0y}^{\mathrm{s},t}\exp\left(-i\left(k_x^t x + k_y^t y + k_z^t z\right)\right),\\
E_z^{\mathrm{s},t} &= t_{\mathrm{s}} E_{0z}^{\mathrm{s},t}\exp\left(-i\left(k_x^t x + k_y^t y + k_z^t z\right)\right).
\end{aligned}
\tag{A.22}
$$

p – polarization:

Incident:

$$
\begin{aligned}
E_x^{\mathrm{p},i} &= E_{0x}^{\mathrm{p},i} \exp\left(-i\left(k_x^i x + k_y^i y + k_z^i z\right)\right), \\
E_y^{\mathrm{p},i} &= E_{0y}^{\mathrm{p},i} \exp\left(-i\left(k_x^i x + k_y^i y + k_z^i z\right)\right), \\
E_z^{\mathrm{p},i} &= E_{0z}^{\mathrm{p},i} \exp\left(-i\left(k_x^i x + k_y^i y + k_z^i z\right)\right).
\end{aligned} \tag{A.23}
$$

Reflected:

$$
\begin{aligned}
E_x^{\mathrm{p},r} &= r_{\mathrm{p}} E_{0x}^{\mathrm{p},r} \exp\left(-i\left(k_x^r x + k_y^r y + k_z^r z\right)\right), \\
E_y^{\mathrm{p},r} &= r_{\mathrm{p}} E_{0y}^{\mathrm{p},r} \exp\left(-i\left(k_x^r x + k_y^r y + k_z^r z\right)\right), \\
E_z^{\mathrm{p},r} &= r_{\mathrm{p}} E_{0z}^{\mathrm{p},r} \exp\left(-i\left(k_x^r x + k_y^r y + k_z^r z\right)\right).
\end{aligned} \tag{A.24}
$$

Transmitted:

$$
\begin{aligned}
E_x^{\mathrm{p},t} &= t_{\mathrm{p}} E_{0x}^{\mathrm{p},t} \exp\left(-i\left(k_x^t x + k_y^t y + k_z^t z\right)\right), \\
E_y^{\mathrm{p},t} &= t_{\mathrm{p}} E_{0y}^{\mathrm{p},t} \exp\left(-i\left(k_x^t x + k_y^t y + k_z^t z\right)\right), \\
E_z^{\mathrm{p},t} &= t_{\mathrm{p}} E_{0z}^{\mathrm{p},t} \exp\left(-i\left(k_x^t x + k_y^t y + k_z^t z\right)\right).
\end{aligned} \tag{A.25}
$$

Then we combine the *s* and *p* polarizations as follows:

Incident:

$$
\begin{aligned}
E_x^i &= E_x^{\mathrm{s},i} + E_x^{\mathrm{p},i}, \\
E_y^i &= E_y^{\mathrm{s},i} + E_y^{\mathrm{p},i}, \\
E_z^i &= E_z^{\mathrm{s},i} + E_z^{\mathrm{p},i}.
\end{aligned} \tag{A.26}
$$

Reflected:

$$
\begin{aligned}
E_x^r &= E_x^{\mathrm{s},r} + E_x^{\mathrm{p},r}, \\
E_y^r &= E_y^{\mathrm{s},r} + E_y^{\mathrm{p},r}, \\
E_z^r &= E_z^{\mathrm{s},r} + E_z^{\mathrm{p},r}.
\end{aligned} \tag{A.27}
$$

Transmitted:

$$
\begin{aligned}
E_x^t &= E_x^{\mathrm{s},t} + E_x^{\mathrm{p},t}, \\
E_y^t &= E_y^{\mathrm{s},t} + E_y^{\mathrm{p},t}, \\
E_z^t &= E_z^{\mathrm{s},t} + E_z^{\mathrm{p},t}.
\end{aligned} \tag{A.28}
$$

In the end, we can adequately describe the general background field $\mathbf{E}_{\mathrm{b}}$ at a two-material interface, which is given by Equation (3.38) in Section 3.6.